

UC San Diego

UC San Diego Electronic Theses and Dissertations

Title

Nano-tribology of discrete track recording media

Permalink

<https://escholarship.org/uc/item/7f92q72x>

Author

Yoon, Yeoungchin

Publication Date

2010

Peer reviewed|Thesis/dissertation

UNIVERSITY OF CALIFORNIA, SAN DIEGO

Nano-Tribology of Discrete Track Recording Media

A dissertation submitted in partial satisfaction of the

requirements for the degree

Doctor of Philosophy

in

Engineering Sciences (Mechanical Engineering)

by

Yeoungchin Yoon

Committee in Charge:

Professor Frank E. Talke, Chair

Professor David J. Benson

Professor Eric Fullerton

Professor Sung Ho Jin

Professor Jack Keil Wolf

2010

Copyright

Yeoungchin Yoon, 2010

All rights reserved.

The dissertation of Yeoungchin Yoon is approved, and it is acceptable in quality and form for publication on microfilm:

Chair

University of California, San Diego

2010

Dedicated to my parents

TABLE OF CONTENTS

Signature Page.....	iii
Dedication.....	iv
Table of Contents.....	v
List of Figures.....	x
List of Tables.....	xix
Acknowledgements.....	xx
Vita.....	xxiii
Publications.....	xxiv
Abstract of the Dissertation.....	xxv
Chapter 1 Introduction.....	1
1.1 History of Hard Disk Drives	1
1.2 Principle of Magnetic Recording	5
1.2.1 Magnetic Hysteresis	5
1.2.2 Write process in magnetic recording [15]	8
1.2.3 Read process in magnetic recording [16]	10
1.2.4 Evolution of Magnetic Read/Write Heads	15
1.3 Evolution of Magnetic Recording Technologies.....	20
1.3.1 Longitudinal Magnetic Recording (LMR)	21
1.3.2 Perpendicular Magnetic Recording (PMR).....	23

1.3.3 Microwave-assisted Magnetic Recording	25
1.3.4 Heat-assisted Magnetic Recording	26
1.3.5 Patterned Magnetic Recording [35-39]	28
1.3.6 Combination of bit patterned media with heat-assisted magnetic recording.....	29
1.4 Head/Disk Interface (HDI)	31
1.4.1 Air-bearing force	34
1.4.2 Air-bearing sliders	36
1.4.3 Intermolecular forces.....	41
1.4.4 Adhesion forces of lubricant	44
1.4.5 Hysteresis of “touch-down” and “take-off”	46
1.5 Organization of the Dissertation.....	49
Bibliography.....	51
Chapter 2 Characterization of Discrete Track Recording Media.....	56
2.1 Manufacturing of Patterned media	56
2.1.1 Substrate patterning method.....	56
2.1.2 Magnetic layer patterning method.....	59
2.2 Dynamic characteristics of magnetic recording sliders on DTR media	62
2.3 Contact behavior on patterned media	66
Bibliography.....	69
Chapter 3 Investigation of the Flyability of Discrete Track Recording Media..	75
3.1 Introduction	72
3.2 Discrete Track Recording Media.....	73
3.3 Atomic force microscopy (AFM) and magnetic force microscopy (MFM) analysis on Discrete Track Recording media	74

3.4 Flyability of Magnetic Recording Sliders	78
3.4. 1 Experimental Setup and Parameters	78
3.4.2 Experimental Results	80
3.5 Numerical Analysis of Flyability of Magnetic Recording Sliders	84
3.5.1 Numerical Models	84
3.5.2 Numerical Results	86
3.6 Summary and Conclusions	88
Bibliography	89
Chapter 4 Touch-down and Take-off Hysteresis of Magnetic Recording Sliders on Discrete Track Media	91
4.1 Introduction	91
4.2 Experimental setup and parameters	92
4.3 Experimental results	95
4.3.1 Touch-down velocity for smooth and DTR media	95
4.3.2 Investigation of touch-down and take-off behavior as a function of ambient pressure for smooth and DTR media	100
4.3.3 Contact start-stop test	106
4.4 Summary and Conclusions	108
4.5 Acknowledgement	109
Bibliography	110
Chapter 5 Investigation of Contact Deformation and Wear Characteristics of Discrete Track Recording Media	112
5.1 Introduction	113
5. 2 Experimental procedure	114

5.2.1	Contacts between slider and DTR disk	115
5.2.2	Nano-indentation and nano-scratch testing	116
5.2.3	Reciprocal wear testing	117
5.3	Experimental investigation.....	118
5.3.1	Wear of DTR media due to contacts between slider and disk.....	118
5.3.2	Contact deformation of smooth and discrete track surfaces using nano-indentation and nano-scratch testing	120
5.3.3	Wear characteristics of discrete track media using reciprocal wear testing	128
5.4	Numerical investigation of static contact behavior	133
5.5	Summary and Conclusions	136
	Bibliography.....	138
Chapter 6 Wettability, Adhesion and Friction Force of Discrete Track Recording Media.....		140
6.1	Introduction	141
6.2	Theoretical background.....	143
6.2.1	Contact angle with rough surfaces	143
6.2.2	Adhesion measurements.....	149
6.2.2.1	Contact mechanics model for adhesive force.....	152
6.2.2.2	Atomic force microscopy (AFM) methodology.....	153
6.2.2.3	Adhesion based on contact mechanics modeling.....	154
6.3	Specimen preparation	152
6.4	Contact angle measurements	153
6.5	Adhesion measurements with atomic force microscopy (AFM).....	158
6.6	Friction force measurement using contact start-stop (CSS) test	162

6.7 Summary and Conclusions	166
Bibliography.....	167
Chapter 7 Planarization of Discrete Track Recording Media to Improve Flyability of Magnetic Recording Sliders.....	170
7.1 Introduction	171
7.2 Procedures and Specimen Preparation	173
7.3 Experimental Procedure	173
7.3.1 Planarization as a function of disk speed	173
7.3.2 Adhesion studies of HSQ	178
7.3.3 Hardness and scratch studies of HSQ.....	180
7.3.4 Comparison of flyability before and after planarization	182
7.4 Summary and Conclusions	183
7.5 Acknowledgment.....	183
Bibliography.....	184
Chapter 8 Summary and Conclusions.....	186
Appendix A The Reynolds Equation.....	191
Appendix B Slider Air Bearing Simulations and the CMRR Air Bearing Simulator	203
Bibliography.....	207

LIST OF FIGURES

Figure 1.1 The Random Access Method of Accounting and Control (RAMAC); demonstrated in Norte Dame Development Lab. on Sep. 13 th , 1956. (Source: IBM)	2
Figure 1.2 Historical areal density increase of hard disk drives (Source: [8], [9]) ..	4
Figure 1.3 Historical price trend of magnetic hard disk drives per Gbyte (Source: Ed Grochowski IDEMA).....	5
Figure 1.4 Alignment of magnetic moments in the case of (a) unmagnetized and (b) magnetized ferromagnetic material.	7
Figure 1.5 Hysteresis loop of ferromagnetic material (Source: [12], [13]).....	8
Figure 1.6 Write process in magnetic medium.....	9
Figure 1.7 Reciprocity between recording head and magnetic medium	10
Figure 1.8 Schematic of read/write head and parameters d , g , and δ	14
Figure 1.9 Schematic of Non-return to zero inverted (NRZI) encoding method ...	14
Figure 1.10 Different types of read/write heads; (a) an inductive read/write head and (b) a MR/GMR/TMR separated read and write head	15
Figure 1.11 Schematic of ferrite head and thin film head (Source: [21]).....	16
Figure 1.12 Schematic of magnetoresistive (MR) head (Source: [22]).....	17
Figure 1.13 Schematic of giant magnetoresistance (GMR) (Source: Magnetic Material Center/National Institute for Materials Science (NIMS)).....	18
Figure 1.14 Schematic of tunneling magnetoresistance (TMR) (Source of image: Magnetic Material Center/National Institute for Materials Science (NIMS)).....	19
Figure 1.15 Schematic of a typical single pole PMR writing head (Source: [26])	20
Figure 1.16 Schematic of longitudinal magnetic recording	21
Figure 1.17 Schematic of the cross-section of the multilayered longitudinal recording medium structure.....	22

Figure 1.18 Schematic of perpendicular magnetic recording (Source: [28])	24
Figure 1.19 Schematic cross-section of the perpendicular recording media and surface observation photography by transmission electron microscopy (TEM) (Source of picture (b): [29])	25
Figure 1.20 Diagram of microwave-assisted magnetic recording.....	26
Figure 1.21 Lowering magnetic coercivity through heating of the magnetic media during Heat Assisted Magnetic Recording.....	27
Figure 1.22 Schematic of heat-assisted magnetic recording (HAMR) (Source: [33])	27
Figure 1.23 (a) Conventional smooth disk and (b) discrete track recording disk and (c) bit patterned disk.....	29
Figure 1.24 Schematic of the writing process using a combination of bit patterned media (BPM) and head-assisted magnetic recording (HAMR) technologies (Source: [38]).....	30
Figure 1.25 Schematic of slider/disk assembly: (a) top view, (b) side view, and (c) magnified view of the interface between head and disk.....	33
Figure 1.26 Schematic of slider-disk interface.....	36
Figure 1.27 (a) Schematic of slider flying over disk and pressure distribution on the air-bearing surface as (b) top view and (c) side view	37
Figure 1.28 (a) Flying height as a function of product year and (b) magnified view of the flying height	38
Figure 1.29 Magnified read/write head (a) before thermal flying height control and (b) after thermal flying height control	39
Figure 1.30 The evolution of self-pressurized air-bearing designs (Source: [46]).	40
Figure 1.31 Typical sub-ambient pressure slider	41
Figure 1.32 (a) Stable flying condition and (b) contact condition due to intermolecular and adhesion forces	42
Figure 1.33 Lennard-Jones potential energy versus distance.....	43
Figure 1.34 In the beginning of the contact of the slider with the lubricant	45

Figure 1.35 Elongated meniscus bridge and adhesion forces between slider and disk	46
Figure 1.36 Hysteresis between “touch-down” and “take-off” velocity of a slider on a disk.....	47
Figure 1.37 Dynamic characteristics of sliders on (a) “touch-down” and (b) “take-off”	48
Figure 2.1 Schematic of discrete track recording (DTR) technology	56
Figure 2.2 Schematic for “substrate patterning” process flow chart using nano-imprint lithography (NIL) to create the land and groove structure on NiP-plated substrate.....	57
Figure 2.3 TEM image of the cross section of a sputtered DTR disk: (a) a land between two grooves and (b) cross section in the vicinity of a groove wall [Source: 3].....	58
Figure 2.4 Schematic for “magnetic layer patterning” process flow using nano-imprint lithography (NIL) to create the land and groove structure on NiP-plated substrate [Source: 4].....	60
Figure 2.5 TEM image of the cross section of the patterned media [Source: 4]....	61
Figure 2.6 Process flow for fabrication of quartz master disk (Source: [6])	62
Figure 2.7 Schematic of a flying slider on the DTR disk.....	64
Figure 2.8 Typical pressure distributions on the center pads of sliders (a) over smooth media and (b) over DTR media	64
Figure 2.9 Flying height loss as a function of groove depth and the ratio of groove width to track pitch.....	65
Figure 2.10 Von Mises stress contour showing yielding on a pattern (yield stress is 3 GPa) [Source: [14]]	66
Figure 2. 11 Von Mises stress contour with filling material [Source: [14]].....	67
Figure 2.12 Von Mises stress contour at the edge of a pattern (unit is 10^9 GPa) [Source: [15]].....	67

Figure 3.1 Schematic of discrete track recording disk; (a) DTR disk and (b) cross section of DTR disk.....	74
Figure 3.2 Layer structure of a discrete track recording medium	75
Figure 3.3 (a) AFM and (b) MFM measurements on a discrete track recording medium with 20 nm groove depth and 90 groove width.....	76
Figure 3.4 (a) AFM and (b) MFM measurements on a discrete track recording medium with 30 nm groove depth and 70 nm groove width.....	77
Figure 3.5 (a) AFM and (b) MFM measurements on a discrete track recording medium with 40 nm groove depth and 80 nm groove width.....	77
Figure 3.6 Schematic of the experimental setup	78
Figure 3.7 SEM images of air- bearing surfaces; (a) Slider “A” and (b) Slider “B”	79
Figure 3.8 Frequency spectra of LDV signal for slider “A”	81
Figure 3.9 Frequency spectra of AE signal for slider “A”	81
Figure 3.10 Frequency spectra of LDV signal for slider “B”.....	82
Figure 3.11 Frequency spectra of AE signal for slider “B”	82
Figure 3.12 Standard deviation of flying height on DTR media.....	83
Figure 3.13 Surface reflectance analysis (SRA) images after flyability testing on DTR media with slider “B”; (a) DTR disk A, (b) DTR disk B and (c) DTR disk C	84
Figure 3.14 Air-bearing surfaces and mesh images; (a) slider “A” and (b) slider “B”	85
Figure 3.15 Typical air-bearing pressure distributions (a) on smooth media and (b) on DTR media	86
Figure 3.16 Numerical predictions of flying height on smooth disk and DTR media	87
Figure 4.1 Schematic of smooth disk (a) and DTR disk (b).....	92
Figure 4.2 Schematic of experimental setup	93

Figure 4.3 Air bearing design of pico-slider used in experiments	94
Figure 4.4 Frequency spectra of disk velocity for smooth disk; (a) S-LDV signal, (b) AE signal.....	96
Figure 4.5 Frequency spectra of disk velocity for disk A; (a) S-LDV signal, (b) AE signal.....	97
Figure 4.6 Frequency spectra of disk velocity for disk B; (a) S-LDV signal, (b) AE signal.....	98
Figure 4.7 Touch-down velocity for smooth and DTR disks.....	99
Figure 4.8 Normalized pressure P^* at touch-down and take-off for a smooth disk at a velocity of 27.9 m/s; (a) touch-down signal, (b) take-off signal	101
Figure 4.9 Normalized pressure P^* at touch-down and take-off for disk A at a velocity of 27.9 m/s; (a) touch-down signal, (b) take-off signal	103
Figure 4.10 Normalized pressure P^* at touch-down and take-off for disk B at a velocity of 27.9 m/s; (a) touch-down signal, (b) take-off signal	104
Figure 4.11 Normalized ambient touch-down pressure P^* for smooth and discrete track recording disks at a velocity of 27.9 m/s	105
Figure 4.12 Touch-down and take-off pressure hysteresis on a smooth disk and DTR media at a velocity of 27.6 m/s.....	106
Figure 4.13 Velocity profile for contact start-stop test.....	107
Figure 4.14 Critical velocity for flying of slider on a smooth disk and discrete track recording disks during start/stop testing.....	108
Figure 5.1 Typical discrete track recording disk layer structure	115
Figure 5.2 Schematic of head-disk interface for DTR disk; (a) stable flying and (b) contact with DTR disk.....	115
Figure 5.3 Schematic of nano-indentation and nano-scratch testing on discrete tracks; (a) schematic of nano-indentation, (b) schematic of nano-scratch testing and (c) typical indentation (load-displacement curve)	117
Figure 5.4 (a) Experimental setup of reciprocal wear test and (b) displacement of PZT versus time.....	118

Figure 5.5 AFM images of typical wear and accumulation of wear particles in discrete tracks; (a) wear on discrete tracks and (b) fill in the grooves 119

Figure 5.6 SEM image of wear on a DTR disk (groove depth = 40 nm, land width = 90 nm, track pitch = 200 nm) after the flyability test..... 120

Figure 5.7 Images of indentation and scratch tests on discrete track disks; (a) nano-indentation, (b) nano-scratch test and (c) cross section of the plastic deformation of the discrete track along the line ($t_1 - t_2$). 121

Figure 5.8 Typical SPM images of indentations on smooth surface and discrete track disk (discrete track B); (a) 200 uN, (b) 300 uN, (c) 400 uN, (d) 500 uN, (e) 600 uN and (f) 700 uN..... 123

Figure 5.9 Load-displacement curves as a function of normal loads; (a) on the smooth surface, (b) discrete track A..... 124

Figure 5.10 Plastic deformation energy (dissipated energy) versus normal load for different disk surfaces..... 126

Figure 5.11 Final depth of plastic deformation as a function of the normal load on the smooth surface and discrete tracks A and B..... 127

Figure 5.12 Typical SPM images of nano-scratch tests on the smooth disk and discrete track B; (a) 10 uN, (b) 20 uN, (c) 35 uN, (d) 75 uN, (e) 100 uN and (f) 130 uN 127

Figure 5.13 Scratch depth as a function of scratch load on a smooth disk surface and discrete track disks A and B 128

Figure 5.14 Comparison of wear scars on smooth and discrete track surfaces; (a) smooth disk area tested at 5Hz/5.6um/10uN/1000, (b) smooth disk area tested at 5Hz/5.6um/20uN/1000, (c) smooth disk area tested at 5Hz/5.6um/20uN/10000, (d) discrete track surface tested at 5Hz/5.6um/10uN/1000, (e) discrete track surface tested at 5Hz/5.6um/20uN/1000 and (f) discrete track surface tested at 5Hz/5.6um/20uN/10000 129

Figure 5.15 SEM images on the spherical wear probes after reciprocal wear tests; (a) tested on smooth disk area at 5Hz/5.6um/10uN/1000 cycles, (b) tested on smooth disk area at 5Hz/5.6um/20uN/1000 cycles, (c) tested on smooth disk area at 5Hz/5.6um/20uN/10000 cycles, (d) tested on discrete track surface at 5Hz/5.6um/10uN/1000 cycles, (e) tested on discrete track surface at

5Hz/5.6um/20uN/1000 cycles and (f) tested on discrete track surface at 5Hz/5.6um/20uN/10000 cycles	130
Figure 5.16 SEM images of wear of discrete track region for different sliding directions; (a) zero degrees and (b) 37 degrees	131
Figure 5.17 Friction coefficient as a function of cycles on smooth surface and discrete tracks at 5Hz/5.6um/10mN/1000 cycles	131
Figure 5.18 Raman spectra of (a) DLC film before reciprocal wear testing in the smooth disk area and the discrete track surface, (b) wear particles from the discrete track surface and (c) wear particles from the smooth disk area	132
Figure 5.19 Raman spectra on the spherical wear probes (a) before the reciprocal wear testing, (b) tested on the discrete track surface and (c) tested on the smooth disk area.....	133
Figure 5.20 Schematics of contact (a) on smooth surface and (c) a discrete track disk (groove depth = 60 nm and land width = 140 nm)	134
Figure 5.21 Von Mises stress contour on (a) a smooth surface and (b) a discrete track (groove depth = 60 nm and land width = 140 nm) (unit is 10^6 GPa)	135
Figure 5.22 Von Mises stress distribution on discrete track (unit is 10^6 GPa).....	135
Figure 6.1 Schematic of (a) smooth and (a) DTR disks	142
Figure 6.2 Schematic of (a) low wettability and (b) high wettability	144
Figure 6.3 Schematic of static contact angle	145
Figure 6.4 Tow-dimensional periodic discrete tracks	146
Figure 6.5 (a) Schematic of a water droplet on a smooth surface, (b) schematic of the Cassie or Cassi-Baxter state for the composite interface with air pockets, and (c) schematic of the Wenzel state for the homogeneous interface	147
Figure 6.6 Schematic of spreading progress.....	148
Figure 6.7 Schematic of pull-off force measurement with AFM; (a) approach, (b) snap to the surface, (c) apply contact force, (d) retract from the surface (pull-off force), and (e) fully back to original position.....	151
Figure 6.8 (a) Schematic of the cross section of a DTR disk and (b) a scanning electron microscopy (SEM) image of discrete tracks.....	152

Figure 6.9 SEM images of 20 nm grooved discrete tracks with respect to different ratios of land with (L)/track pitch (P); (a) L/P = 0.81, (b) L/P = 0.79 and (c) L/P = 0.50	153
Figure 6.10 SEM images of 40 nm grooved discrete tracks with respect to different ratios of land with (L)/track pitch (P); (a) L/P = 0.67, (b) L/P = 0.58 and (c) L/P = 0.48	154
Figure 6.11 Contact angle and contact diameter (a) on smooth surface area and (b) discrete track area	155
Figure 6.12 Before spreading occurred and (b) after spreading reached equilibrium	156
Figure 6.13 Comparison of spreading of water on smooth surface and discrete track disk	156
Figure 6.14 Contact angle (a) at the first moment of spreading and (b) after spreading reached equilibrium	157
Figure 6.15 Comparison of spreading of a water drop on a smooth surface and discrete track disks with groove depths of 40 nm and different ratio of L/P	158
Figure 6.16 Typical pull-off force curves (a) on land area of discrete track disk and (b) on smooth surface of disk	159
Figure 6.17 SEM images of (a) discrete tracks and (b) smooth surface.....	160
Figure 6.18 SEM images of various diameters of AFM tips; (a) tip radius = 10.5 nm, (b) tip radius = 60 nm and (c) tip radius = 175 nm	161
Figure 6.19 Pull-off force measurement with various tip diameter of AFM on smooth surface and discrete tracks (land width = 182 nm and track pitch = 380 nm).....	161
Figure 6.20 Comparison of adhesion on smooth surface and land area on discrete tracks based on the JKR and DMT models	162
Figure 6.21 Schematic of experimental setup	163
Figure 6.22 Velocity profile for contact start-stop (CSS) test.....	163
Figure 6.23 Typical friction forces versus time; (a) on a smooth disk, (b) on DTR disk A, and (c) on DTR disk B	165

Figure 7.1 SEM image of discrete tracks without planarization	172
Figure 7.2 Scanning electron microscopy (SEM) images after planarization; (a) 4000 RPM, (b) 3000 RPM, (c) 2000 RPM and (d) 1000 RPM.....	174
Figure 7.3 Atomic force microscopy (AFM) image of original disk surface; (a) surface image and (b) cross section.....	175
Figure 7.4 Atomic force microscopy (AFM) images after planarization at different RPMs; (a) 4000 RPM, (b) 3000 RPM, (c) 2000 RPM and (d) 1000 RPM	175
Figure 7.5 Schematic of planarization of discrete track recording media at different RPMs; (a) surface roughness for 2000, 3000 and 4000 RPM and (b) surface roughness for 1000 RPM.....	176
Figure 7.6 Typical back etching with RIE; (a) before spin-coating, (b) after spin-coating with 4000 RPM and (c) after back etching process	177
Figure 7.7 Adhesion force as a function of curing temperature	179
Figure 7.8 Adhesion force as a function of oxygen plasma treatment time	179
Figure 7.9 Hardness as a function of oxygen plasma treatment time.....	181
Figure 7.10 Scratch test at 200 uN as a function of oxygen plasma treatment time	181
Figure 7.11 Scratch test at 300 uN as a function of oxygen plasma treatment time	182
Figure 7.12 Standard deviation (STD) of flying height before and after planarization	183
Figure A. 1 Control volume of pivoted slider bearing (Source: after [56])	191
Figure B.1 Schematic of pivoted magnetic slider (Source: [1, 2]).....	201
Figure B.2 Schematic of equilibrium of magnetic recording slider in vertical direction (Source: [1, 2])	202
Figure B.3 Newton-Raphson Scheme to calculate steady state flying height using the CMRR simulator.....	206

LIST OF TABLES

Table 3.1 Configurations of DTR media.....	79
Table 4.1 Configurations of DTR media.....	93
Table 5.1 Characteristics of two different types of discrete track disk surfaces ..	121
Table 5.2 Material properties of a diamond tip and three different layers	134
Table 6.1 Configurations of DTR media.....	153

ACKNOWLEDGEMENT

It gives me great pleasure to express my sincere gratitude to Professor Frank E. Talke for his support and encouragement during my PhD studies. He motivated my interest in engineering and research, and it was a great opportunity to become a self-motivated researcher. His encouragement and countless efforts to review my publications and dissertation were very important for me to become a well-trained PhD graduate. As a non-native speaker, I am also thankful to him for his having me as his teaching assistant. As a teaching assistant, I had the opportunity to improve my communication and teaching skills in English. There are a lot of other items for which I would like to thank him. I may never express all of the appreciation for his advice and training as my advisor.

I am grateful to Chulmin Choi, Young Oh, Dr. Hong and Professor Jin in the Center for Magnetic Recording Research (CMRR). They were very good partners in discussing on patterned media and nano-structures. They focused on manufacturing of patterned magnetic media. We worked on the interaction between slider and patterned medium. Hence, discussions between our group and Prof. Jin's group were very helpful to understand patterned media recording technology. We worked together on three publications and are still continuing collaborations.

I am also grateful to Dr. Yoo and Kim for giving me a chance to do a summer internship in the head/disk interface group at Samsung Electronics. With their help, I had the opportunity to get access to practical problems. With insight into practical issues, I was able to find new research projects.

I would like to give my thanks to Western Digital Corp. (previous Komag Inc.) for supplying discrete track recording (DTR) media for my research. Various types of discrete track recording media were very useful for studying slider flyability and tribological properties of the head/disk interface.

I give my sincere thanks to all Talke lab members, current as well as former, who have had an excellent relationship with each other. They were and are friends and have always helped each other to get familiar with lab facilities. From them I have learned different cultures and the ability to understand people from other countries. It was a very good experience for me to develop a globalized perspective of the world.

I am grateful to my parents and parents-in-law for their support and their prayers. They are always on my side and willing to help me, and want to be my counselors. My mother and father encouraged me all the time.

I would like to thank my younger brother, Young Ho. Sometimes he called me and said “You can do it and cheer up!” He really wanted to help in spite of the fact that we lived far away each other. Thank you, brother.

Finally, I want to thank my wife, Neena. She is beautiful and precious to me. Her energetic and powerful life style has inspired me and her support has been priceless.

Acknowledgement for published work:

Chapter four is a partial reprint of the material as it appears in “Touch-down and take-off hysteresis of magnetic recording sliders on discrete track media,” *Microsyst. Technol.*, vol. 16, pp. 273-278, 2009, by Yeoungchin Yoon and Frank E. Talke. The dissertation author was the primary investigator of this paper and the co-author listed in this paper supervised the research which forms chapter four.

Chapter seven is a partial reprint of the material as it appears in “Planarization of discrete track recording media to improve flyability of magnetic recording sliders,” *IEEE Trans. Mag.*, vol. 45, pp. 3527-3530, 2009, by Yeoungchin Yoon, Chulmin Choi, Young Oh, Daehun Hong, Sung Ho Jin and Frank E. Talke. The dissertation author was the primary investigator of this paper and the co-authors listed in this paper directed and/or supervised the research which consists of chapter six.

VITA

- 1994-2002 B. E., Mechanical Engineering, Dankook University, Korea
- 2003-2005 M. S., Mechanical Engineering, University of California, San Diego
- 2005-2010 Research and Teaching Assistant, Center for Magnetic Recording Research, University of California, San Diego
- Summer 2005 Research position, Samsung Digital & Display Interface (SDI), Suwon, Kyeong Gi Do, Korea
- Summer 2006 Research position, Samsung Electronics, Suwon, Kyeong Gi Do, Korea
- 2010 Ph.D., University of California, San Diego

PUBLICATIONS

M. Yusuke, Y. Yoon, R. Brunner, A. Daugela, O. L. Warren and F. E. Talke, “Nano-hardness testing with ultrasonic excitation”, *Wear of Material*, 259, no. 2, 1497-1501, 2005.

M. Duwensee, D. E. Lee, Y. Yoon, and F. E. Talke, “Tribological testing of sliders on discrete track media and verification with numerical predictions”, *Microsyst. Technol.*, vol. 15, pp. 1597-1603, 2009.

H. Li, H. Zheng, Y. Yoon and F. E. Talke, “Air Bearing Simulation for Bit Patterned Media”, *Tribology Letters*, vol. 33, pp. 199-204, 2009.

Y. Yoon and F. E. Talke, “Touch-down and take-off hysteresis of magnetic recording sliders on discrete track media”, *Microsyst Technol.*, vol. 16, pp.273-278, 2009.

Y. Yoon, C. Choi, Y. Oh, D. Hong, S. Jin and F. E. Talke, “Planarization of Discrete Track Recording Media to Improve Flyability of Magnetic Recording Sliders”, *IEEE Trans. of Mag.*, vol. 45, pp. 3527-3530, 2009.

Quynhhoa T. Nguyen, Benjamin L. Wong, June Chun, Yeoung C. Yoon, Frank E. Talke, Robert L. Sah, “Macroscopic Assessment of Cartilage Shear: Effects of Counter-surface Roughness, Synovial Fluid Lubricant, and Compression Offset”, *Journal of Biomechanics*, published online 02 March 2010.

Chulmin Choi, Yeoungchin Yoon, Daehoon Hong, Karla S. Brammer, Young Oh, Seunghan Oh, Mariana Loya, Frank E. Talke and Sungho Jin, “Strongly Superhydrophobic Silicon Nanowires by Supercritical CO₂ Drying”, *Electronic Materials Letter*, 2010, in press.

Y. Yoon, F. E. Talke, “An experimental investigation of contact deformation and wear characteristics on discrete track recording media,” *accepted in ISPS 2010 conference paper*.

C. Choi, Y. Yoon, Y. Oh, D. Hong, F. E. Talke, S. Jin, “Planarization of Patterned Magnetic Recording Media for Improved Head Flyability,” in preparation.

Y. Yoon, F. E. Talke, “Wetting, adhesion and friction force on discrete track recording media,” in preparation.

Y. Yoon, B. Suen, E. B. Fanslau, F. E. Talke, “Fretting wear at the dimple/gimbal interface in a hard disk drive,” in preparation.

ABSTRACT OF THE DISSERTATION

Nano-tribology of discrete track recording media

by

Yeoungchin Yoon

Doctor of Philosophy in Engineering Sciences (Mechanical Engineering)

University of California San Diego, 2010

Professor Frank E. Talke, Chair

Experimental and numerical methods were used to investigate the flyability of magnetic recording sliders on discrete track recording media. Experiment techniques were developed to study the hysteresis of “touch-down” and “take-off” of magnetic recording sliders on discrete track recording media. The slider dynamics on discrete track recording media was compared with that on conventional smooth (flat) media. Various experimental methods were used to study the contact behavior, wear characteristics and tribological characteristics of discrete recording media. Advantages and disadvantages of discrete track recording media were investigated and compared with conventional smooth media. To improve flyability and mechanical properties of discrete track recording media, planarization of discrete track media was employed.

Chapter 1

Introduction

This chapter gives a brief history of hard disk drives and the basic principles of magnetic recording. The evolution of magnetic recording technology is described, and the organization of this thesis is presented.

1.1 History of Hard Disk Drives

The growing need for “on-line” storage has been the driving factor behind reduced cost per byte, short access time and high data rate in the hard disk drive (HDD). The first commercially available disk drive was unveiled in 1956 by the International Business Machines (IBM) Corporation [1-3]. Figure 1.1 shows a photograph of the so-called RAMAC, the “Random Access Method of Accounting and Control”. The RAMAC disk drive was the size of a large refrigerator in width, and weighed around a ton. It contained fifty iron-oxide-coated aluminum disks, each with a diameter of 24 inches. The disks were rotated at 1200 revolutions per minute (RPM). The RAMAC provided a total capacity of 5 MB and a data transfer rate of 8.8 kilobytes per second (Kbytes/sec). The linear density was 100 bits per inch and the track density was 20 tracks per inch, i.e., the areal density was about 2Kb/in². The maximum seek time was 0.7 seconds and the recording slider was supported by a hydrostatic air bearing. The flying height of the slider over the disk was about 25 μm .



Figure 1.1 The Random Access Method of Accounting and Control (RAMAC); demonstrated in Norte Dame Development Lab. on Sep. 13th, 1956. (Source: IBM)

In 1961 IBM introduced a new product, the IBM 1301, which used a hydrodynamic air bearing. The capacity of the IBM 1301 was 10 times the capacity of the earlier RAMAC and access time was reduced to 0.1 seconds. The areal density and data rate were increased to 25 Kb/in² and 68 Kbytes/sec (one bite = 8 bits), respectively. IBM introduced the first modern “Winchester” hard drive in 1973 [4]. Continuous technology improvements have led to thin film inductive heads, magnetoresistive (MR) heads [5], then giant magnetoresistive (GMR) heads [6] and now tunneling magnetoresistive (TMR) heads. Disks were not only reduced in size, but their surfaces were also made smoother. The magnetic coating

changed from iron-oxide coating to sputtered thin film disks with high complexity [7].

In the past fifty four years, hard disk drives have helped to change the computer industry. Presently, disk drives are used in desktops, laptops, and net-book computers. They are also common in electronic consumer products such as I-Pod's, smart phones, PDA's, or digital TV's. Hard disk drives have met the demand for increasing digital storage.

The increase of the area density versus time is shown in Figure 1.2. Since the days of the RAMAC (2Kb/in²), the areal density has increased more than 250,000,000 times. At present, the highest areal density in commercially available hard disks is approximately 500 Gbit/in². In the near future, we expect the areal densities to increase to 1 and possibly to 10 Tbit/in². In the years from 1960 through 1980, the compound annual growth rate (CAGR) of density was 36 %. During the 1990s, the compound annual growth rate increased to 60 % due to the introduction of magnetoresistive (MR) heads, which replaced the thin film inductive heads. At the end of the nineties, the implementation of the giant magneto resistance (GMR) head increased the compound annual growth rate to 100 %. The growth rate has slowed down in the last decade due to the superparamagnetic limit [10]. In 2005-2007, a new recording technology, perpendicular recording [11], was introduced.

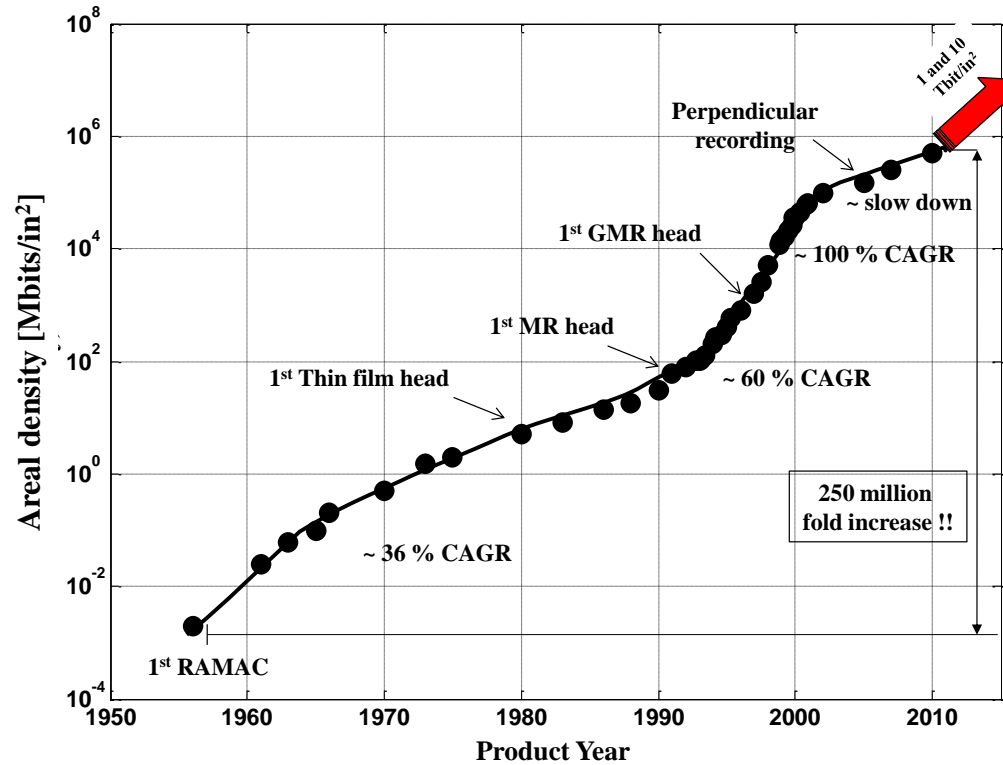


Figure 1.2 Historical areal density increase of hard disk drives (Source: [8], [9])

Figure 1.3 shows the historical price trends per gigabyte (Gbyte). To manufacture one gigabyte of RAMAC HDD in 1956, one would have had to pay \$10,000,000. For comparison, today one can buy one gigabyte of disk storage for less than 10 cents. Hard disk drive technology continues to improve areal density and reduce the price per bit.

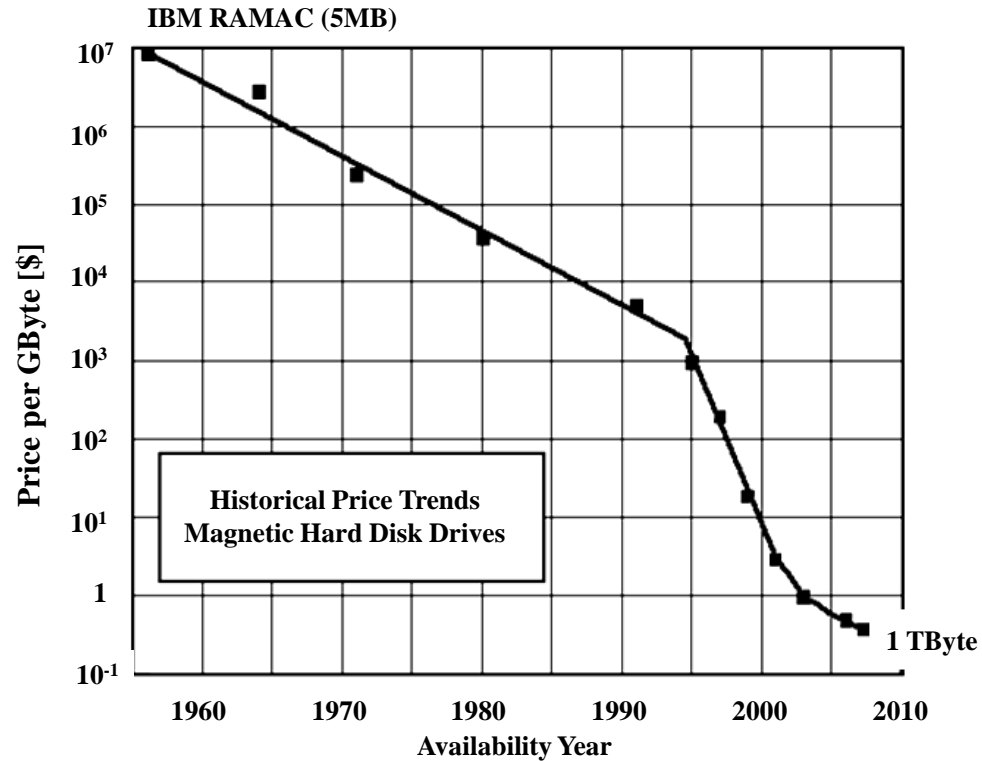


Figure 1.3 Historical price trend of magnetic hard disk drives per Gbyte (Source: Ed Grochowski IDEMA)

1.2 Principle of Magnetic Recording

The fundamental principles of magnetic recording are described in this section. Magnetic hysteresis and the read/write processes are introduced and illustrated. In addition, the evolution of read/write heads is summarized.

1.2.1 Magnetic Hysteresis

Materials are influenced by the presence of a magnetic field in different ways. The magnetic properties of a material can be classified by how the material responds to an externally applied magnetic field. This classification divides

materials in diamagnetic, paramagnetic and ferromagnetic. Diamagnetism creates a magnetic field opposite to the externally applied magnetic field and results in a slightly repulsive effect. The material does not sustain the induced magnetic properties when the applied field is removed. Generally, the strength of the field is very weak. Typical diamagnetic materials are copper, silver, and gold. Paramagnetism is stronger than diamagnetism. Paramagnetism produces magnetization in the direction of the applied magnetic field. The magnetic strength of paramagnetic materials is proportional to the applied magnetic field. If the applied magnetic field is removed, the induced magnetism disappears. This is similar to diamagnetism. Ferromagnetism deals with materials that can retain their magnetic properties even after the magnetic field is removed. Typical examples of ferromagnetic materials are iron, nickel and cobalt. If an external magnetic field is applied, magnetic moments align parallel to the applied magnetic field so that the magnetic force becomes strong. Figure 1.4 (a) and (b) show unmagnetized and magnetized regions in ferromagnetic materials. As shown in Figure 1.4 (a), without an external magnetic field, magnetic moments of the individual domains cancel each other and the materials remain unmagnetized. Figure 1.4 (b) demonstrates that magnetic moments are well aligned in the direction of the externally applied magnetic field. This unique character of ferromagnetic materials is used to record binary information in magnetic recording disks.

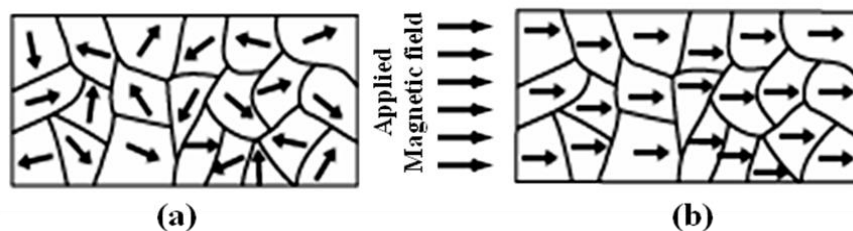


Figure 1.4 Alignment of magnetic moments in the case of (a) unmagnetized and (b) magnetized ferromagnetic material.

If a ferromagnetic material is magnetized in one direction, the magnetization will not return to zero magnetization even if the externally applied magnetic field is removed. The magnetization can only be driven back to zero by applying a field in the opposite direction. To reorient the magnetic moments in a material, energy is required. This process, however, is not reversible. Although the magnetization increases with the applied magnetic field, the reverse path is not the same. This irreversibility of magnetization is known as hysteresis. The hysteresis loop is the representation of the relationship between magnetization (M) and applied magnetic field (H). These properties of ferromagnetic materials are important for the storage of digital information in hard disk drives.

Figure 1.5 shows a typical magnetic hysteresis loop starting at zero magnetic field (H). As the field is increased, the magnetization is increased. The slope of the magnetization curve at $H=0$ is called the initial susceptibility. The maximum value of magnetization is called the saturation magnetization (M_s). Similarly, the value of magnetization (M) at zero magnetic field (H) is called the remanent magnetization (M_r). The zero value of the magnetic field (H) for zero magnetization (M) in the hysteresis loop is the so-called the coercivity (H_c) [13].

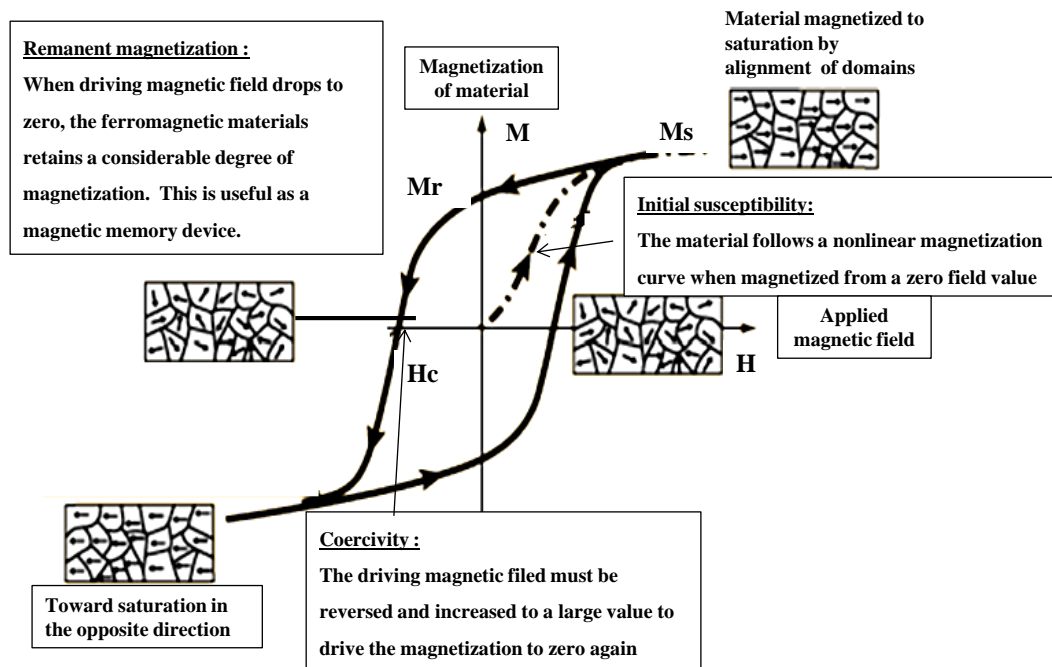


Figure 1.5 Hysteresis loop of ferromagnetic material (Source: [12], [13])

1.2.2 Write process in magnetic recording [14]

The write process is based on the saturation of magnetization. Figure 1.6 shows a schematic of the write process in a longitudinal magnetic recording (LMR) system, i.e., a system in which the magnetic moments are aligned in the horizontal plane. If the magnetic medium moves relative to the head, the write current of the head magnetizes the medium to the right in the direction of the applied current, as can be seen in Fig. 1.6 (a). When the applied field is changed in the opposite direction (Figure 1.6 (b)), a magnetic transition is formed at the trailing edge. Figure 1.6 (c) shows that the magnetic transition moves to the right.

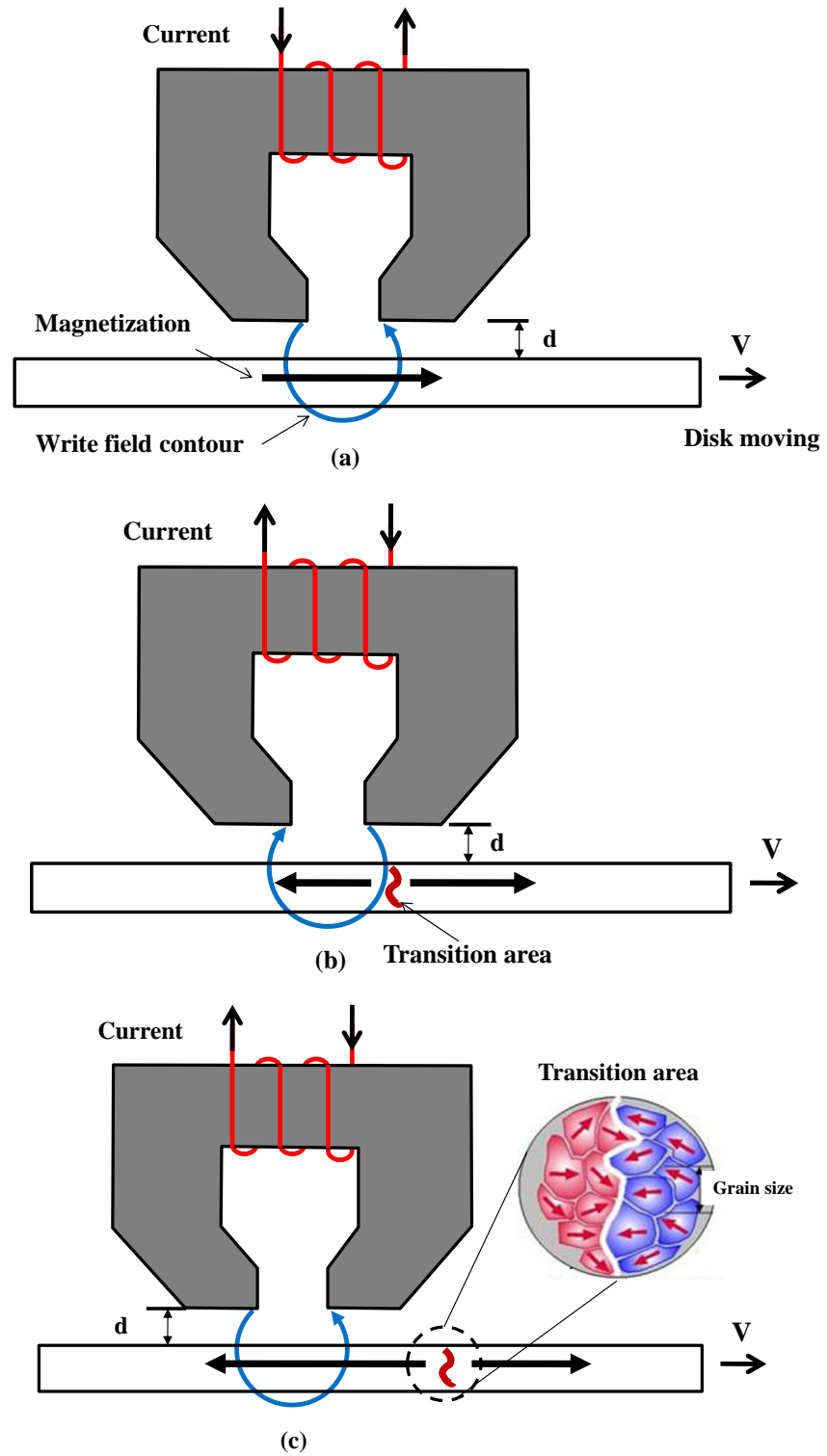


Figure 1.6 Write process in magnetic medium

1.2.3 Read process in magnetic recording

A read head can detect the magnetic flux change generated in the transition area. The variation of the magnetic flux produces an “induced” voltage in the head coil, which is the so-called “read-back signal”.

To calculate the magnetic flux through the head coil, the *reciprocity principle* is commonly used [15]-17]. The *reciprocity principle* states that the mutual inductance between two objects is the same: $M_{12} = M_{21}$. Figure 1.7 explains reciprocity between a recording head (object 1) and a magnetic medium (object 2) for longitudinal magnetic recording. The magnetic element is located at (x, y, z) with a volume of $dx dy dz$. The magnetic spacing “ d ” is the distance between the recording head and the top surface of the magnetic medium.

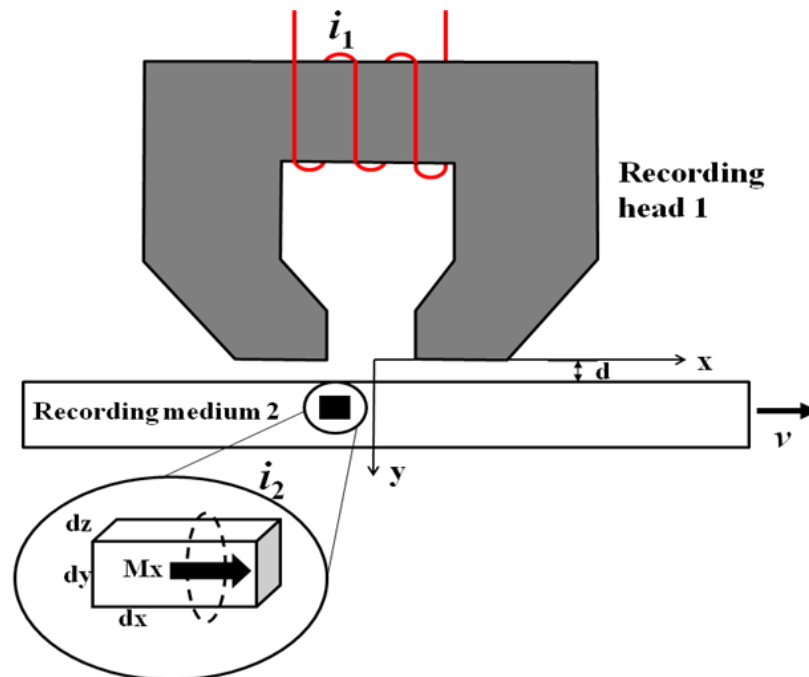


Figure 1.7 Reciprocity between recording head and magnetic medium

The magnetic flux through the element $dx dy dz$ at location x, y, z due to a write current i_1 can be expressed by

$$d\Phi_{21} = \mu_0 H_x(x, y, z) dy dz \quad (1.1)$$

where μ_0 is the magnetic permeability of free space.

The current density along the x-axis of the magnetic element $dx dy dz$ is

$$i_2 = M_x(x - \bar{x}, y, z) dx \quad (1.2)$$

where $\bar{x} = vt$ (v is relative velocity).

The magnetic flux through the recording head coil, $d\Phi_{12}$, is related to the magnetic flux through the recording media, $d\Phi_{21}$, by

$$\frac{d\Phi_{12}}{i_2} = \frac{d\Phi_{21}}{i_1} \quad (1.3)$$

The magnetic flux through the recording head coil due to the magnetic element can be expressed by

$$d\Phi_{12} = \frac{\mu_0 H_x(x, y, z)}{i_1} M_x(x - \bar{x}, y, z) dx dy dz \quad (1.4)$$

Therefore, the total magnetic flux through the recording head coil is given by

$$\Phi = \mu_0 \int_{-\infty}^{\infty} dx \int_d^{d+\delta} dy \int_{-\infty}^{\infty} \frac{H_x(x, y, z)}{i} M_x(x - \bar{x}, y, z) dz \quad (1.5)$$

where δ and d are the thickness of the magnetic medium and the magnetic spacing, respectively.

If we assume that the magnetization and head field are uniform over the data track (track width = W) along the z -axis and through the thickness of the recording medium, the equation can be simplified to

$$\Phi = \mu_o W \int_{-\infty}^{\infty} dx \int_d^{d+\delta} \frac{H_x(x, y)}{i} M_x(x - \bar{x}) dy \quad (1.6)$$

The read-back voltage is expressed by Faraday's law:

$$V_x(\bar{x}) = -\frac{d\Phi}{dt} = -\frac{d\bar{x}}{dt} \frac{d\Phi}{d\bar{x}} = -\mu_o v W \int_{-\infty}^{\infty} dx \int_d^{d+\delta} \frac{H_x(x, y)}{i} \frac{dM_x(x - \bar{x})}{d\bar{x}} dy \quad (1.7)$$

where v is the velocity of the magnetic medium.

Equation 1.7 shows that the recording head detects the moving magnetic charge, which is the derivative of magnetization. If the velocity of the magnetic medium is zero, or if the derivative of the magnetization is zero, the read-back signal is zero. Furthermore, the read-back voltage depends on the magnetic recording pattern. If we assume a single magnetic step transition, the magnetization will be given by

$$M_x(x - \bar{x}) = \begin{cases} -M_r & \text{for } x < \bar{x} \\ M_r & \text{for } x > \bar{x} \end{cases} \quad (1.8)$$

where M_r is the remanent magnetization of the medium.

For the case of a thin medium ($\delta \ll d$), the read-back signal becomes

$$V_x(\bar{x}) = 2\mu_o v W M_r \delta \frac{H_x(\bar{x}, d)}{i} \quad (1.9)$$

A typical magnetic transition can be approximated by an arctangent function rather than a sharp step function. The magnetization in this case is given by

$$M_x(x - \bar{x}) = \frac{2M_r}{\pi} \tan^{-1}\left(\frac{x - \bar{x}}{a}\right) \quad (1.10)$$

where a is the transition parameter. If a is equal to zero, a step function is obtained. In this case, the read-back signal (Wallace equation) is given by

$$V_x(\bar{x}) = \frac{2\mu_o v WM_r}{i} \int_{d+a}^{d+a+\delta} H_x(\bar{x}, y) dy \quad (1.11)$$

If the Fourier transform of Wallace equation (1.11) is taken, the read-back signal is obtained as

$$V_x(k) = 2\mu_o v WM_r \delta \frac{H_g g}{i} e^{-k(d+a)} \frac{1 - e^{-k\delta}}{k\delta} \frac{\sin(kg/2)}{kg/2} \quad (1.12)$$

where k is the wave number and g is the gap width of the head.

From equation (1.12), we observe that the read-back signal is composed of three terms:

- **Spacing loss term** given by $e^{-k(d+a)}$, i.e., the read-back signal decreases exponentially as a function of $y=d+a$.

- **Gap loss term** given by $\frac{\sin(kg/2)}{kg/2}$, i.e., the read-back signal is related to the gap

distance and becomes zero for $kg = 2\pi, 4\pi, 6\pi \dots$.

- **Thickness loss term** given by $\frac{1 - e^{-k\delta}}{k\delta}$, i.e., the read-back signal is a function of the medium thickness.

Figure 1.8 shows a schematic of the read/write head with the parameters d , g and δ .

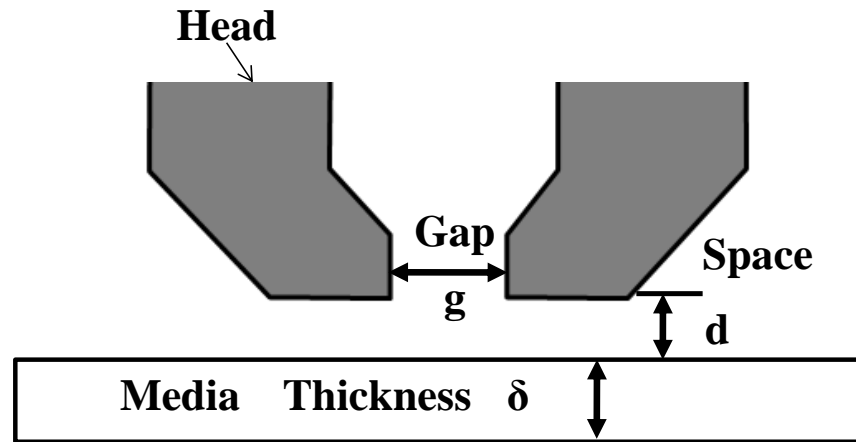


Figure 1.8 Schematic of read/write head and parameters d , g , and δ

Figure 1.9 shows the so-called non return-to-zero inverted (NRZI) encoding method [18], in which the absence of a transition corresponds to a “0” and the presence of a transition to a “1”.

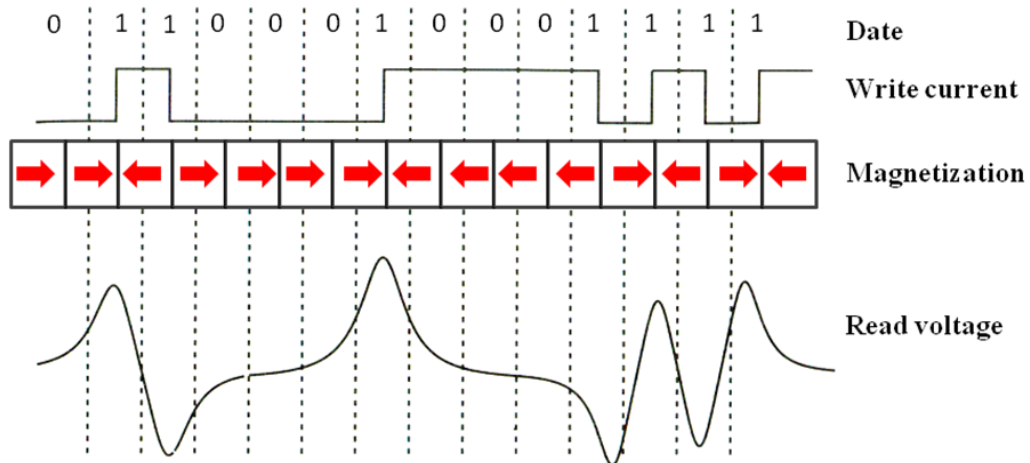


Figure 1.9 Schematic of Non-return to zero inverted (NRZI) encoding method

1.2.4 Evolution of Magnetic Read/Write Heads

In this section, we discuss the development of write and read heads from inductive heads to presently used trailing shield single pole perpendicular magnetic recording writing heads.

Figure 1.10 shows a schematic of an inductive read/write head and a magnetoresistive read head. An inductive head is used for both reading and writing (Figure 1.10 (a)), while in a magnetoresistive head the read and write element are separate (Figure 1.10 (b)).

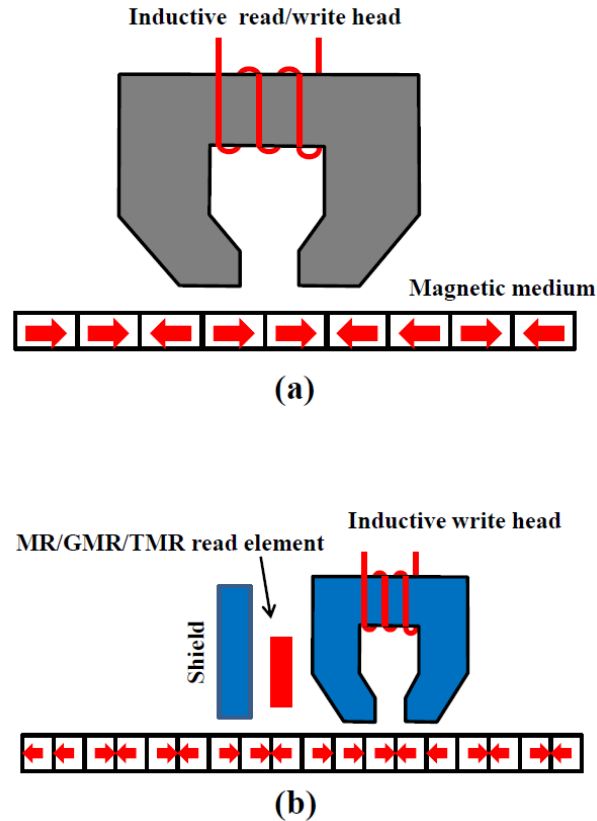


Figure 1.10 Different types of read/write heads; (a) an inductive read/write head and (b) a MR/GMR/TMR separated read and write head

1.2.4.1 Inductive heads

Ferrite head

An inductive head [18] can be used for writing and reading. It is typically made out of ferrite with a fine wire coil wrapped around as shown in Figure 1.10 (a). During writing, a strong magnetic field is generated in the gap due to the current in the coil. During reading, the head detects the change in the magnetic flux, corresponding to a voltage value.

Thin film inductive head

Thin film heads [19] have replaced ferrite heads. They are similar to ferrite heads in their physical characteristics. However they are fabricated using integrated circuit (IC) technology. Thin film heads have higher resolution than ferrite heads and allow writing of much smaller bits, resulting in a substantial increase in areal density.

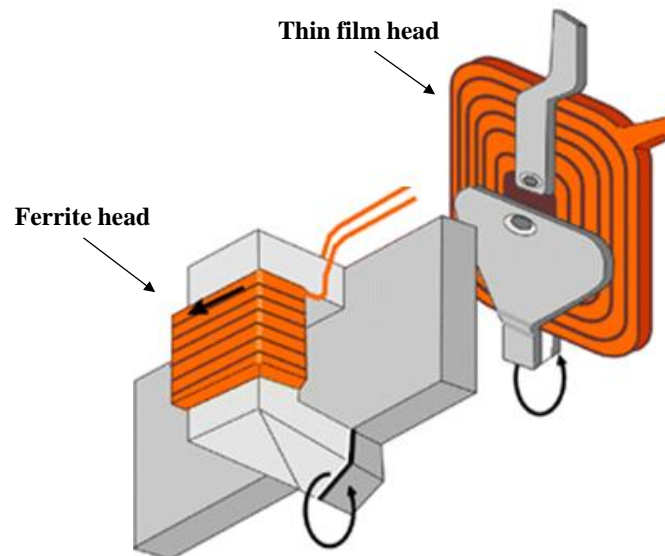


Figure 1.11 Schematic of ferrite head and thin film head (Source: [21])

1.2.4.2 Magnetoresistive (MR) heads

Introduction of the magnetoresistive (MR) [20] head accelerated the increase of area density in HDDs up to a compound annual growth rate (CAGR) of 60 % during the 1990s. The concept was first proposed by Hunt in 1971. In a magnetoresistive head the write and read head are separated (see Figure 1.12). The separate read head uses the magnetoresistive (MR) effect which is the property of a material to change its electrical resistance depending on the magnetic flux.

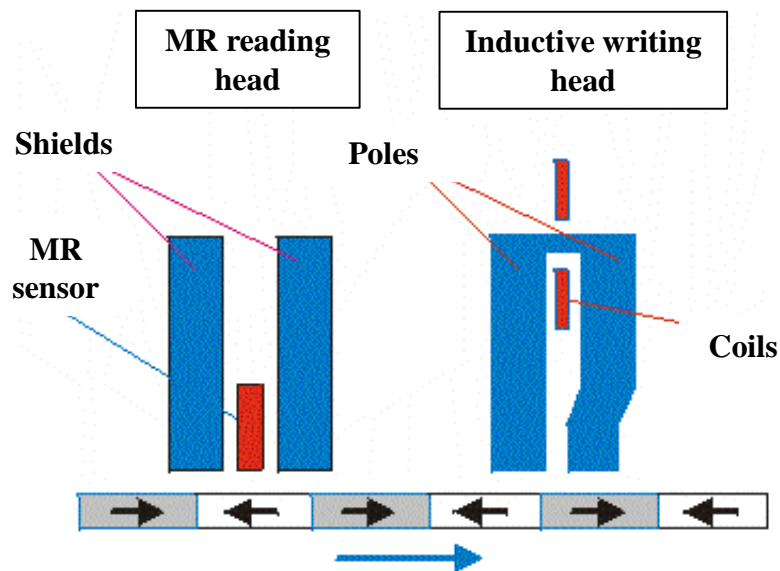


Figure 1.12 Schematic of magnetoresistive (MR) head (Source: [22])

1.2.4.3 Giant magnetoresistive (GMR) heads

When ferromagnetic layers are separated by a non-magnetic layer, electrical resistance of the multilayer depends on the orientations of the magnetizations of the ferromagnetic layers. When the direction of magnetization is parallel to the

ferromagnetic layer, the resistance in the multilayer is low because electron scattering at the interface of the ferromagnetic and non-magnetic layers is reduced. The resistance of the multilayer is significantly increased if the direction of magnetization is reversed. This effect is called giant magnetoresistance (GMR) [23]. Grünberg and Fert discovered the giant magnetoresistance effect. Figure 1.13 shows the schematic of giant magnetoresistance (GMR). If the magnetization of the multilayer is in opposite direction, it results in high resistance (see Figure 13 (a)). If the magnetization of the multilayer is in the same direction, it results in low resistance (see Figure 13 (b)).

Giant Magnetoresistance (GMR)

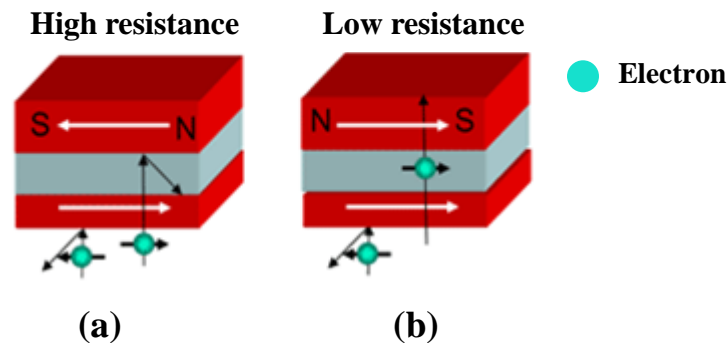


Figure 1.13 Schematic of giant magnetoresistance (GMR) (Source: Magnetic Material Center/National Institute for Materials Science (NIMS))

1.2.4.4 Tunneling magnetoresistance (TMR) heads

Tunneling magnetoresistance (TMR) heads [24] are a recent development and were first introduced by Seagate in 2005. This technology uses the magnetoresistance effect in magnetic tunnel junctions (MTJs). The head consists

of two ferromagnets separated by a thin insulator as shown in Figure 1.14. If the thickness of the insulator is smaller than 2 nm, the electrons can tunnel from one ferromagnetic electrode to the other. When two ferromagnetic electrodes are magnetized in the same directions, high tunneling current occurs. However, if the magnetization of the two ferromagnetic electrodes is opposite, the tunneling current is low. Figure 1.14 shows a schematic of the tunneling magnetoresistance (TMR). TMR is defined as the ratio of the relative resistance between the anti-parallel state and parallel state to the resistance in the parallel state as shown in Figure 1.14.

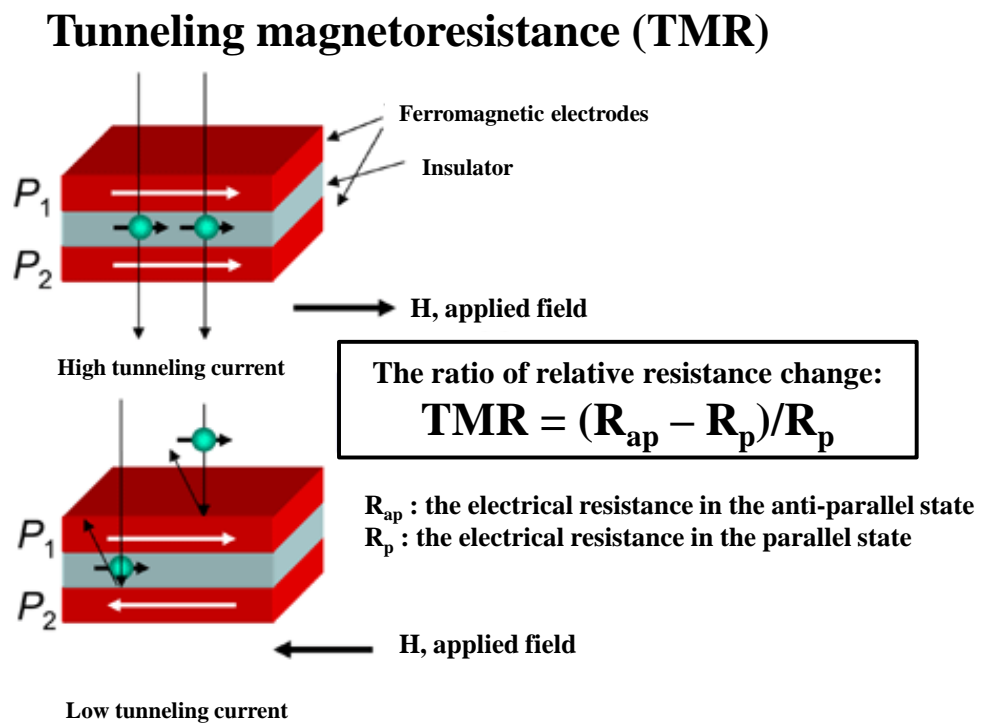


Figure 1.14 Schematic of tunneling magnetoresistance (TMR) (Source of image: Magnetic Material Center/National Institute for Materials Science (NIMS))

1.2.4.5 Future technology for read/write heads

Single pole perpendicular magnetic recording (PMR) writing heads

Perpendicular magnetic recording (PMR) heads [26] use the same read elements as longitudinal heads but different types of write elements. Longitudinal magnetic recording (LMR) and perpendicular magnetic recording (PMR) technologies are discussed in detail in this section along with future magnetic recording technologies.

Figure 1.15 shows a typical PMR write head. A PMR writing head consists of a main pole, a coil and a return yoke.

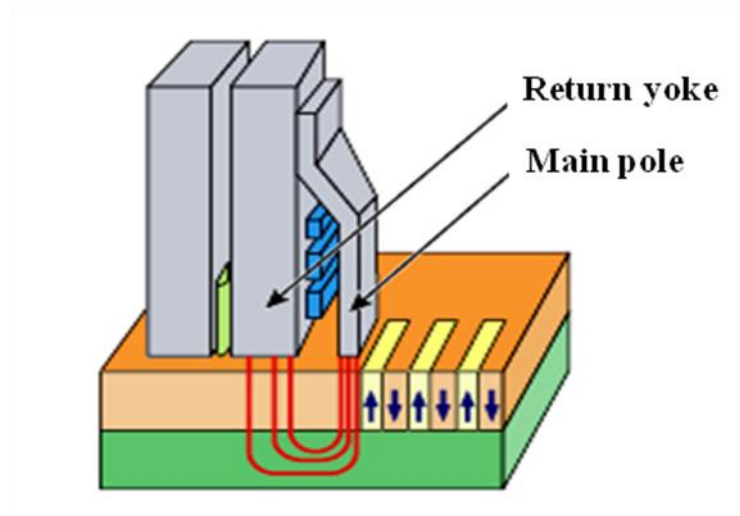


Figure 1.15 Schematic of a typical single pole PMR writing head (Source: [26])

1.3 Evolution of Magnetic Recording Technologies

In this section, we discuss the evolution of magnetic recording technology from conventional longitudinal magnetic recording systems to perpendicular recording systems of today. In addition, promising future technologies are discussed, such as microwave-assisted recording, heat-assisted recording, patterned recording and combined recording (patterned media recording combined with heat-assisted recording).

1.3.1 Longitudinal Magnetic Recording (LMR)

For the last 50 years, longitudinal magnetic recording (LMR) [27] was the standard method of recording. In this method, the magnetization of each bit is aligned horizontally. Figure 1.16 shows a schematic of longitudinal magnetic recording. We note that the magnetization of individual bits is aligned parallel to the surface of the recording media.

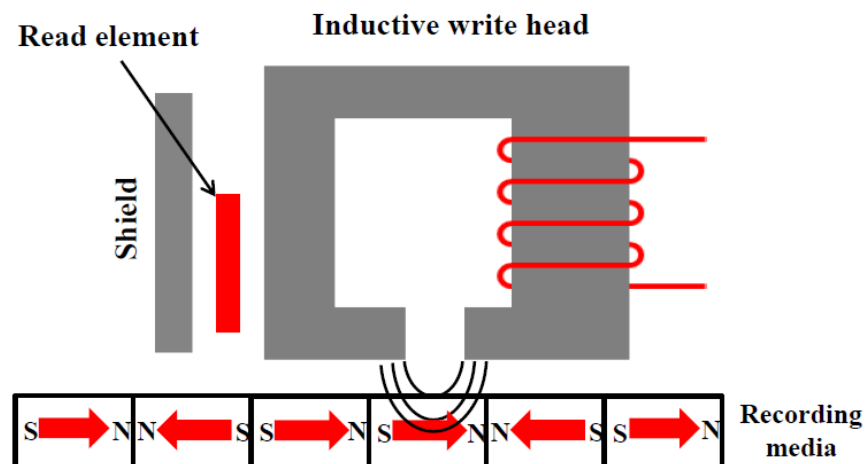


Figure 1.16 Schematic of longitudinal magnetic recording

In order to reduce the bit size, the size of the magnetic grains must be decreased.

Superparamagnetic effect [10]

As the size of magnetic grains decrease, the magnetic energy of individual bits decreases as well. If the magnetic energy equals the ambient thermal energy, the magnetic orientations cannot be sustained and random changes of the magnetic orientation can occur. This results in loss of data. This effect is called the “superparamagnetic effect”.

Figure 1.17 shows the cross section of a typical multilayered longitudinal recording medium. On the top of the medium is the lubricant, which protects the diamond-like carbon (DLC) coating. The lubricant over the coating protects the magnetic layer. Magnetization is aligned in the horizontal direction.

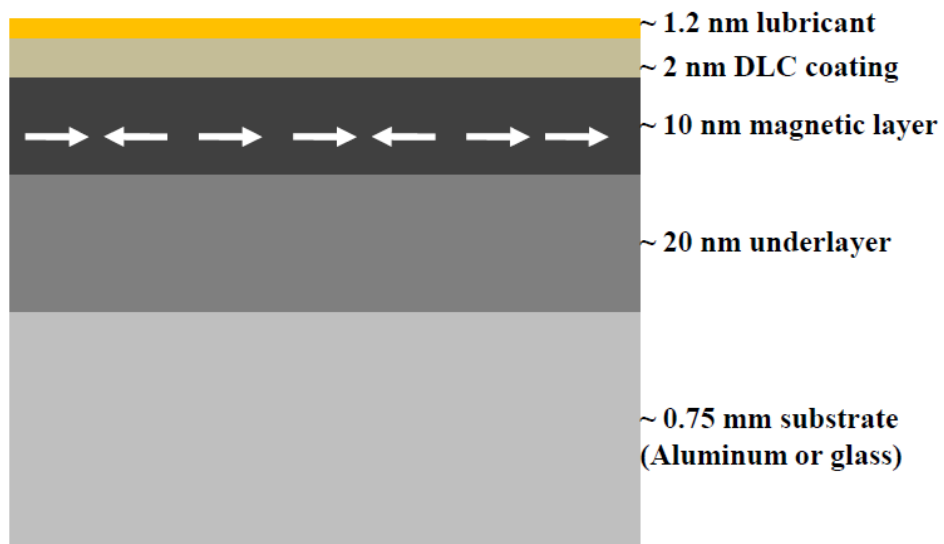


Figure 1.17 Schematic of the cross-section of a multilayered longitudinal recording medium structure

The superparamagnetic effect was predicted to restrict the areal density of hard disk drives to below 150 Gbit/in². Perpendicular magnetic recording (PMR) has overcome this limit and areal densities of several Tbits/in² are presently predicted to be possible. Details are discussed in the following section.

1.3.2 Perpendicular Magnetic Recording (PMR)

Perpendicular magnetic recording (PMR) differs from longitudinal magnetic recording in that the bits are aligned vertically to the media. Perpendicular magnetic recording (PMR) medium consists of a soft magnetic under layer (SUL) and a hard (high coercivity) magnetic layer [27-29]. The high coercivity material shows good resistance against thermal fluctuations, so magnetic bits can sustain their magnetic orientations. In addition, in longitudinal magnetic recording, the transition area is created by changing the alignment of the north and south poles of bits. This makes the system unstable against thermal fluctuations. However, in perpendicular magnetic recording the transition area is created by either north-to-south pole, or south- to-north pole alignment changes. South-to-north or north-to-south alignments are attracted to each other and stable so that bits can be closer [27]. This allows higher areal density in perpendicular magnetic recording systems.

Figure 1.18 shows the schematic of perpendicular magnetic recording [28]. The magnetization is aligned in the perpendicular direction to the surface of the medium. The strength of the write field in a perpendicular recording (PMR) system is larger than that in a longitudinal magnetic recording (LMR) system due

to the high coercivity magnetic layer. The soft magnetic underlayer (SUL) works like a mirror, so the write field can be guided vertically through the hard magnetic layer. The returning field through the soft magnetic underlayer is weaker than the write field. Therefore, the returning field does not have any effect on the magnetic orientations.

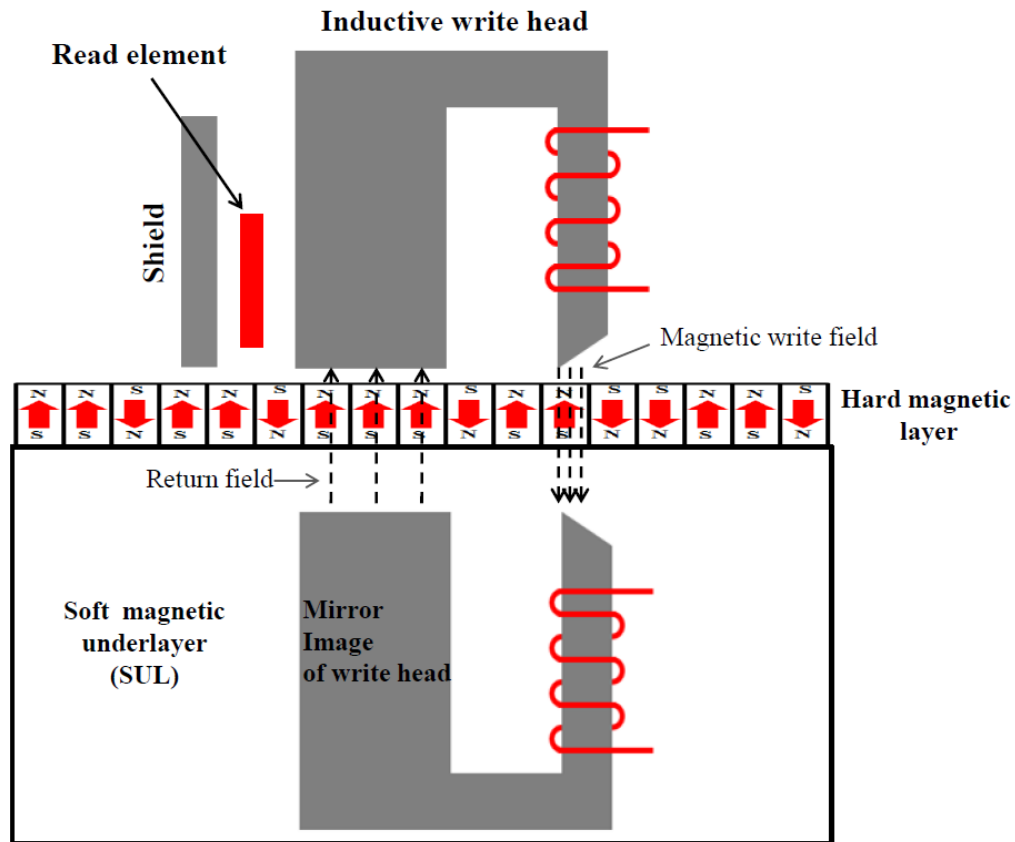


Figure 1.18 Schematic of perpendicular magnetic recording (Source: [28])

Figure 1.19 (a) shows a schematic view of a typical cross-section of perpendicular recording media, while Figure 1.19 (b) shows a transmission electron microscopy (TEM) picture of the magnetic grains in perpendicular media [29]. We observe from Figure 1.19 (b) that very small magnetic grains are present

which are separated by non-magnetic grain boundaries. The average grain size is on the order of 10 nm in present day perpendicular media.

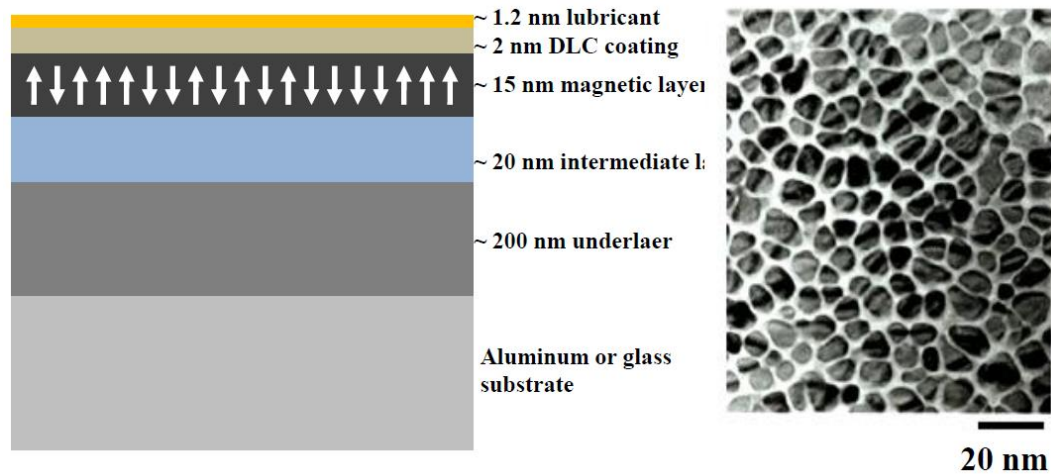


Figure 1.19 Schematic cross-section of the perpendicular recording media and surface observation photograph by transmission electron microscopy (TEM) (Source of picture (b): [29])

1.3.3 Microwave-assisted Magnetic Recording

To overcome the superparamagnetic effect, which leads to the spontaneous reversal of data bits when they are too close, high magnetic anisotropic material is needed. Materials with high magnetic anisotropy can have grains as small as 2 nm to 3 nm in diameter without showing the superparamagnetic effect. However, the coercivity of high anisotropic materials is higher than the write field of current recording heads and additional means are required to enable the writing. Microwave-assisted magnetic reversal (MAMR) is one proposed way to reduce the coercivity during writing of data. In addition to the writing field, a microwave-assisted field is applied simultaneously to the media. The recording principle [30]-

[31] is that when the applied microwave field frequency in the range of 10 to 40 GHz (gigahertz) with kilo-Oe field amplitude matches the magnetization precession frequency of the ferromagnetic media, the coercivity is significantly reduced; then the write field can write on the media. Figure 1.20 shows a simplified diagram of microwave-assisted magnetic recording.

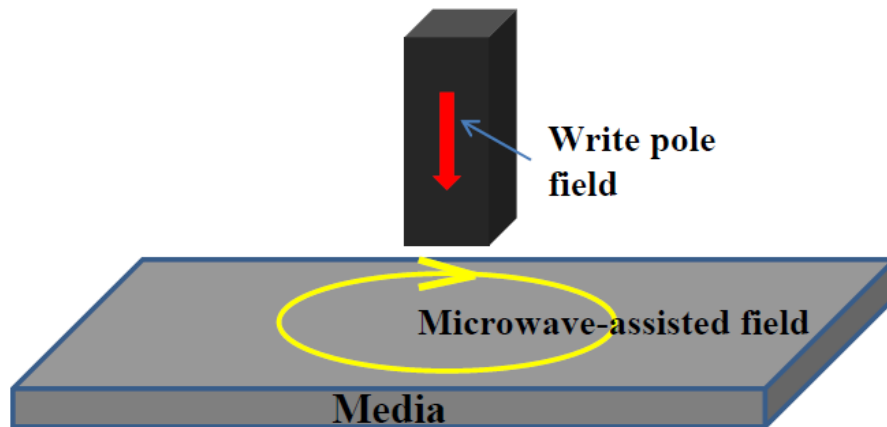


Figure 1.20 Diagram of microwave-assisted magnetic recording

1.3.4 Heat-assisted Magnetic Recording

Heat-assisted magnetic recording (HAMR) [32]-[33] is another way to increase the areal density with the use of very high anisotropy magnetic materials. To write on those materials, the write field must be strong enough. However, present day magnetic heads cannot generate enough field strength to write on high coercivity medium. To allow writing, the magnetic medium must be heated up near the Curie temperature, so that the coercivity decreases temporarily (see Figure

1.21). At this reduced coercivity, writing can be performed. After writing, the material cools down and “freezes” the magnetization pattern.

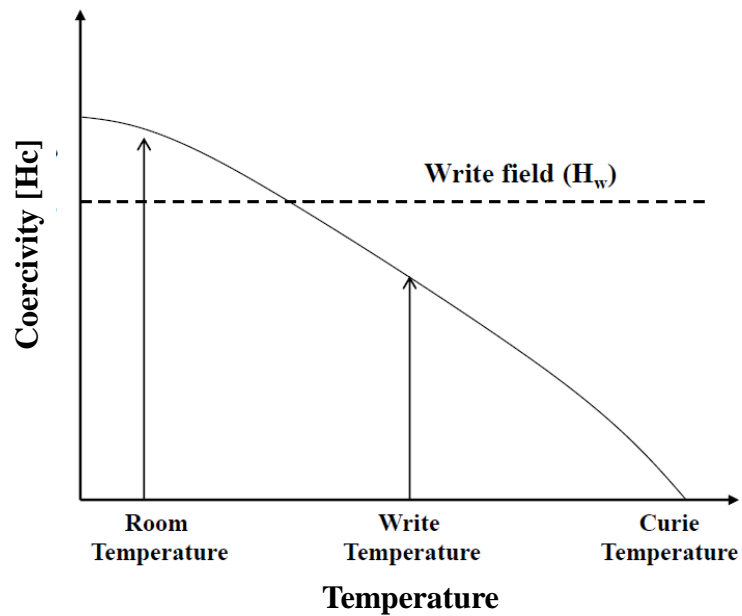


Figure 1.21 Lowering magnetic coercivity through heating of the magnetic media during Heat Assisted Magnetic Recording

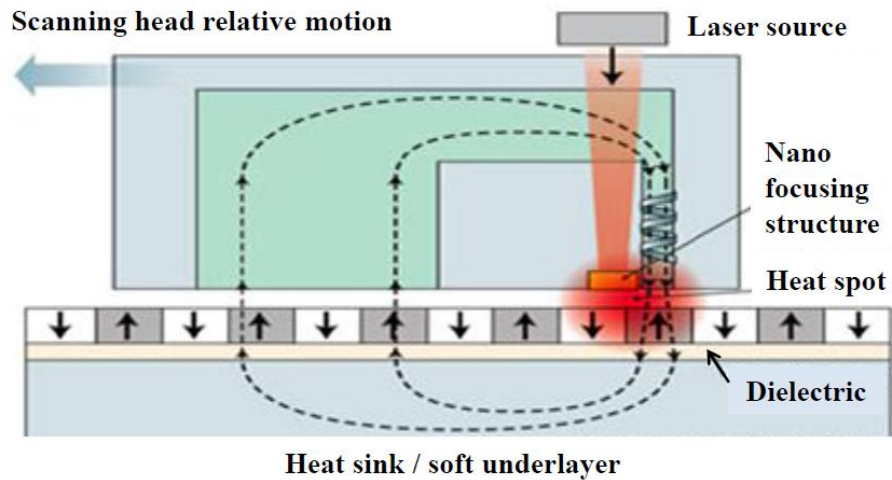


Figure 1.22 Schematic of heat-assisted magnetic recording (HAMR) (Source: [33])

Figure 1.22 shows a schematic of a heat-assisted magnetic recording (HAMR) system. A laser source is used to heat up the magnetic material locally. The temperature in heat-assisted magnetic recording is increased to the order of several hundred degrees Centigrade. Temperatures of several hundreds of Centigrade cause degradation of the lubricant. To prevent lubricant degradation new lubrication systems are required for heat assisted magnetic recording.

1.3.5 Patterned Magnetic Recording [34]-[38]

To reduce cross-talk and increase the recording density, patterned media have been proposed and investigated. Figure 1.23 (a), (b) and (c) shows conventional and patterned magnetic recording media with discrete tracks and bits, respectively. The magnetic recording layer of conventional media is a thin film of a magnetic alloy, which naturally forms a random distribution of nano-sized grains as shown in Figure 1.23 (a). As discussed previously, when the grain size is decreased, the bit distance becomes smaller and the “superparamagnetic limit” is approached. Figure 1.23 (b) shows discrete track recording (DTR) media which can reduce “cross-talk” in the radial direction by physically separating the recording track. In this case, storage density above 1Tbit/in^2 (one terabit, $1\text{Tb} = 1000 \times 10^9$ bits) can be achieved. The specific characterization of discrete track recording (DTR) media is discussed in chapter 2. Figure 1.23 (c) shows bit patterned media (BPM) in which the individual domains are isolated bit by bit. Thus, the “cross-talk” is reduced in both the circumferential and radial direction. In bit patterned media, the information is stored in a single bit on the disk surface.

For storage densities of 1Tbit/in², the diameter of each bit would be approximately 12nm and the bit pitch would be 24nm.

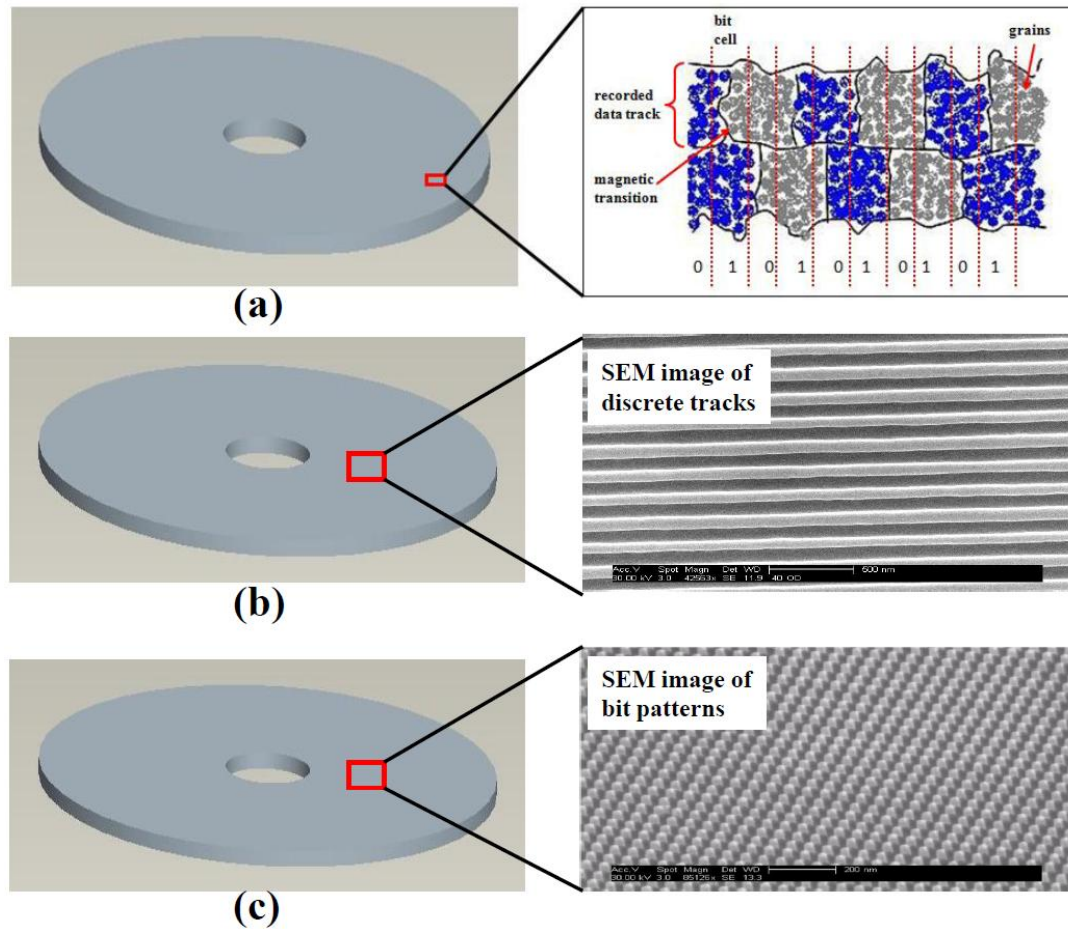


Figure 1.23 (a) Conventional smooth disk and (b) discrete track recording disk and (c) bit patterned disk

1.3.6 Combination of bit patterned media with heat-assisted magnetic recording

Heat assisted magnetic recording (HAMR) systems are currently inadequate in that heat diffusion from a heated spot erases the information on adjacent tracks. Another problem is bit instability after writing due to thermal fluctuation due to a

slow cooling rate. To solve this problem, bit patterned media (BPM) can be combined with heat-assisted magnetic recording (HAMR) technology [38]. Bit patterned media (BPM) can control heat diffusion by using a matrix with a low-heat conductivity material, which controls the thermal instability by using physically separated bits. A combination of bit patterned media (BPM) and heat-assisted magnetic recording (HAMR) is predicted to reach areal densities in excess of 10Tbit/in^2 .

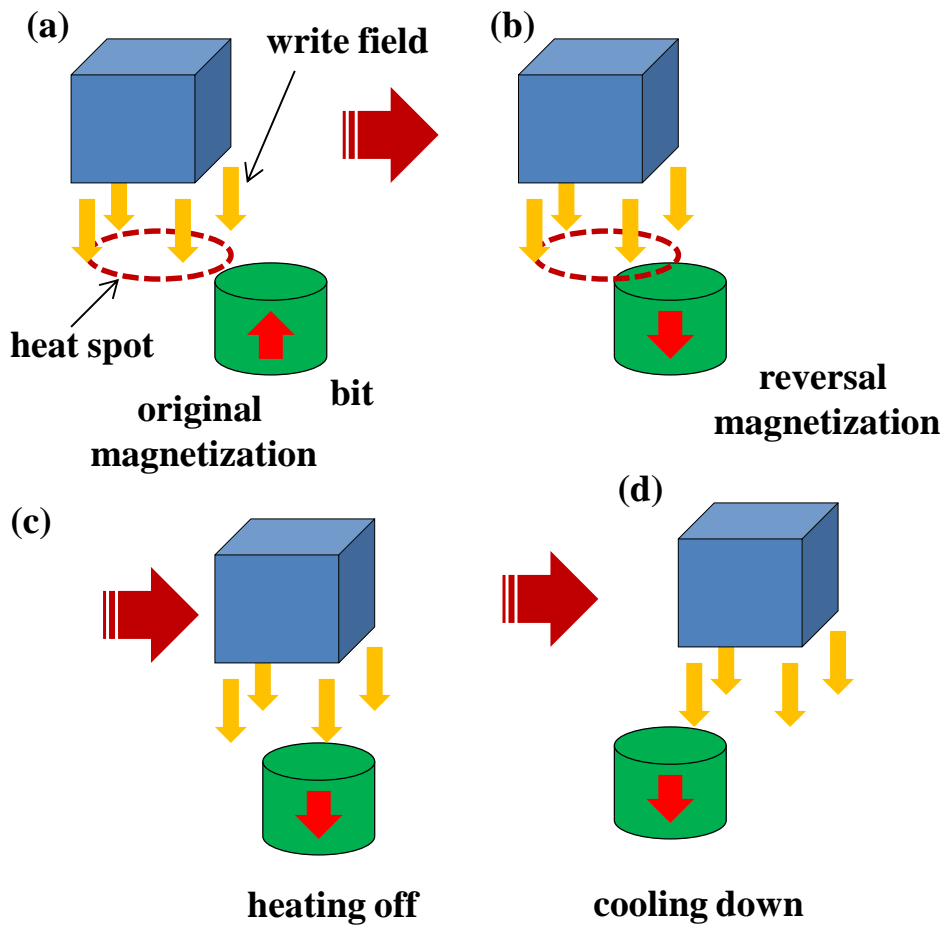


Figure 1.24 Schematic of the writing process using a combination of bit patterned media (BPM) and head-assisted magnetic recording (HAMR) technologies (Source: [38])

Figure 1.24 shows a schematic of the writing process of heat-assisted magnetic recording on bit patterned media. First, a magnetic writing field is applied to a heated dot (see Figure 1.24 (a)). Reversal of the magnetization occurs while the recording head passes over the dot (see Figure 1.24 (b)). Afterwards, the heat source is turned off, while maintaining the applied magnetic field (see Figure 1.24 (c)). Finally, the temperature of the dot is cooled down and the frozen bit securely records the data (see Figure 1.24 (d)).

To achieve larger areal densities, the understanding of the head/disk interface is of utmost importance. In the next section, we discuss the evolution of air-bearing sliders and address the principles of intermolecular and adhesion forces

1.4 Head/Disk Interface (HDI)

The head/disk interface (HDI) is the interface between the flying slider and the rotating disk in hard disk drives. Figure 1.25 shows the schematic of the slider/disk assembly. The slider flies over the magnetic disk to read and write the data (Figure 1.25 (a)). The spindle supports the disk and rotates at constant speed. In current disk drives, the rotational speed of the disk is typically between 1,200 and 15,000 revolutions per minute (RPM). The suspension supports the slider while it reads and writes data over the magnetic recording disk surface. The pre-load of the suspension balances the air-bearing force generated over the disk. The operation of hard disk drives is based on the principle of a self-acting air bearing between the slider and the rotating disk. This establishes a spacing between the slider and the disk, the so-called “flying height” (Figure 1.25 (b)). The details of

air-bearing systems are discussed in the following section. In the first hard disk drives, externally pressurized air was used to create the air bearing before self-pressurized air-bearings were developed. The performance and reliability of the head/disk interface is crucial for achieving high areal densities in today's hard disk drives. Figure 1.25 (c) shows a magnified view of the head/disk interface. The flying height of present day disk drives is on the order of 1 or 2 nm. For comparison, the flying height of the first disk drives (1956) was 20 μm . One of the most important features in the development of hard disk drives is related to the reduction of flying height. In this section, the factors characterizing the head/disk interface are discussed.

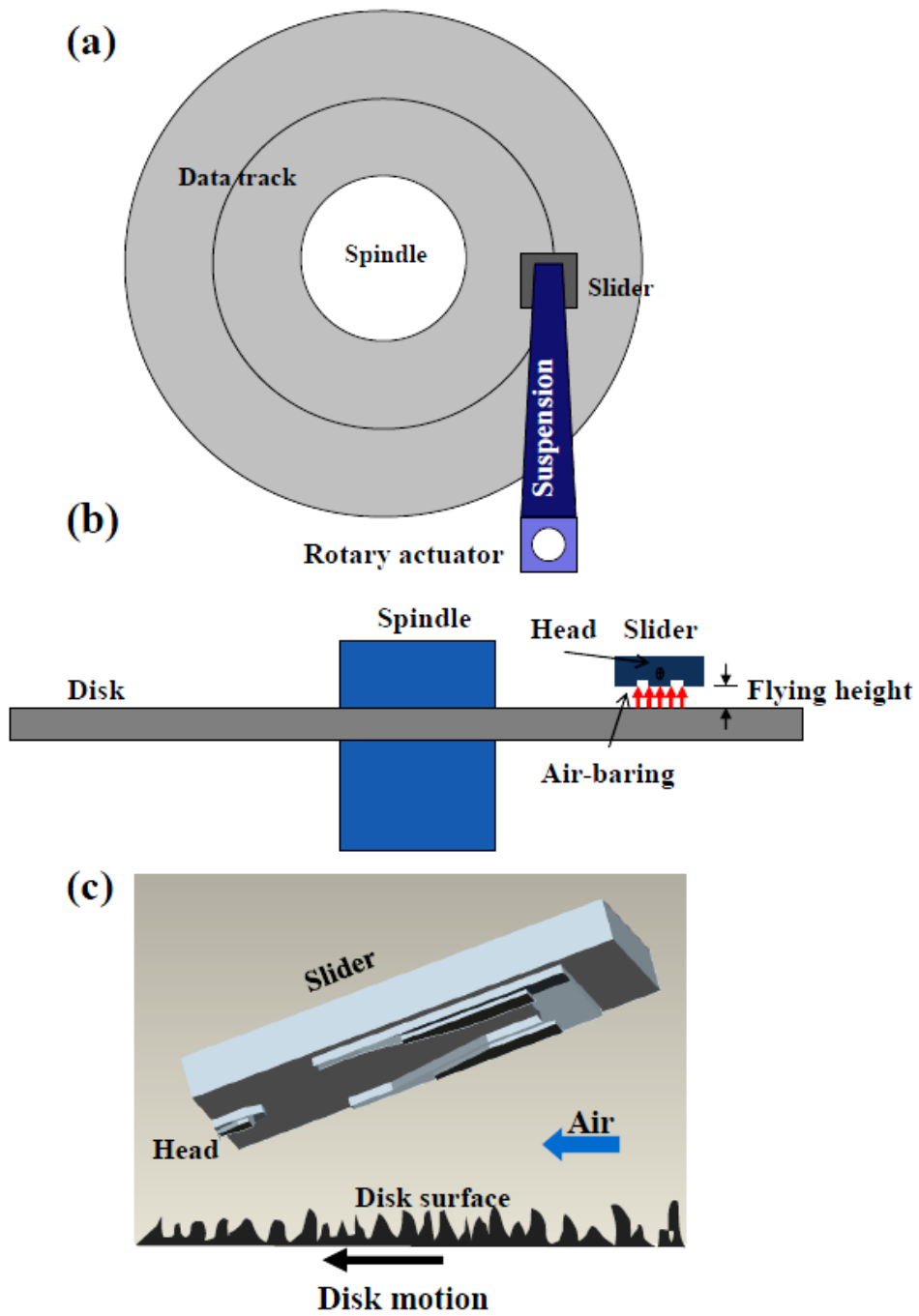


Figure 1.25 Schematic of slider/disk assembly: (a) top view, (b) side view, and (c) magnified view of the interface between head and disk

1.4.1 Air-bearing force

The flying of a magnetic recording slider is governed by the Reynolds equation. The 2-D compressible Reynolds equation [39] is given by (see appendix A)

$$\frac{\partial}{\partial x} \left(ph^3 \frac{\partial p}{\partial x} \right) + \frac{\partial}{\partial y} \left(ph^3 \frac{\partial p}{\partial y} \right) = 6\mu \left(U \frac{\partial ph}{\partial x} + V \frac{\partial ph}{\partial y} \right) + 12\mu \frac{\partial ph}{\partial t} \quad (1.13)$$

where p = pressure, h = spacing between head and disk, μ = dynamic viscosity, U and V = local disk velocity, and t = time.

As shown in appendix A, this equation is valid for a compressible fluid in a narrow gap behaving as a Newtonian fluid. Equation (1.13) represents that the hydrodynamic pressure forces (left hand side) and viscous shear forces (right hand side) are balanced. If the spacing between the two surfaces decreases, so that the Knudsen number $K_n = \frac{\lambda}{h}$ becomes of the order of 0.1, rarefaction effects must be considered. In this case, slip at the boundaries becomes important. The Knudsen (Kn) number, which is the ratio of the mean free path of the molecules (air = 68 nm) and the minimum spacing, is used to define rarefaction effects. Taking into account the rarefaction effects, one can write the Reynolds equation as

$$\frac{\partial}{\partial x} \left(Q(Kn) ph^3 \frac{\partial p}{\partial x} \right) + \frac{\partial}{\partial y} \left(Q(Kn) ph^3 \frac{\partial p}{\partial y} \right) = 6 \left(U \frac{\partial ph}{\partial x} + V \frac{\partial ph}{\partial y} \right) + 12 \frac{\partial ph}{\partial t} \quad (1.14)$$

where $Q(Kn)$ is the slip correction factor.

Burgdorfer [40] first introduced the concept of gas film lubrication with rarefaction effects (slip boundary flow) in the Reynolds equation. Hsia and Domoto [41] showed a second-order slip-flow boundary condition and derived a

modified Reynolds equation. Gans [42] first used the Boltzmann equation for arbitrary Knudsen numbers. Fukui and Kaneko [43] introduced polynomial fitting as a function of the inverse Knudsen number (D) using cubic polynomials.

The correction factors can be summarized as follows

- 1st order correction factor

$$Q_1 = \frac{D}{6} + \frac{\sqrt{\pi}}{2} \quad (1.15)$$

- 2nd order correction factor

$$Q_2 = \frac{D}{6} + \frac{\sqrt{\pi}}{2} + \frac{\pi}{4D} \quad (1.16)$$

- Boltzmann correction (Fukui and Kaneko [43])

$$Q_b = \begin{cases} \frac{D}{6} + 1.0162 + \frac{1.0653}{D} - \frac{2.1354}{D^2} & (5 \leq D) \\ 0.13852D + 1.25087 + \frac{0.15653}{D} - \frac{0.00969}{D^2} & (0.15 \leq D \leq 5) \\ -2.22919D + 2.10673 + \frac{0.01653}{D} - \frac{0.0000694}{D^2} & (0.01 \leq D \leq 0.15) \end{cases} \quad (1.17)$$

where D is the inverse Knudsen number ($D = \frac{\sqrt{\pi}}{2Kn}$)

The modified Reynolds equation with Boltzmann correction terms is considered to be the most accurate model for calculating the air-bearing force in present day sliders.

Figure 1.26 shows a schematic of the force equilibrium at the slider/disk interface. We observe that the air-bearing force F_{ab} is in equilibrium with the suspension force F_s to allow steady state flying of the slider. Figure 1.27 (a)

shows a magnified view of a typical slider air-bearing pressure distribution generated between the slider and the rotating disk. As shown in Figure 1.27 (b) and (c), the maximum pressure is generated near the minimum flying height.

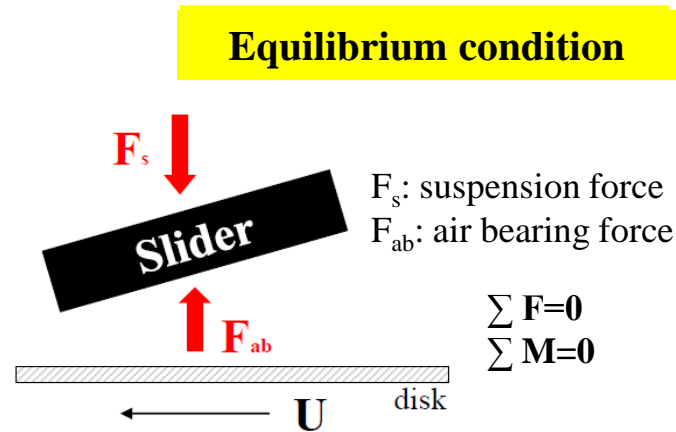


Figure 1.26 Schematic of slider-disk interface

1.4.2 Air-bearing sliders

The main function of air-bearing sliders is to carry the magnetic read/write head at the proper spacing over the disk without causing wear and failure of the disk drive. During operation the air-bearing force, generated as a result of viscous shear between the slider and the rotating disk, supports the slider. The read/write element is located near the minimum of the “flying height” of the sliders. Figure 1.28 (a) shows the trend of the flying height as a function of product year from the first (RAMAC hard disk drive) to today’s commercially available hard disk drives. A magnified view of the flying height in the last decade is shown in Figure 1.28 (b).

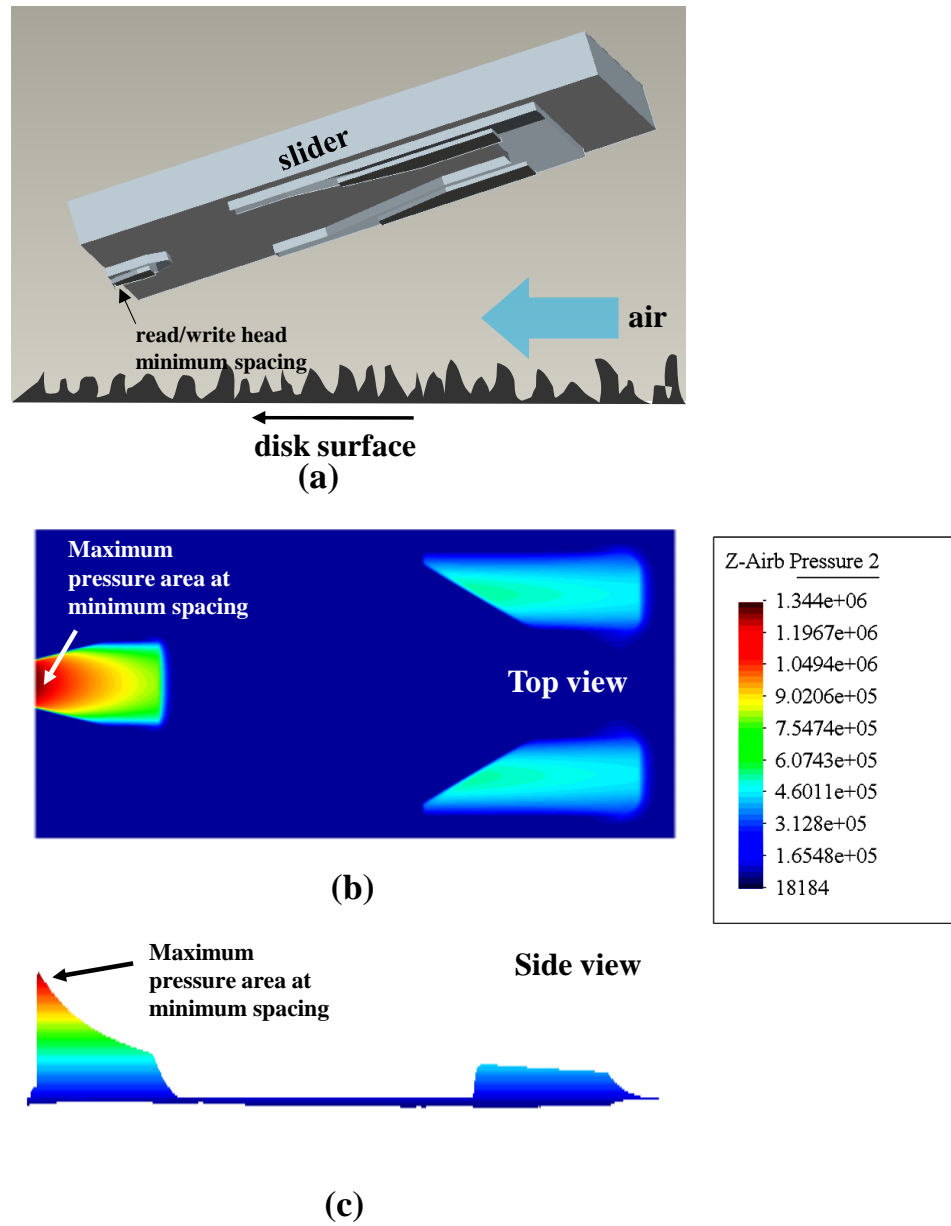


Figure 1.27 (a) Schematic of slider flying over disk and pressure distribution on the air-bearing surface as (b) top view and (c) side view

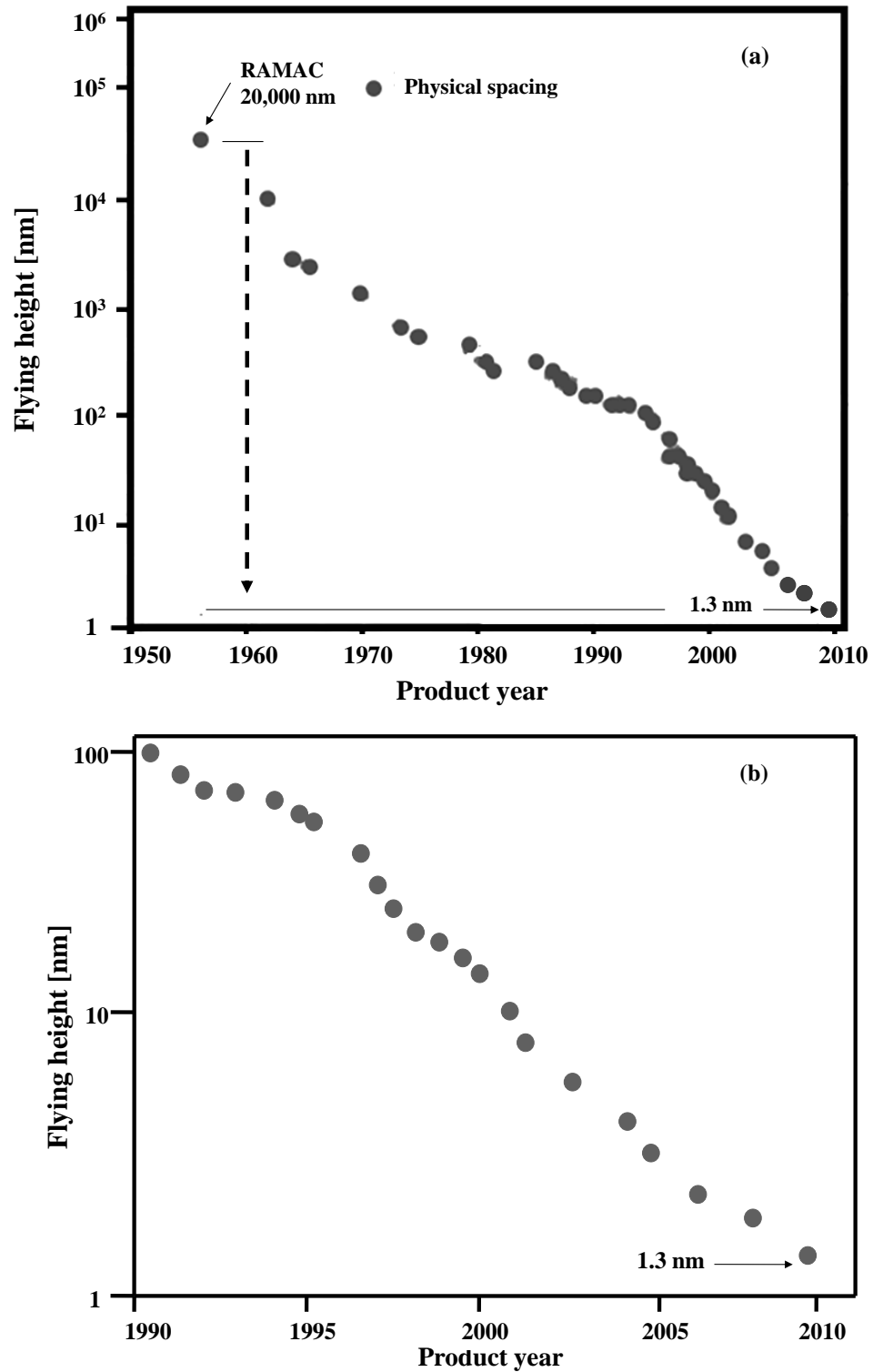


Figure 1.28 (a) Flying height as a function of product year and (b) magnified view of the flying height

As shown in Figure 1.28, the flying height of sliders in the first RAMAC hard disk drive was on the order of 20,000 nm, while the flying height in today's hard disk drives is on the order of 1 to 2 nm.

Thermal flying height control

In order to fly the read/write element at a spacing of 1 to 2 nm, the so-called "thermal flying control technique" is needed [44]. In this approach, a thermal resistor is incorporated in the slider, near the read/write element. If a current is applied to the heater, a thermal deformation of the area covering the heater occurs, moving the read/write element closer to the disk surface [44]. Figure 1.29 (a) and (b) show the schematic of thermal flying height control.

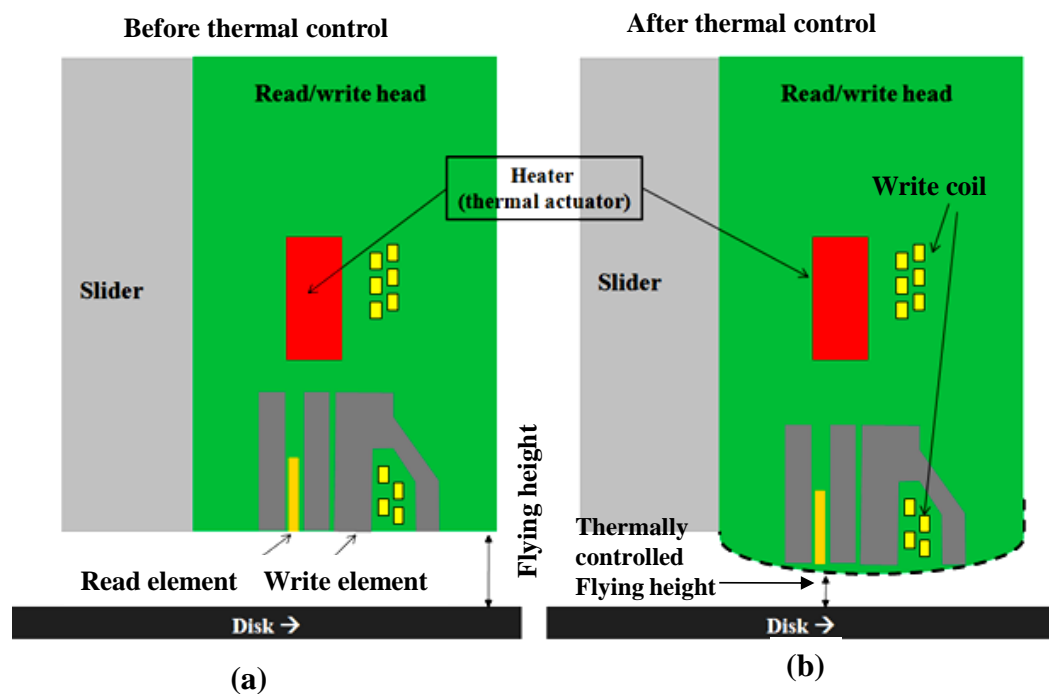
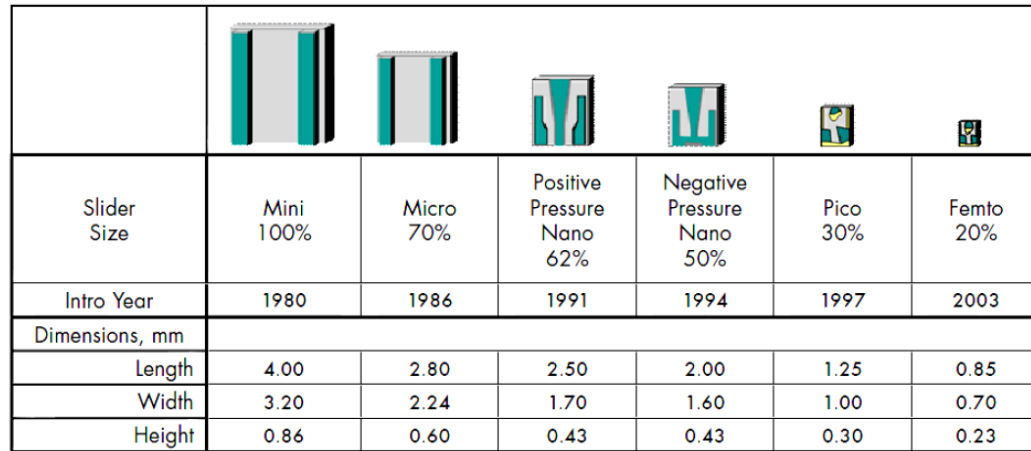


Figure 1.29 Magnified read/write head (a) before thermal flying height control and (b) after thermal flying height control

Figure 1.30 shows the evolution of self-pressurized air-bearing sliders beginning with 1980.



Slider Size	Mini 100%	Micro 70%	Positive Pressure Nano 62%	Negative Pressure Nano 50%	Pico 30%	Femto 20%
Intro Year	1980	1986	1991	1994	1997	2003
Dimensions, mm						
Length	4.00	2.80	2.50	2.00	1.25	0.85
Width	3.20	2.24	1.70	1.60	1.00	0.70
Height	0.86	0.60	0.43	0.43	0.30	0.23

Figure 1.30 The evolution of self-pressurized air-bearing designs (Source: [46])

We observe that the size and the load of the sliders have decreased with time. The reduced size of the sliders has improved the manufacturing efficiency and reduced cost. The size of the slider is referred to as the slider “form” factor. The dimensions of the so-called “mini” slider were 4 mm, 3.2 mm, and 0.86 mm for the length, width and height, respectively. The dimensions of present day femto-sliders (20 % sliders) are 0.85 mm, 0.7 mm, and 0.25 mm for the length, width and height, respectively. Figure 1.31 shows a typical magnified “sub-ambient” pressure slider design as presently used.

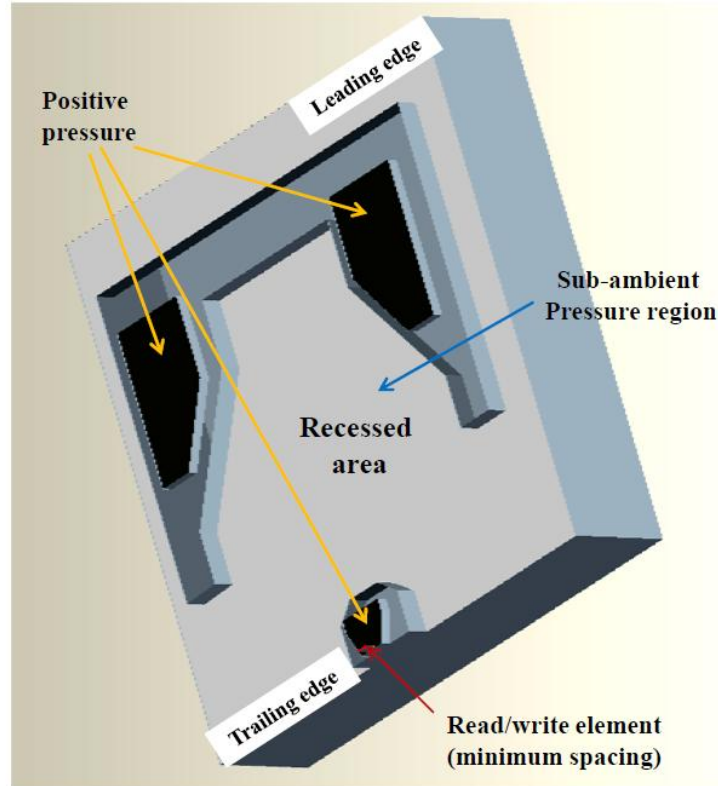


Figure 1.31 Typical sub-ambient pressure slider

As the spacing between slider and disk decreases below 5 nm, intermolecular forces and adhesion forces may become effective. In the next section, these forces will be discussed.

1.4.3 Intermolecular forces

Intermolecular forces exist at small distances between adjacent parts. Intermolecular forces can cause contacts between slider and disk and may result in the instability of the slider [47][51]. Figure 1.32 (a) shows stable flying of a slider over the disk without contact. Figure 1.32 (b) shows contact at the head and disk interface. When a slider contacts the rotating disk surface, slider dynamics

becomes much more complicated due to the intermolecular force (F_a), friction force (F_f) and contact force (F_c) (Figure 1.32 (b)).

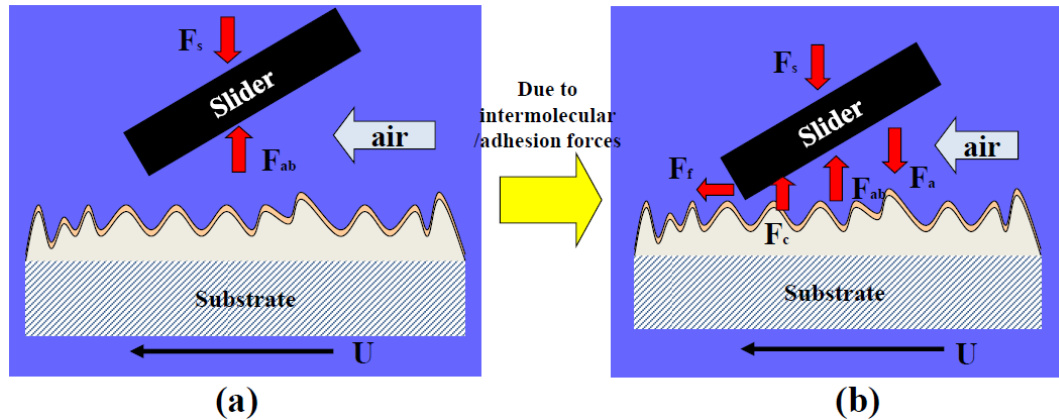


Figure 1.32 (a) Stable flying condition and (b) contact condition due to intermolecular and adhesion forces

Contacts cause wear between the slider and the disk and are undesirable.

Every effort possible is undertaken to avoid contact.

Intermolecular forces [49]

Intermolecular forces are the interaction forces of the electron clouds of two neighboring atoms. Figure 1.33 shows the Lennard-Jones potential, i.e., the potential energy curve versus the distance between two neighboring atoms. At large separations, intermolecular forces are zero. As the spacing decrease to the order of nm, attractive intermolecular forces are present. Attractive forces go through a well defined maximum at a spacing of 0.3 nm, and become repulsive at even smaller spacings. A picture of the Lennard-Jones potential curve is shown in Figure 1.33.

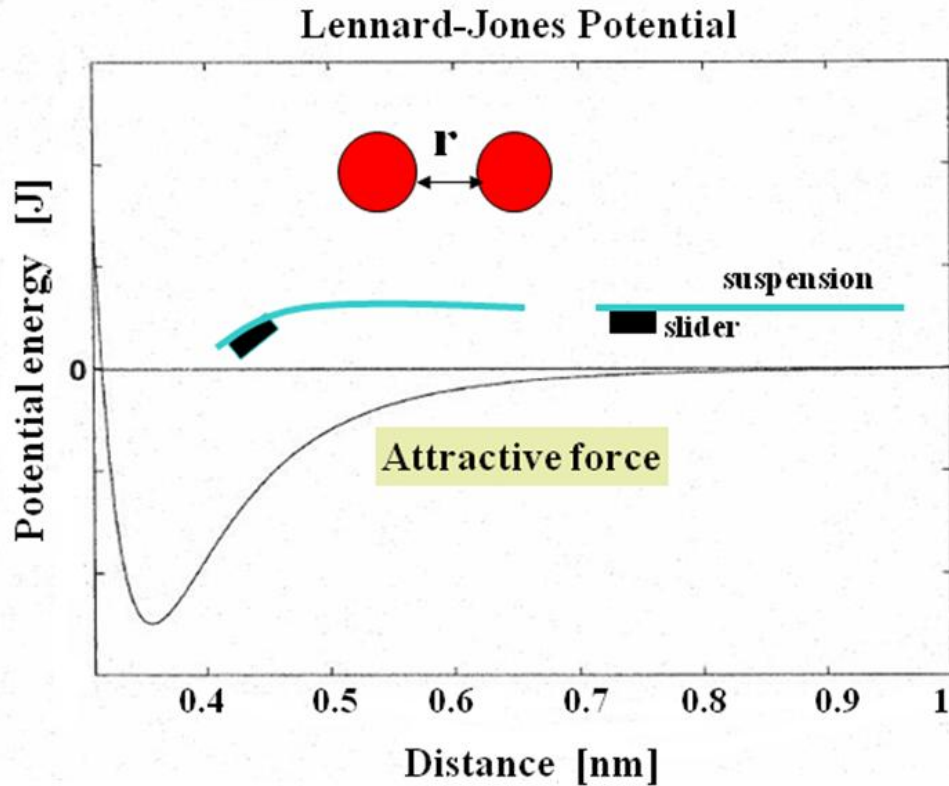


Figure 1.33 Lennard-Jones potential energy versus distance

The Lennard-Jones model is subscribed by an inverse sixth order power function of the distance for the attractive portion and as an inverse twelfth order power function of the distance for the repulsive portion, i.e.,

$$\Phi_{L-J} = -\frac{C}{r^6} + \frac{D}{r^{12}} \quad (1.18)$$

where r is the distance between two adjacent atoms, $C = 10^{-77} \text{ Jm}^6$ and $D = 10^{-134} \text{ Jm}^{12}$.

In equation (1.18), the attractive part is the so-called van der Waals potential given by

$$\Phi_{V-W} = -\frac{C}{r^6} \quad (1.19)$$

The potential between an atom and an infinite plane can be then obtained by integrating equation (1.18) over an infinitely long and infinitely deep half space [49], resulting in

$$\Phi_{atom-plane} = -\frac{\pi C \rho_1}{r^3} + \frac{\pi D \rho_1}{45r^9} \quad (1.20)$$

where r is the distance of atoms from the plane and ρ_1 is the number density of atoms from the plane.

The intermolecular force between a slider and a disk can be described by the following equation [50]:

$$F = \frac{A}{6\pi} \iint \frac{dxdy}{h^3} - \frac{B}{45\pi} \iint \frac{dxdy}{h^9} \quad (1.21)$$

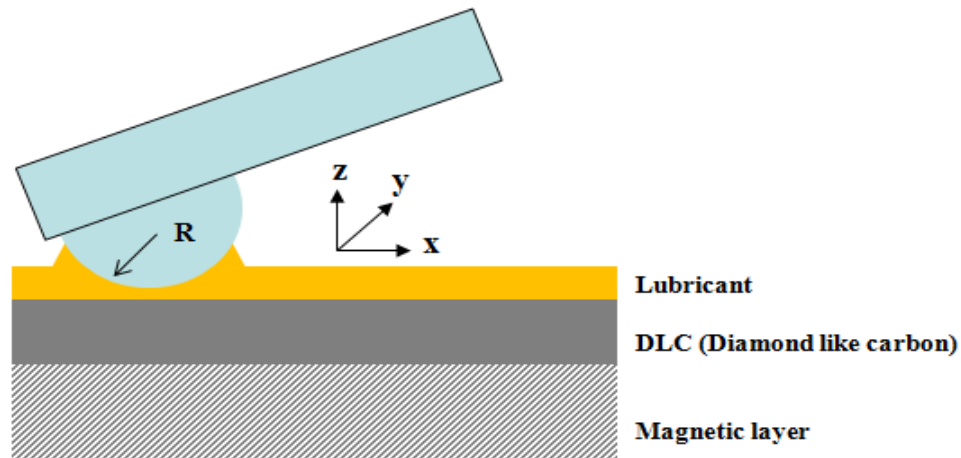
where A is the Hamaker constant, B is a constant and h is the spacing between a slider and a disk.

Typical values of A and B are $1 \times 10^{-19} J$ and $1 \times 10^{-76} Jm^6$, respectively, in the interfaces of condensed phases across a vacuum or air. The Hamaker constant of most condensed matter is in the range from $0.4 \times 10^{-19} J$ to $4 \times 10^{-19} J$ [49].

1.4.4 Adhesion forces of lubricant

The carbon overcoat and lubricant on the top surface of the disk protect the magnetic film from friction and wear. As the flying height is decreased to the nano-meter regime, the possibility of contacts between the slider and the disk is increased. During contacts, the lubricant on the disk forms a meniscus bridge with the slider resulting in adhesion forces which have a similar effect as intermolecular

forces. Kato et al. ([52]- [53]) have presented a model of a spherical slider-lubricant interface (Figure 1.34 Figure 1.35). As can be seen from Figure 1.34, in the beginning of the contact of the slider with the lubricant, the meniscus force in the x and y directions (in-plane) is zero. However, a force in the z direction (out-of plane) pulls down the slider towards the disk. Therefore, the meniscus forces in the x and y directions give rise to “stiction”, while the meniscus forces in the z direction give rise to an attractive force similar to intermolecular forces.



$$\begin{aligned}
 F_x &= 0 & R &= \text{radius of the curvature of the contact pad} \\
 F_y &= 0 & \gamma &= \text{surface tension of the lubricant} \\
 F_z &= -2\pi R\gamma(1 + \cos \theta_c) & \theta_c &= \text{contact angle} \\
 \theta_c &= \text{contact angle}
 \end{aligned}$$

Figure 1.34 In the beginning of the contact of the slider with the lubricant

The meniscus bridge becomes elongated and tilted due to the rotation of the disk and the separation of the slider and the disk. In this situation, adhesion forces occur in x, y and z directions as illustrated in Figure 1.35.

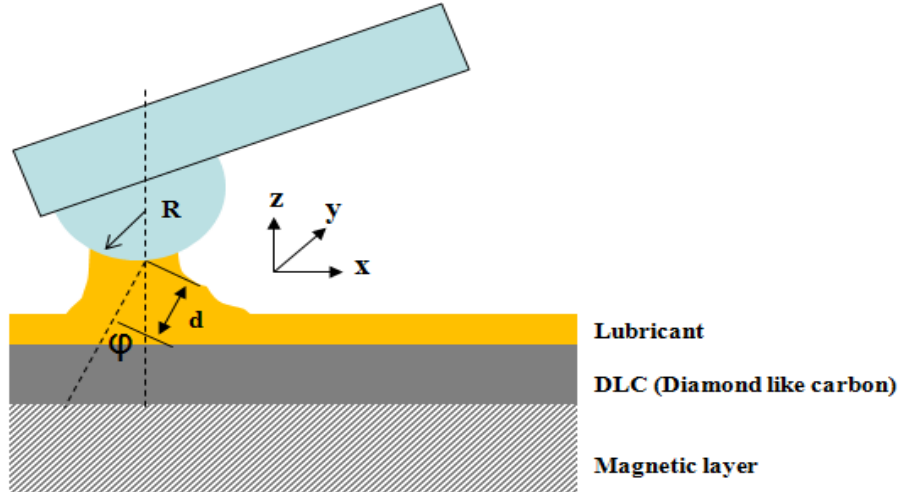


Figure 1.35 Elongated meniscus bridge and adhesion forces between slider and disk

In this case, the meniscus force [52] can be calculated by

$$\begin{aligned}
 F_x &= -2\pi R\gamma(1 + \cos \theta_c) \left(1 - \frac{2d}{\sqrt{4d^2 + R^2\phi_0^4}} \right) \sin(\phi) \cos(k) \\
 F_y &= -2\pi R\gamma(1 + \cos \theta_c) \left(1 - \frac{2d}{\sqrt{4d^2 + R^2\phi_0^4}} \right) \sin(\phi) \sin(k) \\
 F_z &= -2\pi R\gamma(1 + \cos \theta_c) \left(1 - \frac{2d}{\sqrt{4d^2 + R^2\phi_0^4}} \right) \cos(k)
 \end{aligned} \tag{1.22}$$

θ_c = contact angle, ϕ = angle of tilt of the meniscus bridge

ϕ_0 = a filling of angle of the meniscus bridge at $d = 0$

$k = \tan^{-1}(U/V)$, U = seek speed, V = rotating speed

1.4.5 Hysteresis of “touch-down” and “take-off”

As the flying height of the slider is decreased further, a phenomenon may occur that is best described as “snapping” of the slider to the disk. This

phenomenon has been predicted by Deoras and Talke [51], Ambekar et al. [54] and Demczyk [55], and is related to instability of the slider/disk interface at very close spacing. Experimentally, instability of the head/disk interface is observed as a hysteresis between “take-off” and landing of the slider as a function of a speed. In particular, take-off occurs at a higher speed than “touch-down” since the pull-down forces need to be overcome during “take-off” before flying is established. This difference in the velocity for “touch-down” and “take-off” is generally described as hysteresis. During “touch-down”, continuous contacts occur between head and disk, which causes wear of the slider and the disk. To obtain better performance and increase the reliability of hard disk drives, hysteresis should be avoided. Figure 1.36 shows the hysteresis between “touch-down” and “take-off” of a typical slider.

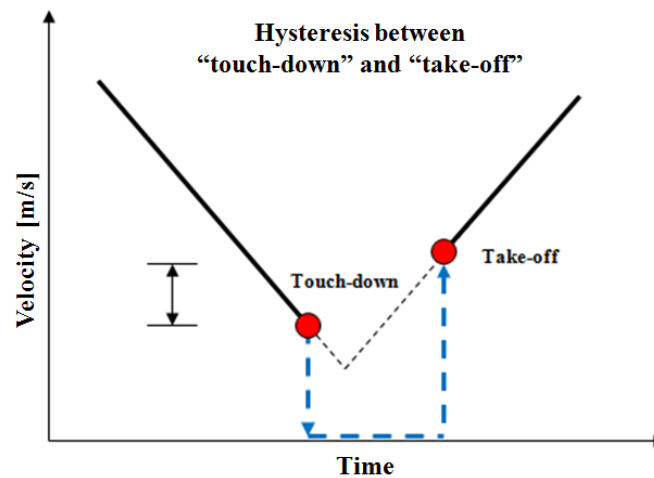
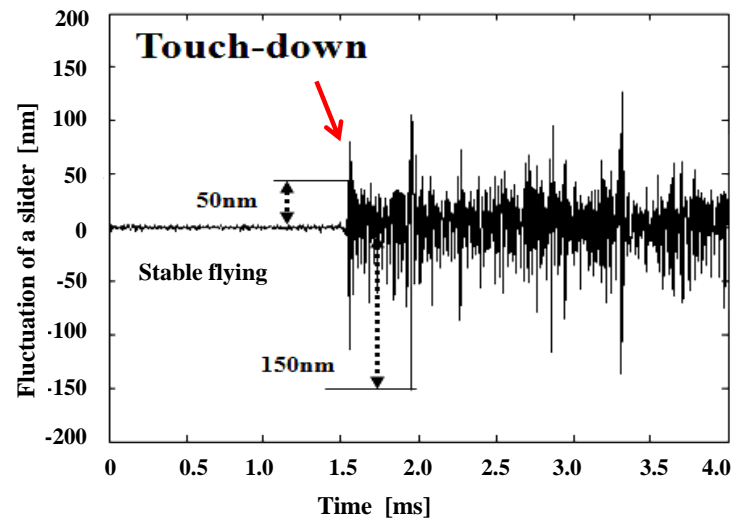


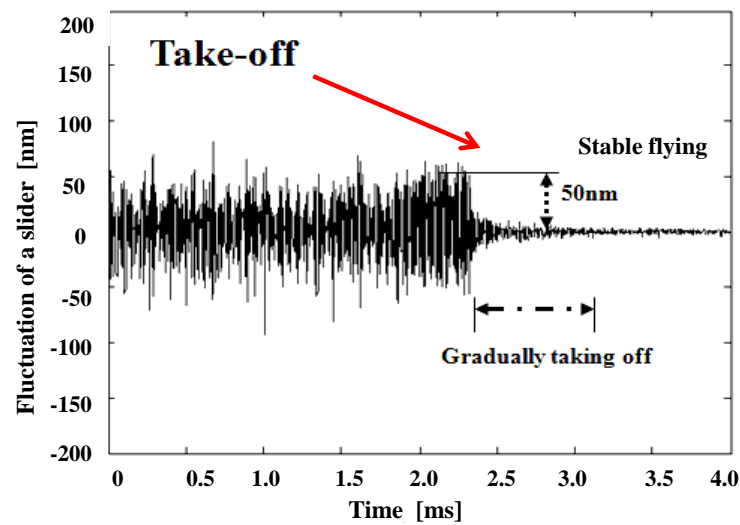
Figure 1.36 Hysteresis between “touch-down” and “take-off” velocity of a slider on a disk

Figure 1.37 shows the dynamic characteristics of sliders during “touch-down” and “take-off”. As can be seen in Figure 1.37 (a), “touch-down” occurs

when the flying height is decreased by reducing the velocity. At the moment of “touch-down” of a slider on the disk, fluctuations of the slider are large. Conversely, at the moment of “take-off”, fluctuations of the slider disappear as shown in Figure 1.37 (b).



(a)



(b)

Figure 1.37 Dynamic characteristics of sliders during (a) “touch-down” and (b) “take-off”

1.5 Organization of the Dissertation

This dissertation focuses on the tribology and slider dynamics of the head/disk interface at very small slider-disk flying heights for discrete track recording media. The investigations are carried out for “smooth” media and discrete track media, the latter being a potentially new approach to achieve areal densities.

Chapter 1 gives an introduction and history of hard disk drive technology and deals with the fundamental principles of magnetic recording.

Chapter 2 presents the characterization of discrete track recording (DTR) media.

Chapter 3 presents an investigation into the “flyability” of magnetic recording sliders over discrete track recording media. Flyability of sliders is investigated experimentally and numerically for various geometries of discrete track recording media.

Chapter 4 discusses the hysteresis between “touch-down” and “take-off” on discrete track recording media. The tribology of discrete track media is investigated and compared with conventional smooth media.

Chapter 5 focuses on contact behavior and wear characteristics of discrete track recording media. Nano-indentation and nano-scratch tests are performed to investigate the plastic deformation of the discrete tracks. Reciprocal wear tests are performed to investigate the effect of normal load and sliding contact in the head disk interface.

Chapter 6 discusses the tribological performance and adhesion characteristics of discrete track recording media. Contact angle measurements and atomic force microscopy (AFM) are used to analyze the adhesion characteristics. The effect of discrete tracks on slider dynamics and friction force is investigated.

Chapter 7 discusses planarization of discrete track recording media to improve the flyability of magnetic recording sliders. Different planarization methods and improvement of mechanical properties are described.

Chapter 8 presents the summary and conclusions of this dissertation.

Bibliography

- [1] A. S. Hoagland, "Early history and a 50 year perspective on magnetic disk storage," *Magnetic Disk Heritage Center*, 2005.
- [2] T. Noyes and W. E. Dickinson, "Engineering design of a magnetic-disk Random-Access Memory," *AFIPS Joint Computer Conference*, 1956.
- [3] T. Noyes and W. E. Dickinson, "The Random-Access Memory Accounting Machine," *IBM Journal*, 1957.
- [4] J. M. Harker, D. W. Brede, R. E. Pattison, G. R. Santana and L. G. Taft, "A quarter century of disk file innovation," *IBM J. RES. DEVELOP.* vol. 25, pp. 677-690, 1981.
- [5] J. K. Howard, M. F. Toney and C. H. Tsang, "Magnetoresistive read transducer and method for making the improved transducer," US patent 4,809,109, 1989.
- [6] S. M. Thompson, "The discovery, development and future of GMR: The Nobel prize 2007," *J. Phys. D: Appl. Phys.* vol. 41, 093001.1-093001.20, 2008.
- [7] T. M. Coughlin, "The once and future hard disk drive," *Coughlin Associates*, 2006.
- [8] T. M. Coughlin, "High density hard disk drive trends in the USA," *Journal of the Magnetics Society of Japan*, vol. 25, 111-120, 2001.
- [9] R. Wood, "Future hard disk drive systems," *JMMM*, vol. 321, pp. 555-561, 2009.
- [10] D. Weller and A. Moser, "Thermal effects in ultrahigh-density recording media," *IEEE Trans. Magn.*, vol. 35, pp. 4422-4439, 1995.
- [11] S. N. Piramanayagam, "Perpendicular recording media for hard disk drives," *J. Appl. Phys.*, vol. 102, pp. 011301-011301-22, 2007.
- [12] <http://hyperphysics.phy-astr.gsu.edu/Hbase/solids/hyst.html>
- [13] K. G. Ashar, Magnetic disk drive technology, *IEEE PRESS*, pp. 30-32, 1997.
- [14] S. X. Wang and A. M. Taratorin, Magnetic information storage technology, *ACADEMIC PRESS*, pp. 49-57, 1999.
- [15] N. Smith, "Reciprocity principles for magnetic recording theory," *IEEE Trans. Magn.*, vol. 23, pp. 1995-2002, 1987.

- [16] J. C. Mallinson, "Some comments on the reciprocity integral used in magnetic recording," *IEEE Trans. Magn.*, vol. 33, pp. 2402-2404, 1997
- [17] N. Smith, "Further comments on the reciprocity integral for magnetic recording," *IEEE Trans. Magn.*, vol. 34, pp. 772-775, 1998.
- [18] K. G. Asher, Magnetic disk drive technology, *IEEE PRESS*, pp. 70-79, 1997.
- [19] A. Kakeshi, M. Oshiki, T. Aikawa, M. Sasaki and T. Kozai, "A thin film head for high density recording," *IEEE Trans. Magn.*, MAG-18, pp. 1131-1133, 1982.
- [20] S. W. Yuan and H. N. Bertram, "Magnetoresistive heads for ultrahigh density recording," *IEEE Trans. Magn.*, vol. 27, pp. 3811-3816, 1993.
- [21] E. Grochowski and R. E. Fontana, Jr., "Nanofilms in giant magnetoresistance heads," *Dekker Encyclopedia of Nanoscience and Nanotechnology*, pp. 2383-2397, 2004.
- [22] www.dataclinic.co.uk, "Data Clinic Knowledgebase: Data Recovery and Hard Disk reference section."
- [23] M. N. Baibich, J. M. Broto, A. Fert, F. N. V. Dan, F. Petroff, P. Eitenne, G. Creuzet, A. Friederich and J. Chazelas, "Giant magnetoresistance of (001)Fe/(001)Cr magnetic superlattices," *Phys. Rev. Lett.*, vol. 61, pp. 2472-2475, 1988.
- [24] M. Julliere, "Tunneling between ferromagnetic film," *Phys. Lett.*, 54A, pp. 225-226, 1975.
- [25] S. Ikeda, J. Hayakawa, Y. Ashizawa, Y. M. Lee, K. Miura, H. Hasegawa, M. Tsunoda, F. Matsukura and H. Ohno, "Tunnel magnetoresistance of 604 % at 300K by suppression of Ta diffusion in CoFeB/MgO/CoFeB pseudo-spin-valves annealed at high temperature," *Appl. Phys. Lett.*, vol. 93, pp. 082508 - 082508-3, 2008.
- [26] I. Kaitzu, R. Knamura, J. Toda and T. Morita, "Ultra high density perpendicular magnetic recording technologies," *FUJITSU Sci. Tech. J.*, 42, 1, pp. 122-130, 2006.
- [27] K. Nguyen, "Perpendicular recording: A boon for consumer electronics," *Hitachi Global Storage Technologies*, 2005.
- [28] R. Wood, Y. Hsu, M. Schultz, "Perpendicular magnetic recording technology," *Hitachi Global Storage Technologies*, 2007.
- [29] "High density magnetic recording Fujitsu, media technology," *FUJITSU Lab.*, 2008.

- [30] J.-G. Zhu, X. Zhu and Y. Tang, "Microwave assisted magnetic recording," *IEEE Trans. Magn.*, vol. 44, no. 1, pp. 125-131, 2008.
- [31] S. Li, B. Livshitz, H. N. Bertram, E. E. Fullerton and V. Lomakin, "Microwave assisted magnetization reversal and multilevel recording in composite," *Journal of Applied Physics*, vol. 105, pp. 07B909-1-3, 2009.
- [32] W. A. Challener, C. Peng, A. V. Itagi, D. Karns, W. Peng, Y. Peng, X. Yang, X. Zhu, N. J. Gokemeijer, Y.-T. Hsia, G. Ju, R. E. Rottmayer, M. A. Seigher and E. C. Gage, "Heat-assisted magnetic recording by a near-field transducer with efficient optical energy transfer," *Nature Photonics*, vol. 3, pp. 220-224, 2009.
- [33] L. Pan and D. B. Bogy, "Data storage: Heat-assisted magnetic recording," *Nature Photonics*, vol. 3, pp. 189-190, 2009.
- [34] D. Wachenschwanz, W. Jiang, E. Roddick and A. Homola, "Design of a manufacturable discrete track recording medium," *IEEE Trans. Magn.*, vol. 41, pp. 670-675, 2005.
- [35] Y. Kanai, H. Watanabe, H. Muraoka, Y. Nakamura, "Single-pole-type head showing a large recording field suitable for 1 Tbps with discrete-track media," *JMMM*, vol. 286, pp. 362-366, 2005.
- [36] H. J. Richter, A. Y. Dobin, O. Heinonen, K. Z. Gao, R. J. M. v. d. Veerdonk and R. M. Brockie, "Recording on bit-patterned media at densities of 1Tb/in² and beyond," *IEEE Trans. Magn.*, vol. 42, pp. 2255-2260, 2006.
- [37] R. Sbiba and S. N. Piramanayagam, "Patterned media towards nano-bit magnetic recording: Fabrication and challenges," *Bentham Science Publishers Ltd.*, pp. 29-40, 2007.
- [38] A. Kikitsu, "Prospects for bit patterned media for high-density magnetic recording," *JMMM*, vol. 321, pp. 526-530, 2009.
- [39] O. Reynolds, "An Experimental Investigation of the Circumstances Which Determine Whether the Motion of Water Shall Be Direct or Sinuous, and of the Law of Resistance in Parallel Channels," *Royal Society of London*, vol. 174, pp. 935-982, 1883.
- [40] A. Burgdortor, "The influence of the molecular mean free path on the performance of hydrodynamic gas lubricated bearings," *ASME J. Basic Eng.*, vol. 81, pp. 94-100, 1959.
- [41] Y.-T. Hisa and G. A. Domoto, "An experimental investigation of molecular rarefaction effects in gas lubricated bearing at ultra-low clearances," *ASME J. Lubr. Technol.*, vol. 105, pp. 120-130, 1983.

- [42] R. F. Gans, "Lubrication theory at arbitrary Knudsen numbers," *ASME J. Tribol.*, vol. 107, pp. 431-433, 1985.
- [43] S. Fukui and R. Kaneko, "A database for interpolation of Poiseuille flow rates for high Knudsen number lubrication problems," *ASME J. Tribol.*, vol. 112, pp. 78-83, 1990.
- [44] Meyer D, Kupinski P E and Liu J C 1999 *US Patent* US5991113
- [45] B. E. Schutz, "Thermal Fly-height Control (TFC) technology in Hitachi hard disk drives," Hitachi Global Storage Technologies, 2007.
- [46] J. Best, S. Bolasna, L. Dorius, Y. Iihara, J. Kotla, T. Matumoto, R. Simmons, A. Tobar and H. Tsuchida, "The femto slider in Hitachi hard disk drives," Hitachi Global Storage Technologies, 2007.
- [47] B. H. Thornton and D. B. Bogy, "Head-disk interface dynamic instability due to intermolecular forces," *IEEE Trans. Magn.*, vol. 39, pp. 2420-2422, 2003.
- [48] B. H. Thornton and D. B. Bogy, "A parametric study of head-disk interface instability due to intermolecular forces," *IEEE Trans. Magn.*, vol. 40, pp. 337-344, 2004.
- [49] J. N. Israelachvili, Intermolecular and surface force, 2nd ed., *ACADEMIC PRESS*, 1992.
- [50] L. Wu, D. B. Bogy, "Effect of the intermolecular forces on the flying attitude of sub-5nm flying height air bearing sliders in hard disk driving," *Journal of Tribology*, vol. 124, pp. 562-567, 2002.
- [51] S. K. Deoras and F. E. Talke, "Effect of intermolecular forces on the dynamic response of a slider," *Transaction of ASME*, vol. 129, pp. 178-180, 2007.
- [52] T. Kato, S. Watanabe and H. Matsuoka, "Dynamic characteristics of an in-contact head slider considering meniscus force: Part-I formation and application to the disk with sinusoidal undulation," *ASME Journal of Tribology*, vol. 22, pp. 633-638, 2000.
- [53] T. Kato, S. Watanabe and H. Matsuoka, "Dynamic characteristic of in-contact head slider considering meniscus force: Part-II application to the disk with random undulation and design conditions," *ASME Journal of Tribology*, vol. 123, pp. 168-174, 2001.
- [54] R. Ambekar, W. Gupta, D. B. Bogy, "Experimental and numerical investigation of dynamic instability in the head disk interface at proximity," *Transaction of ASME*, vol. 127, pp. 530-536, 2005.
- [55] B. Demczyk, J. Liu, C. Y. Chen, S. Zhang, "Lubrication effects on head-disk spacing loss," *Tribology International*, vol. 38, pp. 562-565, 2005.

Chapter 2

Characterization of Discrete Track Recording Media

This chapter describes the manufacturing process and dynamic characteristics of the head/disk interface using discrete track recording (DTR) media (Figure 2.1). Discrete track recording (DTR) technology is considered a candidate for achieving an areal density beyond 1 Tbit/in² [1, 2]. Discrete track recording (DTR) technology is a step between conventional recording technology and bit patterned recording technology. Before bit patterned technology is available to expand areal density beyond 1 Tbit/in², discrete track recording technology is thought to serve as an intermediate bridge between conventional media and bit patterned media.

In discrete track recording (DTR) media, magnetic transition noise between adjacent tracks is eliminated in the radial direction by physically separating adjacent tracks [3]. Figure 2.1 shows a schematic of perpendicular discrete track recording (DTR) technology. The magnetization occurs along each track without influence of adjacent tracks. DTR media are geometrically characterized by their groove depth (D), land width (L) and track pitch (T). Clearly, as the track pitch is decreased, the areal density is further improved.

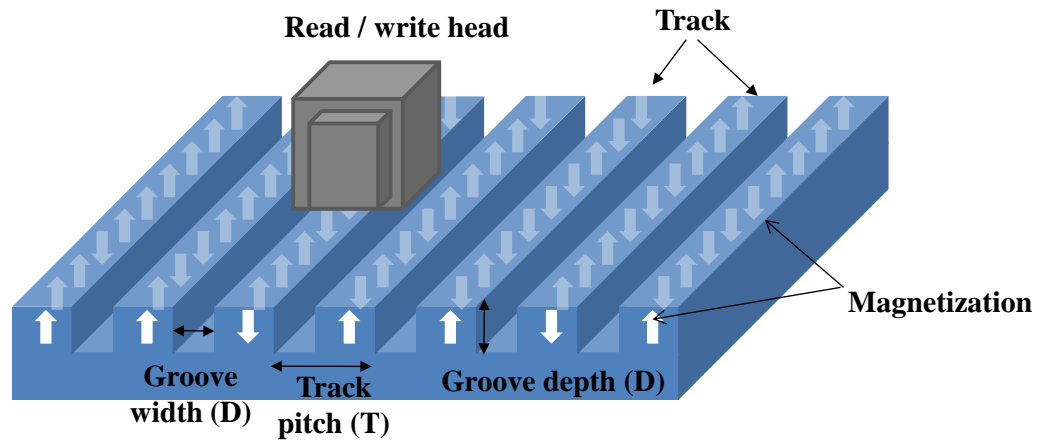


Figure 2.1 Schematic of discrete track recording (DTR) technology

2.1 Manufacturing of Patterned media

Two different manufacturing processes are generally being considered for manufacturing patterned media. They are “substrate patterning” [3] and “magnetic layer patterning” [4]. Both processes use a master template to transfer the patterns to the disk using imprinting.

2.1.1 Substrate patterning method

This method is used to create patterns on the substrate, prior to the deposition of the magnetic film, using nano-imprint lithography (NIL) [3].

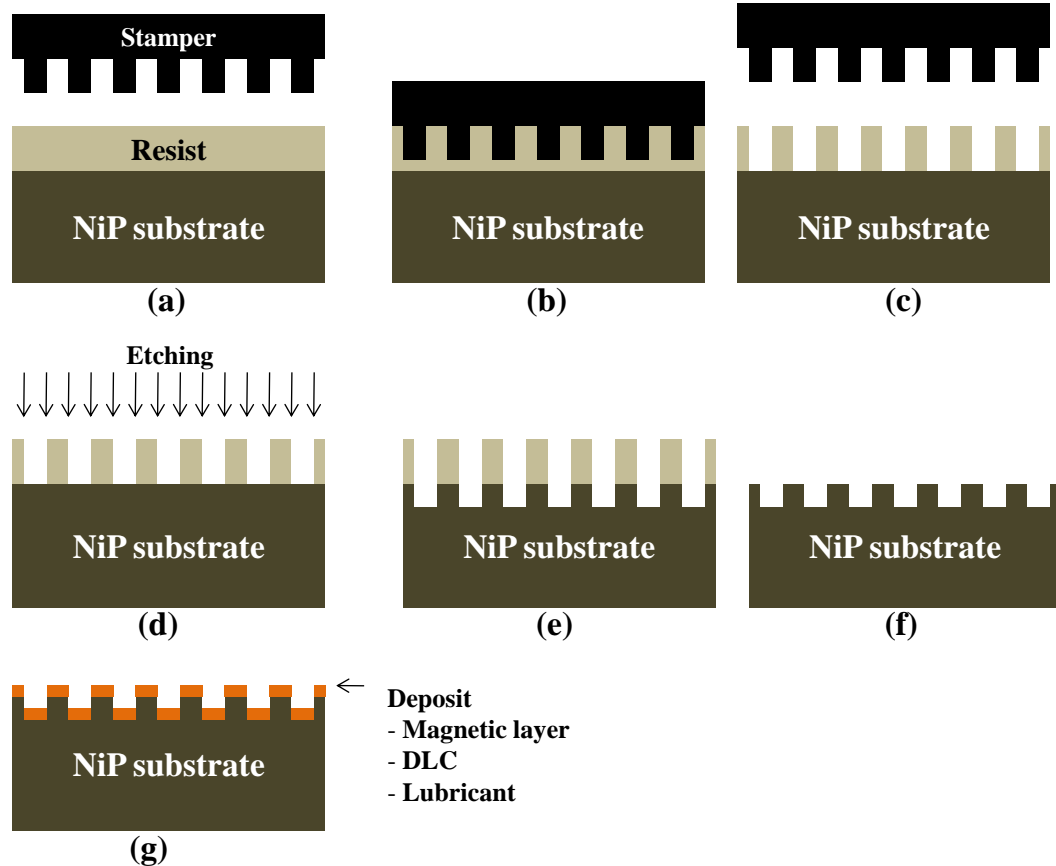


Figure 2.2 Schematic for “substrate patterning” process flow chart using nano-imprint lithography (NIL) to create the land and groove structure on NiP-plated substrate

Figure 2.3 shows a flow chart of “substrate patterning” using nano-imprint lithography (NIL) to create the land and groove structure on a NiP-plated substrate. A “master disk” with the reverse image of the desired pattern is embossed into the disk to be fabricated (Figures 2.3 (a)-(c)). This disk is first coated with photo resist which is applied by spin-coating. The photo resist gets compressed during contact with the master disk, becoming the image of the master disk on the NiP coated disk. The NiP substrate is then etched to form the grooves in the substrate (Figures 2.3 (d)-(e)). The remaining resist is removed and cleaned (Figure 2.3 (f)).

Finally, the magnetic layer, diamond like carbon (DLC) coating and lubricant are deposited on the pattern. Figure 2.3 shows a tunneling electron microscopy (TEM) image of the cross section of a sputtered DTR disk using “substrate patterning” process. As can be seen in Figure 2.3 (b), the magnetic layer is found on the bottom and side walls in the groove areas.

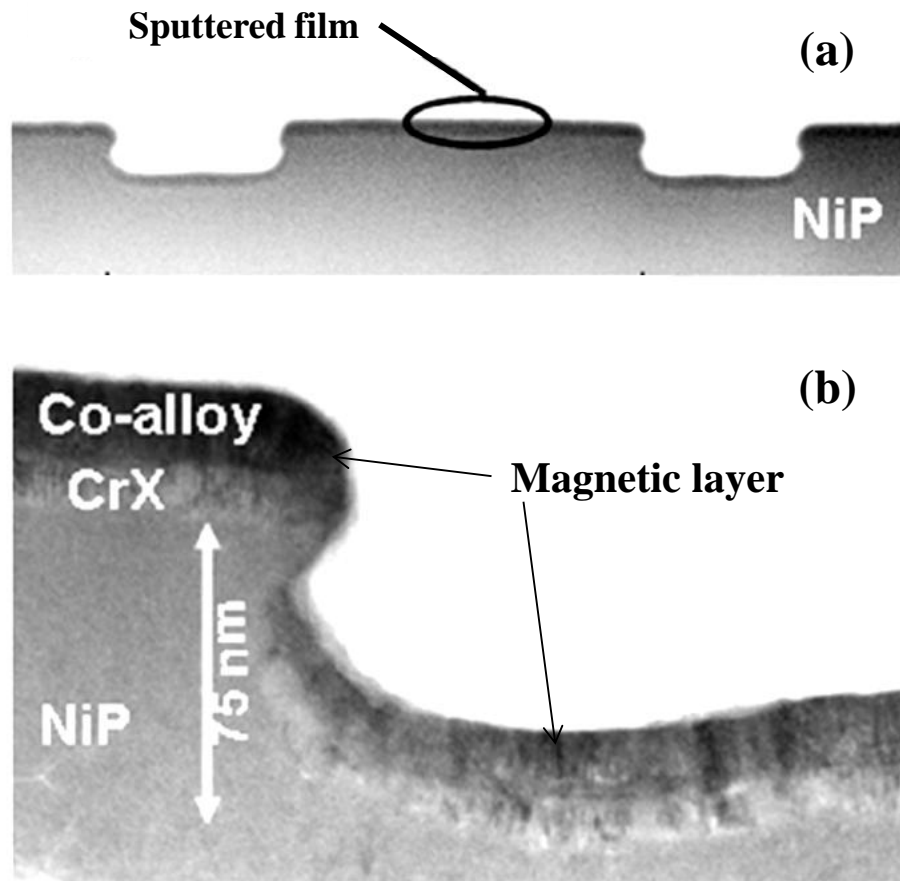


Figure 2.3 TEM image of the cross section of a sputtered DTR disk: (a) land between two grooves and (b) cross section in the vicinity of a groove wall [Source: 3]

2.1.2 Magnetic layer patterning method

The other way to make patterned disks is by a process known as “magnetic layer patterning” [4]. In this method, the disk is manufactured in the conventional way. The disk is then spin-coated and brought in contact with the master disk (stamper). Figure 2.4 indicates the fabrication method. An image of the master disk is produced during contact with the photo resist layer. Etching of the photo resist and the magnetic layer results in a patterned magnetic layer. No magnetic layer exists on the bottom and on the side walls of groove areas. Thus this fabrication method is desirable from the point of view of minimizing or eliminating “cross-talk”. This method, however, results in low fabrication throughput due to difficulty of the etching of a magnetic layer.

Figure 2.4 shows a flow chart of the “magnetic layer patterning” process using nano-imprint lithography (NIL) to create the land and groove structure on the magnetic layer. The magnetic layer is first deposited on the substrate (Figure 2.4 (a)). A resist is spun on the magnetic layer. Then a master disk (stamper) with the reverse image of the desired pattern is embossed in the resist (Figures 2.4 (b)-(c)). The magnetic layer is etched to form the grooves (Figures 2.4 (d)-(e)). The remaining resist is removed and cleaned (Figure 2.4 (f)). Finally, a diamond like carbon (DLC) coating and lubricant are deposited to protect the magnetic layer.

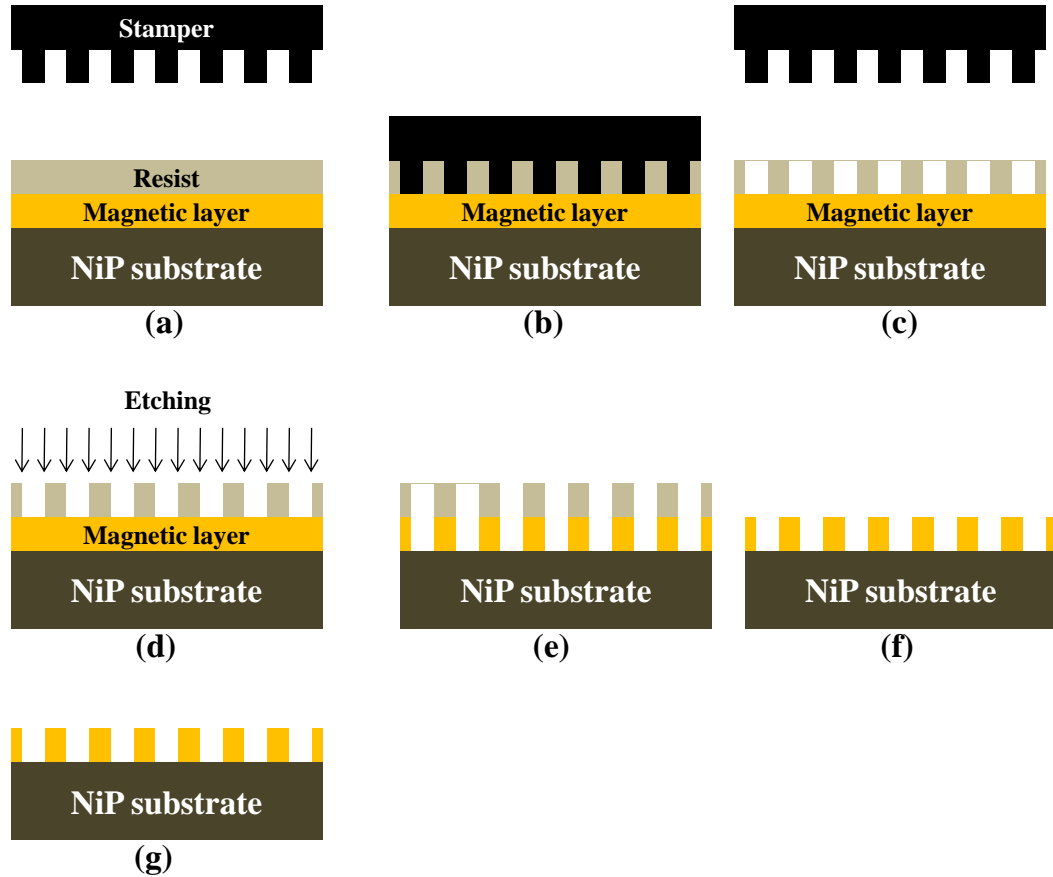


Figure 2.4 Schematic for “magnetic layer patterning” process flow using nano-imprint lithography (NIL) to create the land and groove structure on NiP-plated substrate [Source: 4]

Figure 2.5 shows the cross-sectional tunneling electron microscopy (TEM) image of patterned media using the “magnetic layer patterning” process. The etching process is performed until the underlayer is reached. In the grooves, the hard magnetic layer, which is the recording layer, is totally etched away.

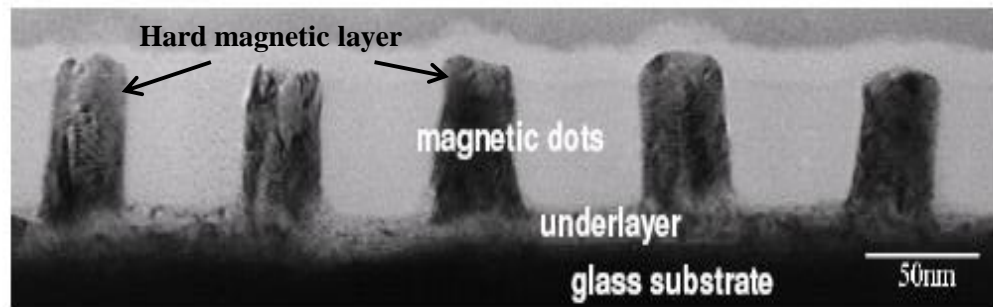


Figure 2.5 TEM image of the cross section of the patterned media [Source: 4]

2.1.3 Fabrication of “master” disk

Manufacturing of the master disk is done using rotational electron beam (E-beam) lithography [5-6]. Figure 2.6 shows the schematic of fabrication of a master disk. E-beam resist is spin-coated on a silicon (Si) wafer (a). Then, a pattern is written on the resist using an electron beam writer and the resist is developed (b). The silicon (Si) wafer is etched using reactive ion etching (RIE) to create a silicon (Si) master (c). Dip coating is then used to apply a so-called “release layer” on the silicon (Si) master (d). A photo-resist for nano-imprint lithography with UV treatment (UV-NIL) is spin-coated on a quartz wafer (e). The silicon (Si) master is pressed in the resist of the quartz wafer to transfer the pattern from the silicon disk (f). Then, the silicon master is released (g) and the residual layer is cleaned by reactive ion etching (RIE) using oxygen (h). Finally, the quartz master template is fabricated by quartz dry etching using fluorocarbon gas and stripping of the resist using oxygen (i).

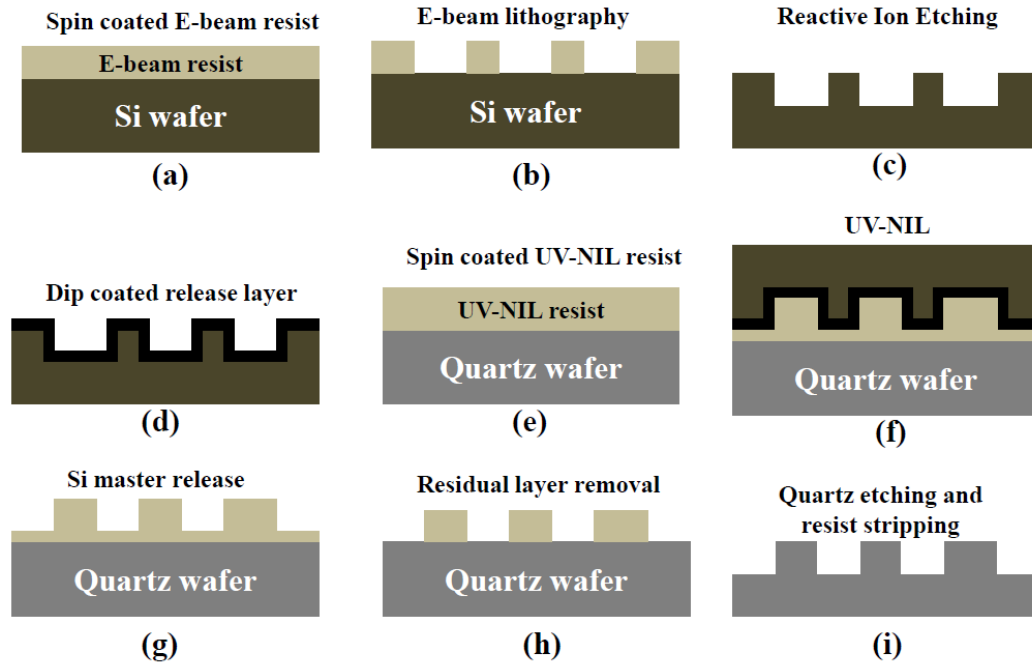


Figure 2.6 Process flow for fabrication of quartz master disk (Source: [6])

2.2 Dynamic characteristics of magnetic recording sliders on DTR media

Figure 2.7 shows the schematic of a slider flying over a discrete track recording (DTR) disk. We observe that the slider flies over thousands of tracks, i.e., the flying height between slider and disk changes as a function of the location of the discrete tracks relative to the air bearing surface. Clearly, the dynamic characteristics of a slider on discrete track recording (DTR) media is affected by the characteristics of the discrete tracks and we can expect that the flying characteristics of a slider on discrete track media is quite different from that of a slider flying on conventional smooth media.

The head/disk interface of a slider over discrete track recording media has been investigated numerically and experimentally by a number of researchers. Duwensee et al. [7-9] proposed an empirical equation for the flying height “loss” of a slider on discrete track media. They found that the “flying height loss” Δh of a slider over discrete track media can be determined by

$$\Delta h = d \frac{w}{p} \quad (2.1)$$

where d is the groove depth, while w and p are groove width and track pitch, respectively.

The flying height loss is defined as the difference in flying height of a slider on smooth and discrete track media.

Li [10] investigated the flying characteristics of sliders using grooves on the air-bearing surface rather than on the disk surface. Peng et al. [11] predicted the flying height loss of discrete track recording (DTR) media using an averaged flow model and verified the results by examining the flying height at touch-down pressure. Kim et al. [12] investigated numerically the flying characteristics of ultralow flying sliders during track seeking on discrete track recording (DTR) media. Yoon et al. [13] studied the dynamic performance of sliders with three different types of discrete track recording (DTR) media using numerical simulations.

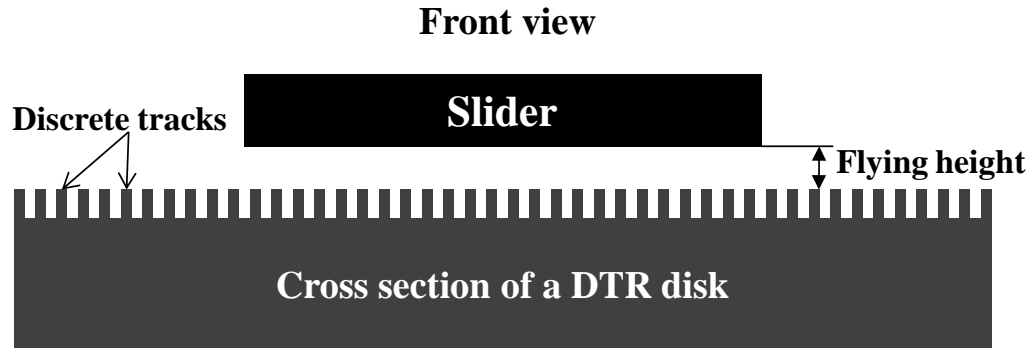


Figure 2.7 Schematic of a flying slider on a DTR disk

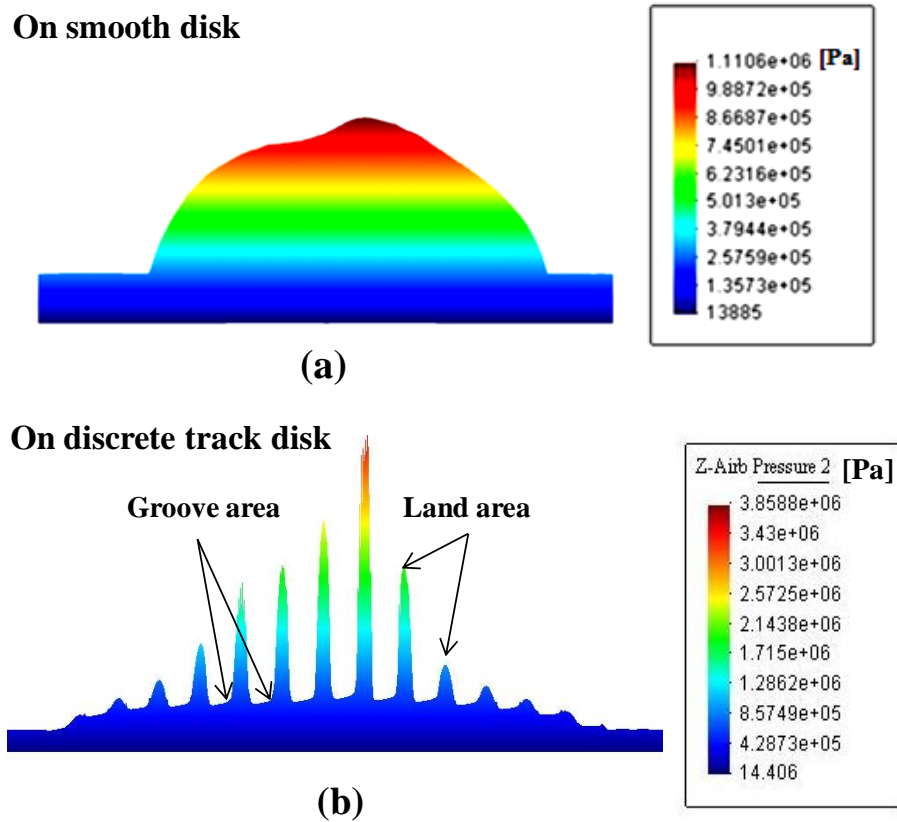


Figure 2.8 Typical pressure distributions on the center pads of sliders (a) over smooth media and (b) over DTR media

Figures 2.8 (a) and (b) represent typical air-bearing pressure distributions on the trailing pads of sliders over smooth media and DTR media, respectively. As can be seen in Figure 2.8 (b), the air-bearing pressure is reduced in discrete track disks due to the groove areas, which cause the so-called “flying height loss”.

Figure 2.9 shows the “flying height loss” based on equation (2.1) as a function of the groove depth and the ratio of groove width to track pitch of discrete track recording (DTR) media. Large “flying height loss” occurs as the ratio of groove width to track pitch is increased.

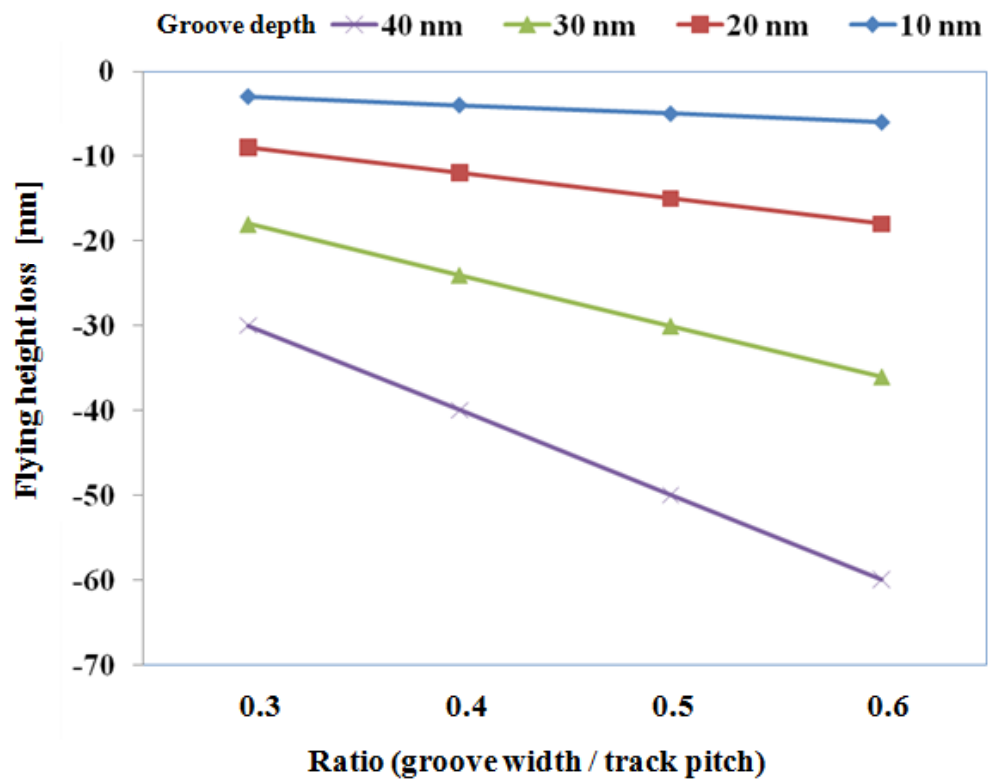


Figure 2.9 Flying height loss as a function of groove depth and the ratio of groove width to track pitch

2.3 Contact behavior on patterned media

The contact characteristics of a slider on patterned media are crucial in achieving high areal density in hard disk drives. However, research in this area is limited and many phenomena are not well understood.

Nunez and Polycarpou [14] investigated the contact behavior of patterned media with and without planarization. Figure 2.10 shows the von Mises stress contour in discrete track media indicating that yielding of the profile occurs [13]. In particular, high stresses were observed at the corners at the bottom of the profile. Clearly, high stress may cause damage during contacts between slider and disk. In addition, Nunez and Polycarpou showed that planarization can reduce contact stress of patterned media (Figure 2.11). Similarly, Hui, Amemiya and Talke [15] also investigated the static contact behavior of discrete track media using finite element simulation. They included the effect of contact at the edges of the discrete patterns. They found that the deformation of the magnetic layer is larger at the edge of the pattern than at the center of the patterns. Figure 2.12 shows the contract stress at the edge of the pattern.

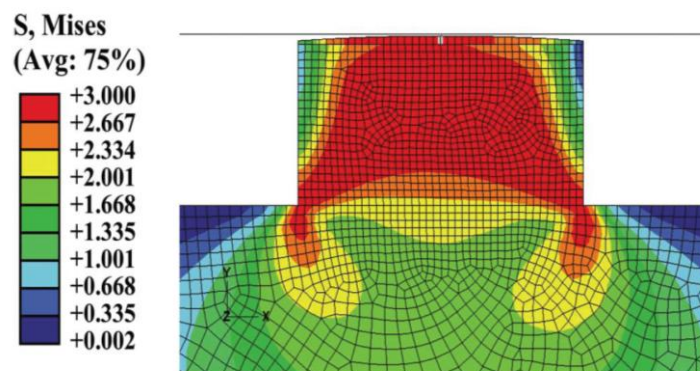


Figure 2.10 Von Mises stress contour showing yielding on a pattern (yield stress is 3 GPa) [Source: [14]]

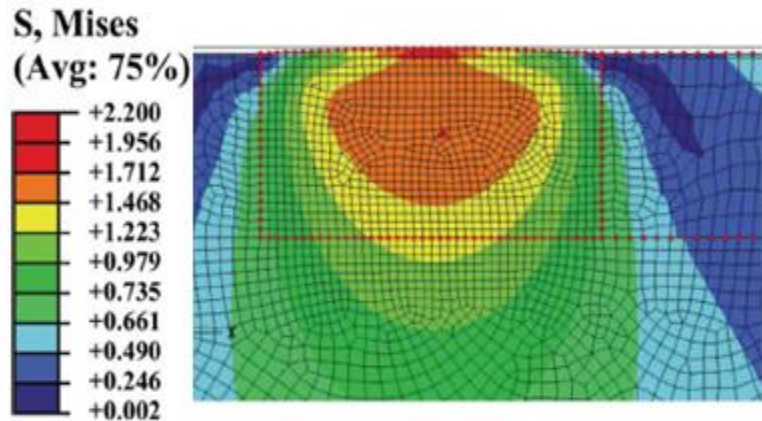


Figure 2. 11 Von Mises stress contour with filling material [Source: [14]]

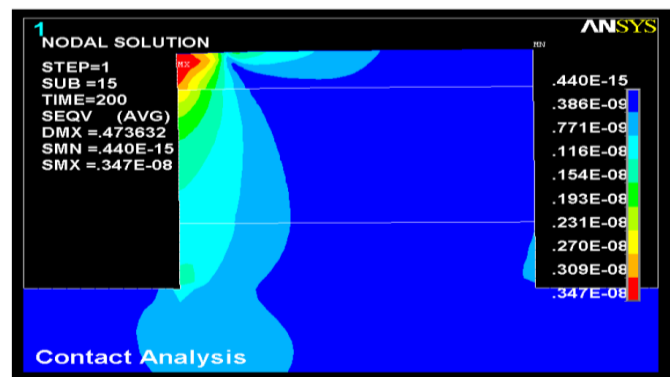


Figure 2.12 Von Mises stress contour at the edge of a pattern (unit is 10^9 GPa) [Source: [15]]

Many issues remain to be studied before patterned media can be applied in high density recording. More work needs to be done to investigate the relationship between magnetic domains and the flyability of magnetic recording sliders with respect to geometry of discrete track recording (DTR) media. Only very limited experimental investigations have been performed concerning the tribological characteristics of the slider/disk interface, i.e., wear, wettability, adhesion and friction force of discrete track media. Little information is known. In the following chapters, we will study in detail the tribological characteristics of

discrete track recording (DTR) media and the interface between sliders and discrete track recording disks.

Bibliography

- [1] R. Wood, "The feasibility of magnetic recording at 1 terabit per square inch," *IEEE Trans. Magn.*, vol. 36, pp. 36-42, 2000.
- [2] Y. Soeno, M. Moriya, K. Ito, K. Hattori, A. Kaizu, T. Aoyama, M. Matsuzaki, and H. Sakai, "Feasibility of discrete track perpendicular media for high track density recording," *IEEE Trans. Magn.*, vol. 41, pp. 670-675, 2005.
- [3] D. Wachenschwanz et al., "Design of a manufacturable discrete track recording medium," *IEEE Trans. Magn.*, vol. 41, pp. 670-675, 2005.
- [4] A. Kikitsu, Y. Kamata, M. Sakurai, and K. Naito, "Patterned magnetic recording media," *Intermag GE-09*, 2006.
- [5] X.-M. Yang, Y. Xu, C. Seiler, L. Wan, and S. Xiao, "Toward 1 Tbit/in² nanoimprint lithography for magnetic bit-patterned media: opportunities and challenges," *J. Vac. Sci. Technol. B*, vol. 26, pp. 2604-2610, 2008.
- [6] N. Yamashita, T. Oomatsu, S. Wakamatsu, K. Nishimaki, T. Usa and K. Usuki, "Duplicated quartz template for 2.5 inch discrete track media," *Proc. of SPIE*, vol. 7488, pp. 74880W1-74880W9.
- [7] M. Duwensee, S. Suzuki, J. Lin, D. Wachenschwanz, F. E. Talke, "Simulation of the head disk interface for discrete track media," *Microsyst. Technol.*, vol. 13, pp. 1023-1030, 2007.
- [8] M. Duwensee, S. Suzuki, J. Lin, D. Wachenschwanz, F. E. Talke, "Direct simulation Monte Carlo method for the simulation of rarefied gas flow in discrete track recording head/disk interface," *Journal of Tribology*, vol. 131, pp. 01220011-0120017, 2009.
- [9] M. Duwensee, D. E. Lee, Y. Yoon, S. Suzuki, J. Lin, F. E. Talke, "Tribological testing of sliders on discrete track media and verification with numerical predictions," *Microsyst. Technol.*, vol. 15, pp. 1599-1603, 2009.
- [10] J. Li, J. Xu, Y. Shimizu, "Performance of sliders flying over discrete-track media," *Transactions of the ASME*, vol. 129, pp. 712-719, 2007.
- [11] J. P. Peng, G. Wang, S. Thirivani, J. Chue, M. Nojaba, and P. Thayamballi, "Numerical and experimental evaluation of discrete track recording technology," *IEEE Trans. Magn.*, vol. 42, pp. 2462-2464, 2006.
- [12] K.-H. Kim, Y. Lee, S. Kim, N.-C. Par, Y.-P. Park, K.-S. Park, J. Yoo, C. S. Kim, "Numerical quasi-static analysis of ultralow flying slider during track-seeking motion over discrete track media," *IEEE Trans. Magn.*, vol. 45, pp. 4990-4993, 2009.

- [13] S.-J. Yoon, S.-H. Son, J. Kang, H. Kim, J. Yoo, D.-H. Choi, "Simulation of a head slider considering a discrete track recording technology," *Journal of Mechanical Science and Technology*, vol. 23, pp. 2679-2685, 2009.
- [14] E. E. Nunez, C.-D. Yeo, R. R. Katta and A. A. Polycarpou, "Effect of planarization on the contact behavior of patterned media," *IEEE Trans. Mag.*, vol. 44, pp. 3667-3670, 2008.
- [15] H. Li, K. Amemiya, F. E. Talke, "Finite element simulation of static contact of a slider with patterned media," *Journal of Advanced Mechanical Design, Systems, and Manufacturing*, vol. 4, pp. 42-48, 2010.

Chapter 3

Investigation of the Flyability of Discrete Track Recording Media

In this chapter, the flyability of magnetic sliders over discrete track recording media is investigated. Atomic force microscopy (AFM) and magnetic force microscopy (MFM) are used to characterize discrete track recording (DTR) media. As the groove depth of DTR media is increased, magnetic isolation of land and groove regions becomes better defined. Flyability of DTR media is investigated using laser Doppler vibrometry (LDV) and acoustic emission (AE) measurements. Flying height of sliders is found to be dependent on design parameters of DTR media. Numerical calculations of the steady state flying height show good qualitative agreement with experimental results.

3.1 Introduction

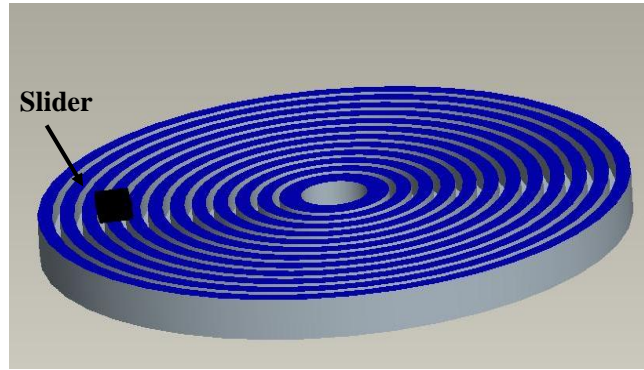
To further increase the storage density in computer hard disk drives, the size of single bits must be decreased. A decrease of the bit size requires a reduction of the average size of the magnetic grains. Decreasing the size of magnetic grains is limited by the size of the domains and leads to the so-called super-paramagnetic limit [1]. The super-paramagnetic limit describes a situation where the magnetic energy stored in a single bit becomes so small that thermal fluctuations can cause an instantaneous reversal of the magnetization direction of a recorded bit, leading to a loss of information. Bertram et al. [2] estimated that the super-paramagnetic limit for conventional magnetic recording media will be reached at a storage density of 500 Gbit/in². Discrete track recording (DTR) and bit pattern media (BPM) are believed to allow an increase in the areal storage density beyond 500 Gbit/in² [3]. In discrete track recording, magnetic transition noise between adjacent tracks is eliminated in the radial direction by physically separating adjacent tracks [4-6]. Wachenschwanz et al. [4] theoretically estimated the minimum groove depth of discrete tracks to avoid unwanted recording in the groove area. In bit pattern media recording, magnetic transition noise is eliminated in both the radial and circumferential directions by isolating each bit from its adjacent bits [7].

This study is concerned with the tribology and “flyability” of magnetic recording slider on discrete track recording media. In particular, atomic force microscopy (AFM) and magnetic force microscopy (MFM) are used to characterize discrete track recording media. The “flyability” of two types of recording sliders is

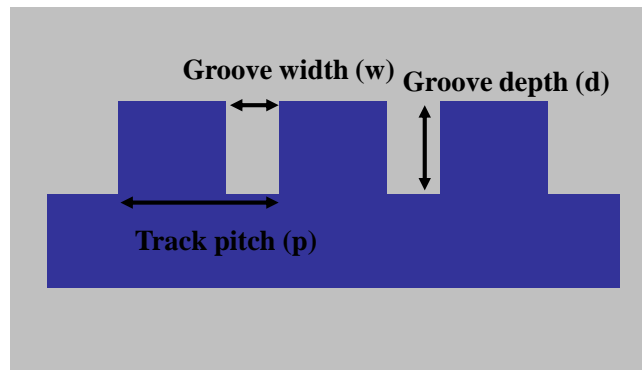
evaluated using laser Doppler vibrometry (LDV) and acoustic emission (AE) measurements. Numerical simulations were performed using sliders identical to those used in the experimental investigation.

3.2 Discrete Track Recording Media

Figure 3.1 (a) shows a schematic of a typical discrete track recording disk. The design parameters defining discrete track recording media are the groove width, the groove depth and the track pitch (Figure 3.1 (b)). The flying behaviour of a slider over discrete track media is affected by the presence of the grooves on the disk. In particular, the steady state flying height of a slider flying over discrete track media is lower than that of a slider over smooth media due to the loss of air-bearing pressure over the grooves. Duwensee et al. [8-10] have shown numerically that the “flying height loss” Δh of a slider over discrete track media can be determined by $\Delta h = d \cdot \frac{w}{p}$, where d is the groove depth, w is the groove width, and p is the track pitch. In their study, numerical predictions and experimental results were performed separately without coincidence of slider designs used for numerical and experimental investigation [10].



(a) DTR disk



(b) Cross section of DTR disk

Figure 3.1 Schematic of discrete track recording disk; (a) DTR disk and (b) cross section of DTR disk

3.3 Atomic force microscopy (AFM) and magnetic force microscopy (MFM) analysis of Discrete Track Recording media

Figure 3.2 shows the layer structure of a typical discrete track recording (DTR) disk. Physically separated tracks are formed by nano-imprint lithography (NIL), with subsequent deposition of the magnetic layer, the diamond like carbon (DLC) coating, and the lubricant film. As can be seen from Figure 3.2, deposition of the magnetic film after nano-imprint lithography implies that the magnetic film is

present on the top of the land and the bottom of the groove area. Deposition of some magnetic material occurs also on the side walls of the grooves.

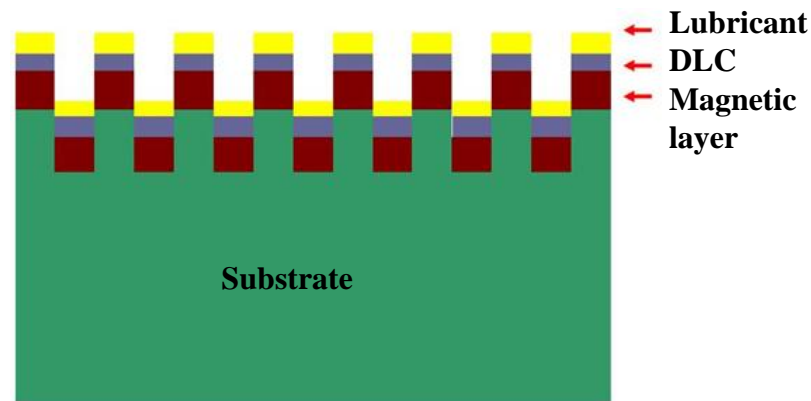


Figure 3.2 Layer structure of a discrete track recording medium

Figures 3.3 (a) and (b) show atomic force microscopy (AFM) and magnetic force microscopy (MFM) measurements of discrete track recording media with a groove depth of 20 nm and a groove width of 90 nm. As can be seen from Figure 3.3 (a), the individual tracks of the discrete track recording (DTR) media are separated completely from each other. However, as is shown in Figure 3.3 (b), the magnetic domains of the discrete track recording (DTR) media do not always end at the boundaries of the discrete tracks but extend in many cases from the land area into the groove area. These magnetic domains are highlighted by circular or oval curves in Figure 3.3 (b).

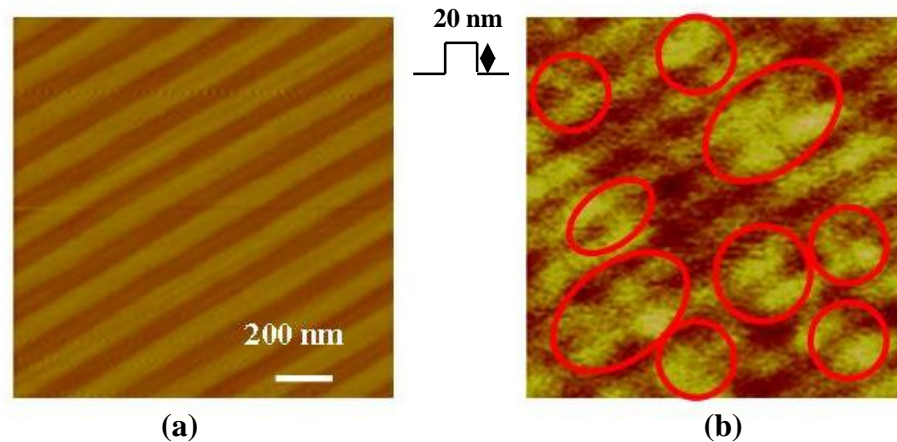


Figure 3.3 (a) AFM and (b) MFM measurements on a discrete track recording medium with 20 nm groove depth and 90 groove width

Figures 3.4 (a) and (b) show atomic force and magnetic force microscopy images of a discrete track disk with a groove depth of 30 nm and a groove width of 70 nm, respectively. In Figure 3.4 (a) well separated tracks are observed. However, magnetically connected regions are still found in some parts of the discrete track recording (DTR) media as indicated in the areas highlighted in Figure 3.4 (b). Figure 3.5(a) shows an AFM image for a disk with a groove depth of 40 nm and a groove width of 80 nm. We observe a surface defect (marked by a dashed circle) where two adjacent tracks are physically connected. This type of defect appears to be caused by incomplete imprinting. Comparing Figures 3.5 (a) and (b), we note that the continuous magnetic domain (marked by the dashed circle) corresponds to the location of the mechanical defect in Figure 3.5 (a), i.e., the continuous magnetic domain is caused by a surface defect. Figure 3.5 (b) shows that additional connected magnetic domains (marked by circles), even at a groove depth of 40 nm. The magnetically connected areas decrease with an increase in groove depth.

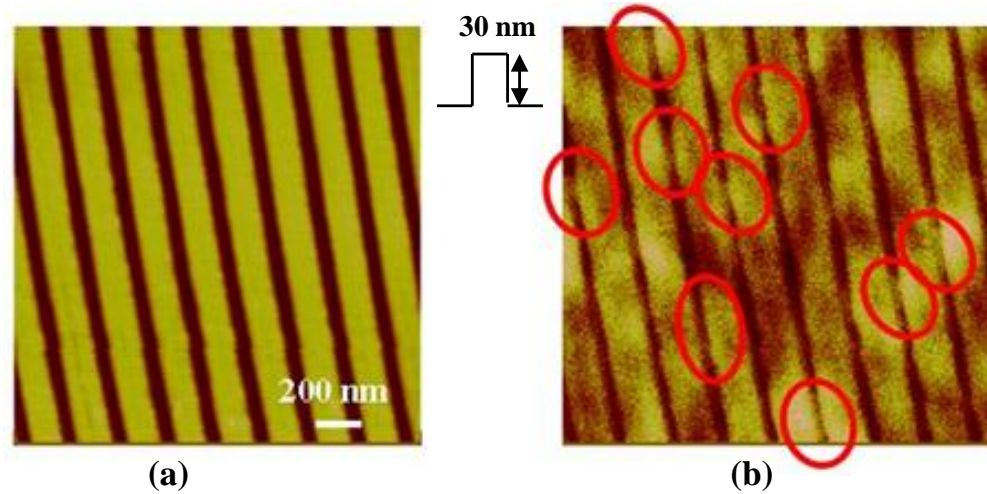


Figure 3.4 (a) AFM and (b) MFM measurements on a discrete track recording medium with 30 nm groove depth and 70 nm groove width

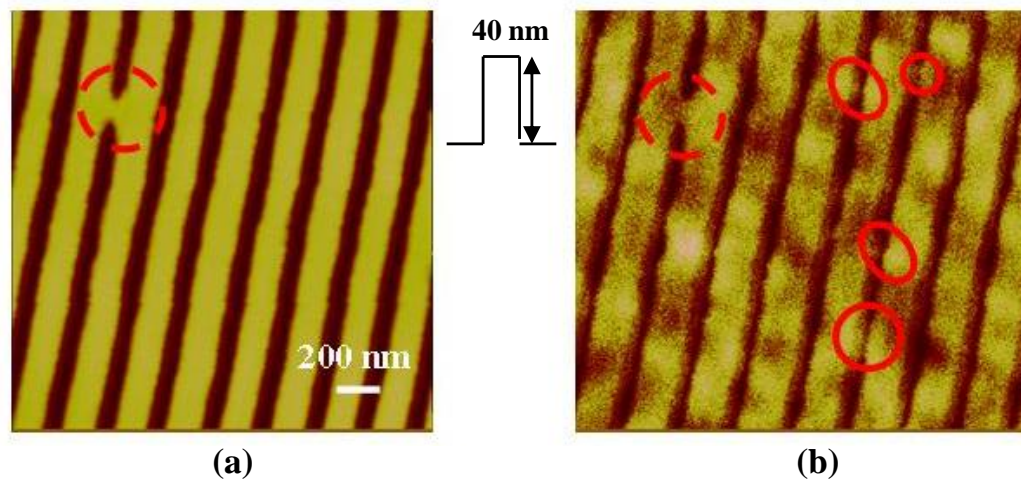


Figure 3.5 (a) AFM and (b) MFM measurements on a discrete track recording medium with 40 nm groove depth and 80 nm groove width

3.4 Flyability of Magnetic Recording Sliders

3.4.1 Experimental Setup and Parameters

Figure 3.6 shows a schematic of the experimental setup used in the flyability investigations described in this chapter. The setup consists of a spinstand, a spinstand controller, a data acquisition system, a laser Doppler vibrometer (LDV) and an acoustic emission (AE) sensor. The LDV and AE sensor were connected to a high-speed data acquisition system to detect dynamic flying height changes and slider-disk contacts. The laser was focused on the back side of the slider. DTR disks were mounted on the spinstand and flyability of specially designed proximity recording sliders was investigated. Throughout the experiments, the skew angle, which is a measurement of the angle of alignment between head and track, was kept at zero degrees.

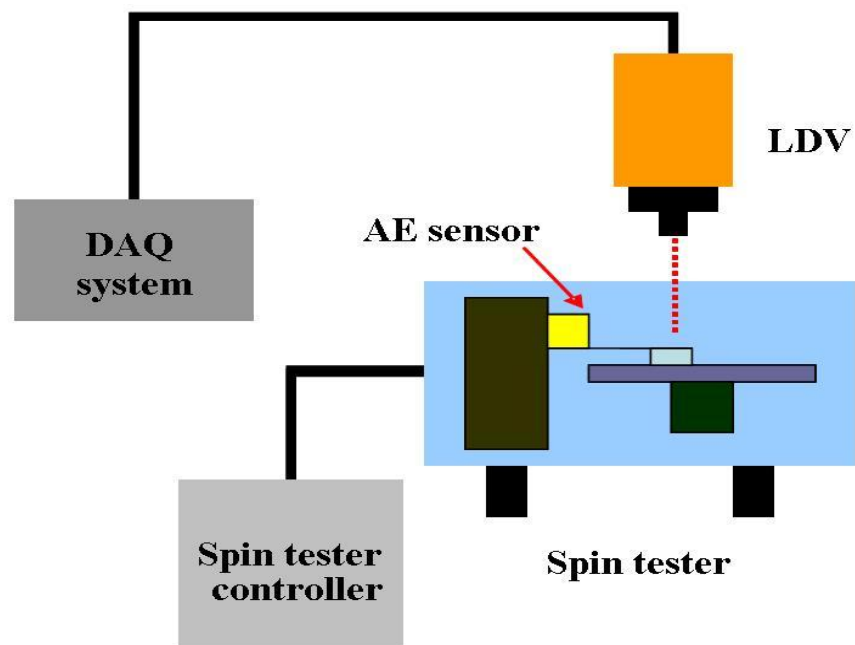


Figure 3.6 Schematic of the experimental setup

Table 3.1 gives details of the track dimensions of the three different types of DTR media used in this study.

Table 3.1 Configurations of DTR media

	Disk A	Disk B	Disk C
Groove depth (d) [nm]	20	30	40
Groove width (w)[nm]	70	90	110
Track pitch (p)[nm]	210	200	200
w / p	0.3	0.45	0.55

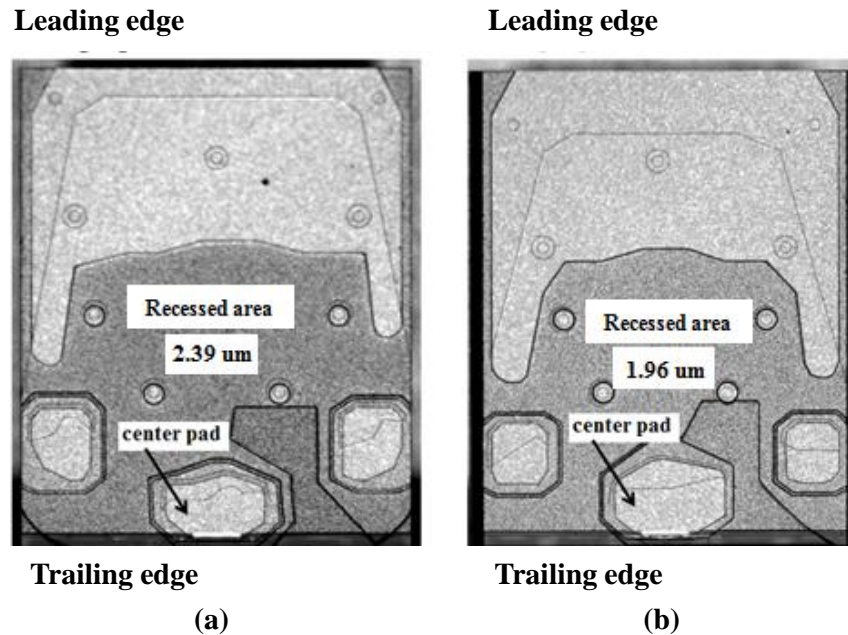


Figure 3.7 SEM images of air-bearing surfaces; (a) Slider "A" and (b) Slider "B"

To investigate the dynamic flying characteristics of magnetic recording sliders over DTR media, two pico-sliders were used as shown in Figure 3.7. At a speed of 22 m/s, the design flying height of slider "A" on a smooth disk is 11 nm, while it is 20 nm for slider "B". As can be seen in Figure 3.7, slider "B" has a larger center pad on the trailing edge. In addition, the recess area of slider "B" is

shallower than that of slider “A”.

3.4.2 Experimental Results

Figures 3.8 and 3.9 shows frequency spectra of LDV and AE measurements for sliders “A” flying over DTR disks A, B and C, while Figures 3.10 and 3.11 show frequency spectra for LDV and AE measurements for slider “B” flying over DTR disks A, B and C. Again, slider “A” is designed to fly on a smooth disk at 11 nm while slider “B” is designed to fly on a smooth disk at 20 nm at 22 m/s velocity. As can be seen in Figure 3.8, stable flying is observed for slider “A” on disk A (groove depth $d = 20$ nm; ratio of groove width to track pitch $w/p = 0.3$). However, large dynamic fluctuations, corresponding to severe contacts are observed on disk B (groove depth $d = 30$ nm; ratio of groove width to track pitch $w/p = 0.45$) and disk C (groove depth $d = 40$ nm; ratio of groove width to track pitch $w/p = 0.55$). The results in Figure 3.8 were obtained using an LDV. A similar trend is found to exist in Figure 3.9 for the AE measurements. In Figures 3.10 and 3.11 results are shown for LDV and AE measurements on the same discrete track recording (DTR) disks using slider “B” which was designed to fly at 20 nm on smooth media. From Figures 3.10 and 3.11 we observe stable flying for disks A and B, while large dynamic fluctuations, corresponding to severe contacts, are observed for disk C. Since slider “B” was designed to fly at a higher flying height than slider “A” on smooth media, it is apparent that the flying height loss of slider “B” on discrete track recording (DTR) disk B is not large enough to cause continuous contact as is observed for slider “A” on disk B.

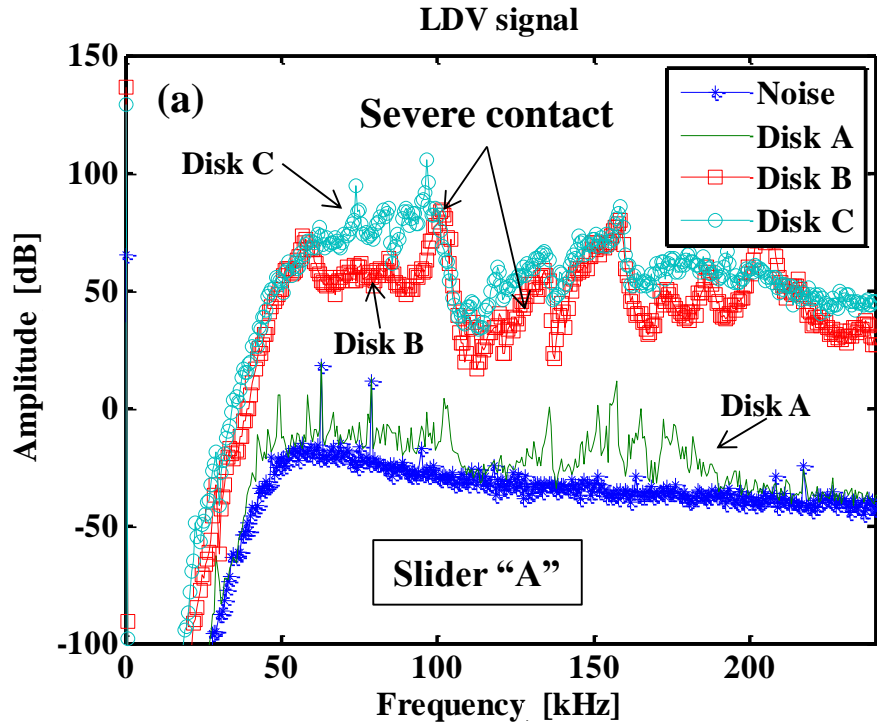


Figure 3.8 Frequency spectra of LDV signal for slider "A"

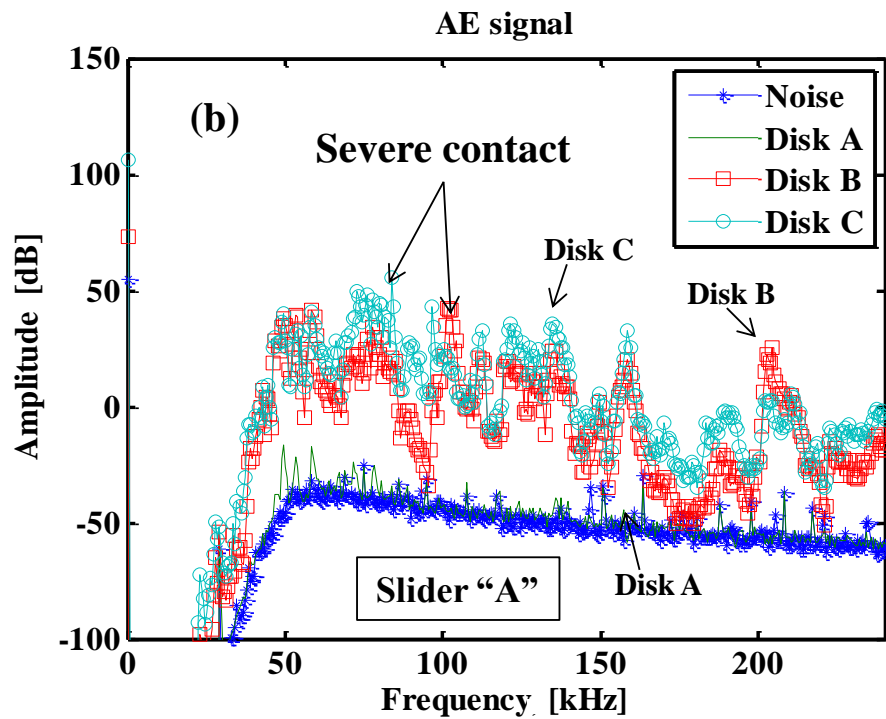


Figure 3.9 Frequency spectra of AE signal for slider "A"

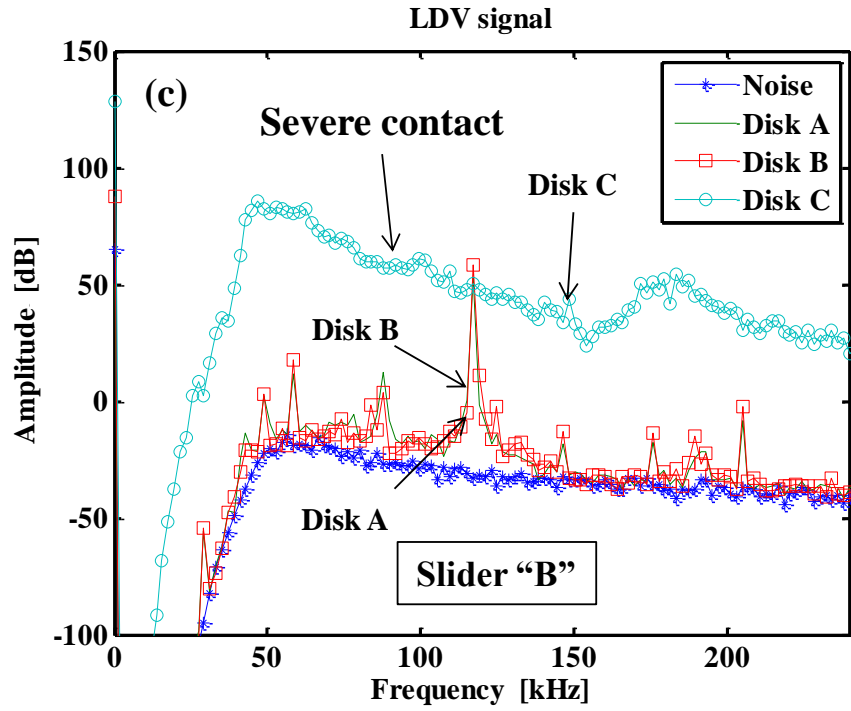


Figure 3.10 Frequency spectra of LDV signal for slider "B"

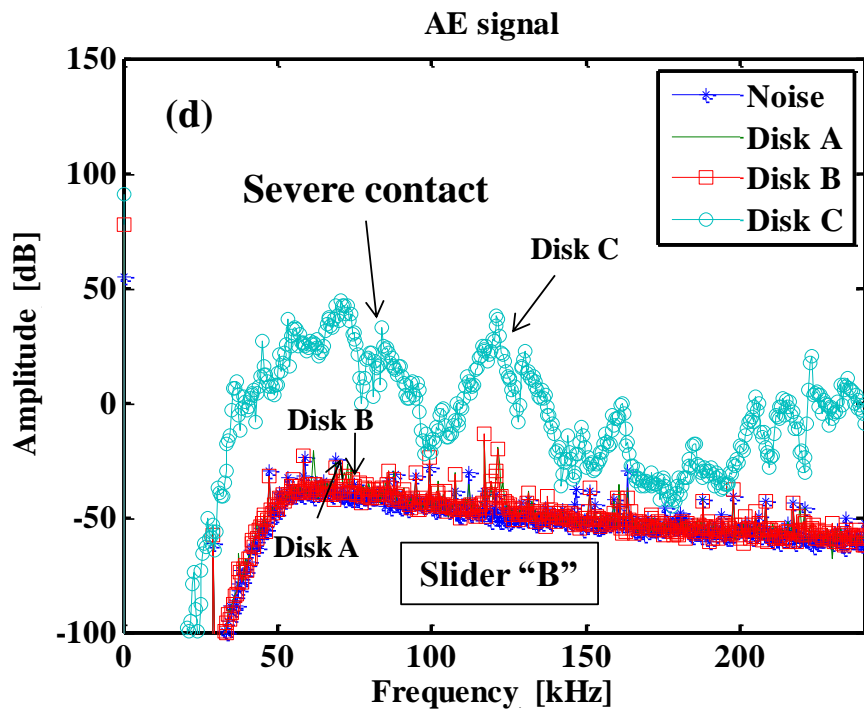


Figure 3.11 Frequency spectra of AE signal for slider "B"

Figure 3.12 shows the standard deviation of flying heights for sliders “A” and “B” on DTR disks A, B and C. For slider “A”, designed to fly at 11 nm over smooth media, a small standard deviation of flying height is observed only on DTR disk A (groove depth $d = 20$ nm; ratio of groove width to track pitch $w/p = 0.3$), indicating that slider “A” flies stably on this media. However, for DTR disks B (groove depth $d = 30$ nm; ratio of groove width to track pitch $w/p = 0.45$) and C (groove depth $d = 40$ nm; ratio of groove width to track pitch $w/p = 0.55$), large flying height fluctuations are observed, showing that slider “A” does not fly stably on DTR disks B and C. For slider “B”, designed to fly at 20 nm over smooth media, stable flying behavior is observed on disks A and B, respectively. For DTR disk C, however, a large standard deviation of flying height is observed, indicating that slider “B” is not flying stably on disk C.

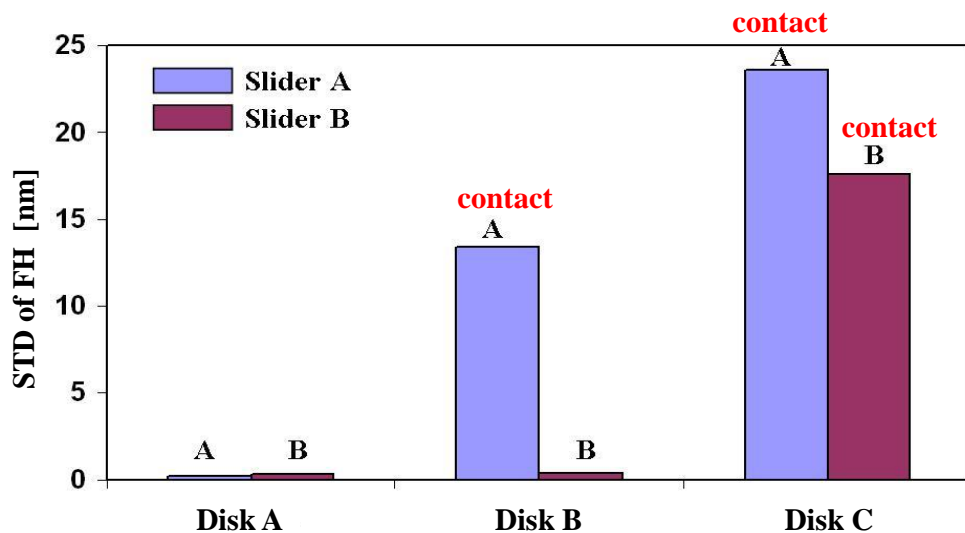


Figure 3.12 Standard deviation of flying height on DTR media

Figure 3.13 shows surface reflectance analysis (SRA) images after flyability testing on DTR disks A, B and C with slider “B”, the latter designed to fly at 20 nm on smooth disks. For DTR disks A and B, wear tracks were absent. However, a well-defined wear track was observed on discrete track recording (DTR) disk C (groove depth $d = 40$ nm; ratio of groove width to track pitch $w/p = 0.55$), indicating severe contacts occurred for slider “B” on discrete track recording (DTR) disk C.

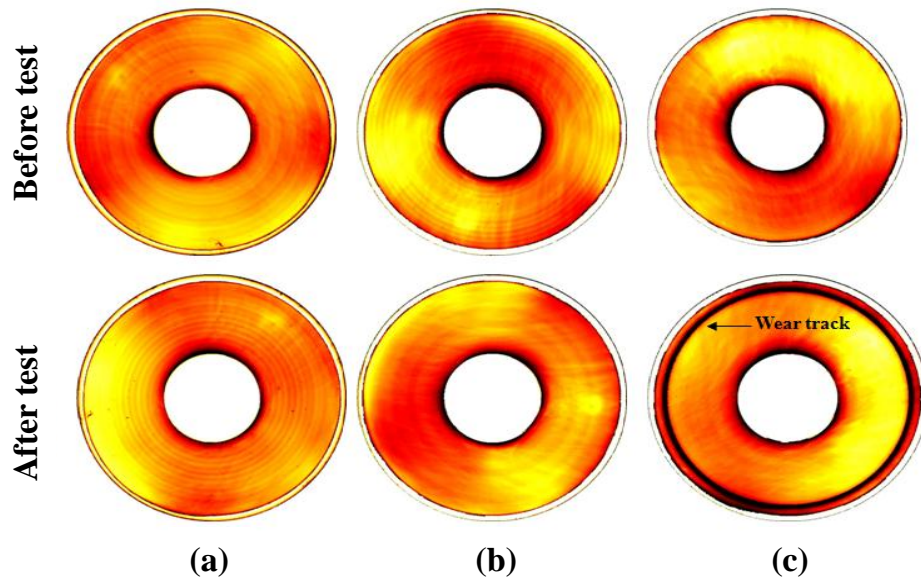


Figure 3.13 Surface reflectance analysis (SRA) images after flyability testing on DTR media with slider “B”; (a) DTR disk A, (b) DTR disk B and (c) DTR disk C

3.5 Numerical Analysis of Flyability of Magnetic Recording Sliders

3.5.1 Numerical Models

To correlate the experimental results with numerical predictions, we have simulated the flying characteristics of sliders “A” and “B” over DTR media using the “CMRR” finite element air-bearing simulator [11]. A summary of the features of this simulator is given in appendix B.

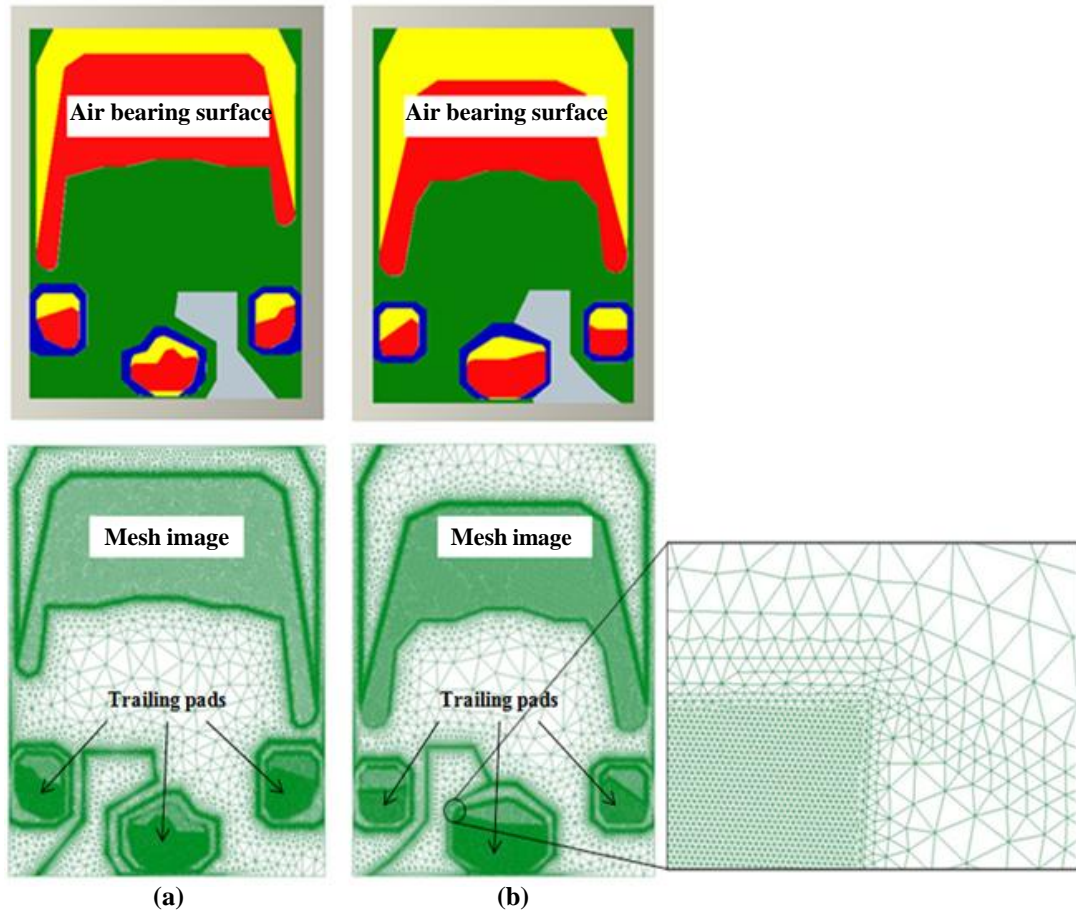


Figure 3.14 Air-bearing surfaces and mesh images; (a) slider “A” and (b) slider “B”

Figures 3.14 (a) and (b) show the air-bearing surface and the finite element mesh of sliders “A” and “B”. The air-bearing surfaces were designed using a 3-D solid design tool (Pro-Engineer) and meshed with the graphical pre-/post-processor (GID). For sliders “A” and “B”, $0.9 \cdot 10^6$ and $1.0 \cdot 10^6$ nodes and $1.8 \cdot 10^6$ and $2.1 \cdot 10^6$ elements were used, respectively. In particular, the trailing pads, where most of the air-bearing force is generated, were meshed with very fine elements to obtain accurate numerical results (see Figure. 3.15). For numerical predictions, the input parameters, i.e., groove depth and the ratio of groove width to track pitch, of DTR media (shown in Table 3.1) were used.

Figures 3.15 (a) and (b) show typical air-bearing pressure distributions on smooth and DTR disks, respectively. As can be seen in Figure 3.15 (b), the air-bearing pressures is reduced over the groove areas resulting in the previously discussed “flying height loss” of sliders over discrete track recording (DTR) media.

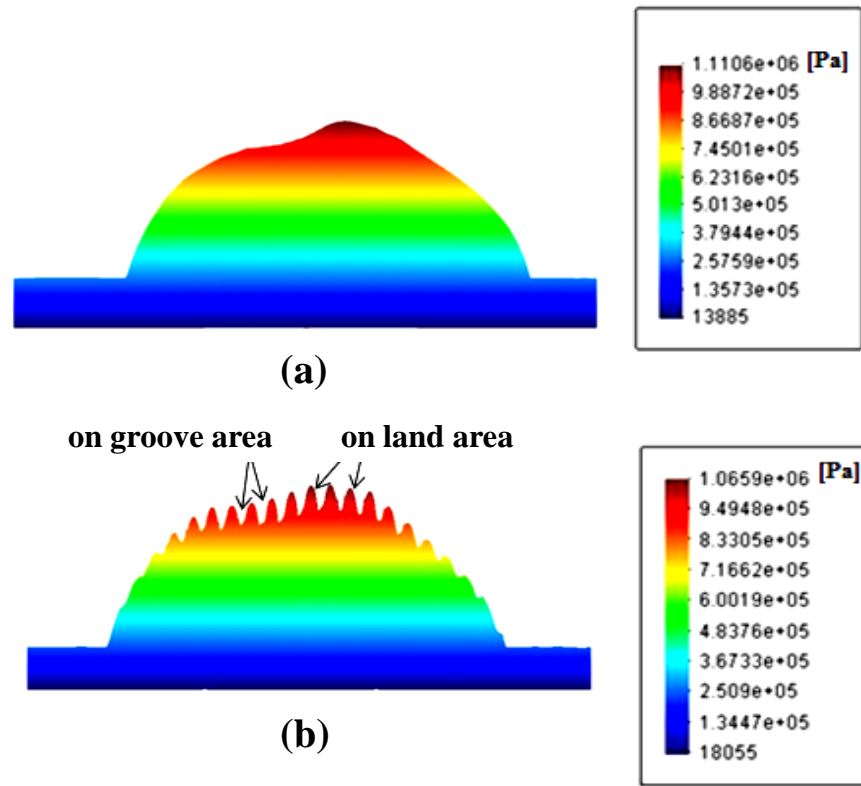


Figure 3.15 Typical air-bearing pressure distributions (a) on smooth media and (b) on DTR media

3.5.2 Numerical Results

Numerical calculations were performed for a speed of 22 m/s and zero skew angle in agreement with the experimental conditions of Figures 3.8-3.11. Figure 3.16 shows the numerical predictions for the steady state flying height of sliders “A”

and “B” on smooth disks and on the three discrete track recording (DTR) media used. We observe that slider “A” is predicted to fly at a flying height of 5.1 nm on discrete track recording (DTR) disk A. However, the flying height of slider “A” is predicted to be only 0.69 nm and 0.13 nm for discrete track recording (DTR) disks B and C, respectively, i.e., slider “A” cannot be expected to fly stably on discrete track recording (DTR) disks B and C. For slider “B”, the numerical predictions show that this slider flies on discrete track recording (DTR) disks A and B, while it does not fly on discrete track recording (DTR) disk C. The above predictions are in excellent qualitative agreement with the experimental measurements as shown in previous Figures 3.8-3.11.

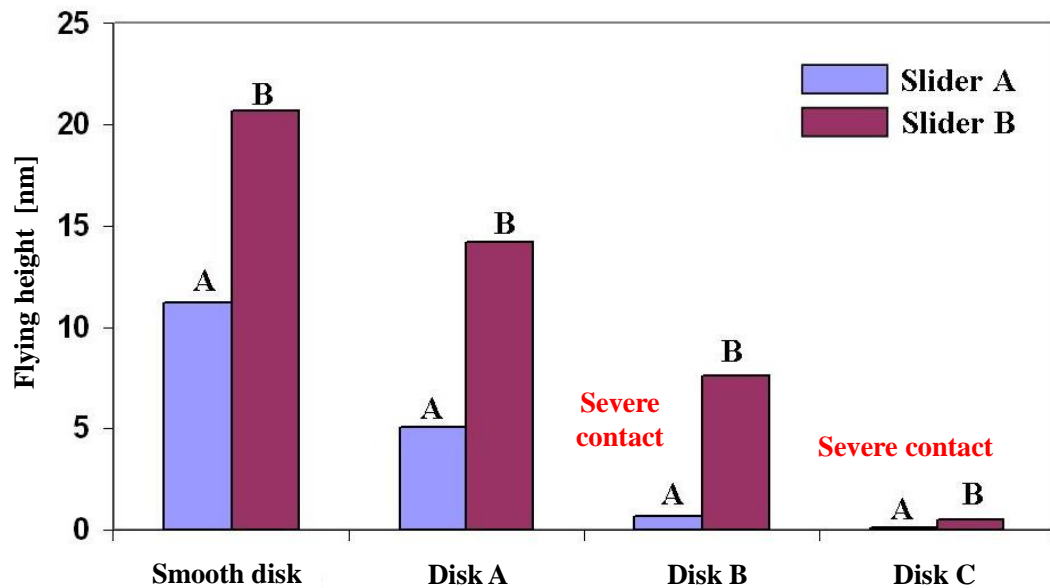


Figure 3.16 Numerical predictions of flying height on smooth disk and DTR media

3.6 Summary and Conclusions

Atomic force microscopy (AFM) and magnetic force microscopy (MFM) measurements have shown that the groove depth is an important factor with respect to magnetic isolation of land and groove regions. As the groove depth is increased, the magnetic isolation of adjacent is improved. From our numerical and experimental investigations of flyability of magnetic recording sliders on DTR media, we have observed that the groove depth is a dominant factor with respect to flying height loss of magnetic recording sliders as well. To prevent flying height changes as a function of groove depth variation, it is apparent that planarization of DTR media should be performed.

Bibliography

- [1] D. Weller, and M. Andreas, "Thermal effect limits in ultrahigh density magnetic recording", *IEEE Trans. Mag.*, vol. 35, pp. 4423-4439, 1999.
- [2] H. N. Bertram, and M. Williams, "SNR and density limit estimates: A comparison of longitudinal and perpendicular recording", *IEEE Trans. Mag.*, 36, pp.4-9, 2000.
- [3] Y. C. Stephen, "Patterned magnetic nanostructures and quantized magnetic disks", *Proceedings of the IEEE*, vol. 85, pp. 652-671, 1997.
- [4] D. Wachenschwanz et al., "Design of a manufacturable discrete track recording medium", *IEEE Trans. Magn.*, vol. 41, pp.670-675, 2005.
- [5] Y. Soeno, et. all, "Feasibility of discrete track perpendicular media for high track density recording", *IEEE Trans. Mag.*, vol. 39, pp.1976-1971, 2003.
- [6] S. J. Greaves, H. Muraoka, Y. Kanai, "Discrete track media for 600 Gbits/in2 recording", *JAP*, vol. 99, pp. 08F903, 2006.
- [7] M. Albrecht, C. T. Rettner, A. Moser, M. E. Best and B. D. Terris, "Recording performance of high-density patterned perpendicular magnetic media," *Applied Physics Letters*, vol. 81, pp. 2875-2877, 2002.
- [8] M. Duwensee, S. Suzuki, J. Lin, D. Wachenschwanz, and F. E. Talke, "Air Bearing Simulation of Discrete Track Recording Media", *IEEE Trans. Mag.*, vol. 42, pp. 2489-2491, 2006.
- [9] M. Duwensee, S. Suzuki, J. Lin, and D. Wachenschwanz, and F. E. Talke, "Simulation of the Head Disk Interface for Discrete Track Media", *Microsys. Tech.*, vol. 13, pp. 1023-1030, 2006.
- [10] M. Duwensee, D. E. Lee, Y. Yoon, S. Suzuki, J. Lin, F. E. Talke, "Tribological testing of sliders on discrete track media and verification with numerical predictions," *Microsyst. Technol.*, vol. 15, pp. 1599-1603, 2009.
- [11] M. H. Wahl, P. R. Lee and F. E. Talke, "An efficient finite element-based air bearing simulator for pivoted slider bearings using bi-conjugate gradient algorithms," *Trib. Trans.*, vol. 39, pp. 130-138, 1996.

Chapter 4

Touch-down and Take-off Hysteresis of Magnetic Recording Sliders on Discrete Track Media

In this chapter, the “touch-down” and “take-off” characteristics of typical pico-type magnetic recording sliders is investigated as a function of pressure level and groove dimensions of discrete track recording (DTR) media. Keeping the ambient pressure constant, we found that the touch-down velocity was higher for discrete track recording disks than for “smooth” disks without discrete tracks. Likewise, the “ambient” touch-down pressure at constant velocity was found to be higher for discrete track recording disks than for smooth media. The hysteresis between touch-down and take-off velocity and touch-down and take-off ambient pressure was found to be larger for discrete track recording media than for smooth media. Start/stop tests on discrete track media were performed to investigate the effect of grooves of discrete track media on the tribology of the head/disk interface.

4.1 Introduction

To achieve an areal density of 1Tbit/in², the separation between the head and the disk must be reduced to approximately 1 or 2 nm [1]. One of the difficulties associated with low magnetic spacing, and, consequently, low flying height, is the increase in the number and severity of slider/disk contacts. Contacts between slider and disk are affected by intermolecular forces and adhesion forces. Contacts are also affected by the speed of the disk and are different during touch-down and take-off.

Thornton [2], Gupta [3] and Ono [4] have studied the effect of intermolecular forces during touch-down and take-off of magnetic recording sliders. Suh [5] introduced an adhesive contact model for sub-5nm ultralow flying sliders. Ono [6] and Tagawa [7] studied the hysteresis of sliders in terms of adhesive meniscus forces of lubricants in the head/disk interface. Tani [8] introduced the influence of stick-slip vibration due to lubricant slider interaction. Many researchers have studied and proposed new designs of sliders indicating so-called “spherical sliders”, which exhibit a small contact area at the head/disk interface to reduce the effect of adhesive forces [9-11]. Tani [12] and Zhou [13] suggested surface texturing to improve the performance of sliders. A number of researchers has investigated the hysteresis of sliders on conventional “smooth” media, but no studies have been performed yet for discrete track recording (DTR) media.

In this chapter, the touch-down and take-off characteristics of pico-type magnetic recording sliders are investigated as a function of groove dimensions of discrete track recording (DTR) media. In addition, the touch-down and take-off

characteristics of pico-sliders are studied as a function of ambient pressure level and velocity for both smooth and discrete track media. Furthermore, contact start-stop (CSS) testing is performed to study the effect of grooves on the tribology of the head/disk interface.

4.2 Experimental setup and parameters

Figure 4.1 shows the schematic of a typical slider flying on “smooth” and “discrete” track recording media. Figure 4.2 shows the schematic of the experimental setup consisting of a spin stand, a spin stand controller, a pressure regulator, a scanning laser Doppler vibrometer (S-LDV), and an acoustic emission (AE) sensor. The spin stand was placed in a sealed chamber to control the ambient pressure level. A scanning laser Doppler vibrometer and acoustic emission sensors were connected to a data acquisition system to record the flying characteristics of the slider over the disk.

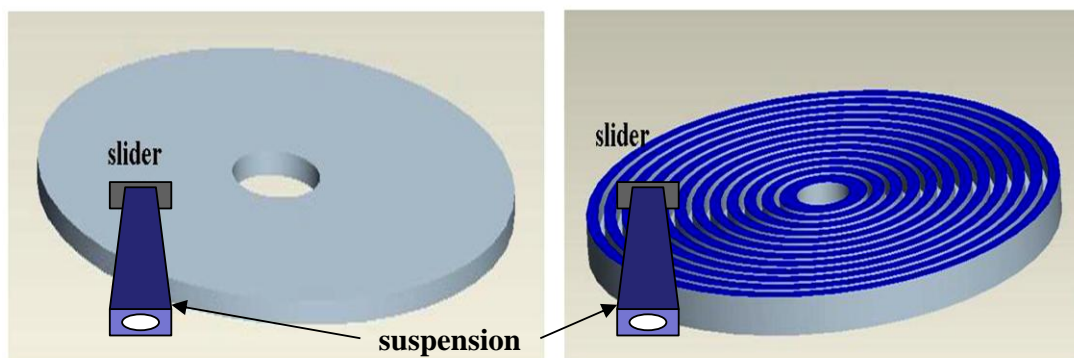


Figure 4.1 Schematic of smooth disk (a) and DTR disk (b)

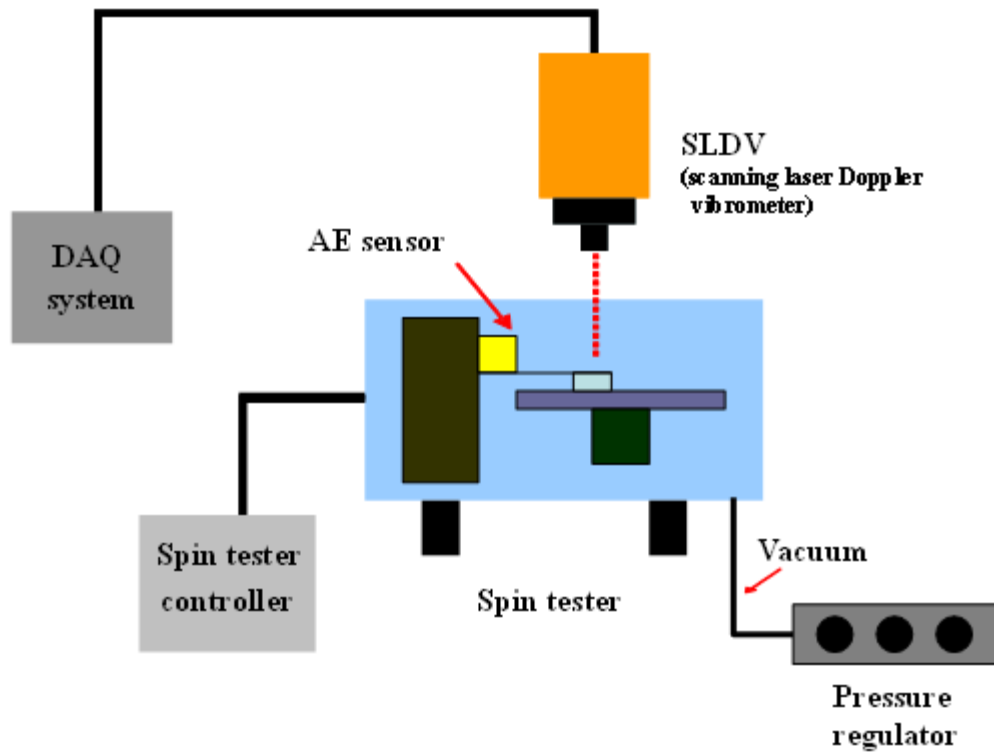


Figure 4.2 Schematic of experimental setup

Table 4.1 shows the types of DTR media used in our experimental work. To compare the touch-down and take-off characteristics of discrete track media disks, we have used one smooth disk and three different DTR disks.

Table 4.1 Configurations of DTR media

	Disk A	Disk B	Disk C
Groove depth (d)[nm]	20	30	40
Groove width (w)[nm]	70	90	110
Track pitch (p) [nm]	210	200	200
w / p	0.3	0.45	0.55
Design flying height [nm]	14	7.4	0

The air bearing design of the slider used throughout our investigation is shown in Figure 4.3. The slider was designed to fly at a flying height of 20 nm on a smooth disk at a velocity of 22 m/s. The flying height of the pico-slider used in our experiments is also shown in table 4.1 for the three discrete track recording disks A, B, and C (based on equation (2.1) in chapter 2). We observe that the flying height of the pico-slider at the design velocity of 22 m/s is 14 nm for disk A and 7.4 nm for disk B. The flying height at 22 m/s is zero for disk C. Based on the flying height predictions for disks A, B, and C, it is apparent that different touch-down velocities should be observed as a function of pressure level and type of disk used.

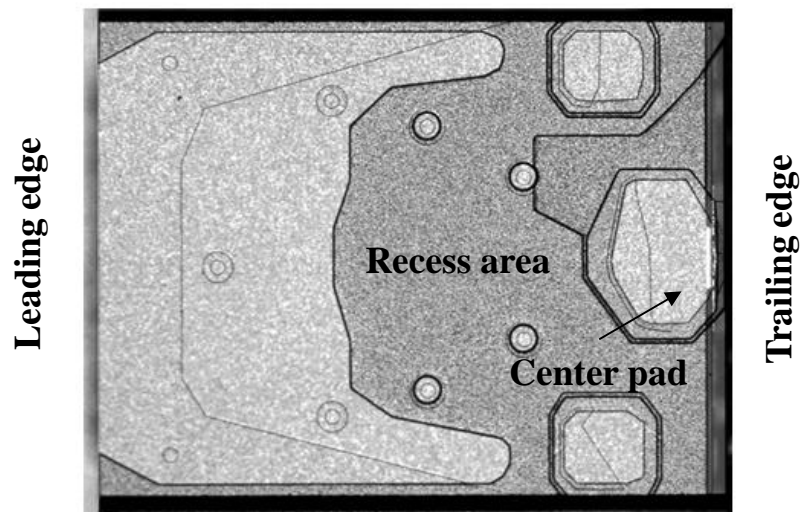


Figure 4.3 Air bearing design of pico-slider used in experiments

4.3 Experimental results

4.3.1 Touch-down velocity for smooth and DTR media

A scanning laser Doppler vibrometer (S-LDV) and an acoustic emission (AE) sensor were used to detect slider/disk contacts for both smooth and DTR media. For this measurement, the slider was first positioned at a radius of 39 mm. Then, the velocity (RPM) was decreased slowly from 29.4 m/s (7200 RPM) in steps of 0.2 m/s (50 RPM) until contact (touchdown) was observed. Figure 4.4 shows the frequency spectrum of the slider on a smooth disk for velocities ranging from 3.1 m/s to 28.6 m/s. We observe that for velocities above 3.3 m/s (800 RPM), contacts are absent, i.e., the slider is flying. However, touch-down occurred at 3.1 m/s (750 RPM). Both the scanning laser Doppler vibrometer (S-LDV) and the acoustic emission (AE) signal show large variations in amplitude with frequency, as can be seen from Figures 4.4 (a) and (b), respectively. The condition where large signal variations occur corresponds to contact.

Figure 4.5 shows the frequency spectrum of a slider on disk A. At velocities above 3.7 m/s (900 RPM), touch-down is not present. However, if the velocity is decreased below 3.7 m/s, touch-down occurs at 3.5 m/s (850 RPM), as can be seen from Figure 4.5. In the case of disk B (Figure 4.6), a few contacts are found already at 8.2 m/s (2000 RPM), but touch-down of the slider occurred at 7.1 m/s (1750 RPM).

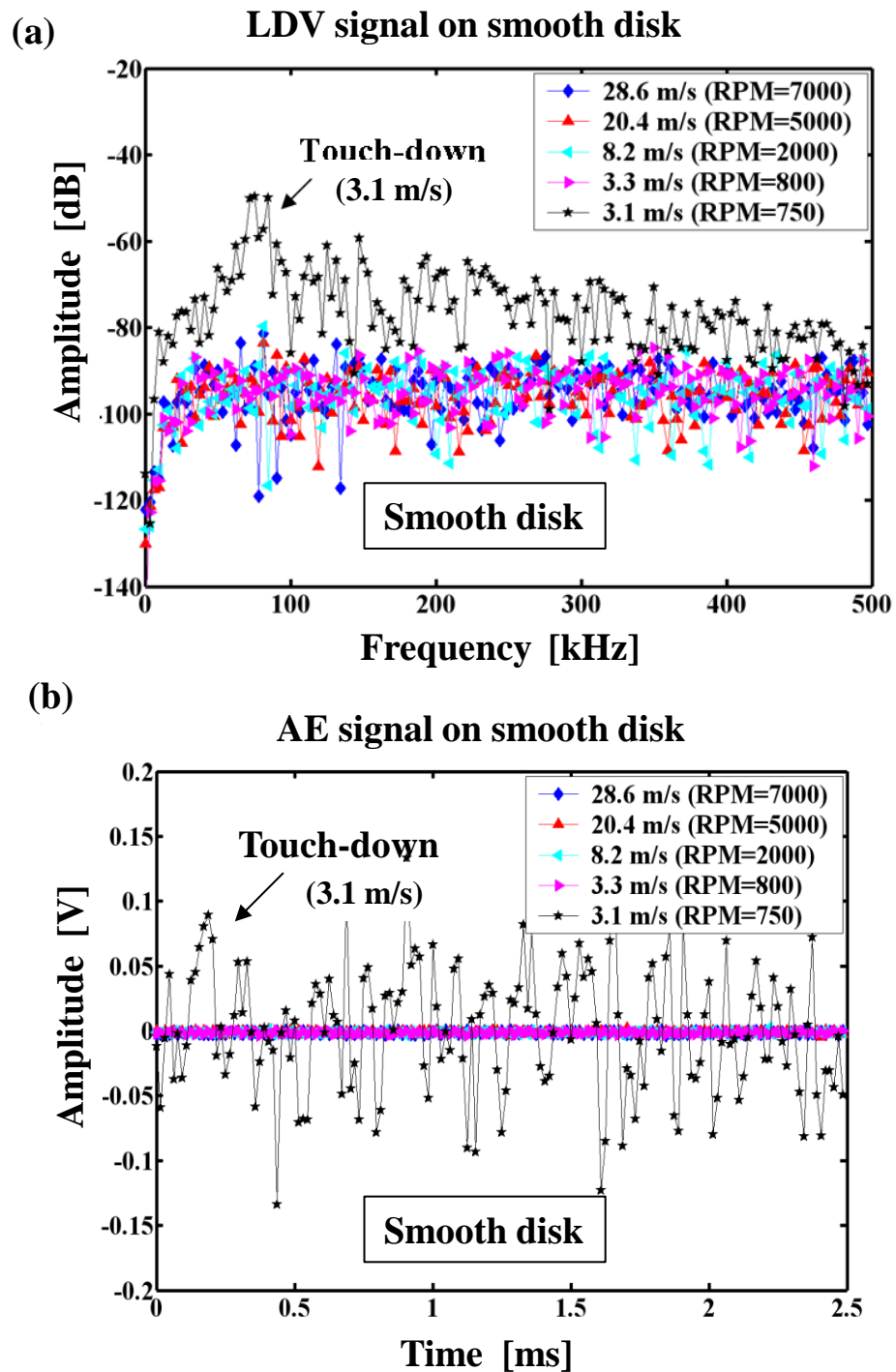


Figure 4.4 Frequency spectra of disk velocity for smooth disk; (a) S-LDV signal, (b) AE signal

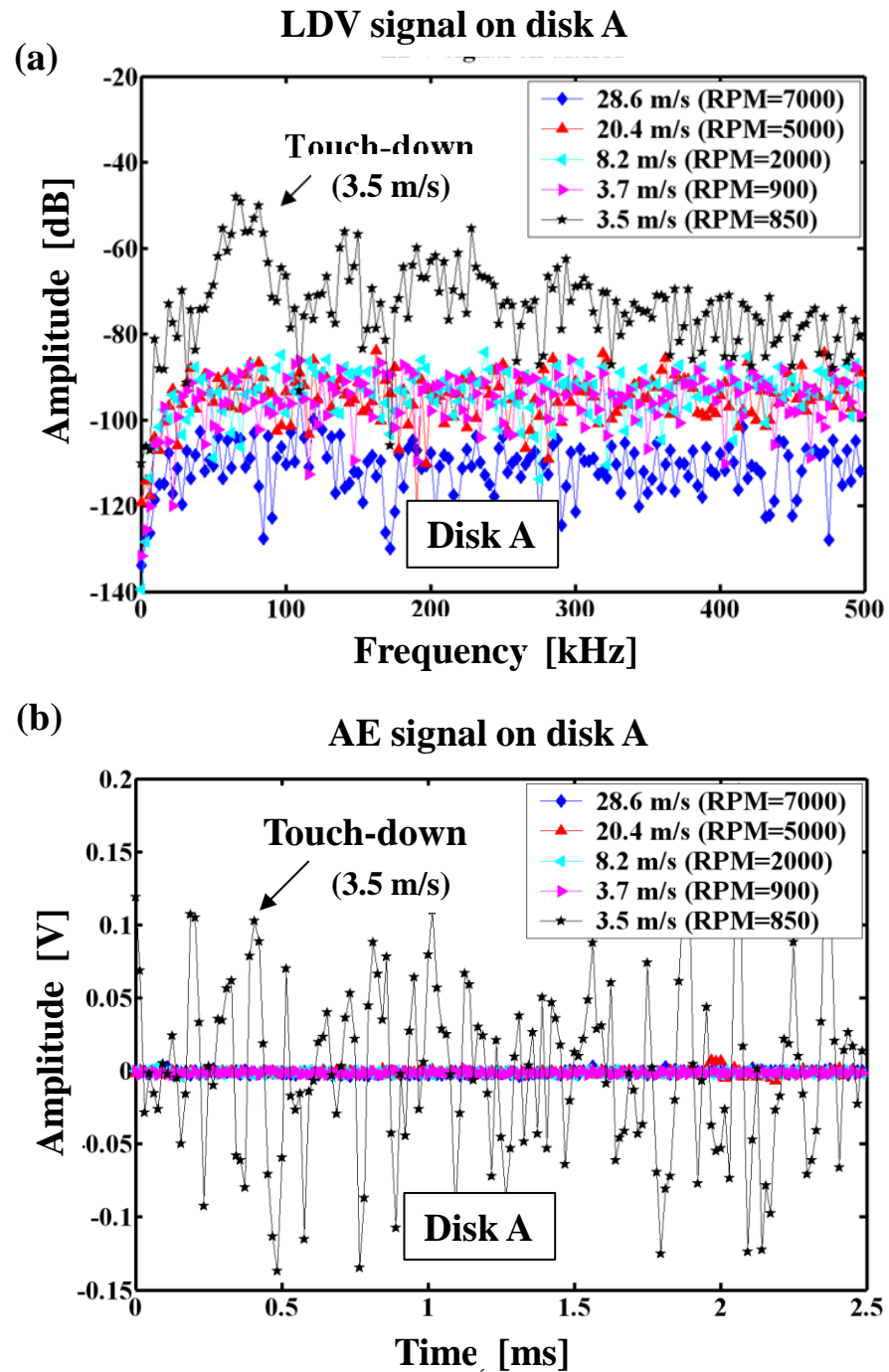


Figure 4.5 Frequency spectra of disk velocity for disk A; (a) S-LDV signal, (b) AE signal

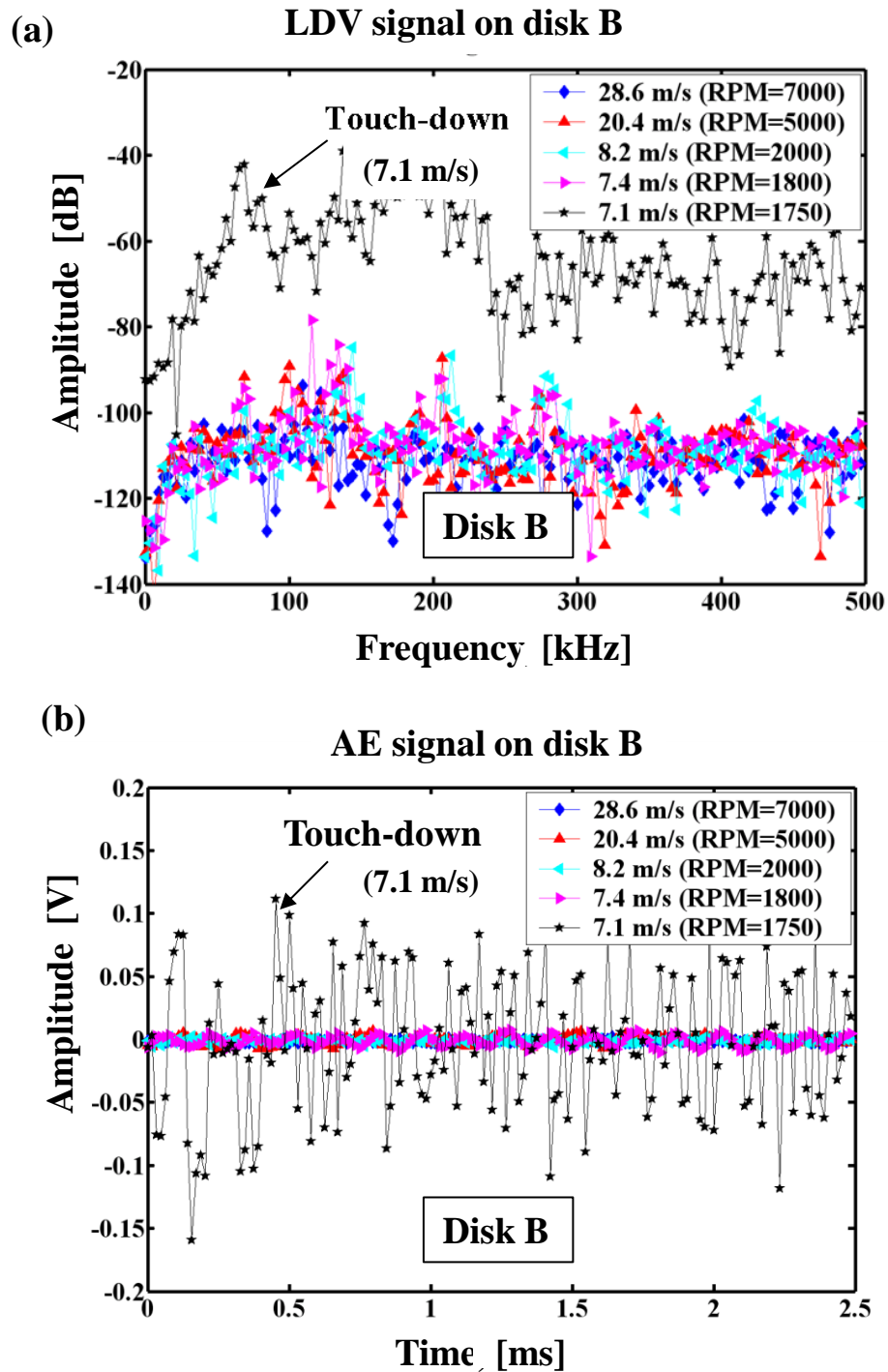


Figure 4.6 Frequency spectra of disk velocity for disk B; (a) S-LDV signal, (b) AE signal

Figure 4.7 shows the summary of the touch-down velocity for the smooth and discrete track recording media under investigation. For discrete track recording disks A and B, touch-down is observed to occur at higher disk velocities than for the smooth disk. For disk C, contact occurred at all velocities throughout the experiment, i.e., the slider did not fly on disk C at all, not even at the highest velocity of 29.4 m/s (7200 RPM). Comparing the touch-down velocity of disk A with the touch-down velocity of the smooth disk, we observe that the difference is small. On the other hand, a much larger difference is observed between disk B and the smooth disk or between disk A and B. Clearly, this difference in the touch-down velocity for disk A and B is a function of the nominal flying height of the slider on disk A and B. In particular, using the flying height data from table 4.1, we see that the design flying height of the pico-slider for disk A is 14.0 nm, while it is 7.4 nm for disk B. Thus, the slider flies lower on disk B than on disk A, and contacts or “touch-down” is likely to occur at a higher velocity on disk B than on disk A.

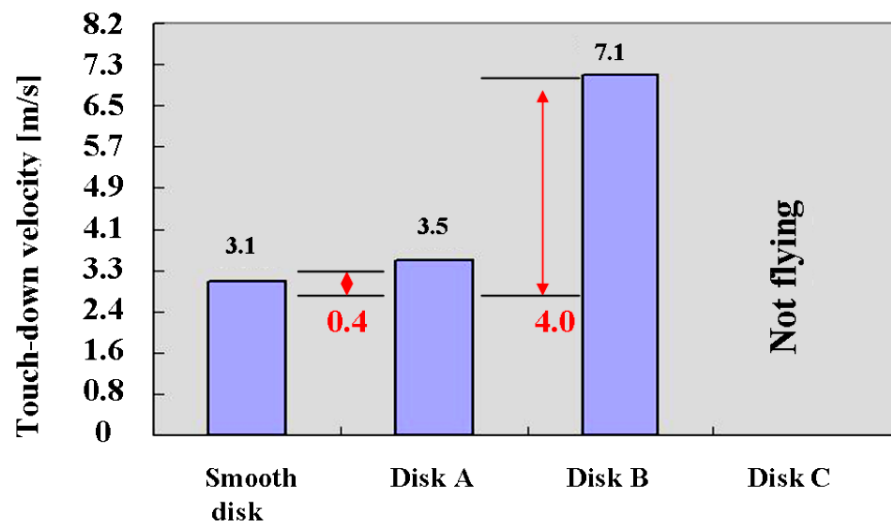


Figure 4.7 Touch-down velocity for smooth and DTR disks

4.3.2 Investigation of touch-down and take-off behavior as a function of ambient pressure for smooth and DTR media

For this test, the slider was positioned at a disk radius of 37 mm and the velocity was kept at 27.9 m/s (7200 RPM). To detect touch-down, the ambient pressure level was decreased in small increments until severe slider/disk contacts were observed. After touchdown, the ambient pressure was increased until contacts between the slider and the disk disappeared.

Figure 4.8 (a) and (b) show AE signals of touch-down and take-off, respectively, as a function of normalized ambient pressure level $P^* = p_{\text{ambient}}/p_{\text{atmospheric}}$ for flying on a smooth disk. We observe that contacts are absent for normalized pressure levels $P^* > 0.4$. However, if the pressure level P^* was decreased below $P^* = 0.4$, severe contacts (i.e., touch-down) occurred at $P^* = 0.33$. In Figure 4.8 (b), the reverse procedure is investigated, i.e., the pressure is increased in small increments above the touch-down pressure of $P^* = 0.33$. We observe that a normalized pressure of $P^* = 0.38$ is needed before flying is re-established. This difference in touch-down and take-off pressure is defined in this thesis as “pressure hysteresis”.

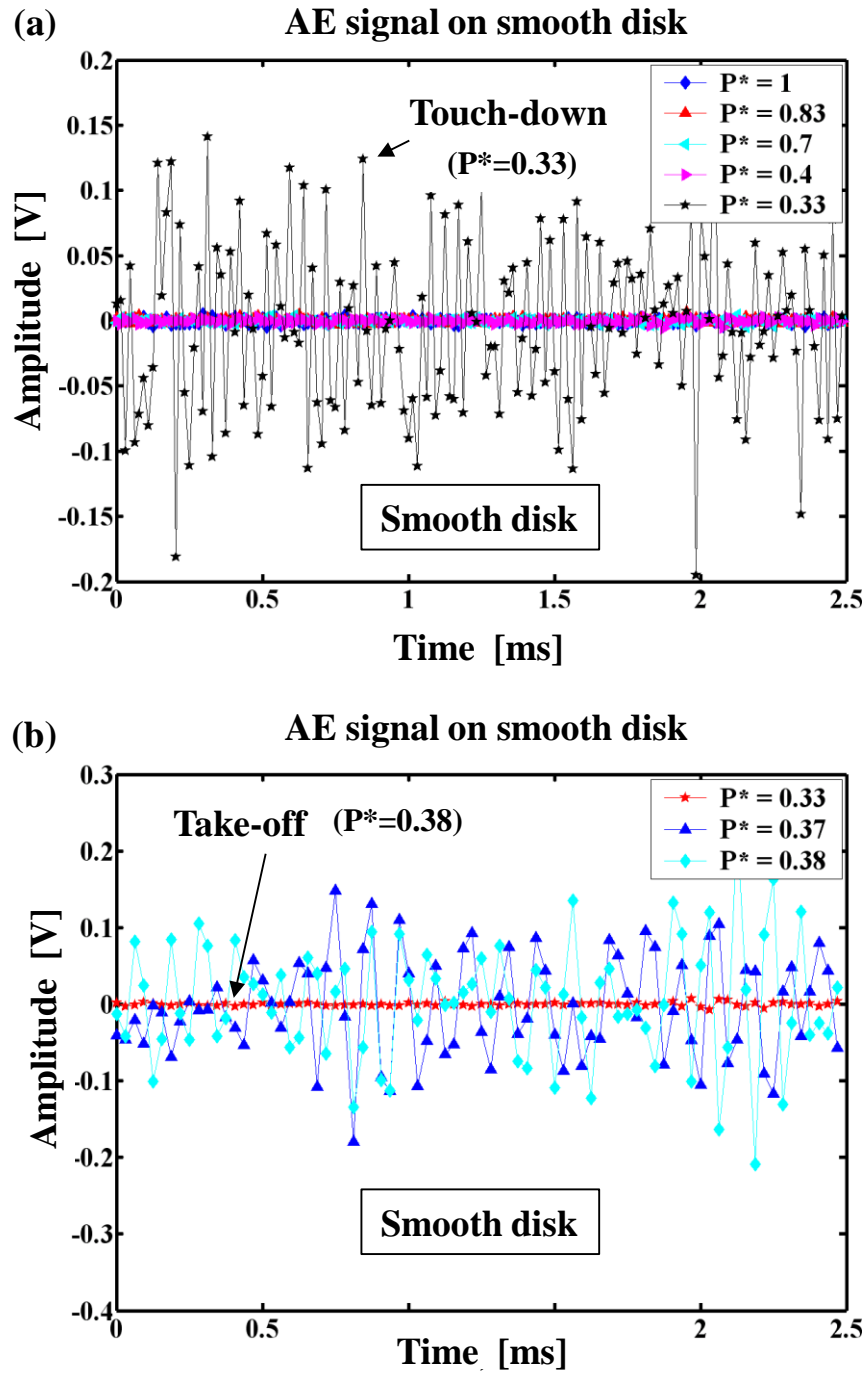


Figure 4.8 Normalized pressure P^* at touch-down and take-off for a smooth disk at a velocity of 27.9 m/s; (a) touch-down signal, (b) take-off signal

Figure 4.9 shows AE signals of normalized touch-down and take-off ambient pressure P^* for disk A. In this case, touch-down of the slider was observed at $P^*=0.39$ while take-off occurred at $P^*=0.66$. In the case of disk B, touch-down and take-off occurred at $P^*=0.67$ and $P^*=0.98$, respectively, as shown in Figure 4.10. Figure 4.11 gives a summary of the pressure data for the normalized touch-down pressure P^* for the head/disk combinations investigated. For discrete track disks A and B, touch-down was found to occur at a higher normalized pressure level P^* compared to the touch-down pressure on a smooth disk. Again, the slider was not flying on disk C. Similar to the results shown in Figure 4.7, the difference in the normalized touch-down pressure for the smooth disk and disk B was much larger than the difference between the smooth disk and disk A. Again, this result is to be expected based on the design flying height data for the pico-slider used on the two types of disks (see table 4.1).

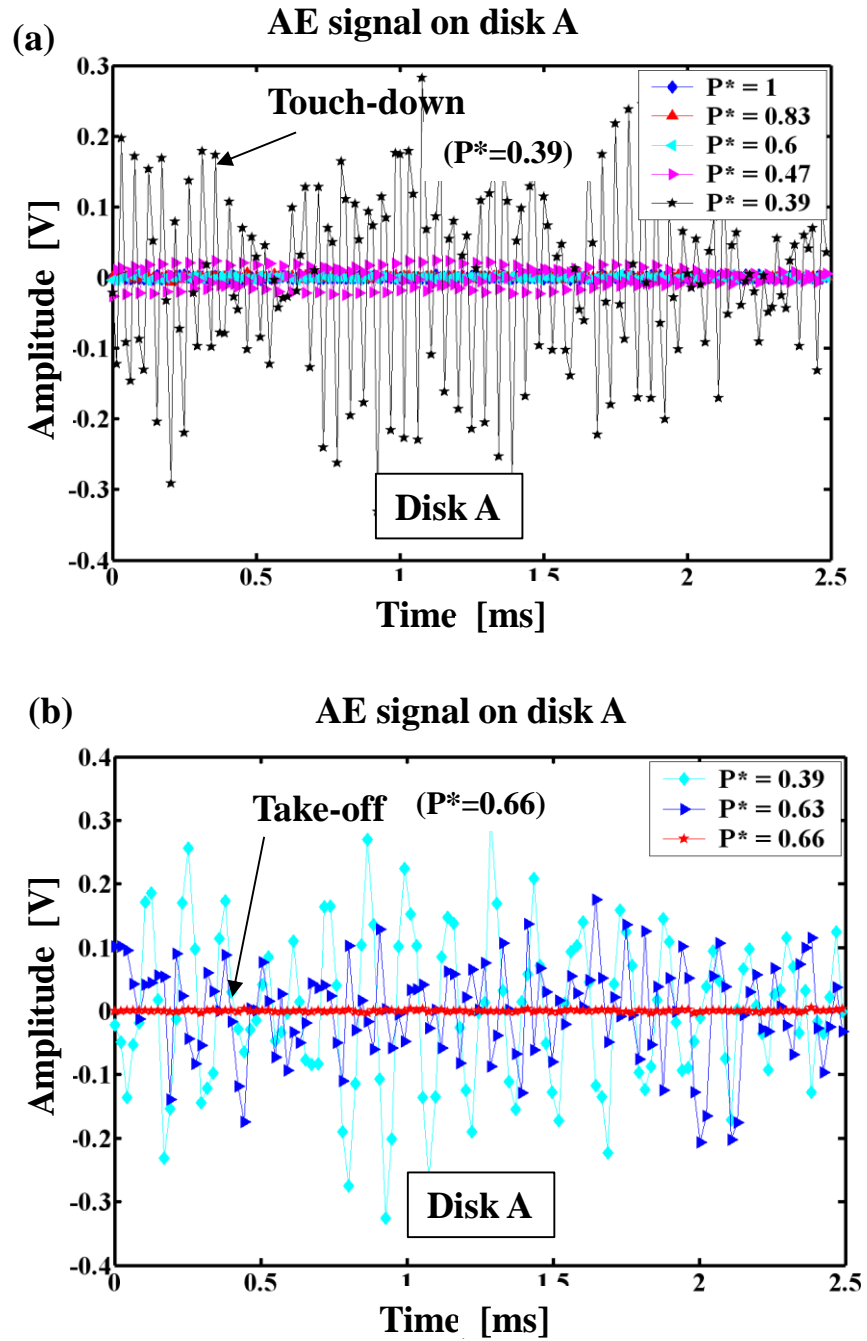


Figure 4.9 Normalized pressure P^* at touch-down and take-off for disk A at a velocity of 27.9 m/s; (a) touch-down signal, (b) take-off signal

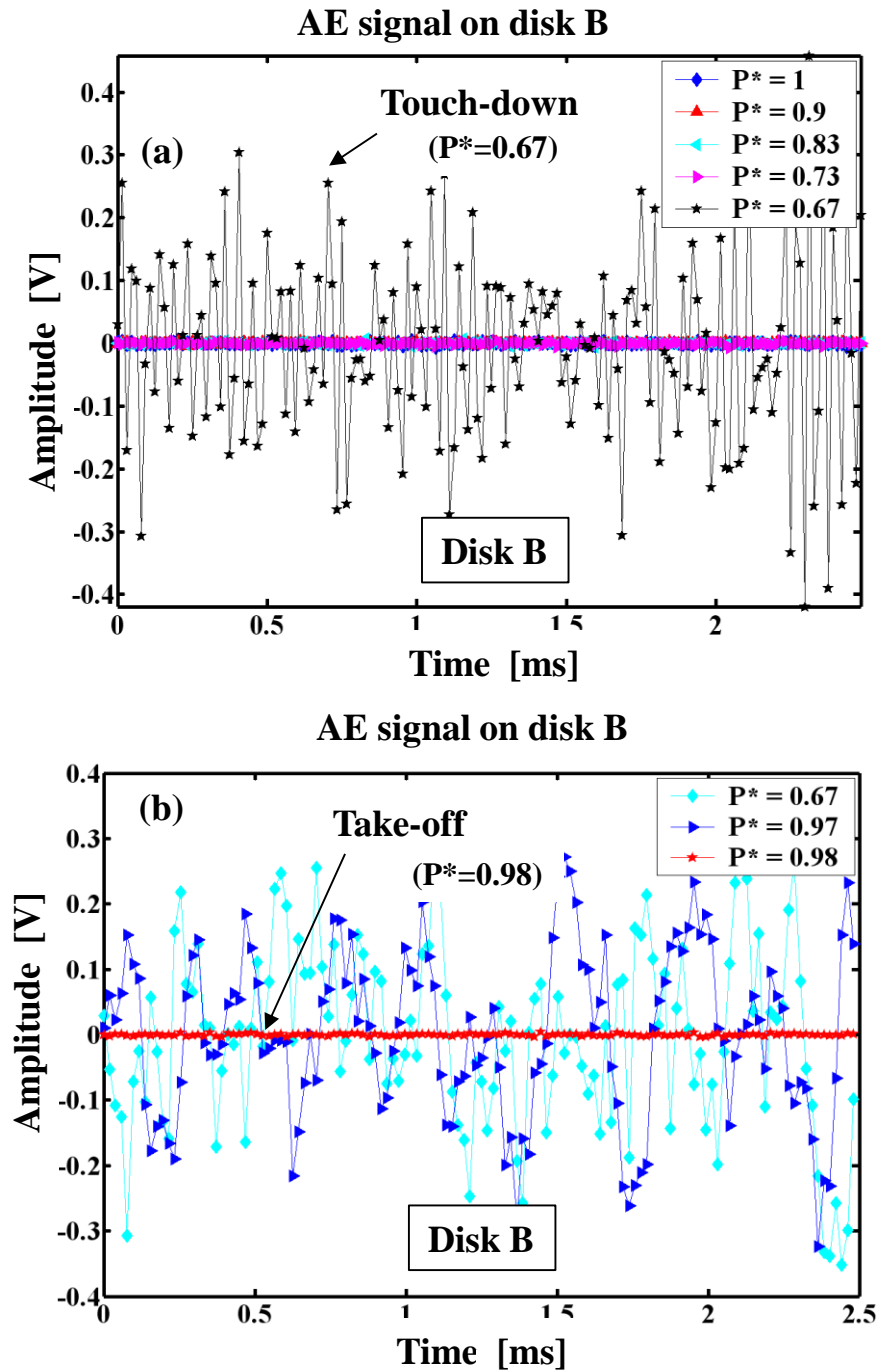


Figure 4.10 Normalized pressure P^* at touch-down and take-off for disk B at a velocity of 27.9 m/s; (a) touch-down signal, (b) take-off signal

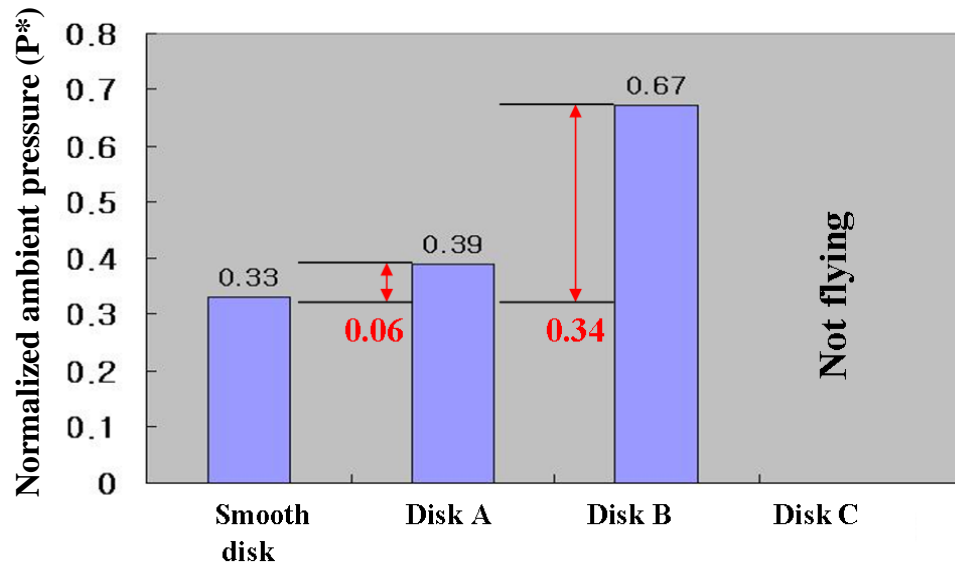


Figure 4.11 Normalized ambient touch-down pressure P^* for smooth and discrete track recording disks at a velocity of 27.9 m/s

Figure 4.12 shows the hysteresis between normalized touch-down and take-off pressure on both the smooth disk and the three discrete track recording disks at a velocity of 27.9 m/s. For the smooth disk, the hysteresis between touch-down and take-off pressure is small. However, both discrete track recording disks A and B show hysteresis between touch-down and take-off pressure, the difference being much larger for disk B than for disk A. Again, the reason for this behavior is related to the nominal flying height of the slider on disk A and B (see table 4.1). No hysteresis occurred for disk C since the slider was not flying on this disk at all.

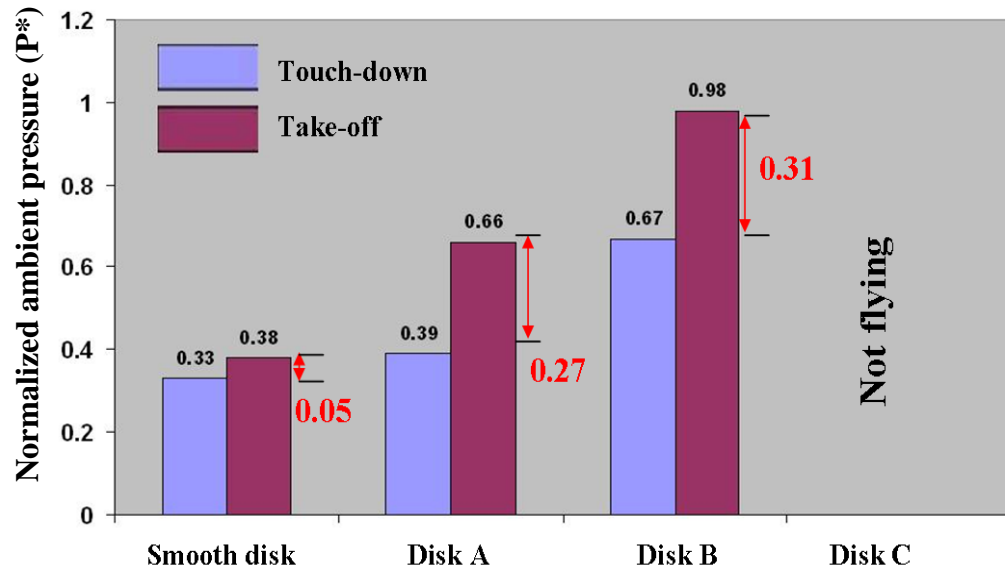


Figure 4.12 Touch-down and take-off pressure hysteresis on a smooth disk and DTR media at a velocity of 27.6 m/s

4.3.3 Contact start-stop test

To evaluate the effect of take-off velocity on the tribological performance of the head/disk interface for smooth and discrete track recording media, contact start-stop tests were conducted at a radius of 35 mm and a skew angle of zero degrees.

Figure 4.13 shows the velocity profile of a typical contact start-stop test performed in this investigation. In the first 3.5 seconds, the velocity was increased to 26.4 m/s (7200 RPM). The velocity was kept constant at this level for five seconds, and was then decreased linearly with time to zero in about 3.5 seconds.

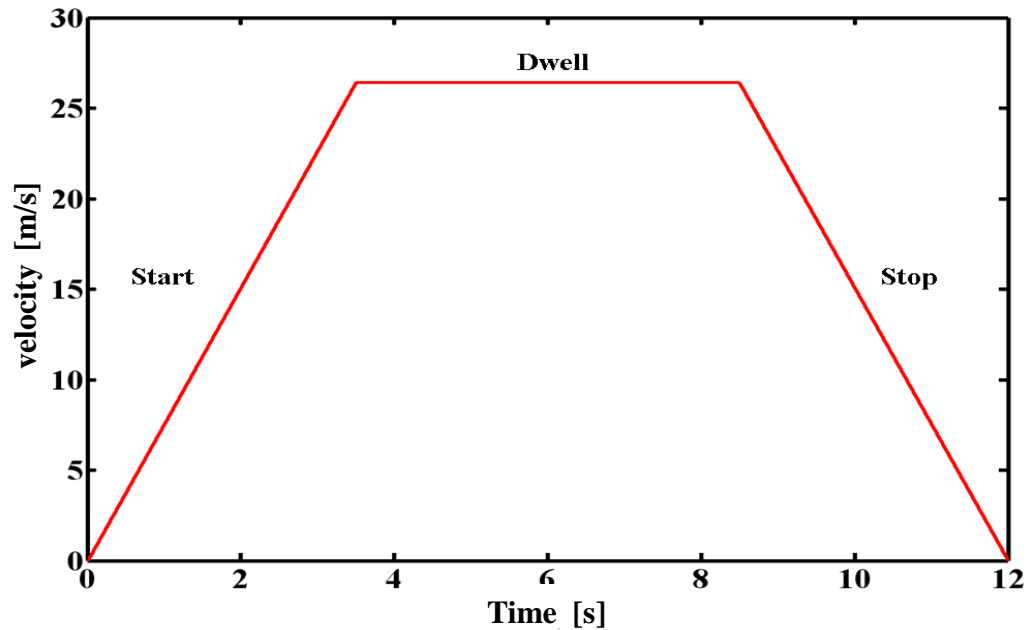


Figure 4.13 Velocity profile for contact start-stop test

Figure 4.14 shows a summary of the velocities at which continuous flying of the slider was established during start/stop testing. We observe that the velocity, at which flying is first observed, is lower on the smooth disk than on the discrete track recording disks. For disks A and B, a higher disk velocity is required to establish hydrodynamic flying than for the smooth disk. As expected from the data in Figures 4.7 and 4.11, the velocity at which flying is established on disk B is much larger than the velocity when flying is established on disk A or the smooth disk. This, again, is a direct function of the lower design flying height of the slider on disk B versus that on disk A (see table 4.1). It is interesting to note that flying of the slider was not observed on disk C.

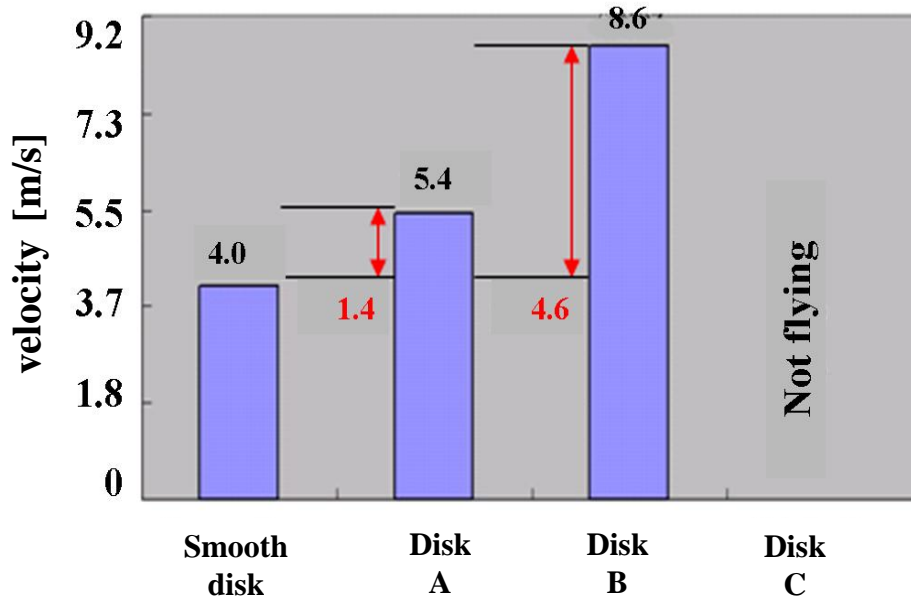


Figure 4.14 Critical velocity for flying of slider on a smooth disk and discrete track recording disks during start/stop testing

4.4 Summary and Conclusions

The touch-down characteristics of a pico-type magnetic recording slider was investigated on discrete track recording media as a function of disk velocity and ambient pressure level. Using the same slider design, we observed that the touch-down velocity was higher for flying of the slider on discrete track recording media than on smooth media. Keeping the velocity constant and reducing the ambient pressure level for the same slider, we observed that touch-down occurred at a higher pressure level on discrete track recording media than on smooth media. This effect is related to the nominal flying height of the slider on smooth and discrete track media. A well-defined hysteresis occurred between touch-down and take-off velocity as well as touch-down and take-off pressure, depending on the design

flying height of the slider and the characteristics of the discrete track media. The results for touch-down and take-off behavior of the slider used in this study are in qualitative agreement with the data from start-stop investigations.

4.5 Acknowledgement

This chapter is a partial reprint of the material as it appears in “Touch-down and take-off hysteresis of magnetic recording sliders on discrete track media,” *Microsyst. Technol.*, vol. 16, pp. 273-278, 2009, by Yeoungchin Yoon and Frank E. Talke. The dissertation author was the primary investigator of this paper and the co-author listed in this paper supervised the research which forms the basis for this chapter.

Bibliography

- [1] R. Wood, "The feasibility of magnetic recording at 1 terabit per square inch," *IEEE Trans. Magn.*, vol. 36, pp. 36-42, 2000.
- [2] B. H. Thornton and D. B. Bogy, "A parametric study of head-disk interface instability due to intermolecular forces," *IEEE Trans. Magn.*, vol. 40, pp. 337-344, 2004.
- [3] V. Gupta, D. B. Bogy, "Effect of intermolecular forces on the static and dynamic performance of air bearing slider: Part II – Dependence of the stability on Hamaker constant, suspension preload and pitch angle," *J. Tribol.*, vol. 128, pp. 203-208, 2006.
- [4] K. Ono, "Effect of van der Waals forces in a near contact head-disk interface," *IEEE Trans. Magn.*, vol. 44, pp. 3675-3678, 2008.
- [5] A. Y. Suh and A. A. Polycarpon, "Adhesive contact modeling for sub-5nm ultralow flying magnetic storage head-disk interfaces including roughness effects," *JAP*, vol. 97, pp. 1043281-10432811, 2005.
- [6] K. Ono, M. Yamane and H. Yamaura, "Experimental and analytical study of bouncing vibrations of a flying head slider in a near-contact regime," *Transactions of the ASME*, vol. 127, pp. 376-386, 2005.
- [7] N. Tagawa, A. Mori and K. Senoue, "Effect of molecularly thin liquid lubricant films on slider hysteresis behavior in hard disk drives," *J. Tribol.*, vol. 129, pp. 579-585, 2007.
- [8] H. Tani, K. Goshi, T. Hamaguchi, "Study of head takeoff phenomenon influenced by stick-slip vibration of slider on head-disk interface," *JAP*, vol. 99, pp. 08N1041-08N11043, 2006.
- [9] Y. Shimizu, K. Ono, J. Xu, R. Tsuchiyama, H. Anam, "Study of a spherical pad head slider for stable low-clearance recording in near contact regime," *Tribol. Lett.*, vol. 30, pp. 161-167, 2008.
- [10] K. Ono, K. Nakagawa, "Dynamic adhesion characteristics of spherical sliders colliding with stationary magnetic disks with a thin lubricant layer," *Tribol. Lett.*, vol. 31, pp. 77-89, 2008.

- [11] K. Ono, "Dynamic instability of flying head slider and stabilizing design for near-contact magnetic recording," *JMMM*, vol. 320, pp. 3174-3182, 2008.
- [12] H. Tani, K. Goshi, K. Suzuki and T. Hamaguchi, "Contact hysteresis behavior of textured pad slider in head-disk interface," *IEEE Trans. Magn.*, vol. 42, pp. 2525-2527, 2006.
- [13] L. Zhou, K. Kato, G. Vurens, F. E. Talke, "Effect of slider surface texture on flyability and lubricant migration under near contact conditions," *Tribology International*, vol. 36, pp. 267-277, 2003.

Chapter 5

Investigation of Contact Deformation and Wear Characteristics of Discrete Track Recording Media

In this chapter, the contact deformation and wear characteristics of smooth and discrete track recording (DTR) media are investigated using nano-indentation and nano-scratch testing. Plastic deformation of the land areas between adjacent grooves was found to be substantially larger than in the smooth regions of the same disk. Reciprocal wear tests showed that wear was more severe for discrete track disks than for smooth disks. To improve the tribology of DTR media, planarization of discrete track disks appears to be necessary.

5.1 Introduction

Discrete track recording (DTR) technology has recently received great interest as a promising approach to increase the areal density in hard disk drives [1, 2]. In discrete track recording, individual tracks are separated from each other by circular “grooves” causing a reduction in “cross-talk” and an improvement in the signal to noise ratio (SNR) [3]. Discrete track recording technology has the potential of achieving areal densities in excess of 1 Tbit/in². One of the main requirements for achieving areal densities in excess of 1 Tbit/in² is that the separation between the recording slider and the disk must be reduced to the order of 1 nm [4]. The reduction of flying height from presently 5 nm to the 1 nm regime increases the likelihood of intermittent contacts, loss of data and failure of the hard disk drive. To prevent this, improvements in the wear characteristics of the head disk interface are essential. Many researchers have studied the effect of contacts [5-8] for conventional smooth media. However, little information is available on the problem of slider/disk contacts in the case of discrete track recording media. Gong and Komvopoulos investigated numerically the effect of patterned surfaces on the contact deformation of layered media [9]. Using finite element analysis, they observed high pressure peaks at the edges of the bit pattern in the direction of sliding. In addition, they observed that high pressure spikes initiate surface cracks and plastic flow in the patterned surface. This behavior is different from smooth surfaces. Nunez et al. [10] simulated numerically the contact behavior of patterned media after planarization. They found that planarization of patterned media

improves the contact resistance compared to non-planarized patterned media. The filler material used can support load during contact thereby reducing the contact stress on the patterned surface. They found that patterned surfaces show very different contact deformation and behavior compared to smooth surfaces. They also observed that the contact stiffness is higher on the planarized (flat) surfaces than on patterned surfaces. In addition, they observed that the magnetic film yielded plastically for non-planarized media.

In this chapter, the contact deformation and wear characteristics of smooth and discrete track recording media are investigated using nano-indentation and nano-scratch testing [11-17]. Plastic deformation of the land area between adjacent grooves is determined and compared with the deformation of smooth media. The dependence of wear characteristics on track geometry is investigated. Atomic force microscopy (AFM), in situ scanning probe microscopy (SPM) [18] and scanning electron microscopy (SEM) are used to observe wear and damage of individual discrete tracks.

5.2 Experimental procedure

Discrete track recording disks were fabricated by nano-imprint lithography (NIP) [3]. The magnetic layer (hard magnetic layer = 20 nm), the diamond like carbon (DLC) coating (2 nm), and the lubricant film (1.2 nm) were deposited after nano-imprinting. A typical discrete track recording disk is shown in Figure 5.1. Discrete track recording disks are characterized by the land width, the groove depth

and the track pitch.

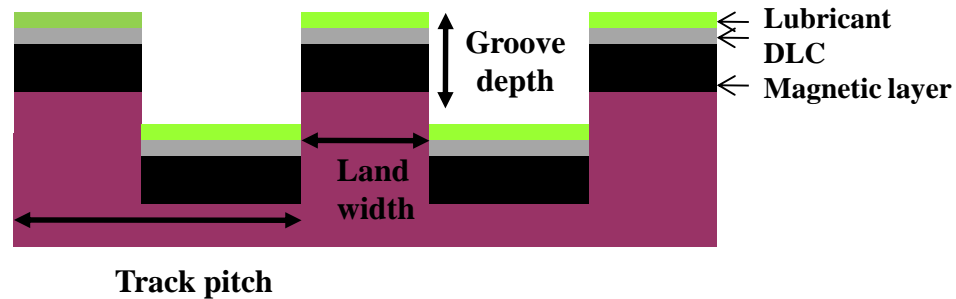


Figure 5.1 Typical discrete track recording disk layer structure

5.2.1 Contacts between slider and DTR disk

In discrete track recording, a slider flies over thousands of parallel discrete tracks during reading and writing.

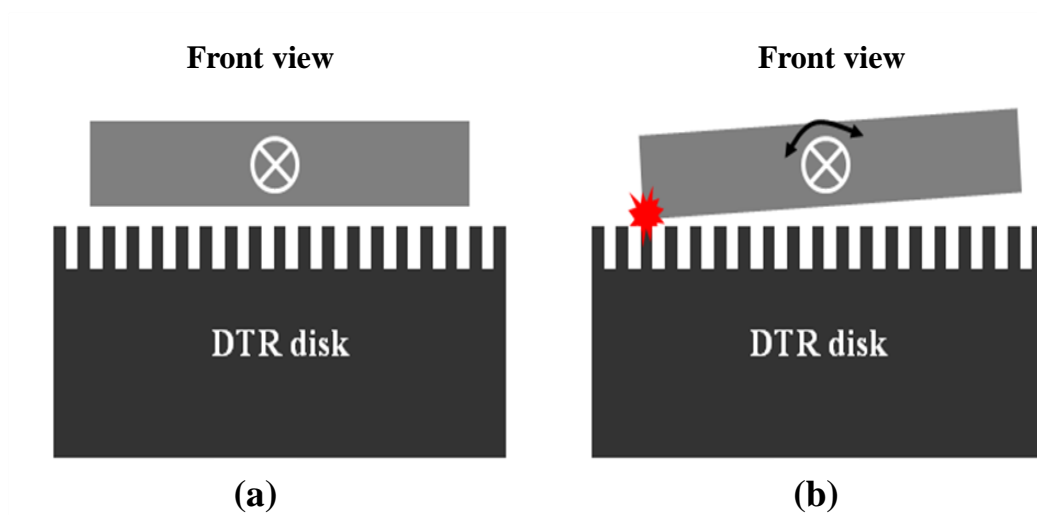


Figure 5.2 Schematic of head-disk interface for DTR disk; (a) stable flying and (b) contact with DTR disk

Figure 5.2 (a) shows the schematic of a slider flying without contacts and Figure 5.2 (b) shows the situation when contacts between a slider and a discrete track recording disk occur. Contacts between slider and disk cause wear of both the

slider and the disk and increase the likelihood of failure of the hard disk drive. Therefore, the understanding of the contact behavior and wear characteristics of discrete track media is of great importance.

5.2. 2 Nano-indentation and nano-scratch testing

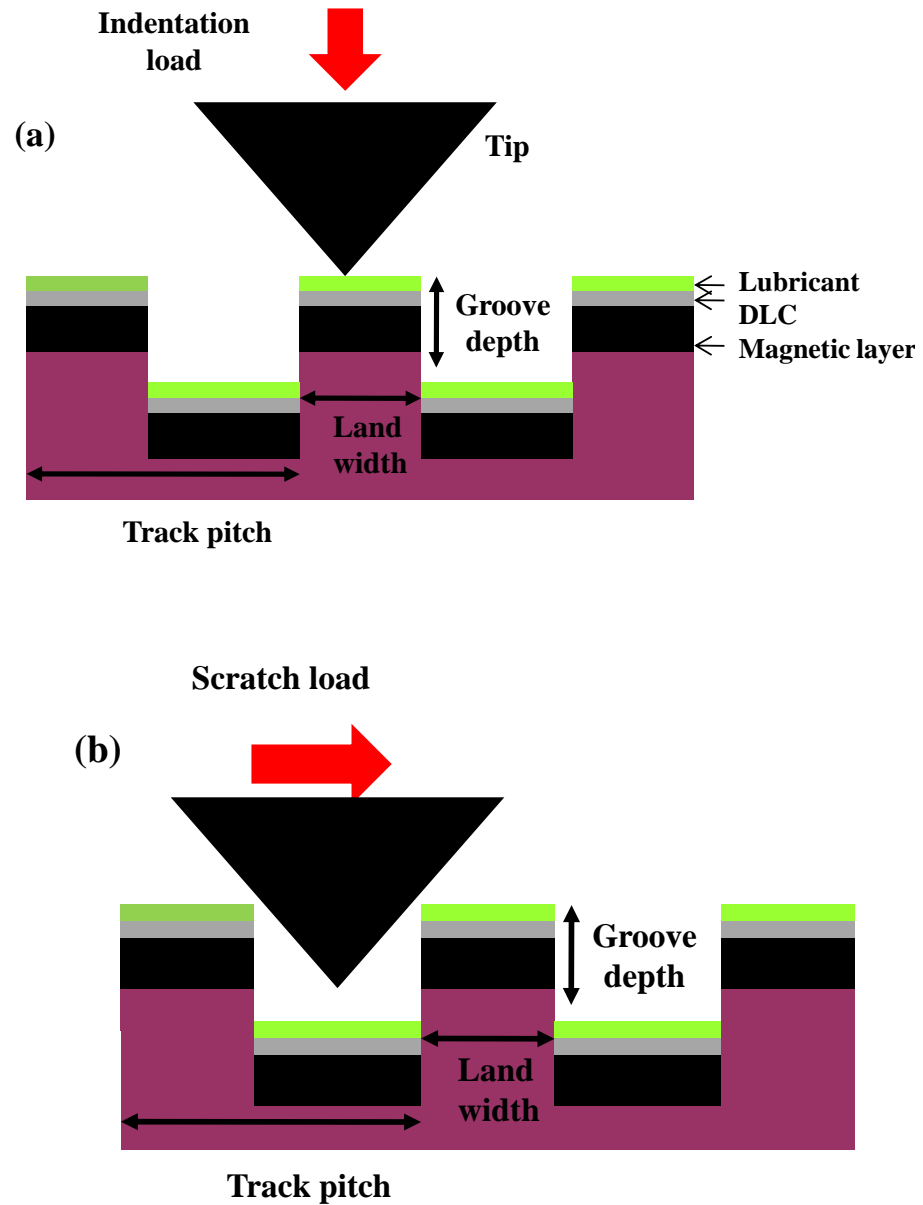


Figure 5.3 Schematic of nano-indentation and nano-scratch testing on discrete track; (a) schematic of nano-indentation, (b) schematic of nano-scratch testing

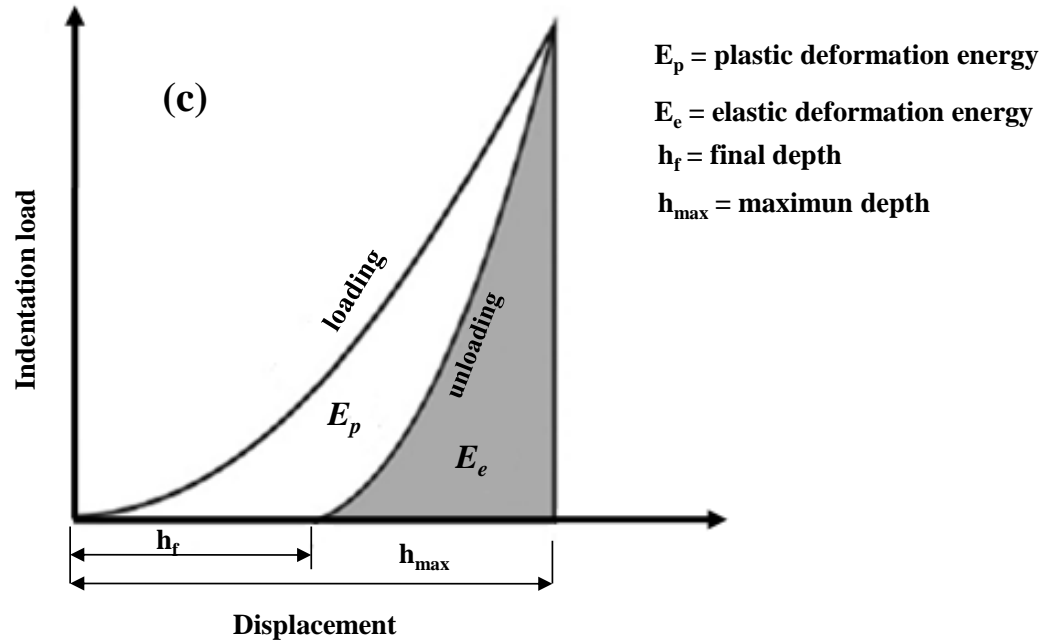


Figure 5.3 (continue) (c) typical indentation (load-displacement curve)

5.2.3 Reciprocal wear testing

Figure 5.4 shows the schematic of the experimental setup used for reciprocal wear testing [17]. To create a reciprocal motion, we used a shear mode piezoelectric (PZT) actuator connected to a signal generator. The shear mode actuator is driven by a triangular input voltage signal of constant amplitude from a signal generator (Figure 5.4 (b)). The displacement of the PZT actuator is measured using an optical displacement sensor (Figure 5.4 (a)). Samples (discrete track surface and smooth surface) are attached on the top of the shear mode PZT as indicated in Figure 5.4 (a). A normal force (N) is applied to the spherical wear probe. The load cell is attached to the spherical wear probe and measures the friction force generated between the

spherical wear probe and the sample as a function of normal force and cycles.

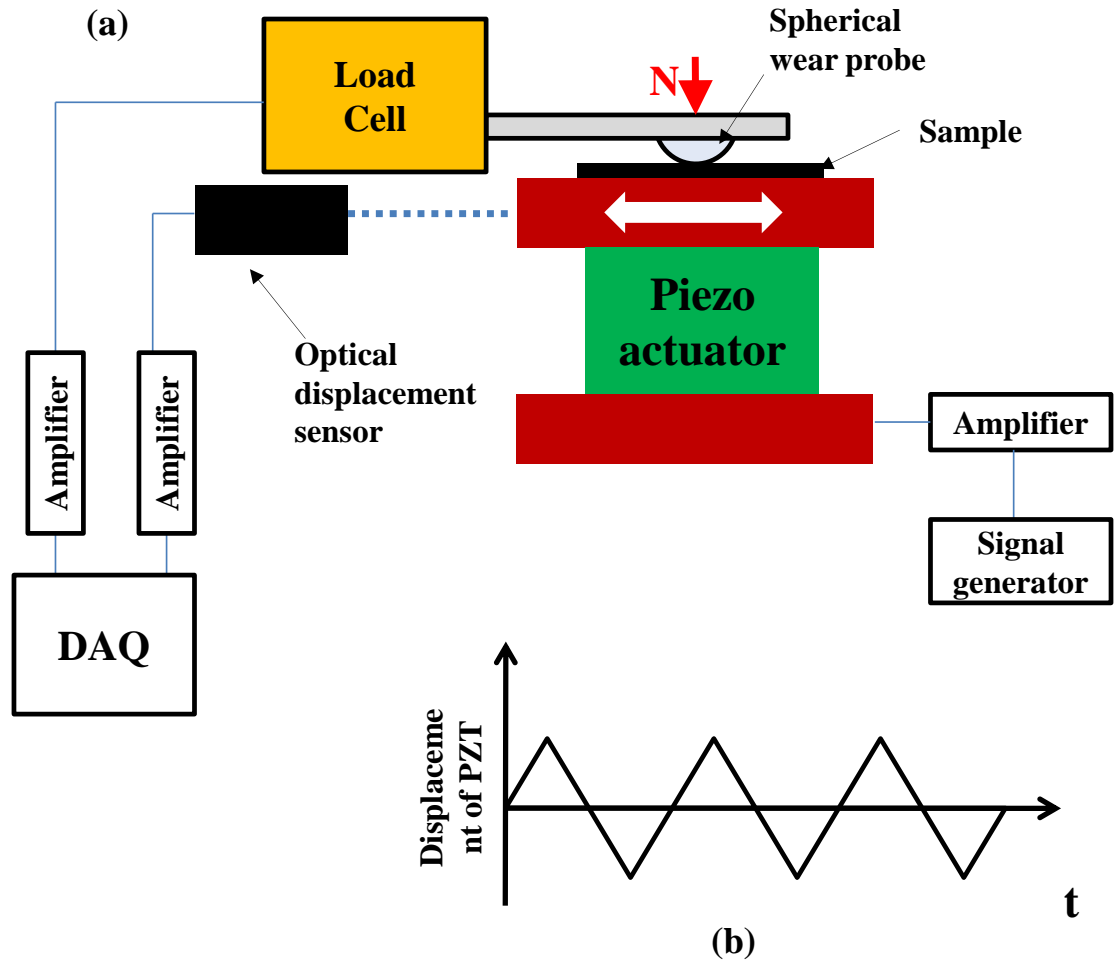


Figure 5.4 (a) Experimental setup of reciprocal wear test and (b) displacement of PZT versus time

5.3 Experimental investigation

5.3.1 Wear of DTR media due to contacts between slider and disk

A so-called “sparsely” populated discrete track disk with a limited number of tracks (Figure 5.5), 9 tracks (land width = 198 nm, groove depth = 63 nm and track pitch = 380 nm) was available for this investigation. First, the disk was spun up to

high speed so that the slider was flying over the discrete track area without contacts. Then, the rotational speed of the disk was decreased gradually until contacts between slider and disk were observed at the so-called “touch-down” velocity. Figure 5.5 (a) shows that the discrete track region experienced substantial wear as a result of contacts between slider and disk. If the same touch-down experiment was repeated on the same disk in the area outside the discrete track region, no wear was observed. Wear particles originating from damaged tracks accumulated in the grooves of the discrete tracks as shown in Figure 5.5 (b). Since the material properties of the disk are the same in the discrete track recording (DTR) zone as in the “smooth” zone, it is apparent that the presence of the grooves affects the contact behavior and wear resistance of the head/disk interface.

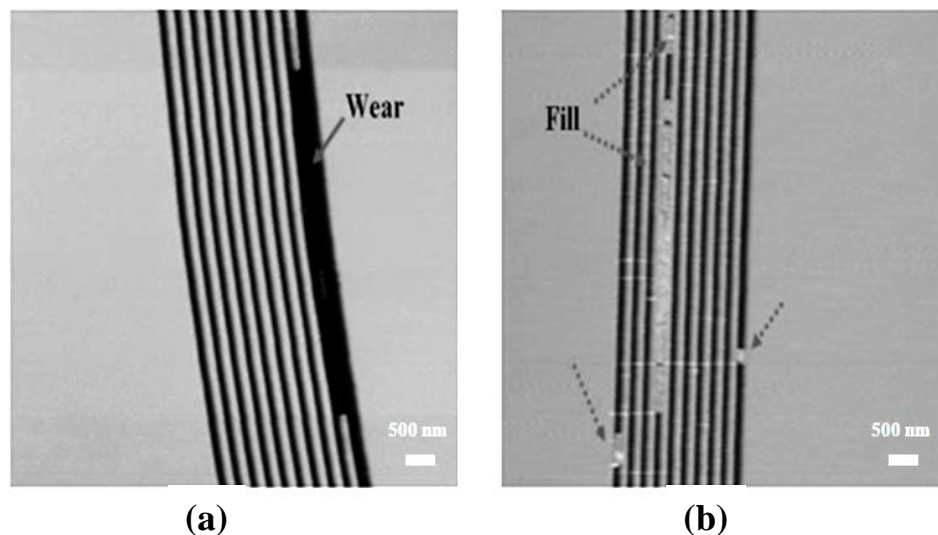


Figure 5.5 AFM images of typical wear and accumulation of wear particles in discrete tracks; (a) wear on discrete tracks and (b) fill in the grooves

Figure 5.6 shows a scanning electron microscopy (SEM) image of a worn DTR disk after a flyability test (groove depth = 40 nm, land width = 90 nm, track pitch = 200 nm). We observe that extended portions of the discrete tracks are

missing, indicating severe wear of the discrete track recording (DTR) media during the flyability test.

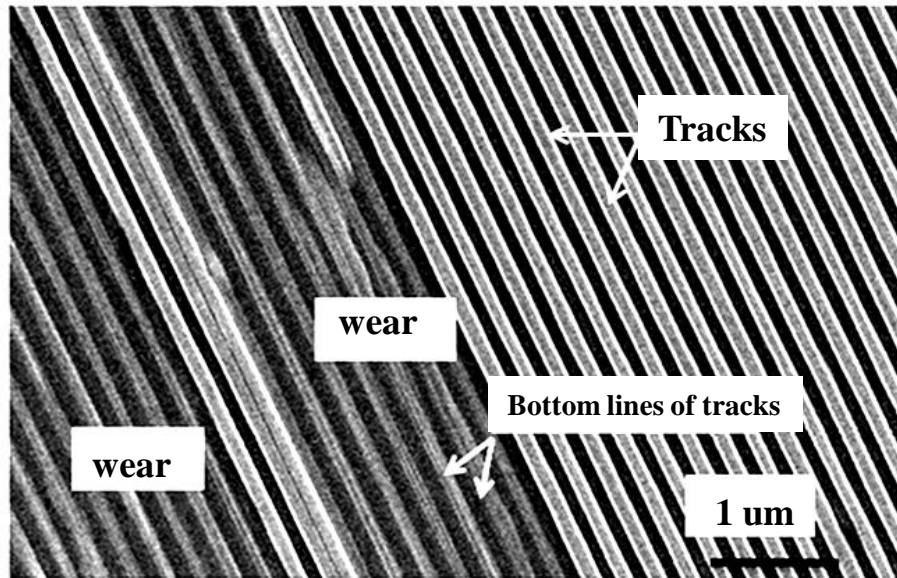


Figure 5.6 SEM image of wear on a DTR disk (groove depth = 40 nm, land width = 90 nm, track pitch = 200 nm) after flyability testing

The above results indicate that discrete track disks can easily be damaged. Thus, discrete track recording media must be designed with great care to guarantee sufficient wear resistance.

5.3.2 Contact deformation of smooth and discrete track surfaces using nano-indentation and nano-scratch testing

In the next set of experiments, the contact behavior of narrow width discrete track disks was investigated using nano-indentation and nano-scratch testing. In each case, the experiments were repeated in the smooth area of the same disk, i.e., outside the discrete track region. To study the effect of geometry of the discrete tracks, we have used two different types of discrete tracks as shown in Table 5.1.

All discrete track disk samples were prepared using the same manufacturing process. Nano-indentations were made at the center of each discrete track and nano-scratches were made in the direction perpendicular to the discrete tracks.

Table 5.1 Characteristics of two different types of discrete track disk surfaces

	Discrete track A	Discrete track B
Land width (W)	198 nm	144 nm
Groove depth (D)	33 nm	63 nm
Track pitch (T)	380 nm	380 nm
Ratio (D/W) (Groove depth / Land width)	0.1667	0.4375

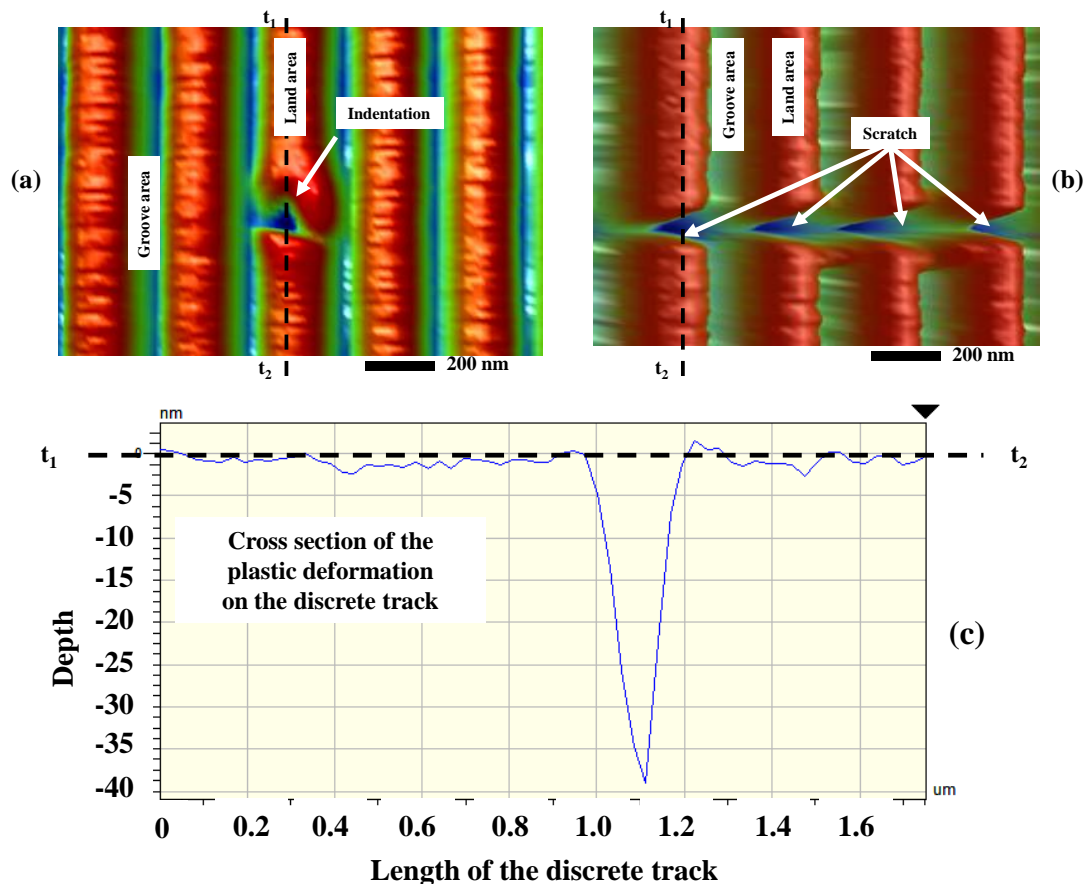


Figure 5.7 Images of indentation and scratch tests on discrete track disks; (a) nano-indentation, (b) nano-scratch test and (c) cross section of the plastic deformation of the discrete track along the line ($t_1 - t_2$).

Figure 5.7 (a) shows a typical micrograph for an indentation in the land area of a discrete track disk while Figure 5.7 shows a micrograph of a scratch test performed perpendicular to the direction of the discrete tracks. We observe from Figure 5.7 (a) that a large indentation is present, indicating large scale plastic deformation. Large scale plastic deformation is also observed in Figure 5.7 (b) for the scratch test across the discrete tracks. Figure 5.7 (c) shows the cross section of the plastic deformation of the discrete track along the line ($t_1 - t_2$).

Figure 5.8 shows scanning probe microscopy (SPM) images of nano-indentations at loads from 200 μN to 700 μN in the land region of discrete track disks and the smooth region outside the discrete track region. The top row of Figure 5.8 shows the indentations at loads from 200 μN to 700 μN in the smooth region of the disk, while the bottom row shows the indentations in the land area of the discrete track disk surface. We observe that the size of the indentation in the smooth area of the discrete track recording (DTR) disk increases with load. A similar trend is also observed for the deformation in the land area. However, the deformation in the land area increases substantially more than the deformation at the smooth area, i.e., a large difference exists in the behavior of the smooth and discrete track region. That is to say, the indentation characteristics in the narrow track area is affected by the geometry and the aspect ratio of the discrete track.

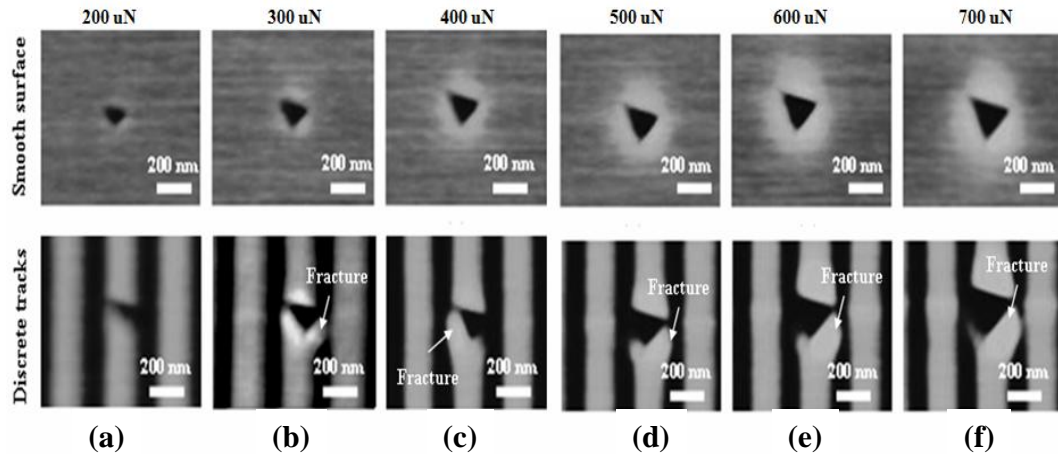


Figure 5.8 Typical SPM images of indentations on smooth surface and discrete track disk (discrete track B); (a) 200 uN, (b) 300 uN, (c) 400 uN, (d) 500 uN, (e) 600 uN and (f) 700 uN

Figures 5.9 shows the load-displacement curves for nano-indentations in the smooth area of a discrete track disk while Figures 5.10 and 5.11 show the same curves taken in the land area of discrete track media A and B at loads ranging from 200 uN to 700 uN. In the case of the smooth region shown in Figure 5.9, plastic behavior was absent at a load of 200 uN. Large plastic deformation was observed, however, at the same load of 200 uN in the land area of the discrete track (Figures 5.10 and 5.11). As the normal load increased, plastic deformation was found to increase in the land area of the discrete tracks (Figures 5.10 and 5.11) relative to the smooth surfaces. The solid arrows in Figures 5.10 and 5.11 marked “D1 and D2” indicate the increased indentation depth in the discrete track region compared to the indentation depth in the smooth surface at a load of 700 uN. These load-displacement curves show clearly that the contact deformation of discrete track media is affected by the aspect ratio between the groove and the land area.

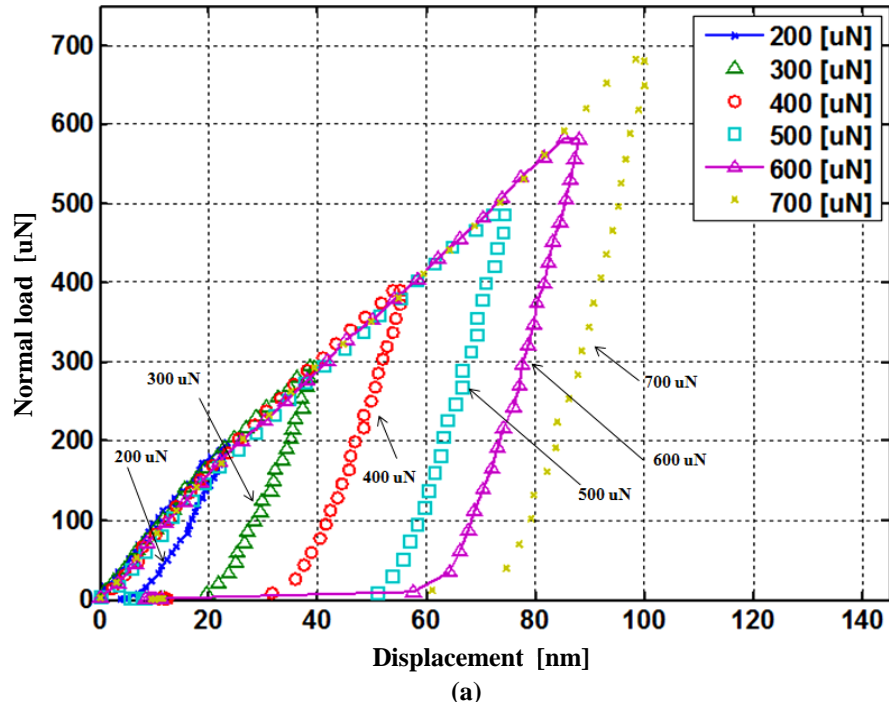


Figure 5.9 Load-displacement curves as a function of normal loads on the smooth surface

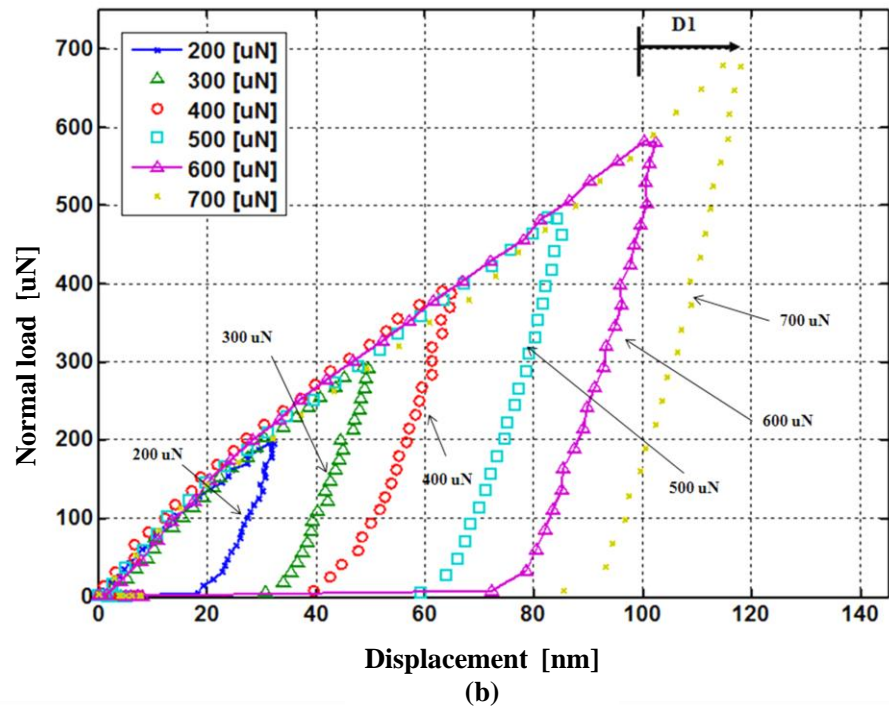


Figure 5.10 Load-displacement curves as a function of normal loads on discrete track A

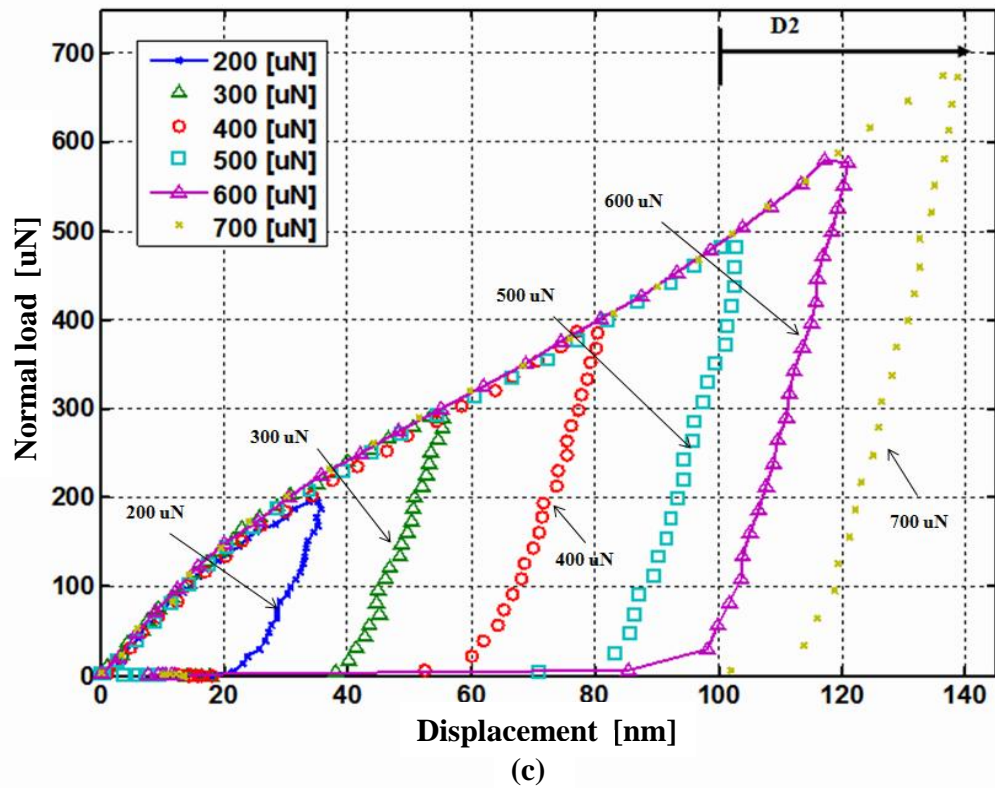


Figure 5.11 Load-displacement curves as a function of normal loads on discrete track B

Figure 5.12 shows the dissipated energy as a function of the normal load based on the results in Figures 5.9-5.11 [20]. The dissipated energy is the integral of the load/unload curve during a single indentation. As seen in Figure 5.12, the dissipated energy of an indentation on a smooth surface is smaller than that on a disk with discrete tracks (A, B). Furthermore, the dissipated energy for discrete track B (land width = 144 nm and groove depth = 63 nm) is larger than that for the smooth region on each discrete track recording (DTR) disk.

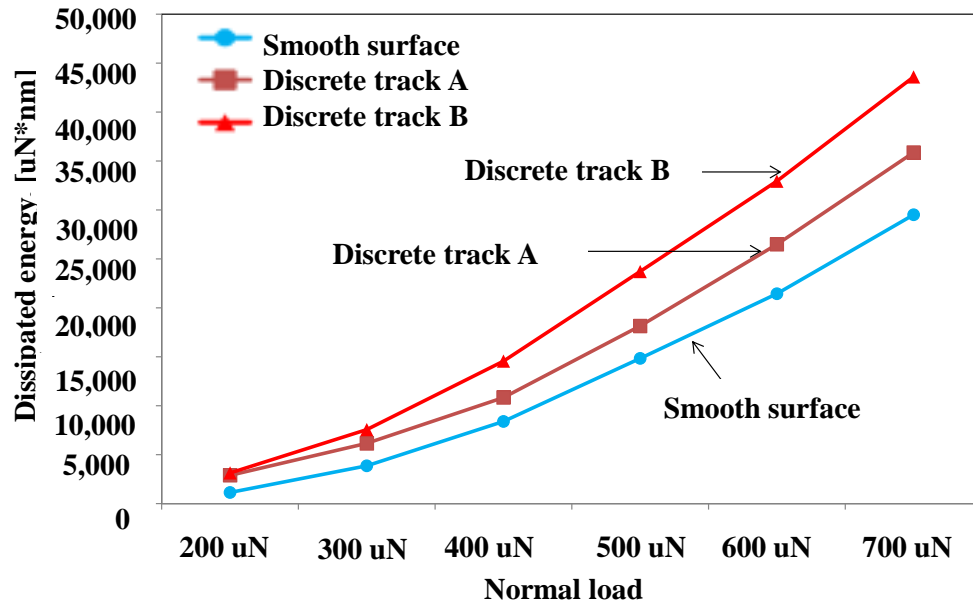


Figure 5.12 Plastic deformation energy (dissipated energy) versus normal load for different disk surfaces

The residual indentation depth in the smooth surface and the discrete track regions of disks A and B is shown in Figure 5.13 as a function of the normal load. Clearly, the residual indentation depth increases with increasing normal load.

In the next series of experiments we performed nano-scratch tests (see Figure 5.14) as a function of load using a lateral force microscopy (Hysitron Inc.). A diamond cube corner tip was used at loads between 10 uN and 130 uN. As the load was increased, the scratches were found to be increasingly more severe on the discrete track surfaces. The scratches were substantially smaller on the smooth areas of discrete track recording (DTR) disks as seen in Figure 5.15. Examining the photo micrographs, we observe that the largest damage occurred at the edges of the discrete tracks [9].

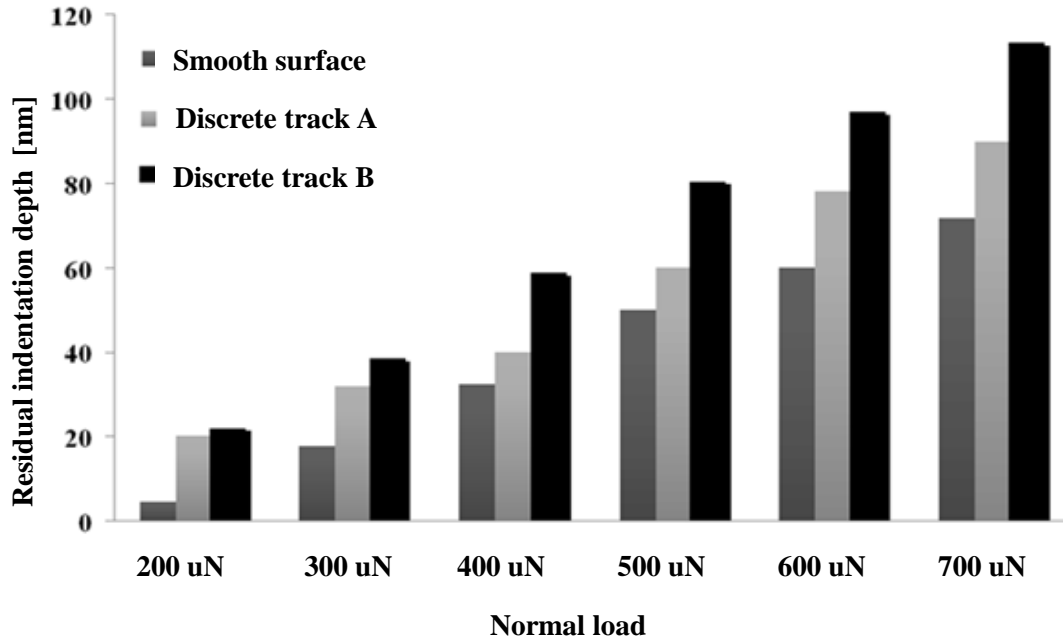


Figure 5.13 Final depth of plastic deformation as a function of the normal load on the smooth surface and discrete tracks A and B

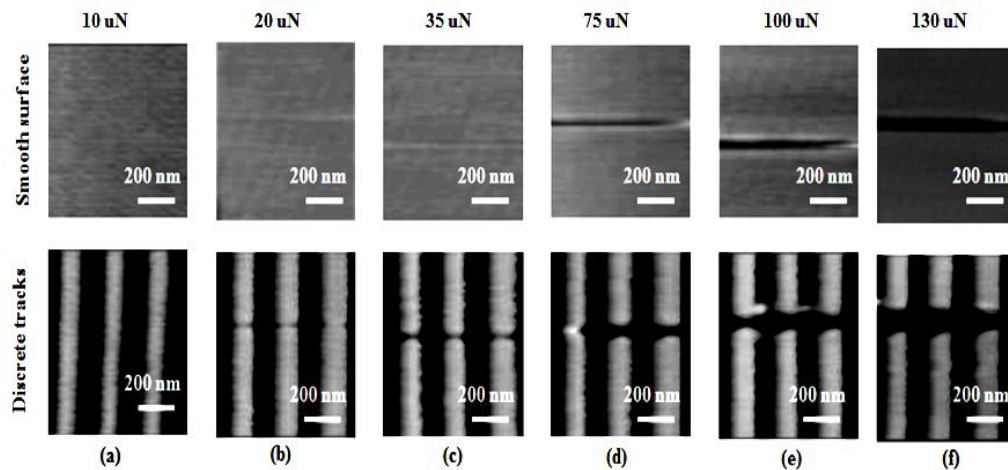


Figure 5.14 Typical SPM images of nano-scratch tests on the smooth disk and discrete track B; (a) 10 uN, (b) 20 uN, (c) 35 uN, (d) 75 uN, (e) 100 uN and (f) 130 uN

Figure 5.15 shows a comparison of scratch depth on smooth and discrete track media as a function of load. We observe that the wear depth of discrete tracks A and B is larger than that on the smooth surface. This result is similar to the result for the

maximum plastic deformation on discrete track B during nano-indentation (Figure 5.13).

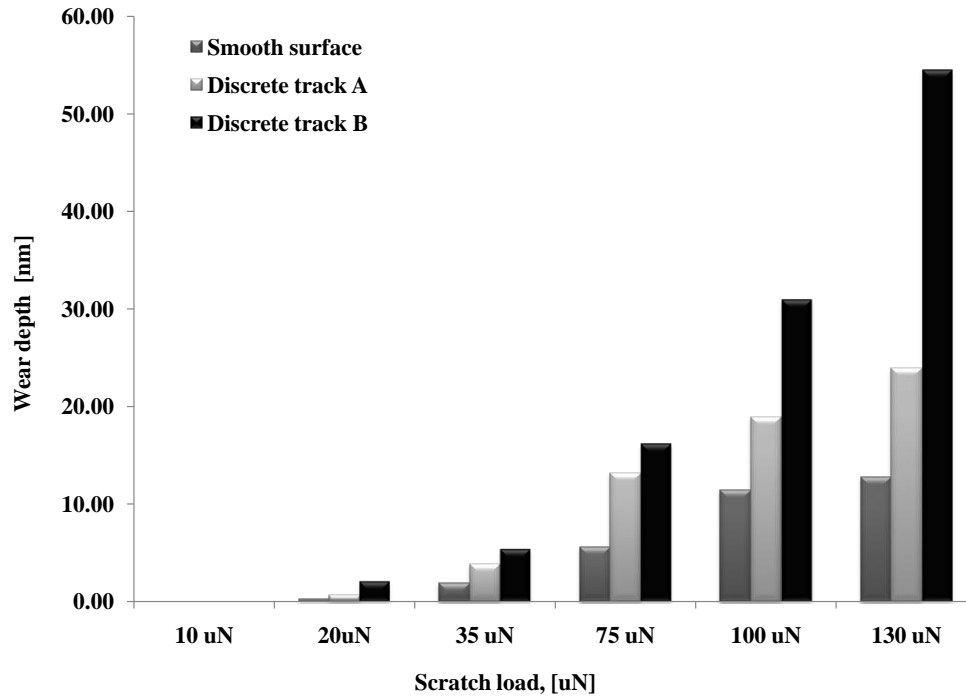


Figure 5.15 Scratch depth as a function of scratch load on a smooth disk surface and discrete track disks A and B

5.3.3 Wear characteristics of discrete track media using reciprocal wear testing

Figure 5.16 shows scanning electron microscopy (SEM) images of wear scars on smooth and discrete track surfaces (Figures 5.16 (a)–(f)) at different loads using the reciprocating wear tester. We observe that the wear scar increases with load and the number of cycles for both the smooth disk area and the discrete track disk area. In addition, we observe that the wear scar is larger in the discrete track area than in the region outside the discrete tracks (Figures 5.16 (d)–(f)). Furthermore, the

number of wear particles generated in the discrete track area is substantially larger than the number of wear particles generated in the smooth area.

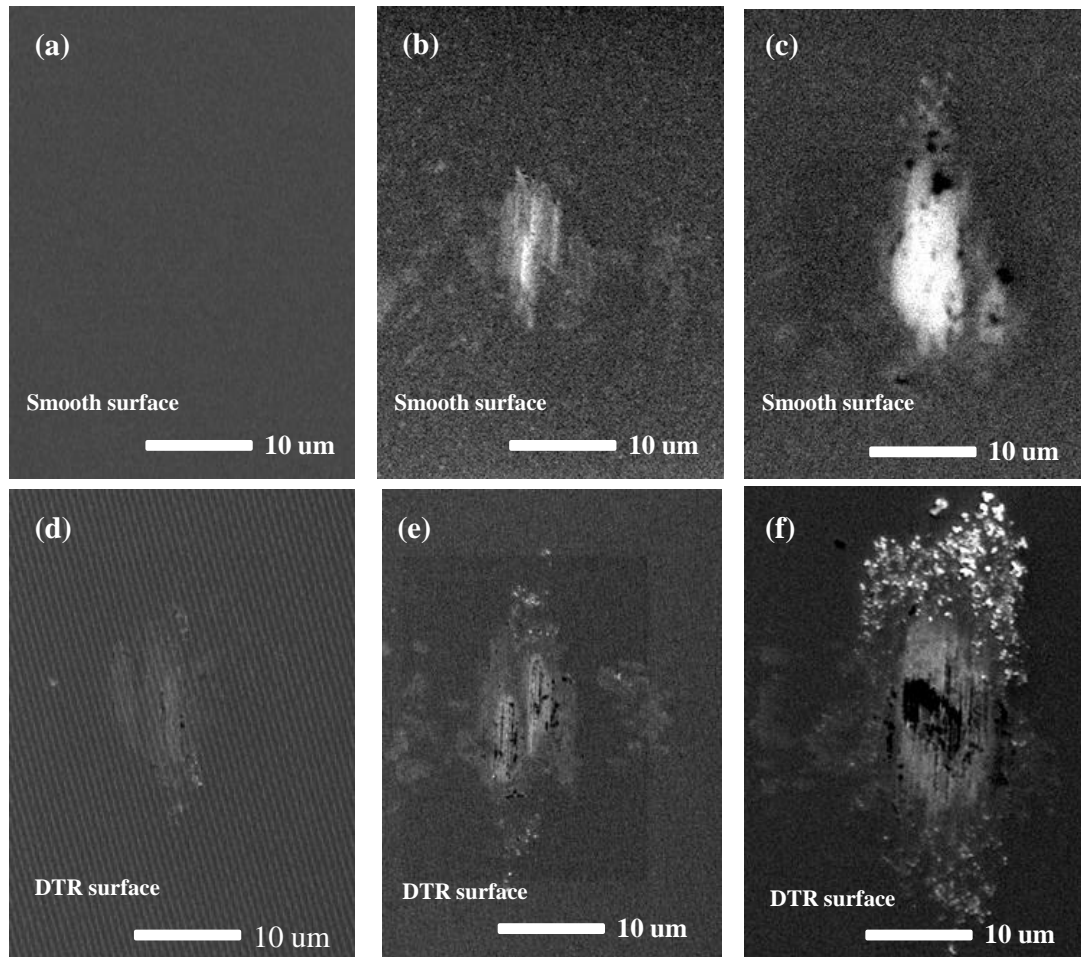


Figure 5.16 Comparison of wear scars on smooth and discrete track surfaces; (a) smooth disk area tested at 5Hz/5.6 μ m/10uN/1000, (b) smooth disk area tested at 5Hz/5.6 μ m/20uN/1000, (c) smooth disk area tested at 5Hz/5.6 μ m/20uN/10000, (d) discrete track surface tested at 5Hz/5.6 μ m/10uN/1000, (e) discrete track surface tested at 5Hz/5.6 μ m/20uN/1000 and (f) discrete track surface tested at 5Hz/5.6 μ m/20uN/10000

In Figure 5.17, scanning electron microscope (SEM) images are shown for a spherical wear probe used in the reciprocal wear test. We observe that a large amount of debris (marked with a dashed circle) adheres to the wear probe.

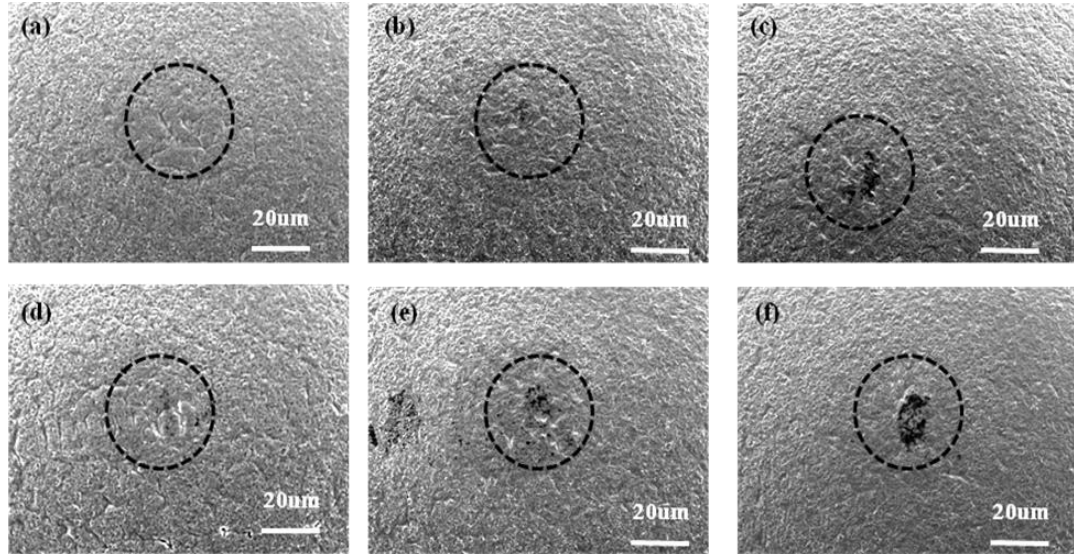


Figure 5.17 SEM images on the spherical wear probes after reciprocal wear tests; (a) tested on smooth disk area at 5Hz/5.6µm/10uN/1000 cycles, (b) tested on smooth disk area at 5Hz/5.6µm/20uN/1000 cycles, (c) tested on smooth disk area at 5Hz/5.6µm/20uN/10000 cycles, (d) tested on discrete track surface at 5Hz/5.6µm/10uN/1000 cycles, (e) tested on discrete track surface at 5Hz/5.6µm/20uN/1000 cycles and (f) tested on discrete track surface at 5Hz/5.6µm/20uN/10000 cycles

Figures 5.18 (a) and (b) show scanning electron microscope (SEM) images of discrete tracks after reciprocal wear testing at an oblique angle of 37 degrees to the track directions. We observe that the damage of the worn surface is more severe than at zero degrees, i.e., discrete tracks can be damaged more easily during reciprocal sliding if the direction of sliding is not parallel to the track direction.

Figure 5.19 shows the variation of the coefficient of friction as a function of wear cycles. We observe that the friction coefficient increases as a function of the number of cycles for the discrete track surface, while the coefficient of friction remains constant on the smooth surface. The increase in the friction coefficient is found to occur earlier for the oblique sliding case.

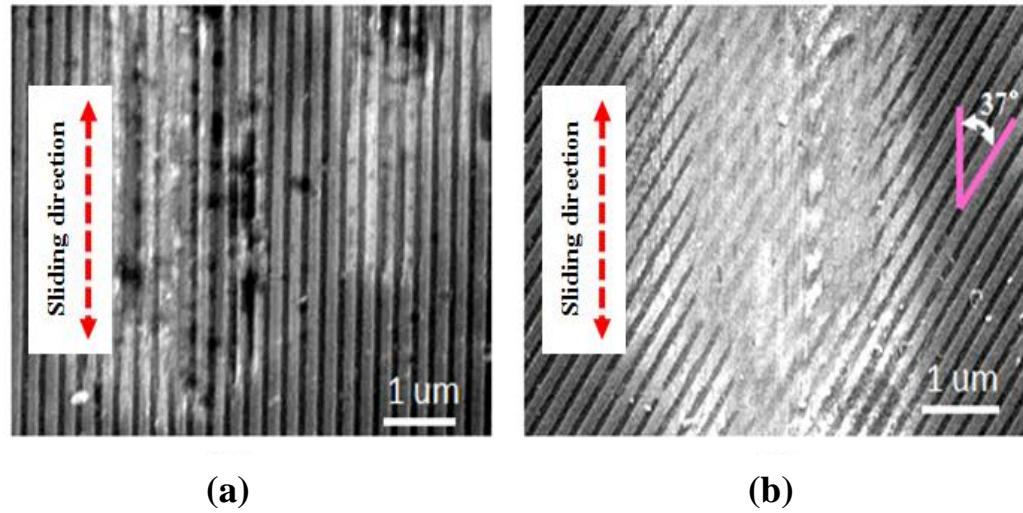


Figure 5.18 SEM images of wear of discrete track region for different sliding directions; (a) zero degrees and (b) 37 degrees

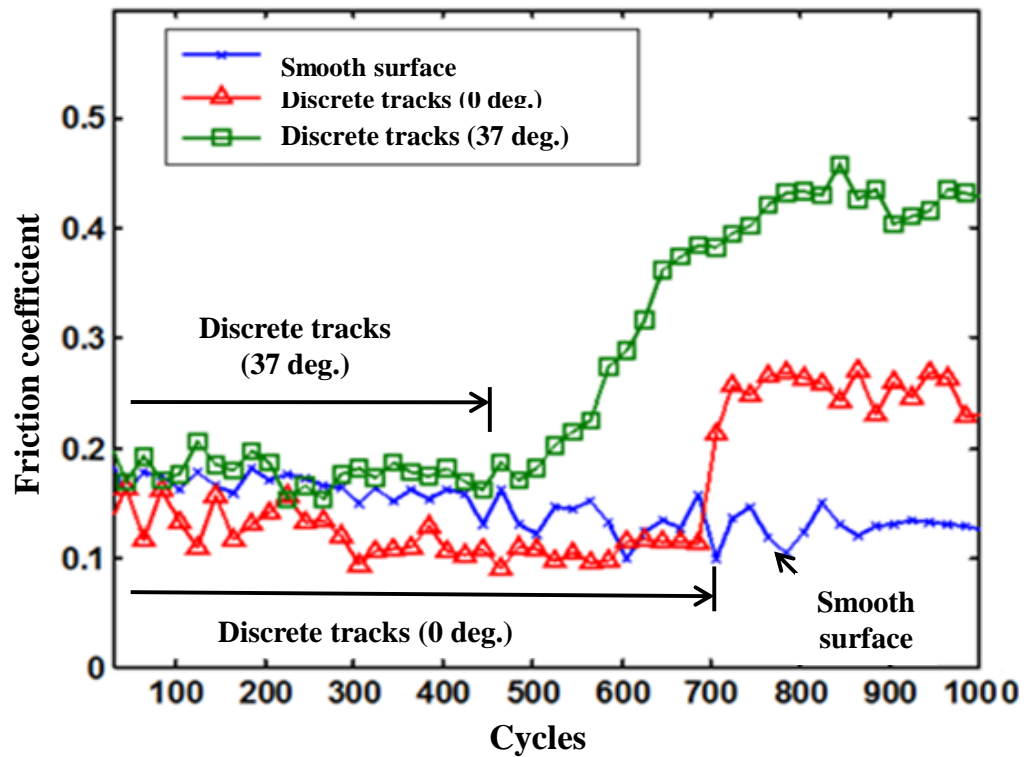


Figure 5.19 Friction coefficient as a function of cycles on smooth surface and discrete tracks at 5Hz/5.6μm/10mN/1000 cycles

Figure 5.20 (a) shows the Raman spectrum of a diamond like carbon (DLC)

coated disk before wear testing. Figures 5.20 (b) and (c) show the Raman spectra of wear particles found on the discrete track disk and the smooth disk, respectively. The Raman spectrum before the reciprocal wear testing shows peaks at approximately 1567 cm^{-1} and at 1386 cm^{-1} , respectively, commonly referred to as the G band (sp^2) and D band (sp^3) (Figures 5.20 (a)) [19]. A slight shift of the peaks is observed in Figures 5.20 (b) and (c) (1600 cm^{-1} and 1360 cm^{-1}) for the Raman spectra of the wear particles.

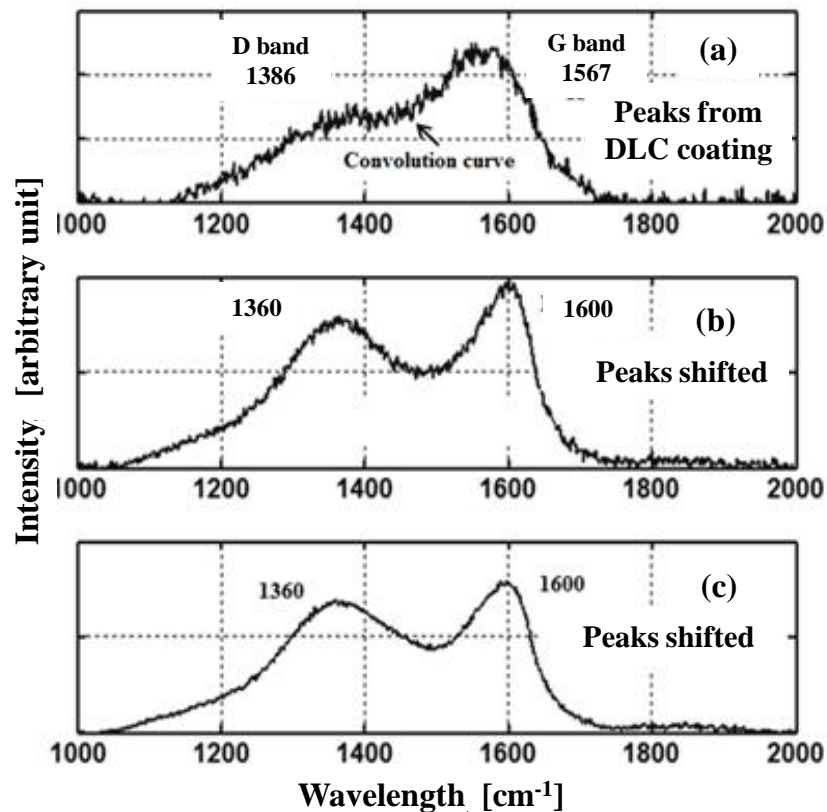


Figure 5.20 Raman spectra of (a) DLC film before reciprocal wear testing in the smooth disk area and the discrete track surface, (b) wear particles from the discrete track surface and (c) wear particles from the smooth disk area

Figures 5.21 (a), (b) and (c) show the Raman spectra of the spherical wear probe. We observe that peaks are absent (Figure 5.21 (a)) on the bare spherical wear

probe before reciprocal wear testing. However, the Raman spectra after reciprocal wear testing show two peaks at the same wavelengths (Figures 5.21 (b) and (c)).

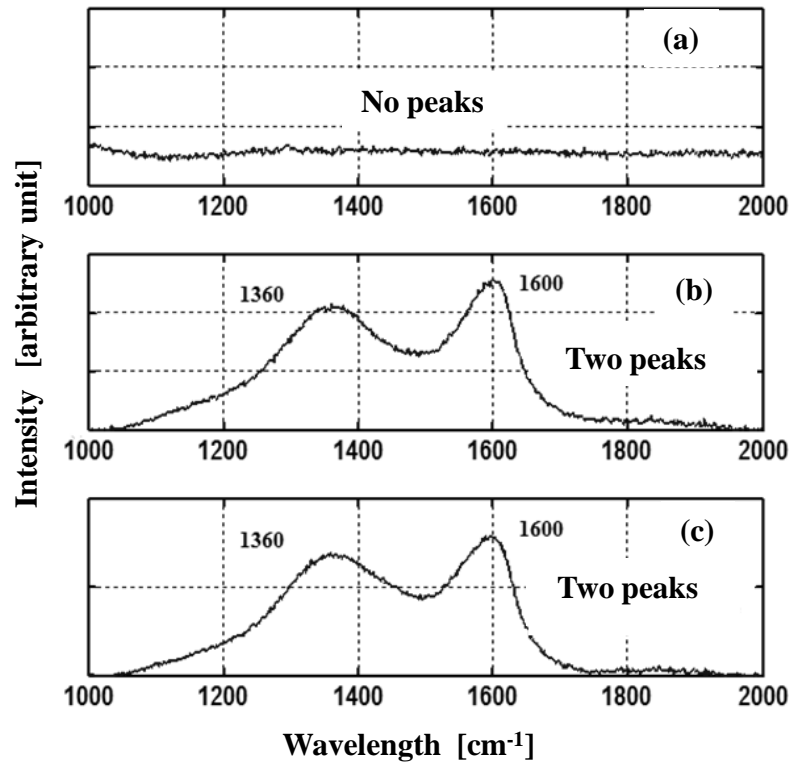


Figure 5.21 Raman spectra on the spherical wear probes (a) before the reciprocal wear testing, (b) tested on the discrete track surface and (c) tested on the smooth disk area

5.4 Numerical investigation of static contact behavior

To evaluate the experimental results, we performed a numerical analysis for the indentation on the discrete track surface. Figures 5.22 (a) and (b) show the schematic of the numerical contact model. In particular, Figure 5.22 (a) show the schematic of contact on a smooth surface, while Figure 5.22 (b) shows contact on a discrete track surface (groove depth = 60 nm and land width=200nm).

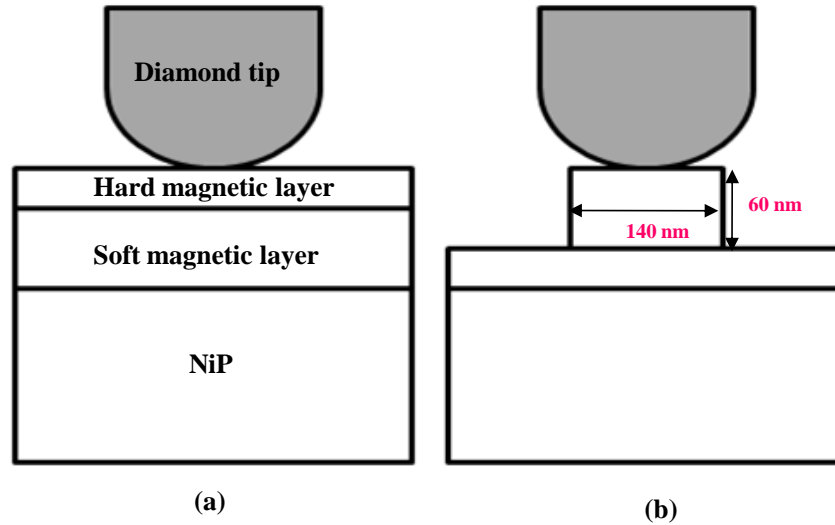


Figure 5.22 Schematics of contact (a) on smooth surface and (c) a discrete track disk (groove depth = 60 nm and land width = 140 nm)

Table 5.2 shows material properties used for the numerical investigation. The thicknesses of hard magnetic, soft magnetic and NiP layers were 20 nm, 60 nm and 200 nm, respectively. Figure 5.23 shows von Mises stress contours for a smooth disk (case 1) and a discrete track disk (case 2). We observe strong stress concentrations at the surface of the discrete track, indicating that yielding of the discrete track is easy to occur. High stress at the corners of the discrete track can cause breakage of the discrete tracks (see Figure 5.8).

Table 5.2 Material properties of a diamond tip and three different layers [21]

	Tip	Hard magnetic layer (20 nm)	Soft magnetic layer (60 nm)	NiP (200 nm)
E (GPa)	1140	150	120	114
Poisson's ratio	0.07	0.3	0.3	0.31
Yield stress(Gpa)	35.7	3.4	3.7	3.0

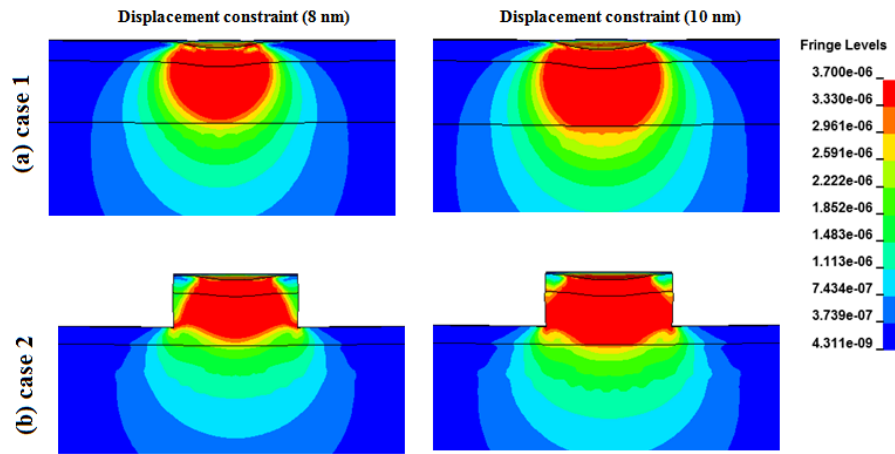


Figure 5.23 Von Mises stress contour on (a) a smooth surface and (b) a discrete track (groove depth = 60 nm and land width = 140 nm) (unit is 10^6 GPa)

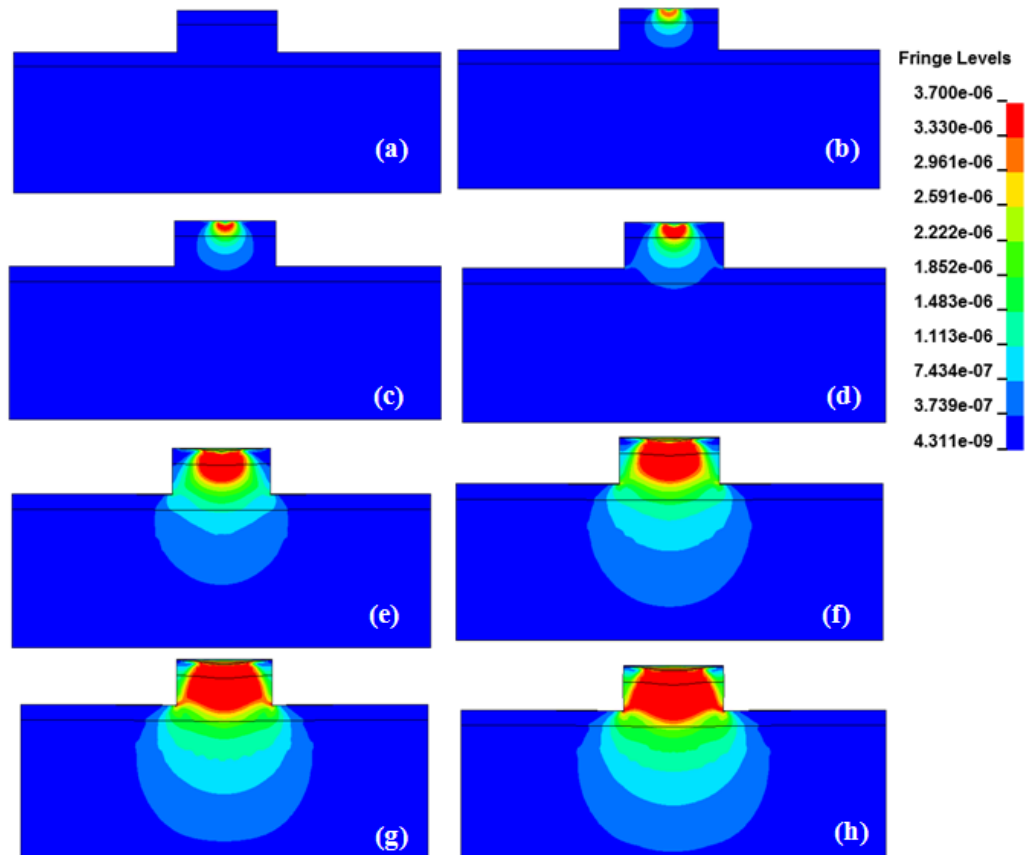


Figure 5.24 Von Mises stress distribution on discrete track (unit is 10^6 GPa)

Figure 5.24 shows von Mises stress distribution in a discrete track as a function of indentation depth. Figure 5.24 (a) shows the undeformed case where contact has not yet occurred. In the initial phase of contact (Figure 5.24 (b) through (c)), the stress distribution is similar to the case of a smooth surface (see Figures 5.23 (a)). However, as the stress is increased, the stress contours increase and reach the corners of the bottom line of the discrete track (see Figure 5.24 (d) through Figure 5.24 (h)). The stress contours and stress distributions were obtained using finite element simulation with LS-DYNA.

5.5 Summary and Conclusions

An experimental investigation of contact deformation and wear characteristics of discrete track and smooth disk surfaces was performed. Damage was found to be much larger in the discrete track areas of the discrete track disks as compared to damage in the smooth areas of the same disks. It is apparent that the stress distribution in the land areas of a discrete track is much higher than the stress distribution in the smooth regions. The latter result is a consequence of the presence of the unsupported edges of the narrow land areas of discrete track disks. These land area showed substantially higher wear and damage than the smooth areas outside the discrete track areas. Numerical calculations are in agreement with experimental observations.

The generation of wear particles in discrete track media increases the possibility of failure of hard disk drives during contacts between slider and disk. Therefore, to improve reliability and durability of discrete track recording media,

contact deformation and wear characteristics of discrete track media must be improved. Planarization of discrete track disks appears to be a necessary step towards improving the tribological properties of discrete track disks [10].

Bibliography

- [1] D. Weller, and A. Moser, "Thermal effect limits in ultrahigh-density magnetic recording," *IEEE Transactions of Magnetism*, vol. 35, pp. 4423-4439, 1999.
- [2] S. J. Greaves and H. Muraoka, "Discrete track media for 600 Gbits/in² recording," *Journal of Applied Physics*, vol. 99, pp. 08F903, 2006.
- [3] D. Wachenschwanz, W. Jiang, E. Roddick, A. Homola, P. Dorsey, B. Harper, D. Treves and C. Bajorek, "Design of a manufacturable discrete track recording medium," *IEEE Transactions of Magnetism*, vol. 41, no.2, pp. 670-675, 2005.
- [4] J.-Y. Juang, D. B. Bogy and C. S. Bhatia, "Design and dynamics of flying height control slider with piezoelectric nanoactuator in hard disk drives," *Journal of Tribology*, vol. 129, pp. 161-170, 2007.
- [5] K. Komvopoulos, "Head-disk interface contact mechanics for ultrahigh density magnetic recording," *Wear*, vol. 238, pp. 1-11, 2000.
- [6] R.-H. Wang, V. Nayak, F.-Y. Huang, W. Tang and F. Lee, "Head-disk dynamics in the flying, near contact, and contact regimes," *Journal of Tribology*, vol. 123, pp. 561-565, 2001.
- [7] H. Kohira, H. Tanaka, M. Matsumoto and F. E. Talke, "Investigation of slider vibrations due to contact with a smooth disk surface," *Transactions of the ASME*, vol. 123, pp. 616-623, 2001.
- [8] J. Xu, H. Tokisue, H. Tanake and M. Matsumoto, "Contact vibration of micro-textured sliders," *Journal of Tribology*, vol. 124, pp. 281-287, 2002.
- [9] Z.-Q. Gong, K. Komvopoulos, "Effect of surface patterning on contact deformation of elastic-plastic layered media," *Transactions of the ASME*, vol. 125, pp. 16-24, 2003.
- [10] E. E. Nunez, C.-D. Yeo, R. R. Katta, and A. Polycarpou, "Effect of planarization on the contact behavior of patterned media," *IEEE Transactions on Magnetism*, vol.44, no. 11, pp. 3667-3670, 2008.
- [11] Z. Jiang, C.-J. Lu, D. B. Bogy, C.S. Bhatia, T. Miyamoto, "Nanotribological characterization of hydrogenated carbon films by scanning probe microscopy," *Thin Solid Films* vol. 258, pp. 75-81, 1995.
- [12] E. V. Anoinin, M. M. Yang, J. L. Chao, J. R. Elings, D. W. Brown, "Nanoscale

scratch resistance of ultrathin protective overcoats on hard magnetic disks,” *J. Vac. Sci. Technol. A*, vol. 16, pp. 1741-1744, 1998.

- [13] X. Li and B. Bhushan, “Micro/nanomechanical and tribological characterization of ultrathin amorphous carbon coatings,” *J. Mater. Res.*, vol. 14, no. 6, pp. 2328-2337, 1999.
- [14] S. Sundararajan, B. Bhushan, “Micro/nanotribology of ultra-thin hard amorphous carbon coatings using atomic force/friction force microscopy,” *Wear*, pp. 225-229, 1999.
- [15] M. Bai, K. Kato, N. Umehara, Y. Miyake, J. Xu, H. Tokisue, “Scratch-wear resistance of nanoscale super thin carbon nitride overcoat evaluated by AFM with a diamond tip,” *Surface and Coatings Technology*, vol. 126, pp. 181-194, 2000.
- [16] B. Bhushan, *Handbook of Micro/Nano Tribology 2nd edition*, CRC press LLC, pp. 433-524, 1999.
- [17] L.-Y. Huang, K.-W. Xu, J. Lu, B. Guelorget, H. Chen, “Nano-scratch and fretting wear study of DLC coatings for biomedical application,” *Diamond and Related Materials*, vol. 10, pp. 1448-1456, 2001.
- [18] B. Bhushan, “Nano-to microscale wear and mechanical characterization using scanning probe microscopy,” *Wear*, vol. 251, pp. 1105-1123, 2001.
- [19] G. Irmer and A. Dorner-Reisel, “Micro-Raman studies on DLC coatings,” *Advanced Engineering Materials*, vol. 7, no. 8, pp. 694-705, 2005.
- [20] A. A. C. Recco, C. C. Viafara, A. Sinatora and A. P. Tschiptschin, “Energy dissipation in depth-sensing indentation as a characteristic of the nanoscratch behavior of coatings,” *Wear*, vol. 267, pp. 1146-1152, 2009.
- [21] A. Ovcharenko, M. Yang, K. Chun and F. E. Talke, “Simulation of magnetic erasure due to transient slider-disk contacts,” *IEEE Transaction on magnetic*, vol. 46, pp. 770-777, 2010.

Chapter 6

Wettability, Adhesion and Friction Force of Discrete Track Recording Media

In this chapter, wettability, adhesion and friction of nano-sized discrete track areas are measured and compared with conventional smooth surfaces. Video contact angle (VCA) measurements were taken to determine the wettability of nano-sized discrete track disks as a function of time. Adhesion of nano-sized discrete tracks was determined using atomic force microscopy (AFM). A contact start-stop (CSS) tester with a strain gauge was used to investigate the friction force between the slider and the disk interface.

6.1 Introduction

Tribological phenomena that occur at the interface between a slider and a disk in hard disk drives (HDDs) pose a continuing challenge to researchers as they push the limits of increasing area density. At the nano-scale level, it is important to reduce surface forces, such as adhesion and stiction, to achieve optimal operation. Two issues that deserve close attention are the effect of humidity on the surface and adhesion. Humidity and deposition of a microscopic water film on the surface of a disk is a particular problem of interest because humidity is a very common source of increased stiction and friction forces at the interface between two bodies during sliding contact. Many researchers have studied the effect of humidity and adhesion at the head and disk interface (HDI) [1-4]. Liu [5] and Wang [6] introduced laser textured disks as a way of reducing stiction and friction forces on media. Xu [7], Zhou [8] and Fu [9] proposed textured sliders to reduce friction forces on the slider. Shukla et al. [10] examined water absorption on lubricated carbon over-coated surfaces. Water absorption can cause corrosion and abrasion of the magnetic media that can ultimately lead to failure of disk drives. Strom [11] and Ma [12] found that the presence of condensed water between the slider and the disk interface changes the air-bearing pressure and influences the flying height of the slider. In addition, they found that the thickness of absorbed water films on the slider and disk surfaces increases exponentially with relative humidity. Brunner, Etsion, Khurshudov, Tyndall and Talke [13-14] have reported a calibration method and the measurements of the contact angle for a direct measurement of surface energy using an atomic force microscope (AFM).

In this chapter, we have investigated the tribological effects of discrete patterned media. Wettability of water on discrete track recording (DTR) media was studied as a function of time. To measure the adhesion force, we have used an atomic force microscope (AFM). In addition, friction forces were obtained using CSS testing. Figures 6.1 (a) and (b) show the cross-section of smooth and discrete track recording disks, respectively.

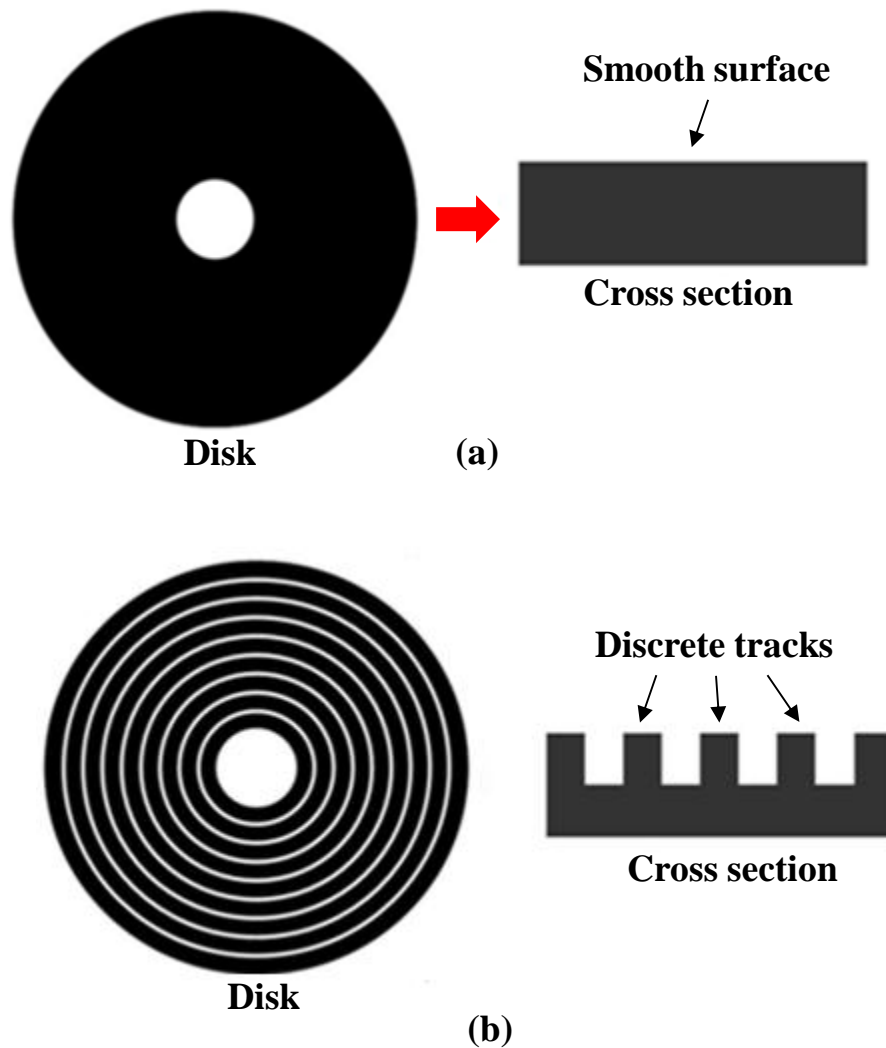


Figure 6.1 Schematic of (a) smooth and (a) DTR disks

6.2 Theoretical background

6.2.1 Contact angle with rough surfaces

As the size of micro/nano-devices becomes smaller and smaller, surface forces become increasingly more important, and adhesion and stiction continue to challenge the proper operation of these devices. A micro-patterned roughness combined with hydrophobic coatings has been suggested to satisfy the need for a non-adhesive and water-repellent surface [15]. Wetting leads to an increase in adhesion and friction due to the formation of menisci at the interface between solid bodies during sliding contact. For those conditions, wet friction can be greater than dry friction [16].

The primary parameter that characterizes wetting is the static contact angle formed by a liquid (water) with a solid [17, 18]. If the static contact angle of a liquid with a surface is in the range of $0^\circ \leq \theta \leq 90^\circ$, the surface is referred as a hydrophilic surface. On the other hand, if the value of the contact angle is in the range of $90^\circ < \theta \leq 180^\circ$, the surface is hydrophobic. In particular, surfaces with a contact angle between 150° and 180° are called superhydrophobic. Surfaces with high contact angle have low surface energy and low wettability (see Figures 6.2 (a) and (b)).

One way to change the wetting properties of a surface consists of adjusting the surface roughness. In 1936, Wenzel found that the overall contact angle of a liquid on a rough surface is different from that on a smooth surface (see Figure 6.5)

[19]. Later on, in 1944, Cassie and Baxter discovered that air pockets trapped in the cavities of a rough surface create a composite solid-liquid-air interface (see Figure 6.5 (c)) instead of a homogeneous solid-liquid interface (see Figure 6.5 (b)) [20]. Nosonovsky and Bhushan demonstrated an extreme increase in the contact angle by increasing the surface roughness. They also discussed stability and the transition of the wetting regimes from a composite solid-liquid-air interface to a homogeneous solid-liquid interface [15].

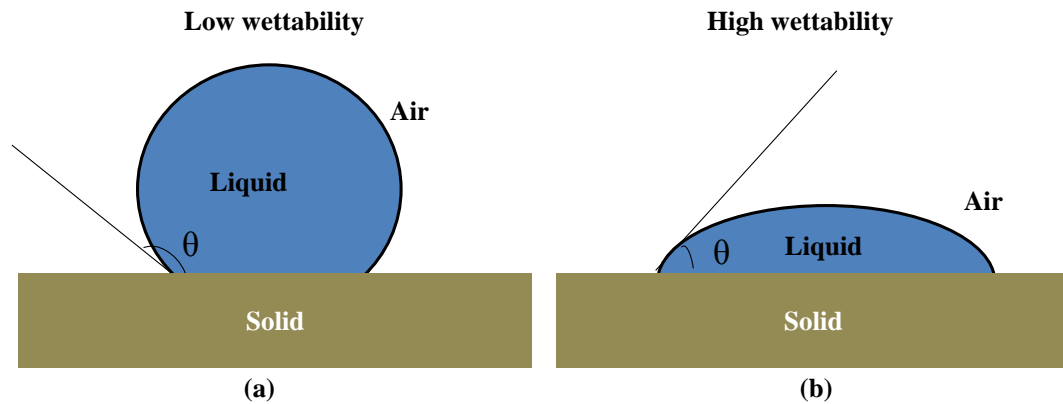


Figure 6.2 Schematic of (a) low wettability and (b) high wettability

6.2.1.1 Static contact angle

The value of the static contact angle is determined by surface tensions (see Figure 6.3). The well known Young equation is given by

$$\cos(\theta_0) = \frac{\lambda_{SA} - \gamma_{SL}}{\gamma_{LA}} \quad (6.1)$$

where θ_0 is the static contact angle, and λ_{SA} , λ_{SL} and λ_{LA} are surface tensions of the solid against air and liquid, and the liquid against air, respectively.

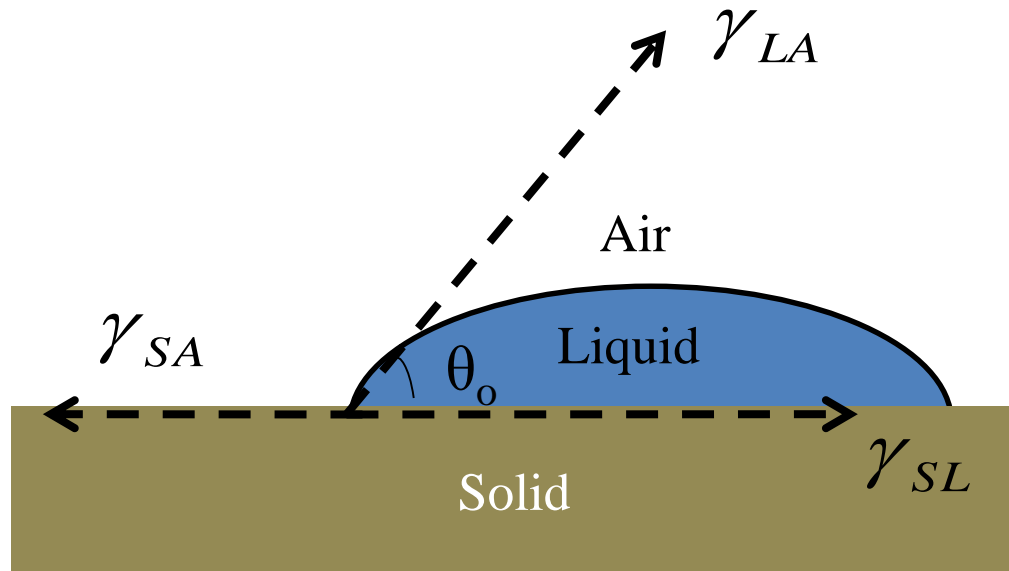


Figure 6.3 Schematic of static contact angle

6.2.1.2 Contact angle with rough and homogeneous surfaces

When a liquid completely wets a rough surface, the interface is said to be in the Wenzel state as shown in Figure 6.5 (b). In this case, the analytical contact angle is obtained by the Wenzel equation. The Wenzel equation derives the contact angle (θ) of a water droplet upon a rough solid surface with the static contact angle (θ_0) upon a smooth surface using the surface roughness factor R_f , which is defined as the ratio of the total homogeneous surface area (A_{SL}) to its flat projection area (A_F). The following equation is the Wenzel equation for rough and homogeneous surfaces.

$$\cos(\theta) = R_f \cos(\theta_0) \quad (6.2)$$

$$R_f = \frac{A_{SL}}{A_F} \quad (6.3)$$

Figure 6.4 shows the two-dimensional periodic discrete tracks. In this case, the roughness factor R_f is calculate as

$$R_f = \frac{A_{SL}}{A_F} = \frac{2h + t}{t} \quad (6.4)$$

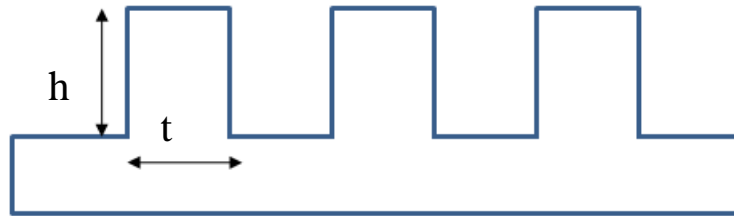


Figure 6.4 Two-dimensional periodic discrete tracks

6.2.1.3 Contact angle with rough and composite interfaces

A composite interface with air pockets trapped in the rough surface is called a Cassie or Cassie-Baxter interface as shown in Figure 6.5 (c). The surface is not completely wetted. In this case, the contact angle with a rough and composite interface is given by

$$\cos(\theta) = R_f f_{SL} \cos(\theta_0) - f_{LA} \quad (6.5)$$

where f_{SL} and f_{LA} are fractional flat areas of the solid-liquid and liquid-air interfaces under the droplet, respectively.

For the case of high R_f , equation (6.5) predicts f_{SL} approaches zero while f_{LA} approaches unity. Theoretically, the contact angle (θ) with rough and composite interfaces will become 180° .

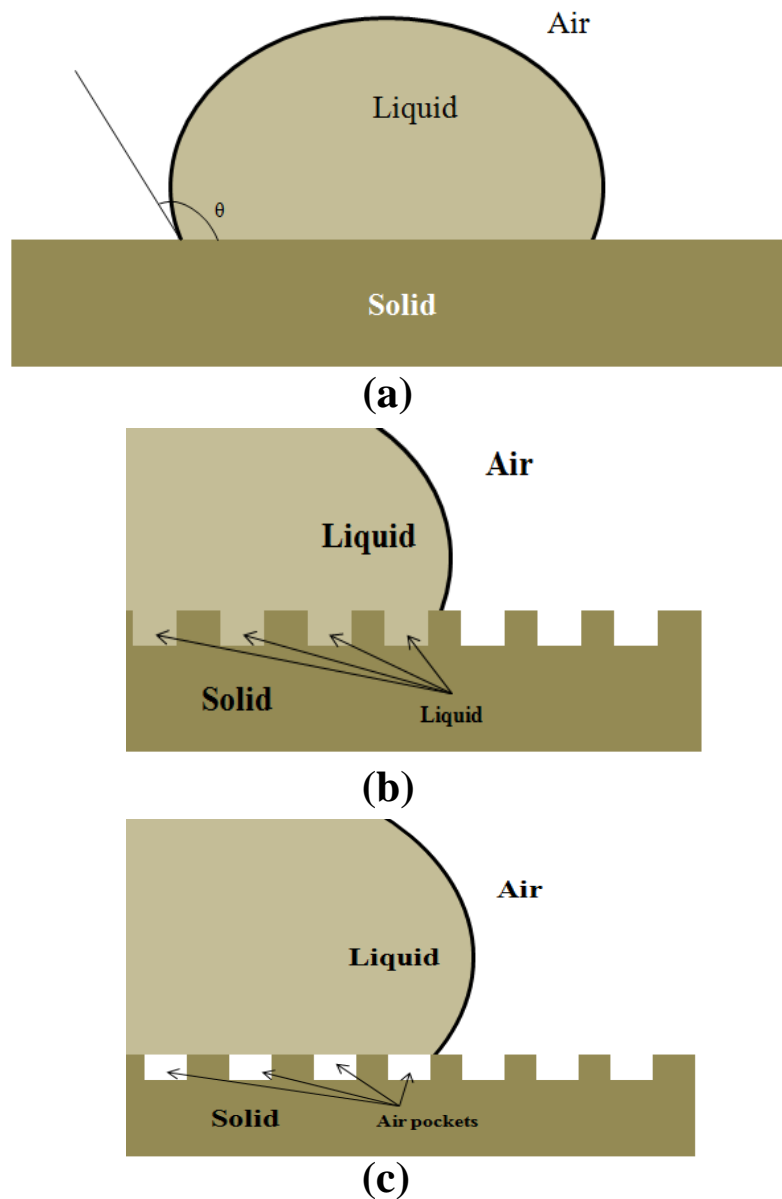


Figure 6.5 (a) Schematic of a water droplet on a smooth surface, (b) schematic of the Wenzel state for the homogeneous interface and (c) schematic of the Cassie or Cassi-Baxter state for the composite interface with air pockets

6.2.1.4 Spreading of a liquid

A liquid will spread until it reaches minimal surface energy and the contact angle decreases during this process. Shuttleworth and Bailey studied the spreading of a liquid over a rough solid surface [21]. They found that the spreading of a liquid over a rough surface of a solid is a complex phenomenon. Semal et al. studied the influence of surface roughness on wetting dynamics and found that the rate of droplet spreading slows with an increase in micro-roughness [22]. Figure 6.6 shows a schematic of spreading progress of a liquid (water) over solid surfaces. As spreading proceeds, the radius of the droplet increases, but the contact angle decreases.

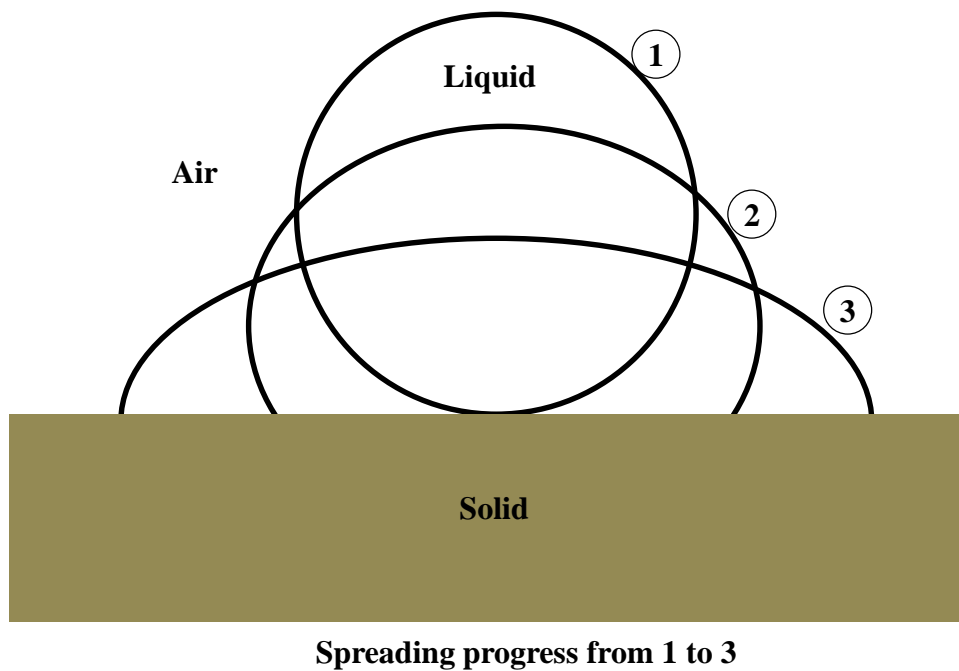


Figure 6.6 Schematic of spreading progress

6.2.2 Adhesion measurements

In the field of hard disk drives (HDDs), the understanding of adhesion and friction is important to further increase the areal density. The fundamental mechanisms of friction and adhesion are presently not well understood, and the relevant parameters and processes involved are still unknown.

Various experimental approaches such as an atomic force microscopy (AFM) [24] and surface forces apparatus (SFA) [25] have been used to determine nano-tribological properties of interfaces. Grierson and Carpick [26] have shown that continuum contact mechanics is applicable to nano-tribology measurements.

6.2.2.1 Contact mechanics model for adhesive force

Heinrich Hertz first introduced the theory of the contact mechanics in 1882 [27]. He determined that a normal load P between a flat plane and a sphere pressed against the plane creates a contact radius a according to the following equation:

$$P = \frac{Ka^3}{R} \quad (6.5)$$

where R is the radius of the sphere, and

$$K = \frac{4}{3} \left(\frac{1-\nu_1^2}{E_1} + \frac{1-\nu_2^2}{E_2} \right)^{-1},$$

E_1, E_2 are Young's moduli of sphere and flat plane, and ν_1, ν_2 are Poisson ratio of the sphere and flat plane, respectively. The Hertz theory is applicable only to fully elastic contacts without considering attractive surface forces (adhesion).

In 1971, Johnson, Kendall and Roberts (JKR) [28] introduced a new theory accounting for adhesion between two elastic bodies. In the JKR theory, contact is considered to be adhesive. In particular, two more properties are measured: a non-zero contact area at zero load and a minimum load that results in a non-zero contact area. This minimum load is called the pull-off force and is given by

$$F_{P(JKR)} = -\frac{3}{2}\pi\gamma R \quad (6.6)$$

where γ ([N/m]) is the adhesion.

Derjaguin, Muller and Toporov (DMT) [29] introduced an improved theory to include van der Waals forces outside the elastic contact regime, which give an additional load. Hence, in the DMT theory, the pull-off force is given by

$$F_{P(DMT)} = -2\pi\gamma R \quad (6.7)$$

6.2.2.2 Atomic force microscopy (AFM) methodology

To determine the interfacial adhesion, atomic force microscopes (AFM) are extensively used as a quantitative tool.

Figure 6.7 shows the schematic of a pull-off force measurement with an atomic force microscope (AFM) [14, 26]. The following steps must be taken. First,

the atomic force microscope (AFM) tip approaches the surface (a) and then snaps onto it (b). This results in a contact force (c). A retracting force is then applied to the tip which pulls the tip off the surface (d). The force at which the tip-surface junction breaks is known as the pull-off force.

Finally, the tip returns to its starting position (e).

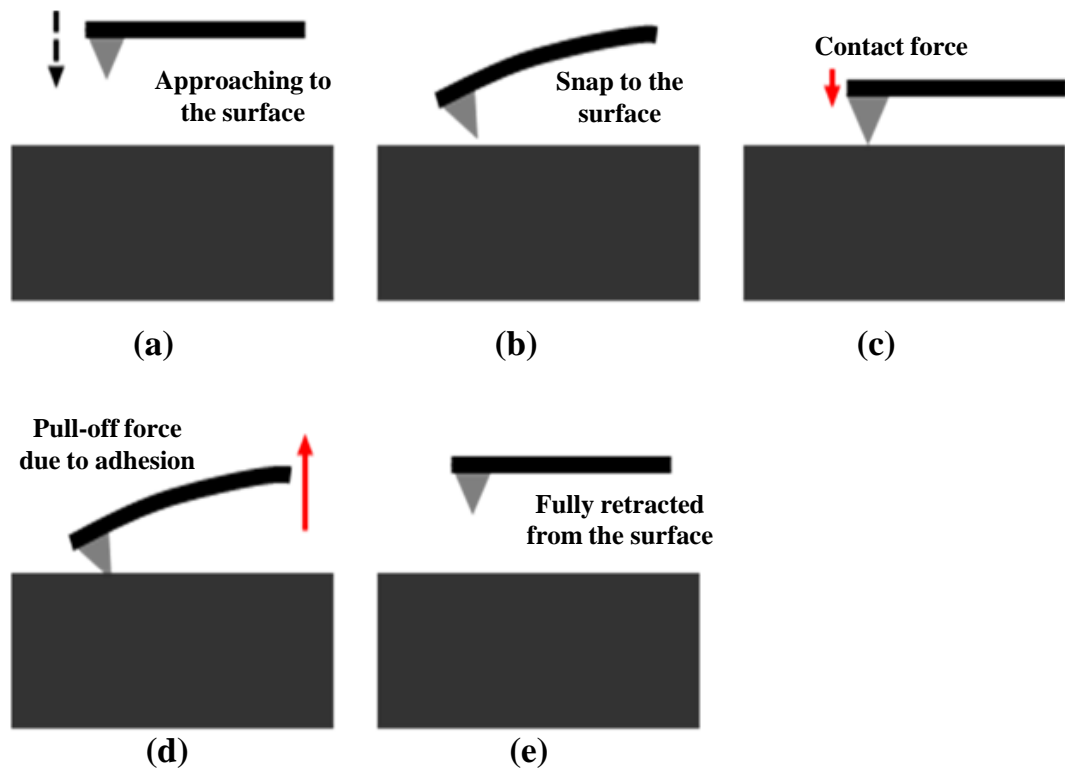


Figure 6.7 Schematic of pull-off force measurement with AFM; (a) approach, (b) snap to the surface, (c) apply contact force, (d) retract from the surface (pull-off force), and (e) fully back to original position

6.2.2.3 Adhesion based on contact mechanics modeling

When the pull-off force (P) is obtained from an atomic force microscopy (AFM), equations (6.6) and (6.7) can be rearranged and then the adhesion (γ) can be quantified by

$$\gamma = -\chi \frac{P}{\pi R} \quad (6.8)$$

where χ is equal to 2/3 for the JKR model and 1/2 for the DMT model, respectively [26].

6.3 Specimen preparation

A schematic of the cross section of a DTR disk and its corresponding scanning electron microscopy (SEM) image are shown in Figures 6.6 (a) and (b), respectively. DTR media are geometrically characterized by the groove depth (D), the land width (L) and the track pitch (P). Nano-imprint lithography (NIL) was used to manufacture the DTR media.

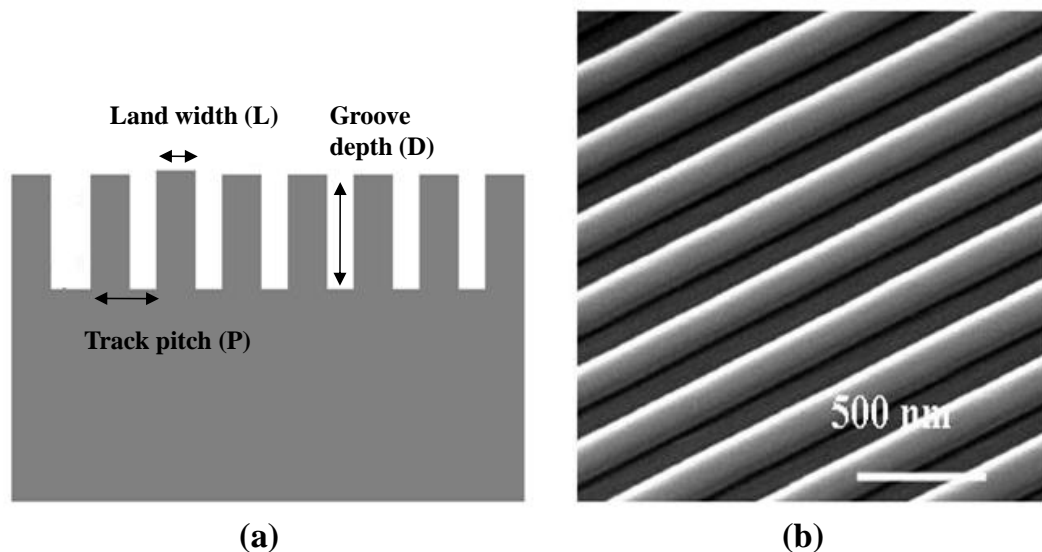


Figure 6.8 (a) Schematic of the cross section of a DTR disk and (b) a scanning electron microscopy (SEM) image of discrete tracks

6.4 Contact angle measurements

Table 6.1 shows the parameters of various DTR media that were used for our experiments. Figures 6.9 and 6.10 are scanning electron microscopy (SEM) images corresponding to Table 6.1. The discrete track disk with a 20 nm groove depth showed good flyability as shown in chapters 3 and 4; however, in the case of a 40 nm groove depth, the slider did not fly at all.

Table 6.1 Configurations of DTR media

Groove depth	20 nm	40 nm
case 1 (L/P)	0.81	0.67
case 2 (L/P)	0.79	0.58
case 3 (L/P)	0.50	0.48

Groove depth 20 nm

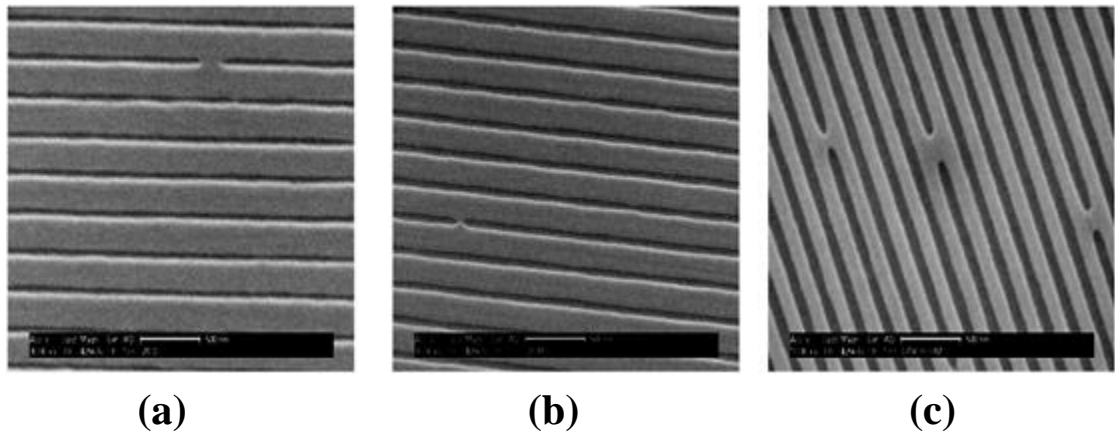


Figure 6.9 SEM images of 20 nm grooved discrete tracks with respect to different ratios of land with (L)/track pitch (P); (a) $L/P = 0.81$, (b) $L/P = 0.79$ and (c) $L/P = 0.50$

Groove depth 40 nm

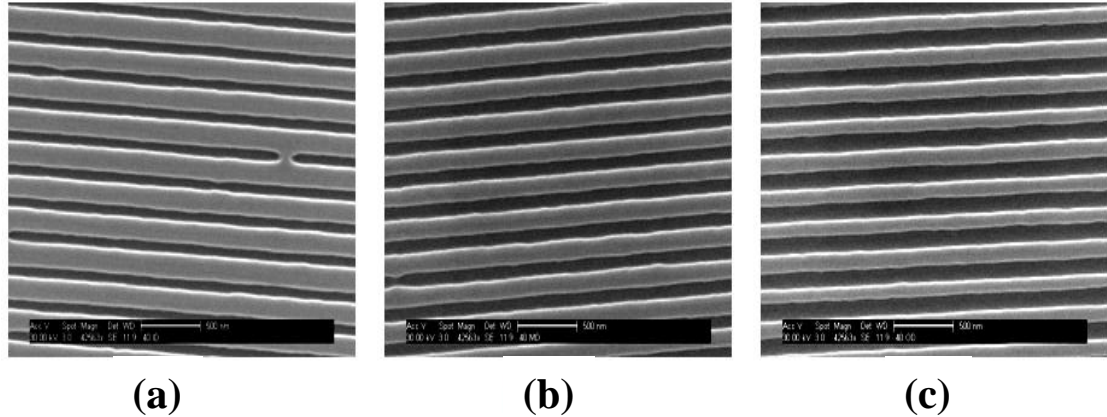


Figure 6.10 SEM images of 40 nm grooved discrete tracks with respect to different ratios of land with (L)/track pitch (P); (a) $L/P = 0.67$, (b) $L/P = 0.58$ and (c) $L/P = 0.48$

For the contact angle measurements, the drop volume was kept constant at $0.5 \mu\text{l}$. Figures 6.11 (a) and (b) show typical contact diameters and contact angles on smooth surface areas and discrete track areas, respectively. The contact diameter and contact angle are measured parallel to the direction of the discrete tracks using video contact angle (VCA) equipment. Each measurement was performed after the spreading of the water drop has slowed down to zero, i.e., after equilibrium was reached. We observe that the contact angle of the water drop is larger for the discrete track media compared to the smooth surface, and that the wetted surface is smaller than in the case of the smooth disk.

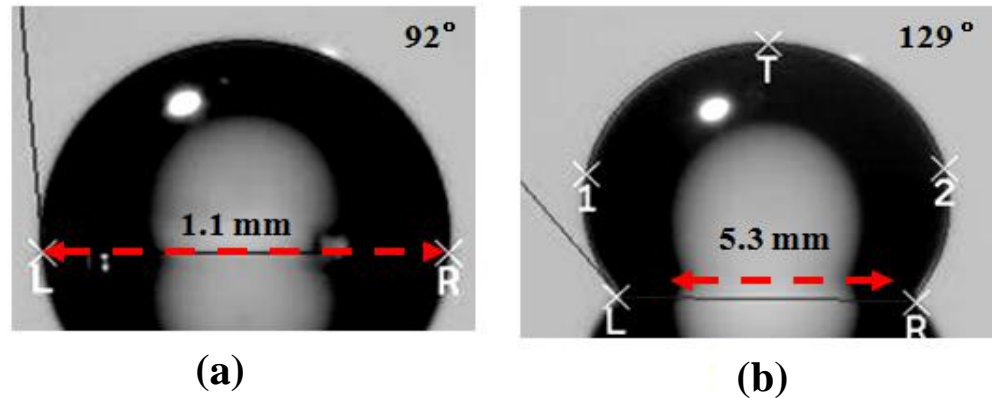


Figure 6.11 Contact angle and contact diameter (a) on smooth surface area and (b) discrete track area

Figure 6.12 (a) shows the contact angle when the water drop is first placed on the discrete track area with a 20 nm groove depth ($L/P=0.5$), whereas Figure 6.12 (b) shows the contact angle after spreading reached equilibrium. From Figure 6.10 we observe that the change in the contact angle before and after spreading was approximately 17%. In addition, the contact diameter was found to increase by 20%. Figure 6.13 shows the contact diameter of a drop of deionized (DI) water as a function of time for smooth surfaces and three different discrete track disks with groove depths of 20 nm. We note that the diameter of the drop is much larger for the smooth surface than for the discrete track disk, and that spreading of the water drop on the smooth disk surface is less pronounced than on the discrete track disk. In addition, we observe that the initial contact diameter of the water drop decreases if the area ratio between land width and track pitch is decreased.

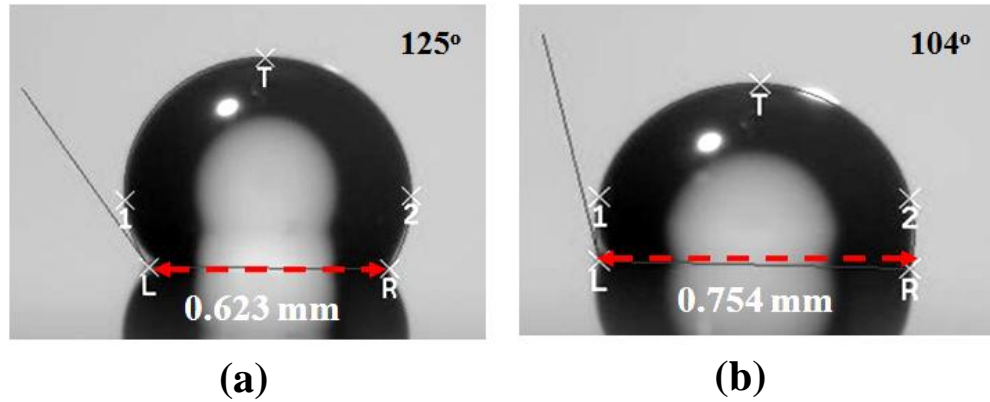


Figure 6.12 Before spreading occurred and (b) after spreading reached equilibrium

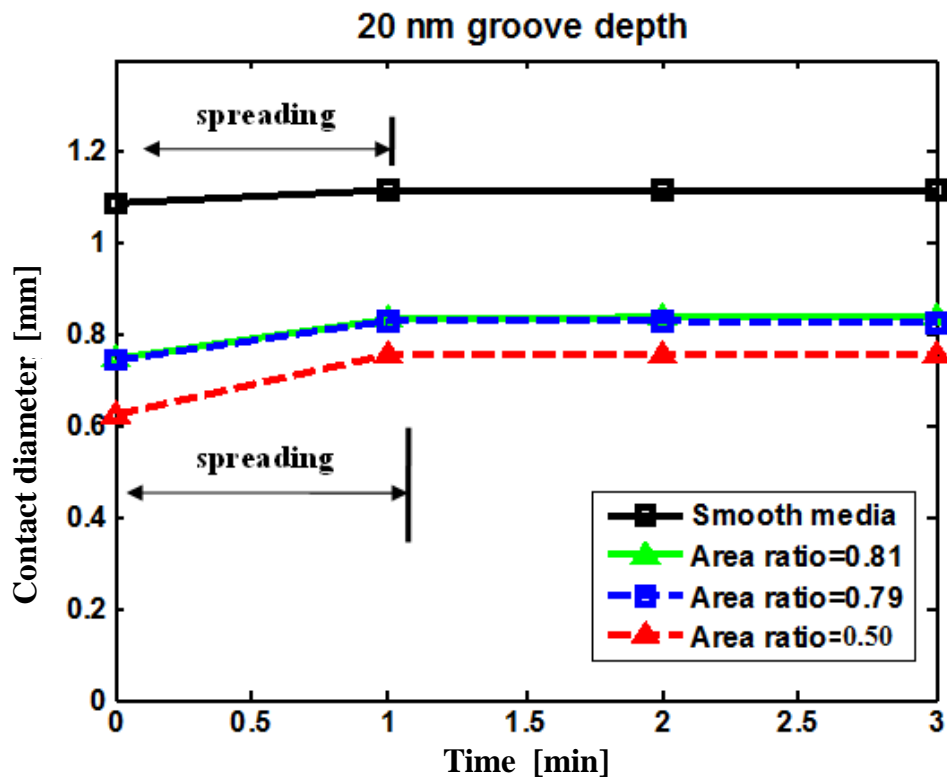


Figure 6.13 Comparison of spreading of water on smooth surface and discrete track disk

Figures 6.14 (a) and (c) show the initial and final contact angle of a water drop over the discrete track of a discrete track recording (DTR) disk with a groove depth of 40 nm ($L/P = 0.48$). We observe that the change of contact angle before and after

spreading was approximately 6%, i.e., the change was much smaller than for the case of 20 nm groove depths. In addition, the change of the contact diameter was 5%. Figure 6.15 shows the contact diameter of a drop of deionized (DI) water as a function of time for a smooth surface and three different discrete track disks with groove depths of 40 nm. Similar to the case of the 20 nm groove depths (see Figure 6.13), we observe that the initial diameter of the drop is much smaller for the discrete track area than for the smooth surface. However, spreading of the drop on the discrete track disks with a groove depth of 40 nm is much less than on the discrete track areas with a groove depth of 20 nm.

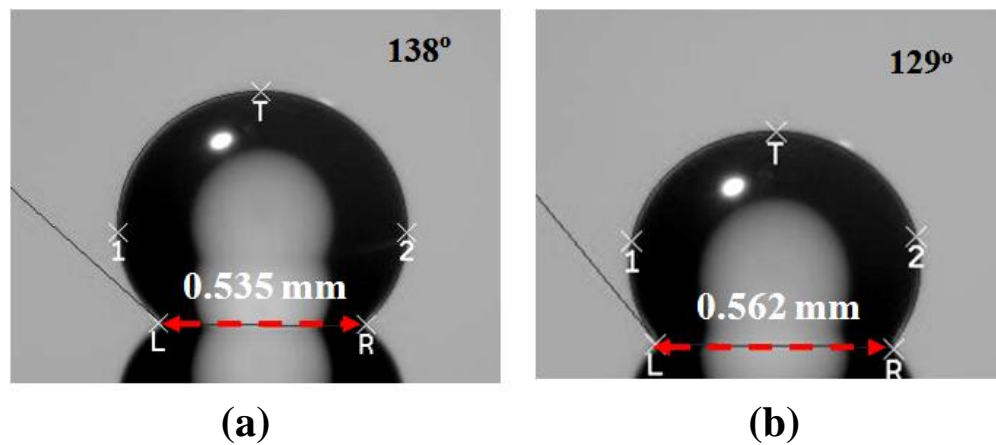


Figure 6.14 Contact angle (a) at the first moment of spreading and (b) after spreading reached equilibrium

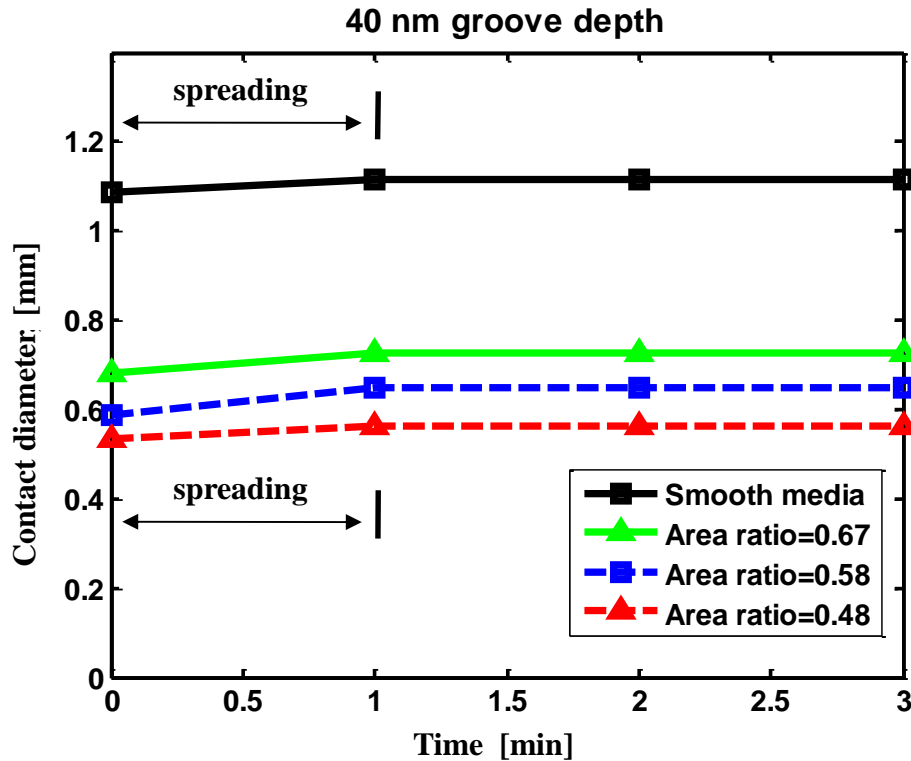
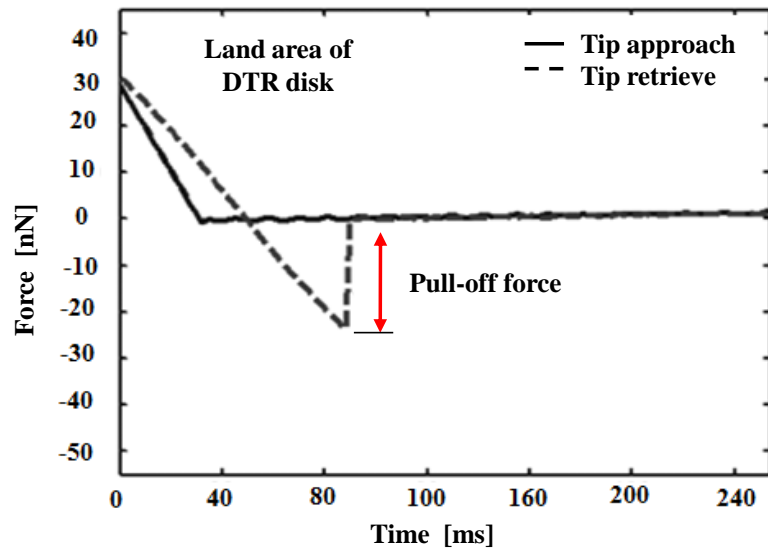


Figure 6.15 Comparison of spreading of a water drop on a smooth surface and discrete track disks with groove depths of 40 nm and different ratio of L/P

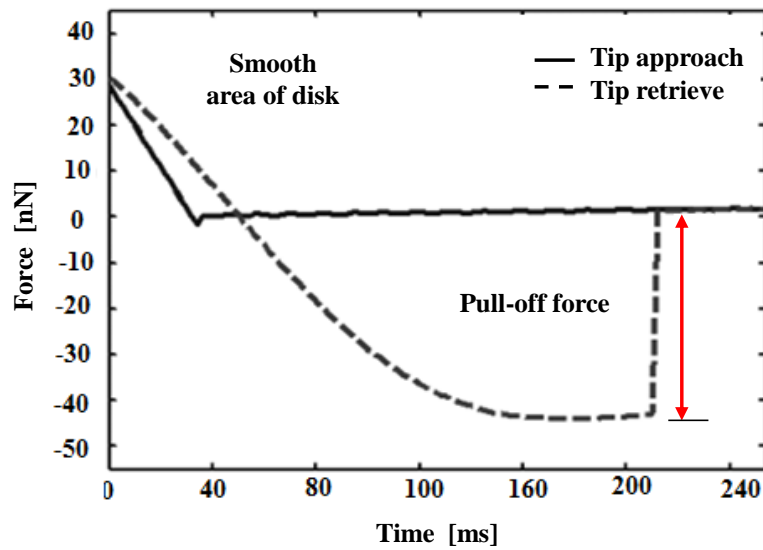
6.5 Adhesion measurements with atomic force microscopy (AFM)

Typical atomic force microscopy (AFM) force curves for the land area of a discrete track disk and the smooth surface of a disk are shown in Figure 6.16. To measure the pull-off force in the land area of a discrete track disk, the tip was placed at the center of the discrete track. A positive force means that the atomic force microscope (AFM) tip is pressed against the surface as a contact load. A negative force means that adhesion keeps the two surfaces in contact while the atomic force microscope (AFM) tip tries to separate the surface in response to an applied pull-off force. We observe a large difference in the pull-off force between the smooth

surface and the land area of the discrete track disk. The pull-off force was observed to be larger on the smooth surface (Figure 6.16 (b)) than on discrete tracks (Figure 6.16 (a)) due to higher adhesion on the smooth disks.



(a)



(b)

Figure 6.16 Typical pull-off force curves (a) on land area of discrete track disk and (b) on smooth surface of disk

To investigate the effect of adhesion in pull-off force measurements, we repeated the experiments with atomic force microscope (AFM) tips of various radii. Figures 6.17 (a) and (b) show a discrete track area of 182 nm land width and 380 nm track pitch and the smooth surface on the same disk, respectively. Discrete tracks have a reduced surface area which is proportional to the ratio of land width to track pitch. The root mean square (RMS) values of surface roughness were 0.22 nm on the smooth surface and 0.42 nm on the land area of the discrete track.

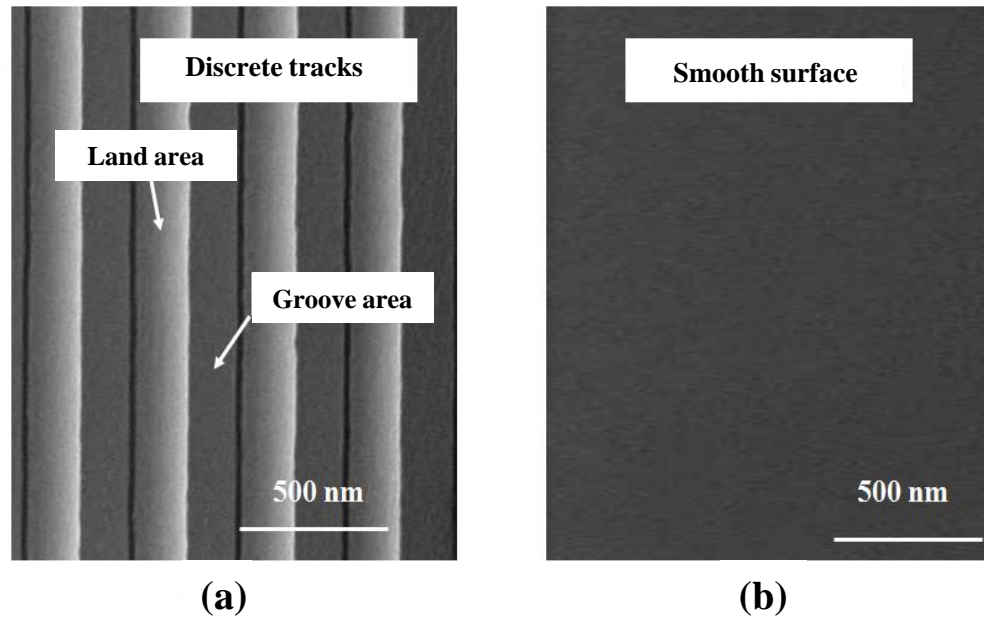


Figure 6.17 SEM images of (a) discrete tracks and (b) smooth surface

To determine the radii of atomic force microscopy (AFM) tips, we have used a scanning electron microscopy (SEM). Figure 6.18 shows typical scanning electron microscopy (SEM) images of the atomic force microscopy (AFM) tips used. Tips A, B and C have diameters of 21 nm, 120 nm and 350 nm, respectively.

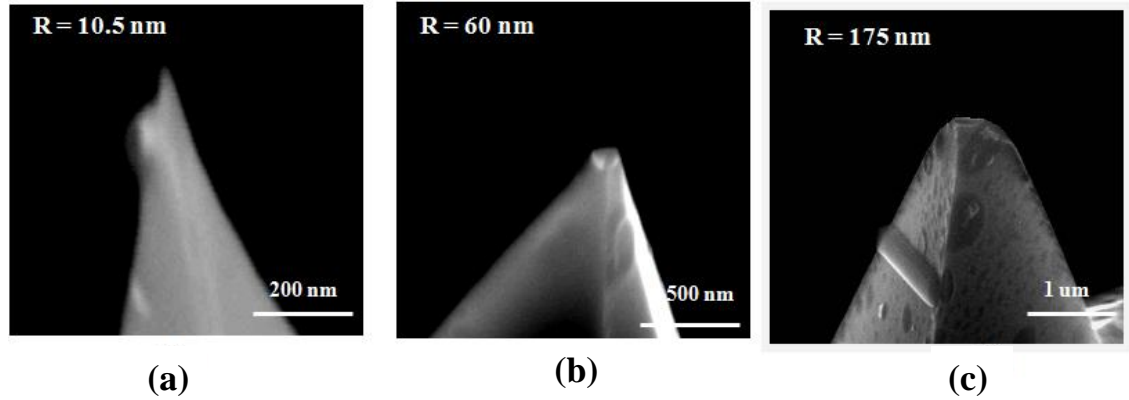


Figure 6.18 SEM images of various diameters of AFM tips; (a) tip radius = 10.5 nm, (b) tip radius = 60 nm and (c) tip radius = 175 nm

Tips A and B have diameters smaller than the land width of the discrete tracks, whereas the diameter of tip C is larger than the land width. Pull-off forces on the smooth surface and the discrete tracks with tip A, B and C are summarized in Figure 6.19. Pull-off forces are found to be larger on the smooth surfaces than on the discrete track area.

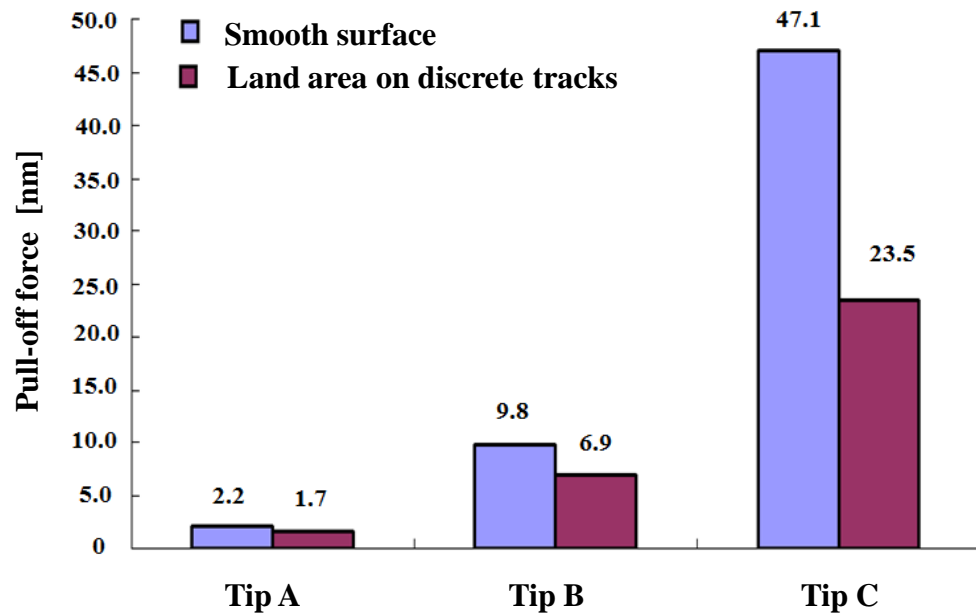


Figure 6.19 Pull-off force measurement with various tip diameter of AFM on smooth surface and discrete tracks (land width = 182 nm and track pitch = 380 nm)

Based on pull-off force measurements in Figure 6.19, adhesion can be determined from equation (6.8) (see Figure 6.20). The values of adhesion showed qualitatively good agreement with adhesion measurements obtained by He [30] using a pin-on-disk test and contact angle measurement by Brunner [15]. As can be seen in Figure 6.20, adhesion in the land area of the discrete track disks investigated is approximately 25% less than that of smooth surfaces using the JKR or DMT model.

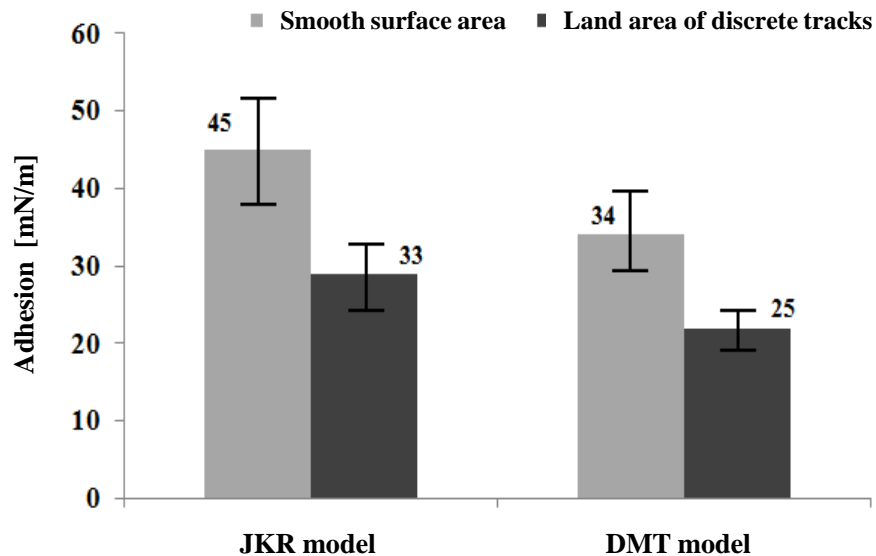


Figure 6.20 Comparison of adhesion on smooth surface and land area on discrete tracks based on the JKR and DMT models

6.6 Friction force measurement using contact start-stop (CSS) test

Contact start-stop (CSS) tests were conducted to examine the effect of adhesion on discrete track recording (DTR) media. The experimental setup is shown in Figure 6.21. A strain gauge was attached to the clip holding the head and gimbal assembly (HGA). Figure 6.22 indicates the velocity profile used during the

CSS tests. In the first five seconds, the rotational speed of the disk was increased from zero to 7200 revolutions per minute (RPM). The rotational speed was maintained at 7200 revolutions per minute (RPM) for the following six seconds. The disk was then decelerated to zero in the next four and one half seconds. All measurements were performed during the first four seconds.

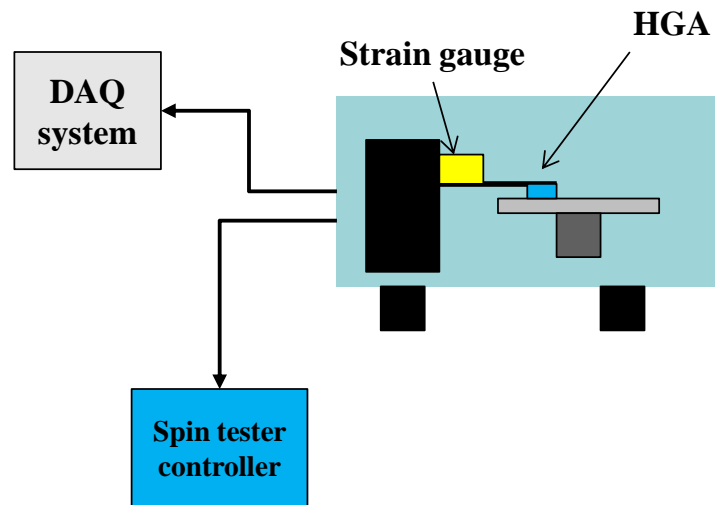


Figure 6.21 Schematic of experimental setup

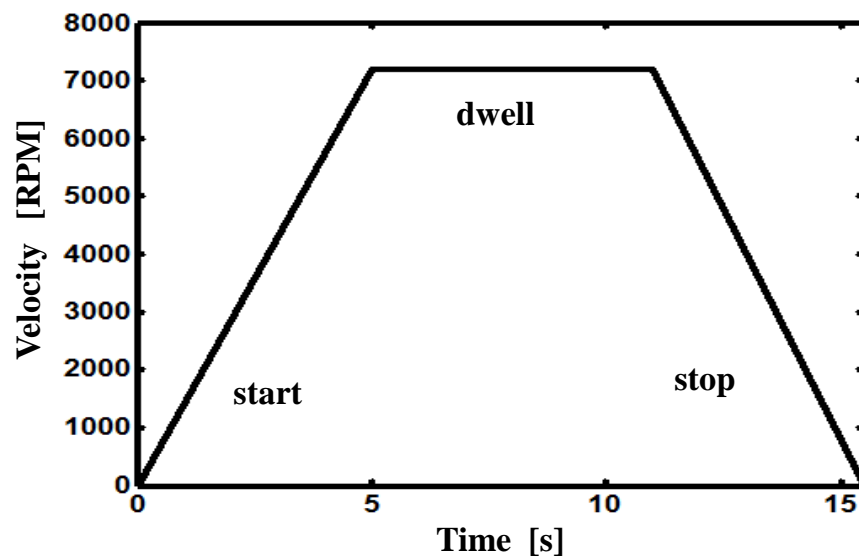


Figure 6.22 Velocity profile for contact start-stop (CSS) test

In these experiments, the sliders used were designed to fly at a flying height of 20 nm on smooth media at a velocity of 22 m/s. A smooth disk and two different DTR disks A ($D = 20$ nm, area ratio = 0.66) and B ($D = 30$ nm, area ratio = 0.58) were used. To evaluate the effect of adhesion force between slider and disk, every measurement was performed at the start of the CSS test. The head and gimbal assembly (HGA) was placed at a radius of 27 mm on the disk with a $+ 10^\circ$ skew angle and a normal load of 30 mN.

Figure 6.23 shows the friction force measurements as a function of time during a CSS test. The static friction (stiction) measured at the initial moment of rotation of the disk was found to be much larger on a smooth disk (see Figure 6.23 (a)) than on discrete track recording (DTR) media (see Figures. 6.23 (b) and (c)). This is due to the high adhesion as shown in Figure 6.20 on smooth surfaces. However, we observe that the slider “takes off” later on discrete track recording (DTR) media than on smooth media due to the reduced air bearing pressure over the grooved areas.

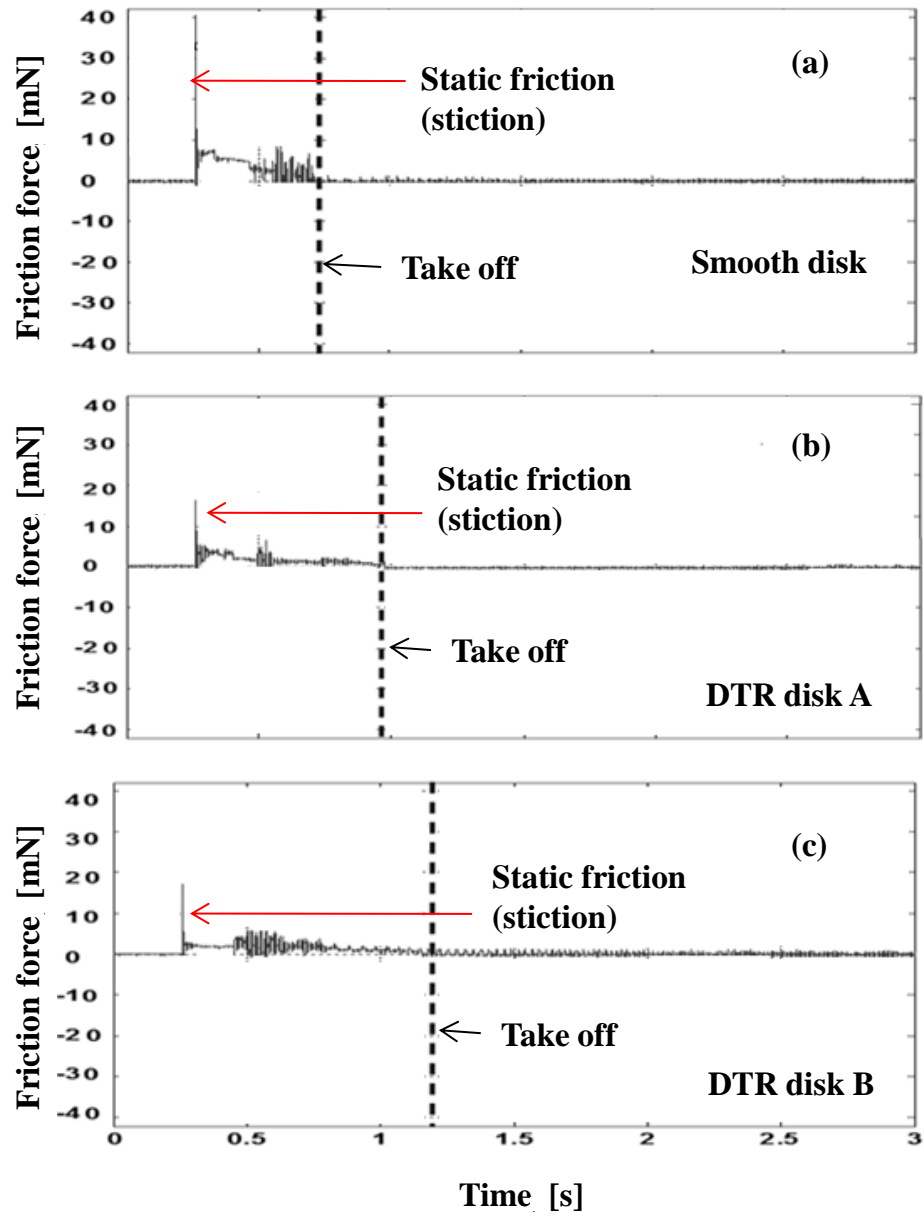


Figure 6.23 Typical friction forces versus time; (a) on a smooth disk, (b) on DTR disk A, and (c) on DTR disk B

6.7 Summary and Conclusions

Wettability, adhesion and friction force of discrete track recording (DTR) media were experimentally investigated and compared with smooth media. Discrete track recording (DTR) media show lower wettability than smooth media. Atomic force microscopy (AFM) was used to obtain the adhesion over the land area of discrete tracks and over smooth surfaces. We found that the land area of discrete tracks experiences lower adhesion than smooth surfaces. From contact start-stop (CSS) testing, static friction (stiction) was found to be much smaller on discrete track recording (DTR) disks than on a smooth disk.

Bibliography

- [1] J. Gui, "Tribology Challenges for Head-Disk Interface Toward 1 Tb/in²," *IEEE Trans. Mag.*, vol. 39, pp. 716-721, 2003.
- [2] F. E. Talke, "On tribological problems in magnetic disk recording technology," *Wear*, vol. 190, pp. 232-238, 1995.
- [3] A. K. Menon, "Interface tribology for 100 Gb/ in² , *Tribology International*," vol. 33, pp. 299-308, 2000.
- [4] A. Khurshudov, R. J. Waltman, "Tribology challenges of modern magnetic hard disk drives," *Wear*, vol. 251, pp. 1124-1132, 2001.
- [5] J. J. Liu, "Optimization of Laser Texture for the head disk interface," *IEEE Trans. Mag.*, vol. 33, no. 5, 1997.
- [6] R.-H. Wang, V. Raman, P. Baumgart, A. M. Spool and V. Deline, "Tribology of laser textured disks with thin overcoat," *IEEE Trans. Mag.*, vol. 33, no. 5, 2007.
- [7] J. Xu, H. Tokisue, H. Tanaka, and M. Matsumota, "Contact vibrations of micro-textured sliders," *J. Tribol.*, vol. 124, pp. 281-287, 2002.
- [8] L. Zhou, K. Kato, G. Vurens, F. E. Talke, "The effect of slider surface texture on flyability and lubricant migration under near contact conditions," *Tribology International*, vol. 36, pp. 269-277, 2003.
- [9] T.-C. Fu and S. Suzuki, "Low stiction/low glide height head-disk interface for high-performance disk drives," *J. of Appl. Physics*, vol. 85, pp. 5600-5605, 1999.
- [10] N. Shukla, A. J. Gellman, X. Ma and J. Gui, "Effect of humidity on lubricated carbon overcoats," *Tribo. Lett.*, vol. 12, pp. 105-109, 2002.
- [11] B. D. Strom, S. Zhang, S. C. Lee, A. Khushudov and G. W. Tyndall, "Effects of humid air on air-bearing flying height," *IEEE Trans. Mag.*, vol. 43, pp. 3301-3304, 2007.
- [12] Y. Ma and B. Liu, "Further Study of the Effect of water vapor on slider air bearing," *IEEE Trans. Mag.*, vol. 45, pp. 5006-5009, 2009.
- [13] R. Brunner, I. Etsion and F. E. Talke, "A simple AFM calibration method for direct measurement of surface energy on nano-structured surfaces covered with

- molecularly-thin liquid films”, *Rev. Sci. Instrum.*, vol. 80, pp. 055109 - 055109-5, 2009.
- [14] R. Brunner, A. Khurshudov, G. W. Tyndall and F. E. Talke, “Adhesion between surfaces separated by molecularly thin perfluoropolyether films”, *Tribo. Lett.*, published online, 2010.
- [15] M. Nosonovsky and B. Bhushan, “Roughness-induced superhydrophobicity: a way to design non-adhesive surfaces,” *J. of Physics : Condens. Matter*, vol. 20, pp. 225009 (30PP), 2008.
- [16] B. Bhushan and M. Nosonovsky, “Scale effects in dry and wet friction, wear and interface temperature,” *Nanotechnology*, vol. 15, pp. 749-61, 2004.
- [17] J. N. Israelachvili and M. L. Gee, “Contact angles on chemically heterogeneous surfaces,” *Langmuir*, vol. 5, pp. 288-2889, 1989.
- [18] R. E. Johnson and R. H. Dettre, “Contact angle hysteresis: Contact angle, Wettability, and Adhesion, adv. Chem. Ser., vol. 43, ed F. M. Fowkes (Washington, DC: American Chemical Society), pp. 112-135, 1964.
- [19] R. N. Wenzel, “Resistance of solid surfaces to wetting by water,” *Industrial and Engineering Chemistry*, vol. 28, pp. 7426–7431, 1936.
- [20] A. Cassie and S. Baxter, “Wettability of porous surfaces,” *Trans. Faraday Soc.*, vol. 30, pp. 546-551, 1944.
- [21] R. Shuttleworth and G. L. J. Bailey, “The spreading of a liquid over a rough solid,” *Discuss. Faraday Soc.*, vol. 3, pp. 16-22, 1948.
- [22] S. Semal, T. D. Blaker, V. Geskin, M. L. de Ruijter, G. Castelein and J. De Coninck, “Influence of surface roughness on wetting dynamics,” *Langmuir*, vol. 15, pp. 8765-8770, 1999.
- [23] A. Lafuma and D. Quere, “Superhydrophobic states,” *Nat. Mater.*, vol. 2, pp. 457-460, 2003.
- [24] R. W. Carpick, PhD Thesis, Department of Physics, University of California at Berkeley, Berkeley, CA, 1997.
- [25] A. M. Homola, J. N. Israelachvili, P. M. McGuigan and M. L. Gee, “Fundamental experimental studies in tribology: The transition from “interfacial” friction of undamaged molecularly smooth surfaces to “normal” friction with wear,” *Wear*, vol. 136, pp. 65-83, 1990.

- [26] D. S. Grierson, E. E. Flatr and R. W. Carpick, "Accounting for the JKR-DMT transition in adhesion and friction measurements with atomic force microscopy," *J. Adhesion Sci. Technol.*, vol. 19, pp. 291-311, 2005.
- [27] K. L. Johnson, "Contact mechanics," Cambridge University Press, Cambridge, 1987.
- [28] K. L. Johnson, K. Kendall and A. D. Roberts, "Surface energy and the contact of elastic solids," *Proc. R. Soc. Lond. A*, vol. 324, pp. 301-313, 1971.
- [29] B. V. Derjaguin, V. M. Muller and Yu. P. Toporov, "Effect of contact deformation on the adhesion of particles," *J. Colloid Interf. Sci.*, vol. 53, pp. 314-326, 1975.
- [30] Y. He, Y. Fujikaa, H. Zhang, K. Fukuzawa and Y. Mitsuya, "Evaluations of tribological characteristics of PFPE lubricants on DLC surfaces of magnetic disks," *Tribology Letters*, vol. 27, pp. 1-11, 2007.

Chapter 7

Planarization of Discrete Track Recording Media to Improve Flyability of Magnetic Recording Sliders

This chapter describes planarization and suggests methods to improve the mechanical properties of discrete track recording media. Discrete track recording (DTR) media which consist of discrete tracks are presently considered a new paradigm to achieve ultra-high areal density in hard disk drives (HDDs). However, due to the presence of the grooves, stable flying of magnetic recording sliders over DTR media is a question of great concern as mentioned previously in chapters 2, 3 and 4. In addition, larger plastic deformation and less wear resistance of discrete track recording media should be improved to perform better than smooth (flat) media for reliable and durable operation of HDDs as described in chapter 5.

In this chapter, planarization of discrete track recording (DTR) media with hydrogen silsesquioxane (HSQ), a non-magnetic material, is investigated. Scanning electron microscopy (SEM) of planarized disks showed very good “gap filling” properties of HSQ in the groove area during the planarization process. Atomic force microscopy (AFM) measurements indicated that the residual groove depth of planarized DTR media decreases with decreasing rotating speed of the disk during spin-coating. Improved flyability of magnetic recording sliders over DTR media was observed after planarization.

7.1 Introduction

The areal density of recording media is approaching the physical limit determined by the “super-paramagnetic effect” [1]. Patterned media such as discrete track recording (DTR) media and bit patterned media (BPM) are promising approaches to achieve even higher storage densities since they offer advantages in terms of signal to noise ratio (SNR) and positioning of read/write heads [2].

Discrete track recording (DTR) media have recently received increased attention [3]. DTR media reduce magnetic “cross-talk” in the radial direction by physically separating adjacent recording tracks from each other [4-5]. Figure 7.1 shows a scanning electron microscopy (SEM) image and a schematic of a cross section of a typical discrete track recording medium. Physically separated tracks are formed by nano-imprint lithography (NIL). Duwensee et al. [6-7] have shown numerically that the flying behaviour of a slider over discrete track media is affected by the presence of the grooves on the disk. In particular, they have proposed that the flying height loss Δh of a slider flying over discrete track media can be determined by $\Delta h = d * \frac{w}{p}$, where d is the groove depth, w is the groove width, and p is the track pitch. From the above studies, it is apparent, that the flying height of a magnetic recording slider decreases if the groove depth increases. In addition, flying height variations are encountered if the groove depth changes as a function of the circumferential position on a single disk or if the groove depth changes from disk to disk. These changes in flying height increase the likelihood that contacts

occur between slider and disk. Wachenschwanz et al. [8] have studied the effect of groove depth and width on the magnetic performance of DTR media. Hong et al. investigated planarization of bit patterned media (BPM) [9]. However, planarization of DTR disks was not included in their study.

In this chapter we investigate planarization of discrete track recording (DTR) media by spin-coating DTR disks with a non-magnetic material, hydrogen silsesquioxane (HSQ) [10-12]. To investigate the tribological performance of HSQ as a function of the spin-coating process parameters, we have varied the rotational speed of the disk during spin-coating between 1000 rotations per minute (RPM) and 4000 rotations per minute. We have measured the residual groove depth of the media before and after spin coating and have investigated the adhesion and hardness of HSQ as a function of the curing temperature and the oxygen plasma treatment time to improve the mechanical properties of HSQ as a filling material in the groove area. Finally, we have studied flyability of a typical pico-type slider before and after planarization.

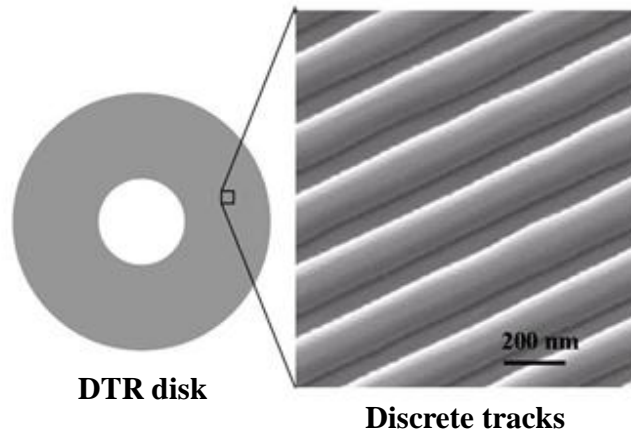


Figure 7.1 SEM image of discrete tracks without planarization

7.2 Procedures and Specimen Preparation

HSQ is a negative resist that can be used to planarize DTR disks. In this study, we have used a two-stage procedure for planarization as described in the following. In the first stage, during the first five seconds, a rotational speed of 500 RPM was used to spread the resist evenly over the sample. In the second stage, the speed was increased to a value between 1000 RPM and 4000 RPM for duration of 40 seconds. After spin coating, the samples were baked on a hotplate at 110°C for 180 seconds to allow vaporization of the solvent in HSQ. To compare flyability of a slider before and after planarization, 3.5 inch DTR disks were used (groove depth = 40 nm, track pitch = 200 nm, and groove width = 110 nm).

7.3 Experimental Procedure

7.3.1 Planarization as a function of disk speed

Low surface roughness and good “gap-filling capability” are essential properties in considering potential planarization materials. Scanning electron microscopy (SEM) images in Figure 7.2 show planarization of discrete track media for rotational speeds from 1000 to 4000 RPM. Figures 7.3 and 7.4 show atomic force microscopy (AFM) images of an original discrete track disk surface (groove depth = 40 nm, track pitch = 200 nm, and groove width = 110 nm) and typical discrete track disk surfaces after planarization.

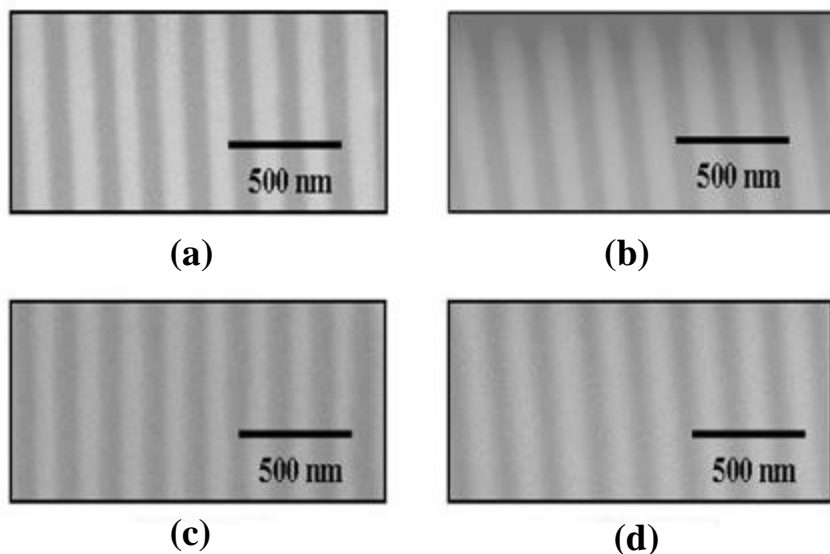


Figure 7.2 Scanning electron microscopy (SEM) images after planarization; (a) 4000 RPM, (b) 3000 RPM, (c) 2000 RPM and (d) 1000 RPM

From the AFM images, we observe that the residual groove depth is a function of the rotational speed during spin-coating. In particular, as the rotational speed of the disk is increased, the residual groove depth was also found to increase. In the case of spin-coating at 4000 RPM (Figure 7.4 (a)), the residual groove depth was found to be 4 nm after planarization. On the other hand, the residual groove depth was 3 and 2.5 nm, in the case of 3000 and 2000 RPM, respectively (Figure 7.4 (b) and Figure 7.4 (c)). The best results with respect to residual groove depth were obtained for a disk speed of 1000 RPM, resulting in a residual groove depth of approximately 0.4 nm (Figure 7.4 (d)).

We have measured the coating thickness of HSQ on control samples using ellipsometry. For a rotational speed of 1000 RPM, the coating thickness was found to be 120 nm on the control sample. For rotational speeds of 2000 RPM, 3000 RPM and 4000 RPM, the coating thickness of the control samples was 100 nm, 89

nm and 83 nm, respectively. An increase in the coating thickness of the control samples was found to correspond to a reduction of the residual groove depths.

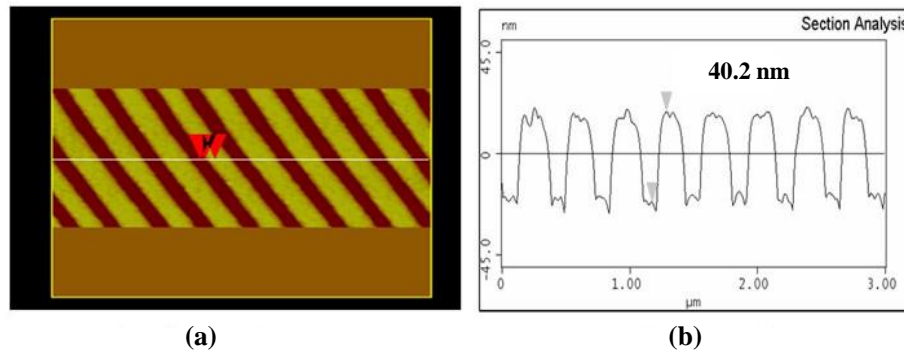


Figure 7.3 Atomic force microscopy (AFM) image of original disk surface; (a) surface image and (b) cross section

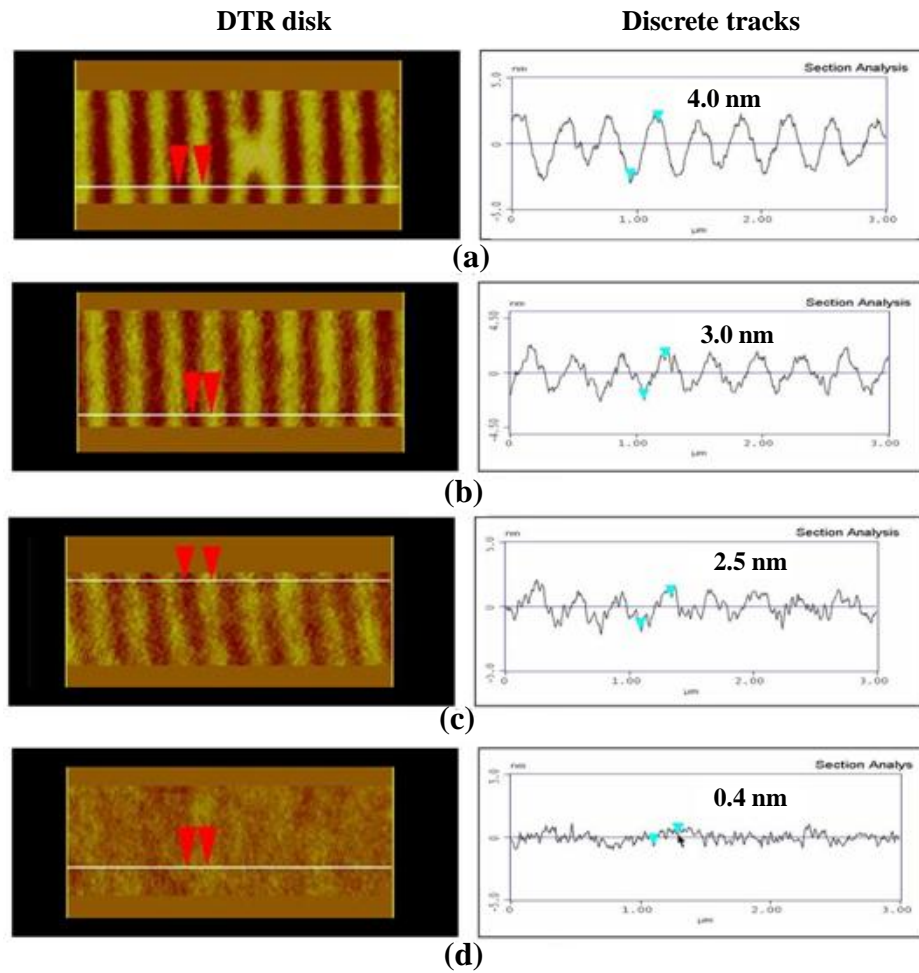


Figure 7.4 Atomic force microscopy (AFM) images after planarization at different RPMs; (a) 4000 RPM, (b) 3000 RPM, (c) 2000 RPM and (d) 1000 RPM

Figure 7.5 shows a schematic representation of a typical planarized disk surface as a function of the rotational speed during spin-coating. We observe that “under-filling” of the discrete tracks is observed if spin-coating is performed at rotational speeds larger than 2000 RPM (Figure 7.5 (a)). On the other hand, no “under-filling” is observed if spin-coating is performed at a disk rotational speed of 1000 RPM as shown in Figure 7.5 (b).

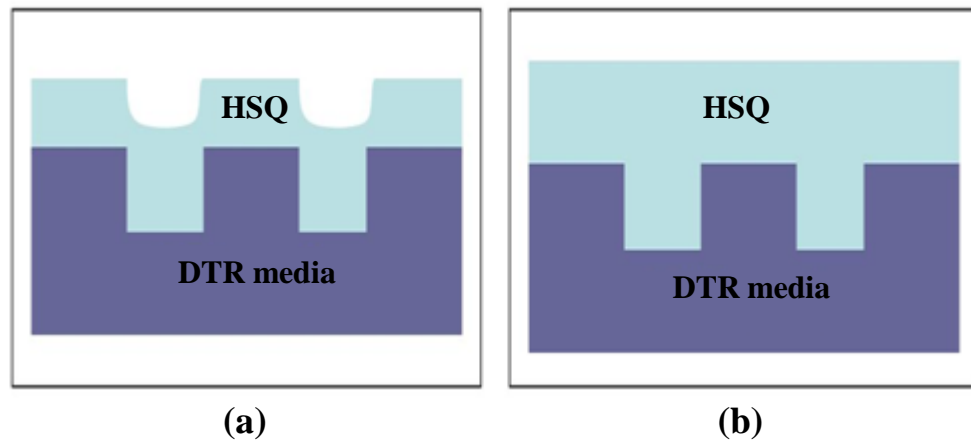


Figure 7.5 Schematic of planarization of discrete track recording media at different RPMs; (a) surface roughness for 2000, 3000 and 4000 RPM and (b) surface roughness for 1000 RPM

Since excess material on top of the disk would increase the magnetic spacing, back-etching of the deposited planarization layer is necessary. Figure 7.6 illustrates the back etching process with reactive ion etching (RIE), to remove excess deposited material on top of the disk. The original groove depth was measured to be 40.2 nm (Figure 7.6 (a)). After planarization the residual groove depth was found to be 4 nm (Figure 7.6 (b)). Excess material was deposited on the top of the disk. After RIE back-etching (Figure 7.6 (c)) for 180 seconds at an etching rate of

0.5 nm/s, we observe that the excess material had been removed from the disk surface, and that HSQ fills the groove area.

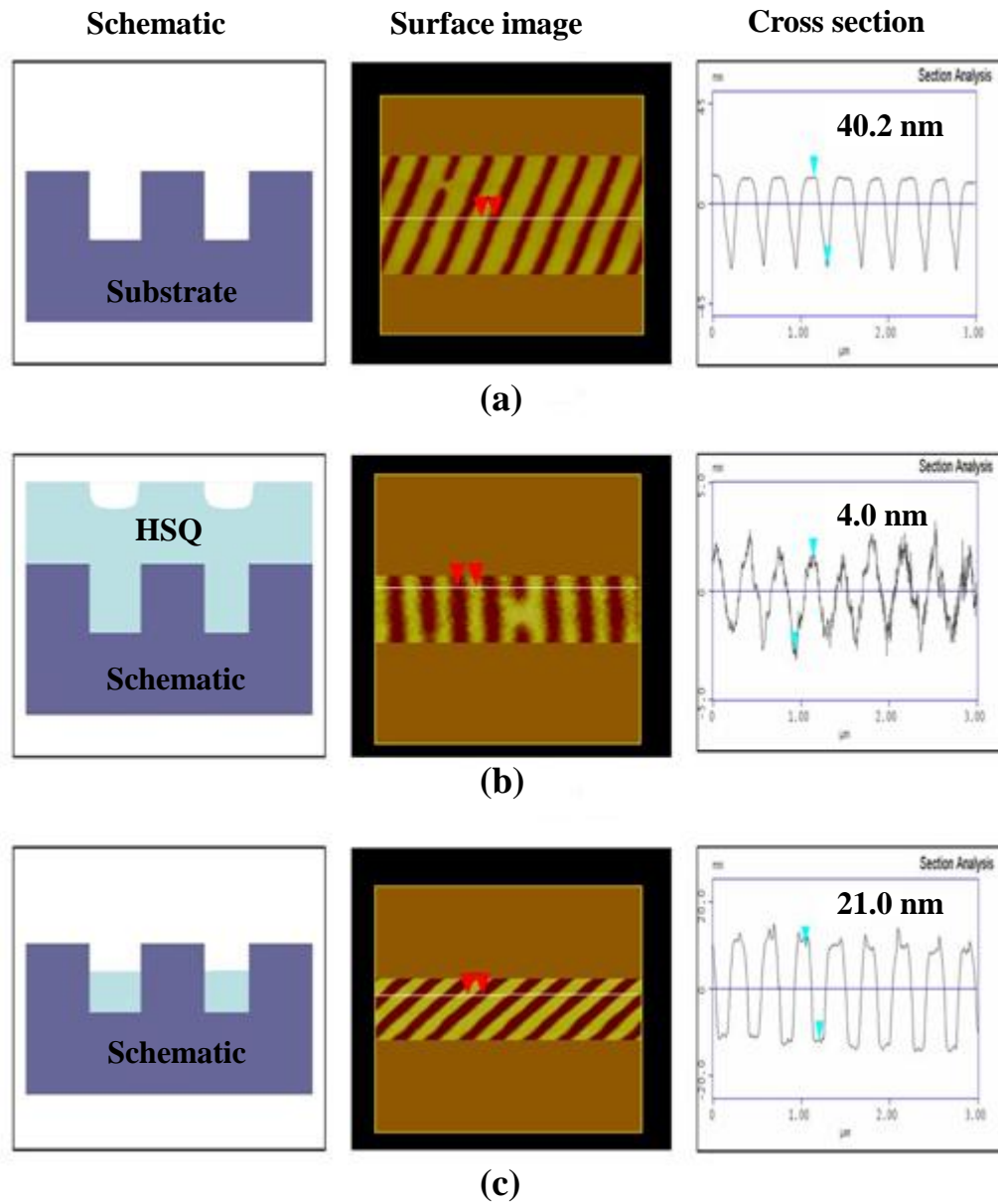


Figure 7.6 Typical back etching with RIE; (a) before spin-coating, (b) after spin-coating with 4000 RPM and (c) after back etching process

7.3.2 Adhesion studies of HSQ

HSQ is mechanically soft material with a “cage” structure. HSQ can be transformed into a mechanically strong network structure by thermal and oxygen plasma treatment [10-12]. To improve adhesion of HSQ, we have investigated the effect of curing temperature on adhesion of HSQ. In addition, we have studied the effect of oxygen plasma treatment on adhesion. To measure the adhesion force, we have used atomic force microscopy (AFM) [13]. Figure 7.7 shows the adhesion force versus curing temperature for a constant curing time of two minutes, while Figure 7.8 shows the adhesion force versus oxygen plasma treatment time using power and oxygen levels of 300 W and 50 sccm, respectively. We observe that adhesion was improved significantly for curing temperatures above 300°C. The adhesion force measurements were performed after the samples were cooled down to room temperature. Six individual measurements were used for each data point. Also, as the duration of the oxygen plasma treatment increased, the pull-off force was found to increase by a factor of ten compared to bare HSQ (see Figure 7.8).

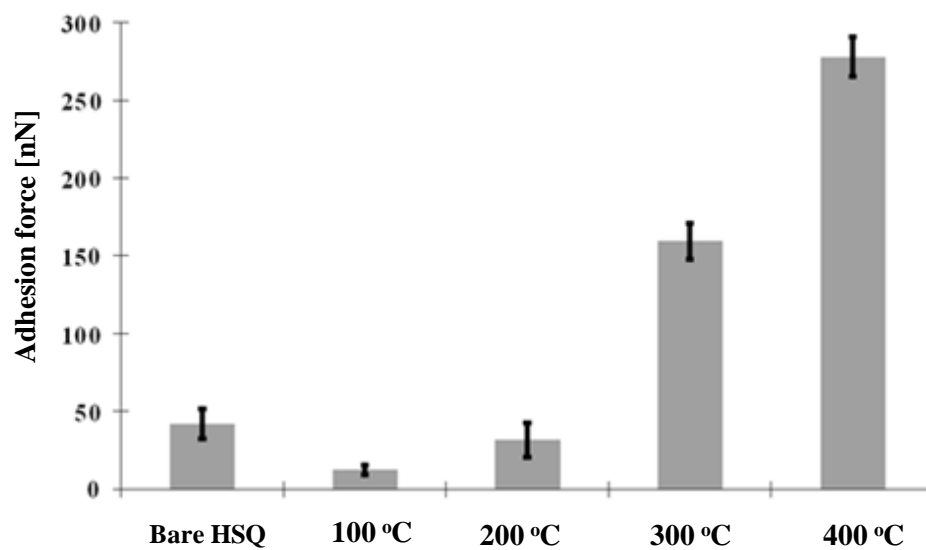


Figure 7.7 Adhesion force as a function of curing temperature

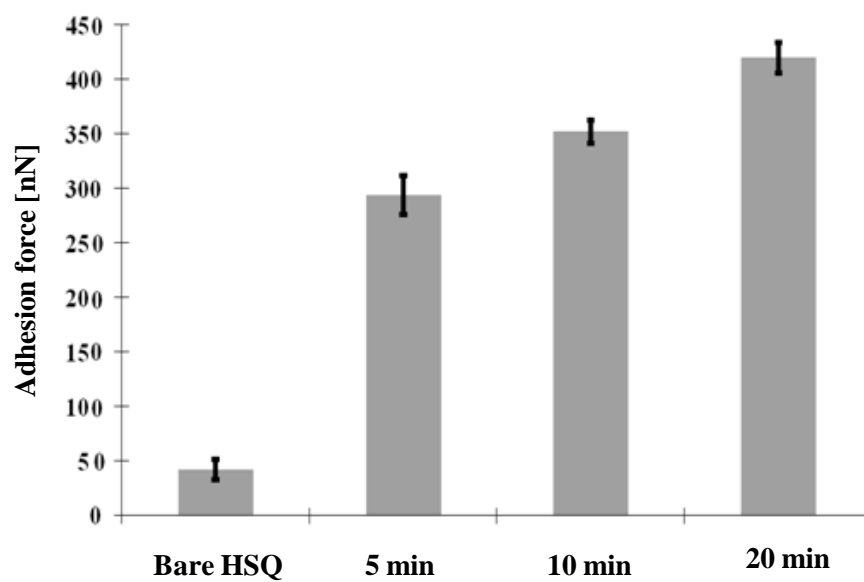


Figure 7.8 Adhesion force as a function of oxygen plasma treatment time

7.3.3 Hardness and scratch studies of HSQ

To study the mechanical strength of HSQ, we have investigated the hardness and delamination resistance of HSQ.

Hardness tests were performed with a commercially available nano-indenter (Hysitron Inc.). A curing temperature up to 400 °C did not show a noticeable increase in the hardness of HSQ (< 1GPa). On the other hand, a large improvement of the hardness was observed after oxygen plasma treatment. Figure 7.9 shows hardness versus time of HSQ sample after oxygen plasma treatment. We observe that an increase in hardness is observed with an increase in the time of oxygen treatment.

To investigate the friction force that causes delamination of planarized HSQ on DTR media, scratch tests were performed along the discrete tracks with a lateral force microscopy (Hysitron Inc.). Figures 7.10 and 7.11 show the friction coefficient versus scratch distance for samples that incurred 5, 10 and 20 minutes of oxygen plasma treatment. At 200 uN (Figure 7.10), a constant friction coefficient was observed during the scratch test, which indicates that no delamination of HSQ has taken place. In Figure 7.10, for a scratch test at 300 uN, we observe a variation in the friction coefficient, which indicates delamination of HSQ.

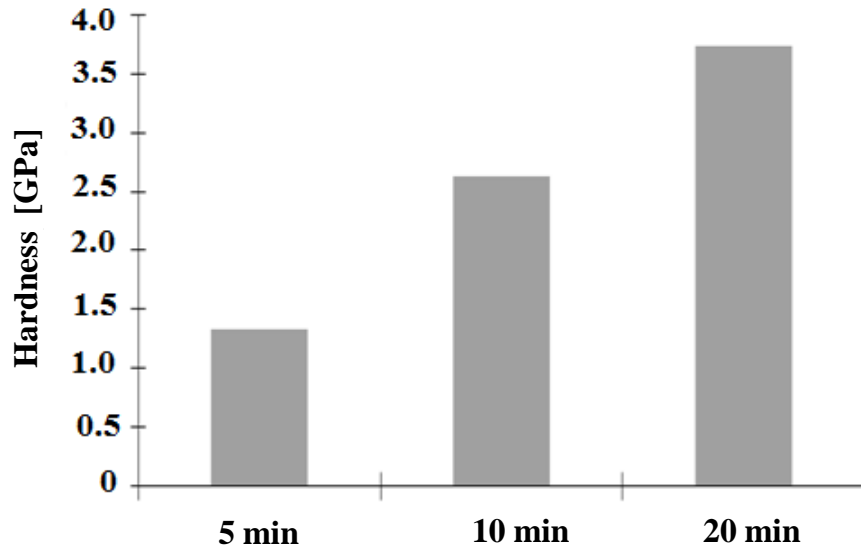


Figure 7.9 Hardness as a function of oxygen plasma treatment time

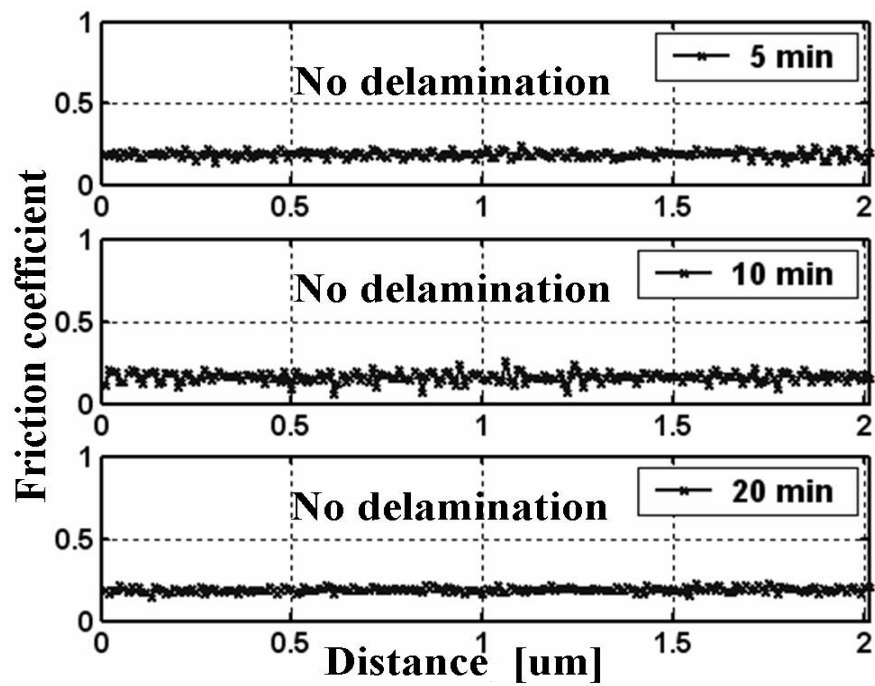


Figure 7.10 Scratch test at 200 uN as a function of oxygen plasma treatment time

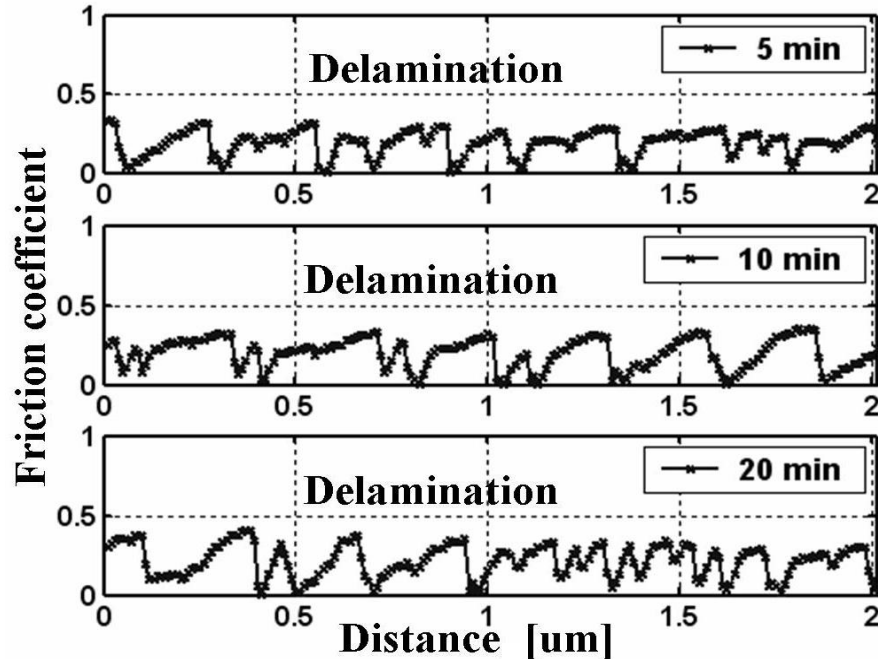


Figure 7.11 Scratch test at 300 uN as a function of oxygen plasma treatment time

7.3.4 Comparison of flyability before and after planarization

To show the benefit of planarization of DTR media, we have performed “flyability” experiments on a DTR disk (groove depth = 40 nm, track pitch = 200 nm, and groove width = 110 nm), which showed severe contacts for magnetic recording sliders designed to fly at 11 and 20 nm over smooth media. For the flying test, we used sliders designed to fly at 11 nm over smooth media. Figure 7.12 shows the standard deviation (STD) of the flying height before and after planarization. Large fluctuations of flying height indicating severe contacts between head and disk were observed before planarization. However, after planarization the standard deviation is two orders of magnitude smaller, indicating improved flyability.

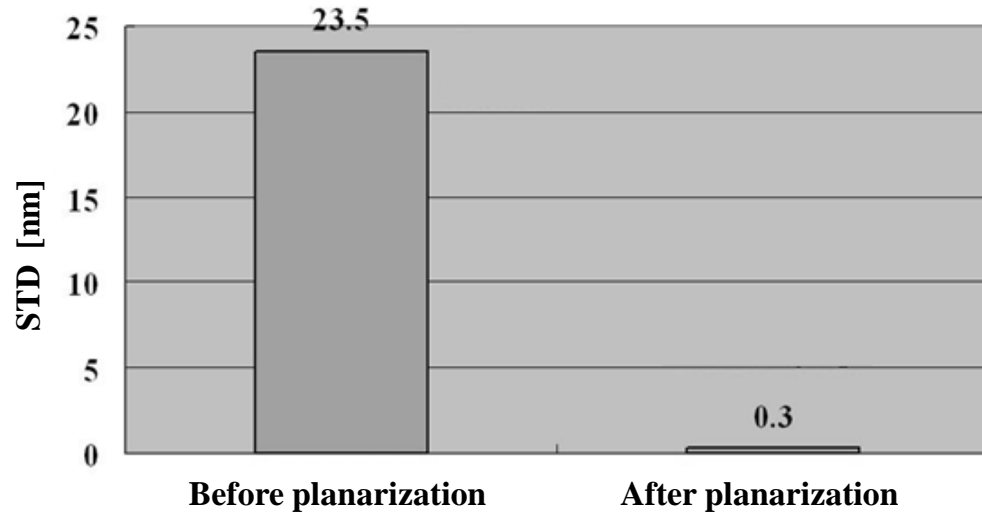


Figure 7.12 Standard deviation (STD) of flying height before and after planarization

7.4 Summary and Conclusions

Hydrogen silsesquioxane (HSQ) shows very good gap filling properties and can be used to planarize DTR disks. The residual groove depth after planarization is dependent on the rotational speed during the spin-coating process. Oxygen plasma treatment improves the mechanical properties of HSQ. Planarized media show improved flyability of magnetic recording sliders on DTR media.

7.5 Acknowledgment

This chapter is a partial reprint of the material as it appears in: “Planarization of Discrete Track Recording Media to Improve Flyability of Magnetic Recording Sliders”, IEEE Transaction on Magnetics, vol. 45, pp. 3527- 3529, 2009, by Y. Yoon, C. Choi, Y. Oh, D. Hong, S. Jin and F. E. Talke. The dissertation author was the primary investigator of this paper while the co-authors listed in this paper directed the research.

Bibliography

- [1] D. Weller, A. Moser, "Thermal Effect Limits in Ultrahigh-Density Magnetic Recording", *IEEE Trans. Mag.* vol. 35, pp. 4423-4439, 1999
- [2] P. S. Chou, "Patterned Magnetic Nanostructures and Quantized Magnetic Disks", *IEEE*, vol. 85, pp. 652-671, 1997
- [3] Y. Kanaia, H. Watanabe, Y. Nakamura, "Single-pole-type head showing a large recording field suitable for 1 Tbit/in² with discrete track media", *JMMM*, vol. 287, pp. 362-366, 2005
- [4] Y. Soeno, et al., "Feasibility of discrete track perpendicular media for high track density recording", *IEEE Trans. Mag.* 39(4):7701266, 2003.
- [5] S. J. Greaves, H. Muraoka, Y. Kanai, "Discrete track media for 600 Gbits/in² recording", *JAP*, 99, 08F903, 2006
- [6] M. Duwensee, S. Suzuki, J. Lin, D. Wachenschwanz, F. E. Talke, "Air Bearing Simulation of Discrete Track Recording Media", *IEEE Trans. Mag.*, 42(10):24892491, 2006.
- [7] M. Duwensee, S. Suzuki, J. Lin, D. Wachenschwanz, F. E. Talke, "Simulation of the Head Disk Interface for Discrete Track Media", *Microsystem Technologies*, vol. 13, pp. 1023-1030, May 2007.
- [8] D. Wachenschwanz, et al, "Design of a manufacturable discrete track recording medium", *IEEE Trans, Mag.*, 41(2):8327247, 2005.
- [9] D. Hong, C. Choi, Y. Oh, Y. Yoon, F. E. Talke, S. Jin, "Planarization of Patterned Magnetic Recording Media for Improved Head Flyability", *Proc. MMM conference*, Austin, TX, #CW-04, 2008.
- [10] H. Liou, J. Pretzer, "Effect of curing temperature on the mechanical properties of hydrogen silsesquioxane thin films", *Thin solid films vol. 335*, pp. 186-191, 1998.
- [11] M. Kawamori, et al., "Effect of Oxygen Plasma Irradiation on Hydrogen Silsesquioxane Nanopatterns Replicated by Room-Temperature Nanoimprinting", *JJAP*, vol. 45, pp. 8994-8996, 2006.
- [12] J. Penaud, F. Fruleux, E. Dubois, "Transformation of hydrogen silsesquioxane properties with RIE plasma treatment for advanced multiple-gate MOSFETs", *Applied Surface Science*, vol. 253, pp. 395-399, 2006.

- [13] H. Butt, B. Cappella, M. Kappl, "Force measurement with the atomic force microscopy: Technique, interpretation and applications", *Surface Science Reports*, vol. 59, pp.1-152, 2005.

Chapter 8

Summary and Conclusions

Since the first hard disk drive (RAMAC) was introduced in 1956, hard disk drives have experienced rapid development in many areas. These developments have led to an increase of areal densities by a factor of two hundred fifty million times. The gap between the head/disk interface has decreased to less than a couple of nanometers. However, there are still many challenges to overcome to achieve ultra-high areal densities such as 1 Tbit/in² and beyond, i.e., 10 Tbit/in².

One of the difficulties in reaching densities of 1 Tbit/in² or more is the limitation due to “superparamagnetism”. To increase the areal density, the magnetic bit size should be reduced. However, as the bit size is decreased, the magnetic energy and the thermal energy of a bit become of the same order of magnitude. In this case, the recorded information randomly flips due to thermal fluctuations and data are lost. To achieve high areal density, this limitation due to the superparamagnetic effect must be overcome.

Much research is currently being conducted to understand this phenomena and to find new recording technologies to overcome the limitation. One promising method is the implementation of patterned media, i.e., discrete track recording

(DTR) media and bit patterned media (BPM). These patterned media can reduce the “cross talk” from adjacent bits by physically separating the magnetic domains.

Also the spacing between the head and the disk interface should be decreased to the range of 1 or 2 nm to achieve 1 Tbit/in² and beyond. Such a low clearance increases the possibility of contact between the head/disk interface, which can result in failure of HDDs. Even for the next generation of patterned media, the challenging issue of contacts should be considered. Furthermore, the tribological issues on patterned media are important factors to be studied.

Discrete track recording medium is a promising new approach. It consists of land area and groove areas that are closely spaced on the disk. To understand the flyability of magnetic sliders on discrete track recording (DTR) media, contact deformation and other tribological properties of discrete track recording media must be investigated.

From atomic force microscopy (AFM) and magnetic force microscopy (MFM) measurements we have found that the groove depth is an important factor with respect to magnetic isolation of land and groove regions. As the groove depth is increased, the magnetic isolation of adjacent grains is improved. Numerical and experimental investigations of flyability of magnetic recording sliders on DTR media have shown that the groove depth is a dominant factor with respect to flying height loss of magnetic recording sliders as well. As the groove depth is increased, the air bearing forces which support the slider decrease. The result is loss of flying height. We have observed the flying characteristics of two different pico-sliders,

designed to fly at 11 nm and 20 nm on smooth media, respectively. Using discrete track recording (DTR) disks with groove depths of 40 nm and a ratio of track pitch to groove width of 0.45, we observed that conventional sliders did not fly well on those disks and that sliders must be designed in such a way that their air bearing force is sufficiently large to support hydrodynamic flying on discrete track recording (DTR) media.

Investigation of hysteresis between “touch-down” and “take-off” of sliders demonstrated that the touch-down velocity was higher for flying of the slider over discrete track recording media than over smooth media. In addition, by keeping the velocity constant and reducing the ambient pressure level for the same slider, we observed that touch-down occurred at a higher ambient pressure level on discrete track recording media than on smooth media. This effect is related to the nominal flying height of the slider over smooth and discrete track media. Hysteresis occurred between touch-down and take-off velocity as well as touch-down and take-off pressure, depending on the flying height design of the slider and the characteristics of the discrete track media. The results for touch-down and take-off behavior of a slider showed qualitative agreement with data from start-stop investigations.

From the experimental investigation of contact deformation and wear characteristics of discrete tracks and smooth surfaces, we observed that damage was found to be much larger in the discrete track areas of discrete track recording (DTR) disk when compared to damage in the smooth areas. It is justifiable to postulate that

the stress distribution in the smooth disk region is much lower than the stress distribution in the narrow land region. The land areas of discrete track disks showed substantially higher wear than the smooth areas outside the discrete track areas.

Spreading and contact angle measurements showed that wettability depends on the geometry of the discrete track recording media. Investigation showed that DTR media are characterized by lower wettability, lower adhesion and lower friction than smooth media. However, the air-bearing force between the slider and the disk decreases due to the groove areas and establishes itself slowly over DTR media. This results in severe contacts between the slider and disk due to poor flyability of the sliders. To get optimal performance of DTR media, we need to determine the trade-off between these advantages and disadvantages.

As a way to improve flyability and the mechanical properties of a slider, planarization of discrete track recording media was performed. In this study, we observed that hydrogen silsesquioxane (HSQ) shows very good gap filling properties and can be used to planarize DTR disks. The residual groove depth after planarization depends on the rotational speed during the spin-coating process. Oxygen plasma treatment improves the mechanical properties of HSQ. Planarized media have improved flyability of magnetic recording sliders over DTR media.

Finally, from the above experimental and numerical studies, we conclude that discrete track recording media has an advantage in terms of well isolated magnetization, low wettability by water, and low surface adhesion. However, flyability of magnetic sliders, plastic deformation and wear characteristics were

worse when compared to conventional smooth media. To improve the reliability and durability of discrete track recording media, planarization of discrete track recording media is essential. In addition, these studies offer further insight to improve bit patterned media (BPM) recording technology to transcend areal densities of 10 Tbit/in².

Appendix A

The Reynolds Equation

To simulate the fluid flow between the slider disk interface, the Reynolds equation is commonly used. The Reynolds equation is valid for very thin fluid films, i.e., the fluid flow of the slider-disk interface. The fluid flow is considered to be laminar and isothermal, and inertial effects are negligible. Due to the very thin fluid film approximation, there exists no velocity component in the direction normal (z -direction) to the interface. In particular, the pressure profile does not vary over the thickness of the fluid film, thus the pressure field can be determined by solving the two-dimensional problem. The fluid is also assumed to be a Newtonian fluid with constant viscosity.

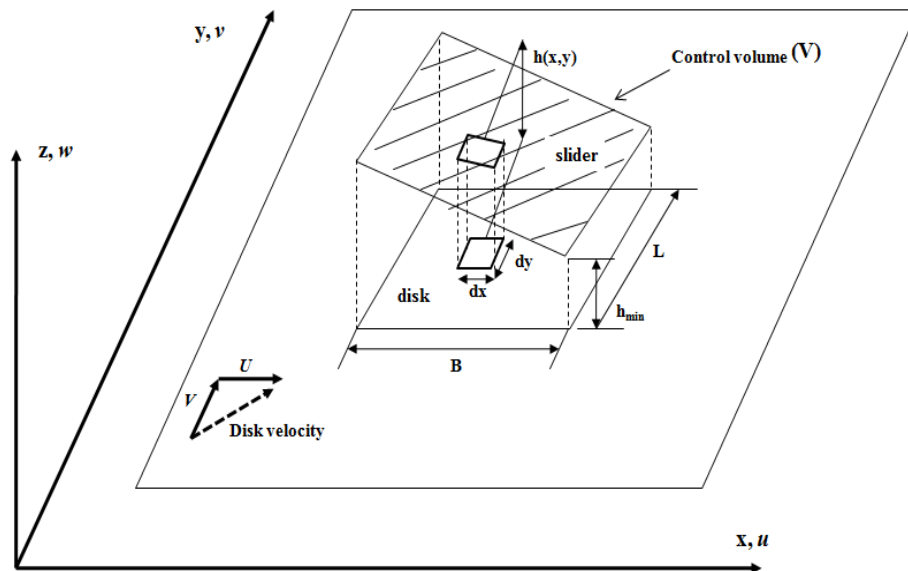


Figure A.1 Control volume of pivoted slider bearing (Source: after [56])

Figure A.1 illustrates the inclined slider bearing. In Figure A.1, B represents the length of the slider, L is the width of the slider, U and V are the velocity components of the disk in the x and y direction, $h(x, y)$ indicates the spacing between slider and disk as a function of x and y , and h_{min} shows the minimum spacing. In the control volume, the conservation of mass and momentum laws must satisfy the condition that the net mass and the net momentum transfer between the inlet and the outlet across the surface area are equal to the rate of change within the volume V .

The conservation of mass is described by

$$\iint_A \rho u_j n_j dA + \iiint_V \frac{\partial \rho}{\partial t} dV = 0 \quad (\text{A.1})$$

where ρ is the density and t is time.

The conservation of momentum is represented by

$$\iint_A \rho u_i u_j n_j dA + \iiint_V \frac{\partial}{\partial t} (\rho u_i) dV = \iint_A \tau_{ij} n_j dA \quad (\text{A.2})$$

where τ_{ij} is the stress tensor.

From the divergence theorem, we can reduce that equations (A.1) and (A.2) are fundamentally independent to the chosen control volume. Thus, the conservations of mass and momentum can be rewritten, respectively, as

$$\frac{\partial}{\partial x_j}(\rho u_j) + \frac{\partial \rho}{\partial t} = 0 \quad (\text{A.3})$$

and

$$\rho \frac{\partial u_i}{\partial t} + \rho u_j \frac{\partial u_i}{\partial x_j} = \frac{\partial \tau_{ij}}{\partial x_j} \quad (\text{A.4})$$

The stress tensor due to the traction forces can be written as

$$\tau_{ij} = \left(-p - \frac{2}{3} \mu \frac{\partial u_k}{\partial x_k}\right) \delta_{ij} + \mu \left(\frac{\partial u_i}{\partial x_j} + \frac{\partial u_j}{\partial x_i}\right) \quad (\text{A.5})$$

where δ_{ij} is the Kronecker delta.

To obtain the fundamental principle for the lubrication problem, an order-of-magnitude analysis is performed by normalizing the continuity and the momentum equations. Dimensionless variables for the coordinates x , y , and z is obtained by the characteristic dimensions of B , L and h_{\min} as follows

$$\bar{x} = \frac{x}{B}, \bar{y} = \frac{y}{L}, \bar{z} = \frac{z}{h_{\min}} \quad (\text{A.6})$$

The mass density is normalized by the ambient density (ρ_a) as

$$\bar{\rho} = \frac{\rho}{\rho_a} \quad (\text{A.7})$$

The dimensionless pressure is obtained by the following

$$\bar{p} = \frac{P}{\tilde{p}} \quad (\text{A.8})$$

where \tilde{p} has yet to be determined.

The dimensionless velocities are defined by U and V as follows

$$\bar{u} = \frac{u}{U}, \bar{v} = \frac{v}{V}, \bar{w} = \frac{w}{W} \quad (\text{A.8})$$

where W has yet to be determined.

To determine the unknown quantity, W , the above dimensionless equations (A.6), (A.7), (A.8), and (A.9) are substituted into the continuity equation to yield

$$\frac{U\rho_a}{B} \frac{\partial}{\partial x} (\bar{\rho}\bar{u}) + \frac{W\rho_a}{h_{\min}} \frac{\partial}{\partial z} (\bar{\rho}\bar{w}) = 0 \quad (\text{A.9})$$

In equation (A.9), the two terms have to be of the same order, thus the velocity scale W in the z direction can be determined by

$$W = \frac{h_{\min}}{B} U \quad (\text{A.10})$$

The undetermined pressure scale \tilde{p} can be obtained by substituting equations (A.6), (A.7), and (A.8) into the x-momentum equation (A.4). The momentum in the x-direction becomes

$$\begin{aligned} & \frac{\rho_a UB}{\mu} \left(\frac{h_{\min}}{B}\right)^2 \left[\frac{\partial}{\partial x} (\overline{\rho u^2}) + \frac{\partial}{\partial z} (\overline{\rho u w}) \right] = \\ & - \frac{\tilde{p}}{\mu UB} \frac{\partial \overline{p}}{\partial x} + \left(\frac{h_{\min}}{B}\right)^2 \left(\frac{1}{3} \frac{\partial^2 \overline{w}}{\partial x \partial z} + \frac{4}{3} \frac{\partial^2 \overline{u}}{\partial x^2} \right) + \frac{\partial^2 \overline{u}}{\partial z^2} \end{aligned} \quad (\text{A.11})$$

The quantity in front of the inertia terms on the left-hand-side of equation (A.11) is defined as a modified Reynolds number

$$\text{Re}^* = \frac{\rho_a UB}{\mu} \left(\frac{h_{\min}}{B}\right)^2 = \text{Re} \left(\frac{h_{\min}}{B}\right)^2 \quad (\text{A.12})$$

where Re is the Reynolds number.

In lubrication theory, the key assumption is that B is much larger than h_{\min} , $\frac{h_{\min}}{B} \ll 1$, so the terms including $\left[\frac{h_{\min}}{B}\right]^2$ are much smaller than unity, and can be neglected in equation (A.11). Thus, the following shows a simplified equation.

$$\frac{\partial \overline{p}}{\partial x} = \frac{\partial^2 \overline{u}}{\partial z^2} \quad (\text{A.13})$$

Equation (A.13) represents the principle equation used in lubrication theory, i.e., pressure forces balance viscous forces.

The pressure scale \tilde{p} is given by

$$\tilde{p} = \frac{\mu UB}{h_{\min}^2} \quad (\text{A.14})$$

Thus, dimensionless variables in a lubrication problem are:

$$\bar{x} = \frac{x}{B}, \bar{y} = \frac{y}{L}, \bar{z} = \frac{z}{h_{\min}}$$

$$\bar{u} = \frac{u}{U}, \bar{v} = \frac{v}{V}, \bar{w} = \frac{wB}{h_{\min}U} \quad (\text{A.15})$$

$$\bar{p} = \frac{ph_{\min}^2}{\mu UB}, \quad \bar{\rho} = \frac{\rho}{\rho_a}$$

If we apply the dimensionless variables (A.15) to equation (A.13), the following result is obtained as

$$\frac{\partial \bar{p}}{\partial \bar{x}} = \frac{\partial}{\partial \bar{z}} \left(\mu \frac{\partial \bar{u}}{\partial \bar{z}} \right) \quad (\text{A.16})$$

For the y-direction, the relationship between the pressure force and the viscous force is determined by

$$\frac{\partial \bar{p}}{\partial \bar{y}} = \frac{\partial}{\partial \bar{z}} \left(\mu \frac{\partial \bar{v}}{\partial \bar{z}} \right) \quad (\text{A.17})$$

From the momentum equation (A.4) for the z-direction, we can obtain the following equation

$$\text{Re}^* \left(\frac{h_{\min}}{B} \right)^2 \left[\frac{\partial}{\partial \bar{z}} (\bar{\rho} \bar{w}^2) + \frac{\partial}{\partial \bar{x}} (\bar{\rho} \bar{u} \bar{w}) \right] =$$

$$-\frac{\partial \bar{p}}{\partial \bar{z}} + \left(\frac{h_{\min}}{B} \right)^2 \left[\frac{1}{3} \frac{\partial^2 \bar{u}}{\partial \bar{x} \partial \bar{z}} + \frac{4}{3} \frac{\partial^2 \bar{w}}{\partial \bar{z}^2} + \left(\frac{h_{\min}}{B} \right)^2 \frac{\partial^2 \bar{w}}{\partial \bar{x}^2} \right] \quad (\text{A.18})$$

By virtue of the assumption of $\frac{h_{\min}}{B} \ll 1$, it can be deduced that

$$\frac{\partial \bar{p}}{\partial z} = 0 \quad (\text{A.18})$$

After integrating equations (A.16) and (A.17) with respect to the z -direction and applying the boundary conditions below,

$$\begin{aligned} u = U, v = V & \quad \text{at } z = 0 \\ u = 0, v = 0 & \quad \text{at } z = h \end{aligned} \quad (\text{A.19})$$

the velocity components are obtained as

$$u = \frac{1}{2\mu} \frac{\partial p}{\partial x} (z^2 - zh) + U \left(1 - \frac{z}{h}\right) \quad (\text{A.20})$$

$$v = \frac{1}{2\mu} \frac{\partial p}{\partial y} (z^2 - zh) + V \left(1 - \frac{z}{h}\right) \quad (\text{A.21})$$

For the continuity of mass across the boundaries of the differential fluid element in Figure A.1 to be satisfied, the continuity equation is invoked, i.e.,

$$\frac{\partial \rho}{\partial t} + \frac{\partial}{\partial x}(\rho u) + \frac{\partial}{\partial y}(\rho v) + \frac{\partial}{\partial z}(\rho w) = 0 \quad (\text{A.22})$$

where the pressure is assumed to be governed by the laws of an ideal gas as below

$$\begin{aligned} p &= \rho RT \\ \rho &= \text{constant}(1/RT) * p \end{aligned} \quad (\text{A.23})$$

The integration of the continuity equation (A.22) over the film thickness, $h(x, y)$, can be expressed by

$$\int_0^h \left[\frac{\partial \rho}{\partial t} + \frac{\partial}{\partial z}(\rho u) + \frac{\partial}{\partial z}(\rho v) + \frac{\partial}{\partial z}(\rho w) \right] dz = 0 \quad (\text{A.24})$$

After rearranging equation (A.24), the following is obtained,

$$\begin{aligned} \int_0^h \frac{\partial}{\partial z}(\rho w) dz &= - \int_0^h \left[\frac{\partial \rho}{\partial t} + \frac{\partial}{\partial z}(\rho u) + \frac{\partial}{\partial z}(\rho v) \right] dz \\ \rho w|_0^h &= - \int_0^h \left[\frac{\partial \rho}{\partial t} + \frac{\partial}{\partial z}(\rho u) + \frac{\partial}{\partial z}(\rho v) \right] dz \end{aligned} \quad (\text{A.25})$$

Here, the vertical velocity w at the disk surface, $w(0)$, is zero.

Thus, the vertical velocity w at the slider, $w(h)$, can be written by

$$w(h) = \frac{\partial h}{\partial t} + u(h) \frac{\partial h}{\partial x} + v(h) \frac{\partial h}{\partial y} \quad (\text{A.26})$$

Due to the no-slip boundary conditions, i.e., $u(h) = 0$ and $v(h) = 0$, the vertical velocity in the z -direction will be

$$w(h) = \frac{\partial h}{\partial t} \quad (\text{A.27})$$

After substituting equation (A.27) into equation (A.25), we can obtain

$$\rho \frac{\partial h}{\partial t} = - \int_0^h \left[\frac{\partial \rho}{\partial t} + \frac{\partial}{\partial z}(\rho u) + \frac{\partial}{\partial z}(\rho v) \right] dz \quad (\text{A.28})$$

By rearranging equation (A.25) after applying Leibnitz rule, we obtain

$$\rho \frac{\partial h}{\partial t} = -\frac{\partial}{\partial t} \int_0^h \rho dz + \rho \frac{\partial h}{\partial t} - \frac{\partial}{\partial x} \int_0^h \rho u dz + \frac{\partial h}{\partial x} \rho u \Big|_{z=h} - \frac{\partial}{\partial y} \int_0^h \rho v dz + \frac{\partial h}{\partial y} \rho v \Big|_{z=h} \quad (\text{A.29})$$

After no-slip boundary conditions are applied and the results are rearranged, equation (A.29) can be written as

$$\frac{\partial \rho h}{\partial t} = -\frac{\partial}{\partial x} \int_0^h \rho u dz - \frac{\partial}{\partial y} \int_0^h \rho v dz \quad (\text{A.30})$$

Finally, by substituting the velocity profiles in equations (A.20) and (A.21), and the laws of an ideal gas in equation (A.29) into equation (A.30), the 2-D compressible Reynolds equation can be obtained written in the following form

$$\frac{\partial}{\partial x} \left(\rho h^3 \frac{\partial p}{\partial x} \right) + \frac{\partial}{\partial y} \left(\rho h^3 \frac{\partial p}{\partial y} \right) = 6\mu(U \frac{\partial \rho h}{\partial x} + V \frac{\partial \rho h}{\partial y}) + 12\mu \frac{\partial \rho h}{\partial t} \quad (\text{A.31})$$

Appendix B

Slider Air Bearing Simulations and the CMRR Air Bearing Simulator

The numerical solution of the Reynolds equation calculates the pressure distribution and spacing over the air bearing surfaces. The air bearing force is balanced by the suspension pre-load.

In hard disk drives, the magnetic recording slider has three degrees of freedom, i.e., a translation in the vertical direction and two rotations about the pivot point which are referred to as pitch (α) and roll (β) (see Figure B.1). The spring represents the stiffness of the suspension. The pitch and roll motions are measured with respect to the pivot point. The translation in the z-direction is related with the vertical stiffness of the suspension k_z while the pitch angle (α) and roll angle (β) are affected by the stiffness of k_α and k_β , respectively.

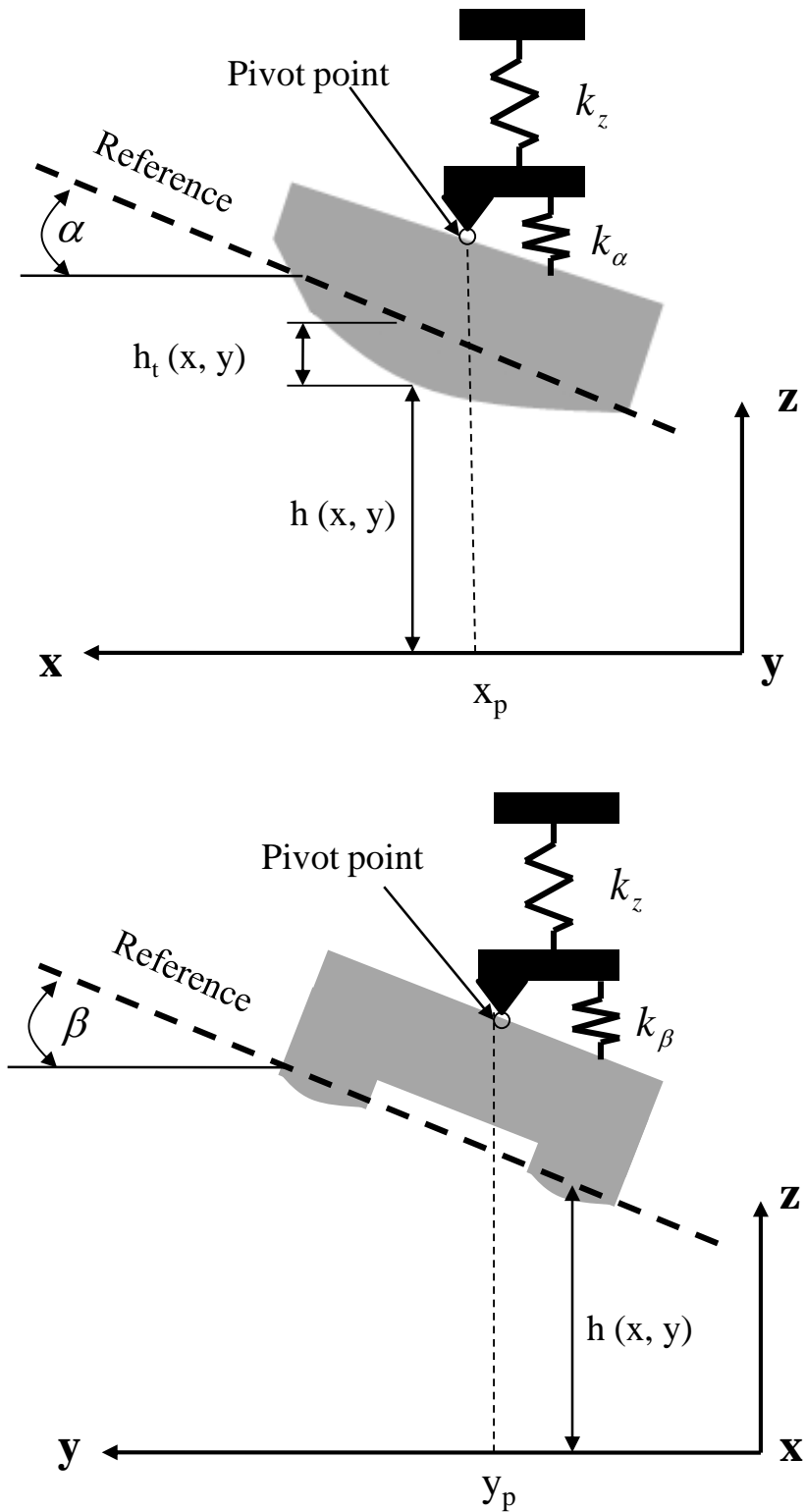


Figure B.1 Schematic of pivoted magnetic slider (Source: [1, 2])

The equilibrium in the z -direction is illustrated by Figure B.2. The unloaded slider at position z_0 is compressed by the air bearing force until equilibrium is reached between air bearing force and suspension pre-load. For the case of small perturbations, the reaction force can be written by

$$k_z(z_2 - z_1) = F_{air} - F_{ext} \quad (\text{B.1})$$

where F_{air} is the air bearing force.

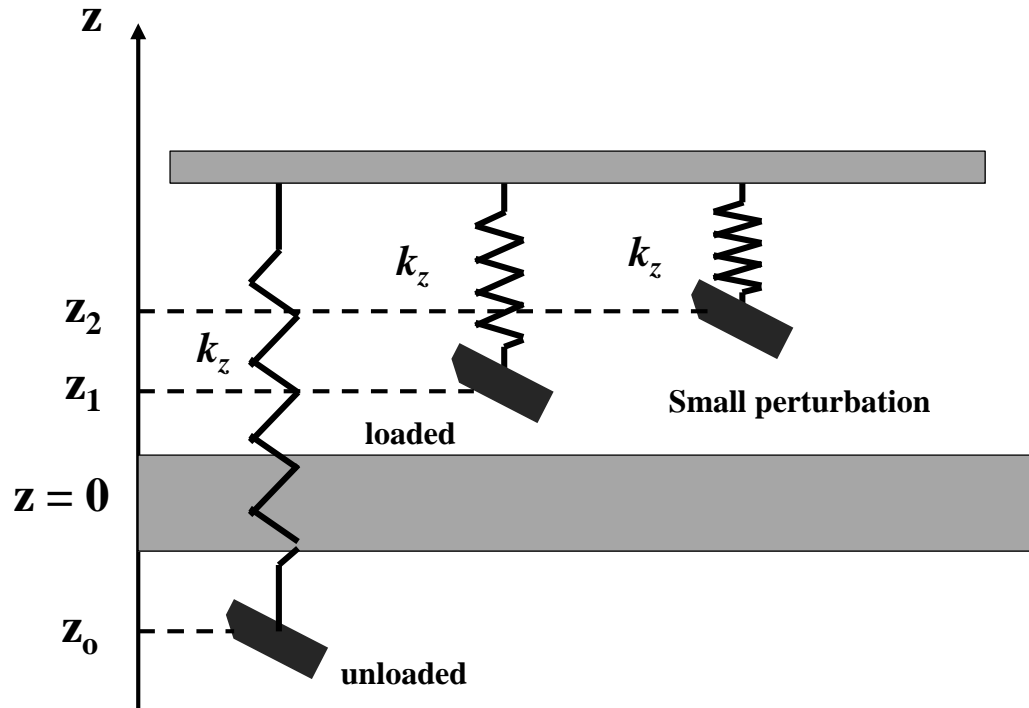


Figure B.2 Schematic of equilibrium of magnetic recording slider in vertical direction (Source: [1, 2])

The air bearing force is calculated by integrating the pressure over the air bearing surfaces, i.e.,

$$F_{air} = \iint_A p(x, y) dA \quad (B.2)$$

where $p(x, y)$ is pressure generated between slider and disk.

The equilibrium of the pitch and roll motions is obtained in a similar way.

The equilibrium equation for the pitch motion is given by

$$k_\alpha d\alpha = \iint_A p(x, y)(x - x_p) dA - M_\alpha^{ext} \quad (B.3)$$

where x_p is the position of the pivot point in x-direction.

For the roll motion, the equilibrium equation is expressed by

$$k_\beta d\beta = \iint_A p(x, y)(y - y_p) dA - M_\beta^{ext} \quad (B.4)$$

where y_p is the position of the pivot point in y-direction.

Using the above three equilibrium equations (B.2), (B.3) and (B.4), we obtain the matrix formation

$$\left\{ \begin{array}{l} \iint_A p(x, y) dA - F_z^{ext} \\ \iint_A p(x, y)(x - x_p) dA - M_\alpha^{ext} \\ \iint_A p(x, y)(y - y_p) dA - M_\beta^{ext} \end{array} \right\} = \begin{bmatrix} k_z & 0 & 0 \\ 0 & k_\alpha & 0 \\ 0 & 0 & k_\beta \end{bmatrix} \begin{Bmatrix} dh \\ d\alpha \\ d\beta \end{Bmatrix} \quad (B.5)$$

Equation (B.5) represents that the air bearing force and external suspension pre-load are balanced. The position obtained by these equilibrium equations is the

so-called steady state position of a magnetic recording slider. This is referred to as the flying height of the slider at steady state.

To calculate the steady state position, the Center for Magnetic Recording Research (CMRR) air bearing simulator is used. In the CMRR air bearing simulator, the Reynolds equation and the slider equilibrium equation are simultaneously solved using Finite Element Analysis and a Newton-Raphson Scheme.

The Reynolds equation is a second order non-linear partial differential equation giving the pressure distribution over the air bearing surface as a function of the spacing h . A finite element formulation is used to calculate the Reynolds equation in the CMRR air bearing simulator. The finite element formulation of the CMRR air bearing simulator was originally developed by Wahl [1]. A number of improvements have been made in the past by various students in the Talkelab, including Duwensee [2-4]. The fundamental concept of the finite element method is to divide the air bearing surface into a finite number of small elements over which the Reynolds equation must be satisfied. Galerkin's "weighted residual approach" is then used to satisfy the differential equation by introducing a weight function W .

Hence, the weighted residual formulation of the Reynolds equation is given by

$$\iint_{\Omega} \left\{ \nabla \cdot (Qph^3 \nabla p) - 6\mu V \cdot \nabla(ph) - 12u \frac{\partial}{\partial t}(ph) \right\} W d\Omega = 0 \quad (\text{B.6})$$

where W is the weight function and Ω represents the domain. By choosing the weight function to be zero at the boundary, which is equal to ambient pressure, equation (B.6) can be written as

$$\iint_{\Omega} \left\{ -\cdot(Qph^3\nabla p)\nabla W - 6\mu V \cdot \nabla(ph)W - 12u \frac{\partial}{\partial t}(ph)W \right\} d\Omega = 0 \quad (\text{B.7})$$

If the time dependant terms in equation (B.7) are zero, we obtain the “steady state” problem given by

$$\iint_{\Omega} \left\{ -\cdot(Qph^3\nabla p)\nabla W - 6\mu V \cdot \nabla(ph)W \right\} d\Omega = 0 \quad (\text{B.8})$$

Equation (B.8) is the finite element formulation of the steady state Reynolds equation.

The Newton-Raphson scheme is applied to the coupled system of equations, i.e., the Reynolds equation and the slider equilibrium equation. The Newton-Raphson scheme is an accurate second order method to determine the stiffness matrix given by

$$[K] \cdot \{dp\} = \{r\} \quad (\text{B.6})$$

In equation (B.6), the matrix $[K]$ is the so-called stiffness matrix, $\{dp\}$ represents the vector of the unknown pressure and $\{r\}$ is the right hand side. The stiffness matrix in equation (B.6) is expanded by three rows and columns corresponding to

the three degrees of freedom of the slider equilibrium equation (B.5). Therefore, the partitioned form can be written by

$$\begin{bmatrix} \frac{\partial R}{\partial p} & \frac{\partial R}{\partial \zeta} \\ -\frac{\partial F}{\partial p} & K_s \end{bmatrix}^n \begin{bmatrix} dp \\ d\zeta \end{bmatrix} = \begin{bmatrix} -R^n \\ F^n - F_{\text{ext}} \end{bmatrix} \quad (\text{B.7})$$

where R is the discretized Reynolds equation using the finite element method, i.e.,

$$R(\zeta, p(\zeta)) = 0 \quad (\text{B.8})$$

where ζ are normalized Cartesian coordinates and p is the pressure. The other terms are related to the slider equilibrium equations of

$$F(p(\zeta)) - F_{\text{ext}} = K_s d\zeta \quad (\text{B.9})$$

Finally, Figure B.3 shows the block diagram of the Newton-Raphson scheme for steady state flying height using the CMRR air bearing simulator. An iterative procedure is used .

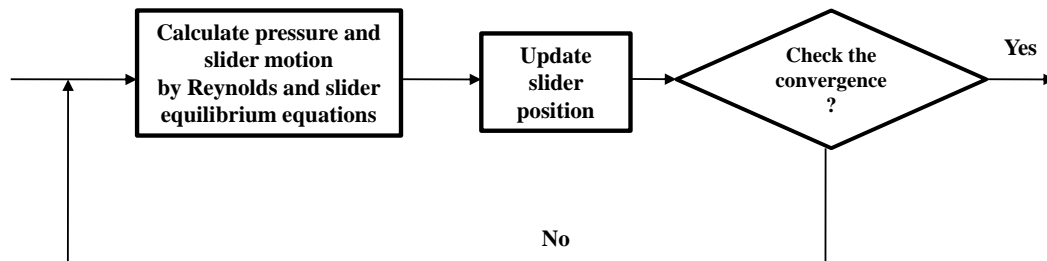


Figure B.3 Newton-Raphson Scheme to calculate steady state flying height using the CMRR simulator

Bibliography

- [1] M. Wahl, Numerical and experimental investigation of the head/disk interface, PhD thesis, University of San Diego, 1994.
- [2] M. Duwensee, Improvements in the Pre- and Post-processing software for a finite element based air bearing simulator and analysis of intermolecular forces in the head/disk interface, Master's thesis, University of California, San Diego, 2004.
- [3] M. Duwense, S. Suzuki, J. Lin, D. Wachenschwanz, F. E. Talke, "Air bearing simulation of discrete track recording media," *IEEE Trans. Mag.*, vol. 42, pp. 2489-2491, 2006.
- [4] M. Duwense, S. Suzuki, J. Lin, D. Wachenschwanz, F. E. Talke, "Simulation of the head/disk interface for discrete track media," *Microsyst. Technol.*, vol. 13, pp. 1023-1030, 2006.